I: Interannual Variability of Stratospheric Ozone and Temperature

II: Seasonal Cycle of N_2O

Thesis by

Xun Jiang

In Partial Fulfillment of the Requirements

for the Degree of

Doctor of Philosophy

California Institute of Technology

Pasadena, California

2006

(Defended July 24, 2006)

Acknowledgements

I would like to thank the many people without whom this thesis would not have been possible. Foremost is my advisor, Yuk L. Yung, whom I thank for his insightful guidance and generous support. I also want to thank Dr. Runlie Shia, who helped my understanding of the chemistry and transport model, in addition Andrew Ingersoll, Paul Wennberg, and Tapio Schneider for their advice in the thesis research.

I would like to thank Alexander Ruzmaikin, Joan Feynman, and Duane Waliser at JPL. I also want to thank Dylan Jones at the University of Toronto, Var Limpasuvan at Coastal Carolina University, and Steven Pawson and Eric Nielsen in the Global Modeling and Assimilation Office, for their advice and assistance in the research.

I would like to thank the following graduate students and postdocs for their help and discussions. David Camp, Dave Noone, Chris Walker, Dan Feldman, Maochang Liang, and Vijay Natraj.

I must thank Mike Black for his computer help and staff members Loreta Young, Linda Scott, Leticia Calderon, Nora Oshima, and Irma Black, for their support.

To my family, Zuzhang, Xiucui, and Liming: thank you for all your encouragement and advice. This truly would have been impossible without you. It is to you this thesis is dedicated.

Abstract

This dissertation is a collection of empirical and modeling studies focusing on the interannual variability (IAV) of the stratospheric ozone and temperature. The IAV of O_3 in the high latitude is characterized by four main modes in both hemispheres. Similar spatial patterns and trends are simulated by the Goddard Earth Observation System, Version 4 (GEOS-4) chemistry-climate model (CCM). The El Niño-Southern Oscillation signal in column ozone is also simulated well by the GEOS-4 CCM in the tropics.

To study the Quasi-biennial oscillation (QBO) and QBO-Annual Beat (QBO-AB) in column ozone, the Caltech/JPL two-dimensional (2-D) chemistry and transport model (CTM) has been used. The 2-D CTM provides realistic simulations of the seasonal and IAV of ozone in the tropics. The phase and amplitude of the QBO are well captured by the model. The QBO-AB found in the simulated ozone agrees well with that in the observed data. An idealized 2-D interactive chemistry, radiation, and dynamic model (CRDM) is used to investigate the spatial patterns of, and mechanism for, the QBO-AB signal in ozone in the tropics and subtropics. An extended EOF analysis reveals the characteristic pattern of the downward propagation of QBO and upward propagation of QBO-AB. The model results are compared to those from the Merged Ozone Data.

To understand the IAV and trend in the stratospheric temperature, we apply principal component analysis to observations and global climate model simulations. The cooling trend in the stratosphere is associated with a spatially uniform pattern of stratospheric variability, which is isolated from more common modes of natural IAV

such as the Northern Annular Mode. These results are supported by a number of coupled ocean-atmosphere climate model simulations.

Finally, a systematic study of the seasonal cycle and its latitudinal variation is carried out for the nitrous oxide data. In order to confirm the weak seasonal signal in the observations, we applied the multi-taper method for the spectrum analysis. The amplitude (peak to peak) of the seasonal cycle of N_2O varies from 0.29 ppb (parts-per-billion by mole fraction in dry air) at the South Pole to 1.15 ppb at Alert.

Contents

List of Figures

List of Tables

Overview

This dissertation is a collection of empirical and modeling studies focusing on the interannual variability (IAV) of the stratospheric ozone and temperature. The highlights for each chapter are listed in Table1 at the end of overview.

In Chapter 1[1], the Caltech/JPL two-dimensional (2-D) chemistry and transport model (CTM) has been used to study the ozone IAV. The National Centers for Environmental Prediction (NCEP)/Department of Energy (DOE) Reanalysis 2 data are used to calculate the monthly mean meridional circulation and eddy diffusivity from 1979 to 2002 for use in CTM. This allows for an investigation of the impact of dynamics on the interannual variability (IAV) of the total column ozone for all years for which the Merged ozone data (MOD) are available. The first empirical orthogonal function (EOF), accounting for over 70% of the interannual variance, is related to the quasi-biennial oscillation (QBO) and its interaction with annual cycles, the QBO-annual beat (QBO-AB). The 2-D CTM provides realistic simulations of the seasonal and IAV of ozone in the tropics. The phase and amplitude of the QBO are well captured by the model. The magnitude of the QBO signal is somewhat larger in the model than in the data. The QBO-AB found in the simulated ozone agrees well with that in the observed data. It also has reasonable agreement for the ozone anomaly in Northern Hemisphere (NH) and Southern Hemisphere (SH).

[1] Chapter 1 has appeared as "Jiang, X., C. D. Camp, R. Shia, D. Noone, C. Walker, and Y. L. Yung, Quasi-biennial oscillation and quasi-biennial oscillation-annual beat in the tropical total column ozone: A two-dimensional model simulation, Journal of Geophysical Research, 109, doi:10.1029/2003JD004377". It is reproduced in this dissertation with permission of the publisher.

In Chapter 2[2], an idealized 2-D interactive chemistry, radiation, and dynamic model (CRDM) is used to investigate the spatial patterns of, and mechanism for, the QBO-AB signal in ozone in the tropics and subtropics. An extended EOF analysis reveals the characteristic pattern of the downward propagation of QBO and upward propagation of QBO-AB. The model results are compared to those from the MOD. Sensitivity experiments indicate that the QBO-AB is produced primarily as a result of the dynamical QBO-AB in the mean meridional circulation and by the interaction between the QBO and the annual cycle in transport, each contributing roughly equally to the forcing of QBO-AB. The interaction between the QBO in the transport fields and the annual cycle in chemistry plays a minor role.

In Chapter 3[3], principal component analysis (PCA) is applied to the total column ozone data from the combined MOD and European Center for Medium-Range Weather Forecasts assimilated ozone. The IAV of O_3 in the high latitude is characterized by four main modes in NH and SH. Attributable to dominant dynamical effects, these four modes account for nearly 60% and 75% of the total ozone variance in the NH and SH, respectively. In both hemispheres, the first two leading modes are nearly zonally symmetric and represent the connections to the Annular Modes and the Quasi-Biennial Oscillation. The latter two modes exhibit in-quadrature, wavenumber-1 structures that

[2] Chapter 2 has appeared as "Jiang, X., D. B. A. Jones, R. Shia, D. E. Waliser, and Y. L. Yung, Spatial patterns and mechanisms of the Quasi-biennial oscillation-Annual beat of ozone, Journal of Geophysical Research, 110, doi:10.1029/2005JD006055". It is reproduced in this dissertation with permission of the publisher.

[3] Chapter 3 was submitted as a journal article, "Jiang, X. S. Pawson, C. D. Camp, E. Nielsen, R. Shia, T. Liao, K. Jeev, V. Limpasuvan, and Y. L. Yung, Interannual variability in high latitude stratospheric ozone".

represent the displacement of the polar vortex in response to planetary waves. In NH, these combined modes have preferred extremal location that suggests fixed topographical and land-sea thermal forcing of the involved planetary waves. Such stationary forcing is not apparent in the SH modes. Similar spatial patterns and trends are simulated by the Goddard Earth Observation System, Version 4 (GEOS-4) chemistry-climate model (CCM). To relate the results to the atmospheric dynamics, similar decompositions are performed for geopotential thicknesses between 30 hPa and 100 hPa. The results reveal close connections between the IAV of ozone and that of the atmospheric dynamics. The decreasing O_3 trends in both hemispheres are captured in the first mode and are successfully reproduced by the GEOS-4 CCM. However, the model overestimates the trend in the NH, especially after 1997.

In Chapter 4, El Niño-Southern Oscillation (ENSO) signals in the stratospheric column ozone and tropopause pressure are simulated by the GEOS-4 CCM in the tropics. The first mode for the stratospheric column ozone, capturing 65.8% of the total variance, is related to the ENSO. The spatial pattern of the first mode is very similar to the ENSO signal in the column ozone observed by Total Ozone Mapping Spectrometer (TOMS) instrument. However, there are some discrepancies for the model ozone in the southern hemisphere. There is also a clear ENSO signal in the tropical tropopause in the chemistry-climate model, which may be cause for the ENSO signal in the stratospheric ozone.

In Chapter 5[4], to understand the IAV and trend in the stratospheric temperature, we apply PCA to observations and global climate model simulations to investigate the variability of stratospheric temperature. Most (~76%) of the IAV of temperature in the northern hemisphere can be characterized by the first four principal modes. The cooling trend in the stratosphere is associated with a spatially uniform pattern of stratospheric variability, which is isolated from more common modes of natural IAV such as the Northern Annular Mode (NAM). These results are supported by a number of coupled ocean-atmosphere climate model simulations of the 20th century that were contributed to the International Panel on Climate Change's 4th Assessment Report. Given the spatial uniformity of the increased GHG forcing, this separation and identification of a spatially uniform stratospheric temperature response is not only plausible but might be expected and provides a simple yet useful test for global climate models used for projecting global warming.

In Chapter 6[5], a systematic study of the seasonal cycle and its latitudinal variation is carried out in the nitrous oxide (N_2O) data collected by National Oceanic and Atmospheric Administration-Global Monitoring Division (NOAA-GMD) and the Advanced Global Atmospheric Gases Experiment (AGAGE). In order to confirm the weak seasonal signal in the observations, we apply the multi-taper method for the spectrum analysis and imposed the criterion that the seasonal signal must be below 1% significance level. In addition, the measurement errors must be small compared with the

[4] Chapter 5 will be submitted as a journal article, "Jiang, X., D. E. Waliser, R. Shia, and Y. L. Yung, Distinguishing climate change from natural variability in the stratosphere".
[5] Chapter 6 was accepted as "Jiang, X., W. Ku, R. Shia, Q. Li, J. W. Elkins, R. G. Prinn, and Y. L. Yung, The seasonal cycle of N2O: Analysis of data, Global Biogeochemical Cycles, Accepted, 2006".

seasonal cycle. The N_2O seasonal cycles from seven stations satisfy these criteria and are analyzed in detail. The amplitude (peak to peak) of the seasonal cycle of N_2O varies from 0.29 ppb (parts-per-billion by mole fraction in dry air) at the South Pole to 1.15 ppb at Alert. The month at which the N_2O concentration is at a minimum varies monotonically from April (South Pole) to September (Alert). The seasonal cycle in the northern hemisphere shows the influence of the stratosphere; the seasonal cycle of N_2O in the southern hemisphere suggests greater influence from surface sources. Preliminary estimates are obtained for the magnitude of the seasonally varying sources needed to account for the observations.

Table 1: Highlights for all Chapters.

	Highlights
Chapter 1	Successfully simulate the IAV of the tropical ozone using 2-D Caltech/JPL chemistry and transport model
Chapter 2	Investigate the spatial patterns of, and mechanism for, the QBO-AB signal in ozone. Reveal the vertical propagation of QBO and QBO-AB.
Chapter 3	Examination the IAV of O_3 in the high latitudes using observation and 3-D chemistry-climate model. 3.5-year signal in the leading mode of NH.
Chapter 4	ENSO signal in O_3 simulated by 3-D chemistry-climate model
Chapter 5	IAV and trend in the stratospheric temperature
Chapter 6	Systematic study of the seasonal cycle in nitrous oxide

I: Interannual Variability of Stratospheric Ozone and Temperature

Chapter 1: Quasi-biennial Oscillation and Quasi-biennial Oscillation-Annual Beat in the Tropical Total Column Ozone: A Two-Dimensional Model Simulation

1.1 Abstract

The National Centers for Environmental Prediction/Department of Energy (NCEP/DOE) Reanalysis 2 data are used to calculate the monthly mean meridional circulation and eddy diffusivity from 1979 to 2002 for use in the Caltech/JPL two-dimensional (2-D) chemistry and transport model (CTM). This allows for an investigation of the impact of dynamics on the interannual variability (IAV) of the tropical total column ozone for all years for which the Total Ozone Mapping Spectrometer and the Solar Backscatter Ultraviolet merged total ozone data are available. The first two empirical orthogonal functions (EOFs) of the deseasonalized and detrended stratospheric stream function capture 88% of the total variance on interannual timescales. The first EOF, accounting for over 70% of the interannual variance, is related to the quasi-biennial oscillation (QBO) and its interaction with annual cycles, the QBO-annual beat (QBO-AB). The 2-D CTM provides realistic simulations of the seasonal and IAV of ozone in the tropics. The equatorial ozone anomaly from the model is close to that derived from the observations. The phase and amplitude of the QBO are well captured by the model. The magnitude of the QBO signal is somewhat larger in the model than in the data. The QBO-AB found in the simulated ozone agrees well with that in the observed data.

1.2 Introduction

One of the major goals of upper atmosphere research is to observe the expected recovery of the ozone layer resulting from the regulation of chlorofluorcarbons (CFCs) and other ozone-depleting substances by the Montreal Protocol [*Austin et al*. 2000; see also *World Meteorological Organization* (WMO), 2003, Chapter 4]. Before the Montreal Protocol was implemented, the average rate of ozone depletion between 60°S and 60°N was about 2% per decade. The derivation of this loss rate was more reliable in the Southern Hemisphere (SH), where it was dominated by the occurrence of the Antarctic Ozone Hole in the austral spring. The signal was smaller in the Northern Hemisphere (NH) and subject to interference by a large seasonal cycle (5%) and an uncertain interannual variability (IAV) of about 2% [*World Meteorological Organization* (WMO), 2003, Chapter 4]. Indeed, a substantial fraction of the observed ozone depletion may be attributed to the natural IAV in atmospheric dynamics [*e.g., Hood et al.*, 1997; *Fusco and Salby*, 1999; *Hadjinicolaou et al.*, 2002]. The question of what fraction of the change is chemical versus dynamical has never been satisfactorily resolved. The unambiguous detection of the expected recovery would be even more difficult because of the slow rate of decay of CFCs. *Stevermer and Weatherhead* [2001] estimated that it might take 15-35 years to detect this gradual recovery in the total column ozone, even under the best of circumstances. Therefore, a better characterization of the IAV of ozone is urgently needed.

Shiotani [1992] found QBO and El Niño-Southern Oscillation (ENSO) signals in the total column ozone derived from the Total Ozone Mapping Spectrometer (TOMS) from 1979 to 1989. Using the Merged Ozone Data set (MOD), which combined the monthly mean column abundances collected by the TOMS and the Solar Backscatter Ultraviolet (SBUV and SBUV/2) instruments, *Camp et al.* [2003] carried out a principal component analysis (PCA) of the temporal and spatial patterns of the IAV of the total column ozone in the tropics from late 1979 to 2000 on a $5^{\circ} \times 10^{\circ}$ latitude-longitude grid. This study was a complete analysis of tropical ozone data using simultaneously the longitudinal, latitudinal and temporal patterns. The first four empirical orthogonal functions (EOFs) of their study captured over 93% of the variance of the detrended and deseasonalized data on interannual timescales. The leading two EOFs, respectively accounting for 42% and 33% of the variance, displayed structures attributable to the quasi-biennial oscillation (QBO), with influence from a decadal oscillation (most likely the solar cycle). The third EOF (15% of the variance) represented an interaction between the QBO and an annual cycle. The fourth EOF (3% of the variance) was related to the ENSO. In this chapter we will concentrate on the modeling of the QBO and the QBO-annual beat (QBO-AB), which together account for more than 50% of the IAV of tropical ozone. Other interannual variability, *e.g*. ENSO, will be studied in the future.

The mechanism by which the QBO modulates ozone column abundance in the stratosphere is well known [*Plumb and Bell*, 1982; see also *Baldwin et al.*, 2001]. When the QBO is in the westerly (easterly) phase, there is descending (upwelling) anomalous motion in the tropical stratosphere and upwelling (descending) anomalous motion in the

subtropical stratosphere. This results in more (less) ozone at the equator in the westerly (easterly) QBO phase [*Tung and Yang*, 1994a; *Randel and Cobb*, 1994]. The QBO period varies from about 22 to 32 months, with an average of 28 months. The interaction of the annual cycle with the QBO will produce two cycles with periods of approximately 20 and 8.6 months [*Tung and Yang*, 1994a]. These periods were first found in the total column ozone data obtained by TOMS in the tropics and extra-tropics [*Tung and Yang*, 1994a; *Tung and Yang*, 1994b].

Several idealized numerical models have been developed to study the influence of the QBO on the ozone. Using a mechanistic model, *Hasebe* [1994] found that the phase of the ozone QBO approaches that of the temperature QBO. *Politowicz and Hitchman* [1997] introduced an analytic forcing of the stratospheric QBO in a two-dimensional (2-D) middle atmosphere model in three different ways. They used a different amplification factor for each method seeking good agreement with the observed QBO in the column ozone, and found that the diabatic forcing method was better than that of wave-driving and thermal-nudging. Similarly, using an equatorial wave forcing parameterization, *Jones et al*. [1998] successfully generated a QBO with a period of about 28 months. The induced circulation in their model was stronger in the winter hemisphere. Further analysis of the *Jones et al.* [1998] model [*Jiang et al*., 2005] reveals the existence of a QBO-AB signal at about 20 months. However, the *Jones et al.* [1998] model is an idealized model and it cannot simulate the IAV of the observed ozone.

Kinnersley and Tung [1999] used an interactive stratospheric model by relaxing the equatorial zonal wind to the observed Singapore zonal wind. Their model simulates the observed ozone anomaly satisfactorily. However, there appears to be some underestimation of the equatorial QBO amplitude in the ozone column.

Fleming et al. [2002] used the meteorological data from the United Kingdom Meteorological Office (UKMO) model and constituent data from the Upper Atmospheric Research Satellite (UARS) to calculate yearly zonal mean dynamical fields to drive the NASA/Goddard Space Flight Center (GSFC) 2-D chemistry and transport model. This study provides a good simulation of the IAV of the total column ozone from 1993 to 2000. However, it underestimates the QBO amplitudes at the equator — partially because the UKMO temperatures underestimate the QBO amplitude by at least 40% [*Randel et al*., 1999]. To compensate, *Fleming et al.* [2002] also calculated the total column ozone by increasing the QBO amplitude in the UKMO temperatures by 40%; however, their result still underestimates the QBO signal in MOD by nearly a factor of 2.

Pawson and Fiorino [1998a and 1998b] studied the annual cycle and the QBO in the NCEP/NCAR Reanalysis 1 (NCEP1) and ECMWF Reanalysis (ERA). They found high correlations between the zonal winds of both reanalyses and the observations. The northward velocities in the NCEP1 data showed a more realistic structure than those in the ERA data. *Randel et al.* [2000] found that the signatures of the QBO and ENSO events were strong in tropopause statistics from NCEP1 from 1957 to 1997.

Using monthly mean meridional circulation to drive the Caltech/JPL 2-D chemical transport model (CTM), we carry out the first realistic simulation of the ozone QBO and QBO-AB from 1979 to 2002, coincident with the MOD record. The mean meridional circulation is derived from the NCEP/DOE Reanalysis 2 (NCEP2), provided by the NOAA-CIRES Climate Diagnostics Center. We then apply PCA to the simulated ozone calculated by the 2-D CTM. The model ozone results for QBO and QBO-AB are compared to the signals obtained by *Camp et al.* [2003] from the MOD observations.

1.3 NCEP-derived Transport Fields

Stream Function

NCEP2 4-times-daily spectral coefficients are used to calculate the monthly mean meridional circulations from 1979 to 2002, using the method of *Johnson* [1989]. Recently, the same method was used by *Bartels et al.* [1998] to study the Ertel potential vorticity flux in the upper troposphere and lower stratosphere. *Held and Schneider* [1999] also applied this method to study the near-surface branch of the overturning mass transport circulation in the troposphere.

The NCEP2 spectral coefficients are available on 28 sigma levels and with T62 (triangular wavenumber truncation at 62) resolution in the horizontal [*Kalnay et al.*, 1996; *Kistler et al.*, 2001]. On the pressure surface, the three-dimensional (3-D) meridional mass flux, $\psi_p(\lambda, \varphi, p)$, is determined by

$$\psi_P(\lambda, \varphi, p) = \frac{2\pi a \cos\varphi}{g} \int_o^p V(\lambda, \varphi, p')dp' , \quad (1)$$

where a is the earth radius, λ, φ, p is the longitude, latitude and pressure, V is the meridional velocity, g is the gravitational acceleration rate. Then we interpolate the 3-D meridional mass flux to isentropic surfaces, using a mass-conserving linear interpolation scheme [*Juckes et al*., 1994]. The 2-D isentropic mass stream function, $\psi_\theta(\varphi, \theta)$, is derived by zonal averaging of the 3-D isentropic meridional mass flux, $\psi_\theta(\lambda, \varphi, \theta)$, along isentropes. Finally, we interpolate the 2-D isentropic mass stream function, $\psi_\theta(\varphi, \theta)$, to pressure coordinates and scale by the density to produce the pressure surface stream function, $\psi_P(\varphi, p)$, which is used to drive the 2-D CTM.

Figure 1.1 shows the 2-D isentropic mass stream function, $\psi_\theta(\varphi, \theta)$, in the stratosphere in January, April, July and October of 1985. The air is drawn upward and poleward from the tropical lower stratosphere and pushed downward into the extratropical troposphere by the wave-induced forces [*Holton et al*., 1995]. This circulation is important for the transportation of ozone and other trace species in the stratosphere. The seasonal variation is also captured well by this stream function. The stream function is strong in the NH in January, when the temperature gradient and wave activity are strong. As a result more ozone is transported to the northern polar region. The stream function becomes weaker in the spring and summer in the NH, when the temperature gradient and wave activity are weaker. Less ozone is transported to the northern polar region in these seasons. In the fall, the stream function becomes strong again and there is more poleward transport of ozone. The hemispheric asymmetry of the

circulation verifies that the wave activity in the NH stratosphere is stronger than that in the SH.

No previous results for the isentropic mass stream function in the stratosphere have been published, so we compare our results with the mass stream function computed in pressure coordinates shown in Figure 2 of *Shia et al.* [1989]. There is general agreement in the shape of these stream functions. The annual mean flux through the tropopause in the *Shia et al*. [1989] model is 9.3×10^9 kg/s, which is consistent with ^{14}C data. The analogous flux for our study is 14×10^9 kg/s. This is the flux through the 400 K isentropic surface, which is close to the tropical tropopause. These values demonstrate a reasonable agreement in the strength of the circulation from both studies.

In previous studies, the meridional circulation was usually computed from the net radiative heating rates using a diagnostic stream function model [see, *e.g.*, *Ko et al*., 1985]. However, these studies tended to exaggerate the tropical vertical transport through the tropopause. They therefore underestimated the total column ozone in the tropics and overestimated it in the extra-tropics [*Kinnersley and Tung*, 1999; *Fleming et al*., 2002].

Alternatively, the meridional circulation can also be represented by the direct transformed Eulerian-mean (TEM) circulation. Since there tends to be a strong cancellation between the eddy heat flux convergence and the adiabatic cooling, the diabatic heating term is the small residual of this cancellation [*Andrew et al*., 1987]. The

TEM circulation calculated from the residual velocity is shown in the Figure 1.10 in the appendix. This circulation displays counter-rotating cells in the polar stratosphere that will cause unphysical transport of ozone. This may due to the strong cancellation mentioned above or the poor quality of the meridional wind data in the polar stratosphere. In our model, we adopt the computed isentropic stream function, which is a closer approximation to the Lagrangian motion than the residual mean meridional circulation.

Isentropic Mixing Coefficient K_{yy}

In the lower stratosphere, zonal mean transport mainly takes the form of advection by the mean diabatic circulation in the meridional plane and eddy mixing approximately along isentropic surfaces [*Mahlman et al*., 1984; *Tung*, 1984]. The isentropic mixing coefficient, K_{yy}, can be related to the Eliassen-Palm flux divergence [*Tung*, 1986; *Yang et al*., 1990]. We calculate K_{yy} in the stratosphere from 1979 to 2002 using NCEP2 data. It is defined by

$$K_{yy} = -\widehat{P^* V^*} / \left(\frac{\partial \hat{P}}{\partial y} \right), \qquad (2)$$

where $P = \frac{\varsigma + f}{\sigma}$ is the Ertel potential vorticity; ς is the relative vorticity, f is the planetary vorticity, and $\sigma = -\frac{1}{g}\frac{\partial p}{\partial z}$ denotes the density in the isentropic coordinates, where p and z are the pressure and height of the isentropic surfaces. V is the meridional velocity, and $y = a \cdot \sin\varphi$, where a is the earth's radius and φ is the latitude. The overbar denotes a zonal average along isentropes, *e.g.*, for an arbitrary field $h(\lambda)$,

$\bar{h} = \frac{1}{2\pi}\int_0^{2\pi} h d\lambda$. The hat denotes a mass-weighted zonal average, $\hat{h} = \overline{\sigma h}/\bar{\sigma}$, and star denotes the deviation from the mass-weighted zonal average, $h^* = h - \hat{h}$.

The K_{yy} values are interpolated from the isentropic surfaces to the pressure surfaces for use in the 2-D CTM. Figure 1.2 shows the K_{yy} field on the pressure surfaces in January, April, July and October of 1985. For surfaces between 15 and 35 km, the K_{yy} values are calculated from the NCEP2 data set. Above 35 km and below 15 km, the values are from *Fleming et al.* [2002] and consist of a climatologically seasonal cycle with no IAV. The values are large in the mid-latitudes, on the order of 10^6 m^2 s^{-1}, and small in the high latitudes and tropics, on the order of 10^5 m^2 s^{-1}. K_{yy} is larger in the NH than in the SH, as a result of more wave activity in the NH. There are some negative K_{yy} values calculated from the NCEP2 data set where $\partial\hat{P}/\partial y$ changes sign. For this study, negative values of K_{yy} were set to zero to avoid the numerical instability.

1.4 IAV of the Stream Function

In order to study the IAV of the pressure surface stream function used to drive the 2-D CTM, we define a stream function anomaly in the following manner. First, the time series for each grid point is decomposed as

$$\psi_p(t) = A_p^0 + A_p^1 t + \psi_p^a(t) + \psi_p'(t), \qquad (3)$$

where the first two terms, $A_p^0 + A_p^1 t$, constitute a linear trend determined by a least squares fit. The mean annual cycle, $\psi_p^a(t)$, is determined by evaluating the mean value for each month independently. To isolate the IAV from higher frequency oscillations, a spectral filter is applied to the anomaly, $\psi'_p(t)$. The filter is constructed as the convolution of a step function with a Hanning window and chosen to obtain a full signal from periods above 15 months and no signal from periods below 12.5 months. PCA is then performed on the filtered stream function anomaly. The details of the methodology are explained in *Camp et al.* [2003]. The first three EOFs from this analysis, along with the associated principal component (PC) time series and their power spectral estimate, are shown in Figure 1.3 and Figure 1.4. All spectral estimates are calculated by Welch's method averaging three half-length segments with 50% overlap; a Welch window is applied to each segment prior to averaging [*Press et al.*, 1992]. These three EOFs account for 95% of the total variance of the filtered stream function anomaly. The correlations (lag = 0) and maximum cross correlations between the PCs of the stream function and the relevant indices are given in Table 1.1. The corresponding significance levels are also listed. The significance statistics for correlations were generated by a Monte Carlo method [*Press et al.*, 1992]. A distribution of correlations was generated by determining the correlations of three thousand isospectral surrogate time series with the relevant indices. This distribution was transformed into an approximately normal distribution by the Fisher transformation [*Devore*, 1982]. The significance level of the actual correlation within the normal distribution was then determined. A small numerical value of the significance level denotes a high statistical significance.

The first EOF, Figure 1.3a, captures over 70% of the variance and represents an oscillation in the strength of Brewer-Dobson circulation caused by the QBO. During the westerly (easterly) phase of the QBO, the Brewer-Dobson circulation is weakened (strengthened). The associated principal component time series, PC1, is plotted in Figure 1.4a against the inverted 30 mbar QBO index (the zonal average of the 30 mbar zonal wind at the equator computed from the NCEP2). The power spectral estimate of PC1, Figure 1.4b, shows the 28-month mean period characteristic of the QBO. PC1 leads the 30 mbar QBO index by 4 months (derived from the maximum cross correlation position), which is consistent with the occurrence of the maximum of the stream function anomaly variation above the 30 mbar level, since the QBO is characterized by a downward propagation. A secondary 20-month-period oscillation is also evident. The modulation of the annual cycle of the Brewer-Dobson circulation by the QBO results in the creation of two oscillations with frequencies equal to the difference and sum of the source frequencies; *i.e.*, at periods of 20 and 8.6 months [*Tung and Yang*, 1994a]. Only the 20-month signal is evident, since the spectral filtering destroys the signal from the higher frequency. Variations in QBO captured by the EOF are distinctly asymmetric about the equator; the amplitude of variations of the northern lobe is greater than that of the southern by more than a factor of three. This is the first time that an asymmetric QBO circulation has been found in the stream function derived from the NCEP2 data.

The second EOF, Figure 1.3b, captures about 18% of the variance and represents a smaller variation in just the southern cell of the circulation. It oscillates with the 20-month period characteristic of the QBO-AB. The pattern of the 20-month signal is thus a

linear combination of EOF1, containing the entire northern cell variability and some of the southern cell variability, and EOF2, containing the remaining southern variability. In Figure 1.4c, PC2 is shown against a constructed index for the QBO-AB (PC3 of the EOF results for the zonal mean MOD; see Section 1.5 for details). PC2 correlates well with the QBO-AB (see Table 1.1).

The third EOF, Figure 1.3c, captures about 6% of the variance and represents an oscillation in the height of the upwelling branch of the Hadley cell at the equator. Similar to PC1, the PC3 time series is dominated by a 28-month-period signal with a secondary 20-month-period signal. In Figure 1.4e, PC3 is shown along with the 30 mbar QBO index. PC3 lags the 30 mbar QBO index by 3 months, which is consistent with the occurrence of the center of the stream function anomaly variation below the 30 mbar level.

1.5 Modeling of Total Column Ozone in the Tropics

The Caltech/JPL 2-D CTM is a zonally averaged model for trace species in the terrestrial troposphere and middle atmosphere (see *Shia et al.*, 1989 and Appendix A in *Morgan et al.*, 2003, for details). The model has 18 latitude boxes, equally spaced from pole to pole, and 40 layers, equally spaced in log(p) from the surface to the upper boundary at 0.01 mbar. Transport in the model is by the stream function and K_{yy} calculated from NCEP2 data sets. The values for K_{zz} are taken from *Summers et al.* [1997]. They are not important except in the mesosphere. The model includes all the gas

phase chemistry in the NASA recommendations for stratospheric modeling [*DeMore et al*., 1997]. There is no heterogeneous chemistry. The numerical method used for solving the continuity equation in the model is the Prather scheme [*Prather*, 1986; *Shia et al*., 1990].

To understand the IAV of ozone, we model the total column ozone from 1975 to 2002. *Husemann and Hitchman* [2001 and 2003] and *Pawson and Fiorino* [1999] showed that there is a large discontinuity of the NCEP1 data when the TOVS satellite data becomes available in 1979, so we use the first four years of data from NCEP1 only as spin-up time for the 2-D CTM. The stream function and eddy mixing coefficients from 1979 to 2002 are calculated from NCEP2. The climatology of total column ozone in these 24 years from the MOD [*McPeters et al*., 1996] and the model results are compared in Figure 1.5. The model simulates the total column ozone well. In agreement with observations, more ozone is transported to the polar region by the stronger meridional circulation in the winter hemisphere than in the summer. Because the model does not incorporate heterogeneous chemistry, there are some differences in the high latitudes of the polar spring in both hemispheres. Furthermore, the strength of SH stream function derived from NCEP2 is exaggerated; therefore, the simulated total column ozone is lower than the MOD in the tropical summer. The NCEP2 meridional wind field may not be realistic in the high latitudes of the SH because there are relatively few radiosonde measurements. Correlation coefficients and significance levels between monthly mean column ozone from MOD and the model over the period from 1979 to 2002 are shown in

Figure 1.11 in the appendix. The correlation coefficients are high in most areas and are significant.

The ozone anomaly is calculated by removing the mean monthly seasonal cycle from the original total column ozone. Figure 1.6a presents model results (solid line) for the equatorial total column ozone anomaly from 1979 to 2002. The linear trend has been removed by a least squares fit. The model provides a good simulation of the MOD anomaly (dotted line). The correlation coefficient of these two curves is 0.75 and the corresponding significance level is 0.4%. *Fleming et al.* [2002] first successfully calculated the residual mean meridional stream function using data from the UKMO GCM and UARS observations. Their results for the total column ozone are a good simulation of the MOD from 1993 to 2000. However, their model underestimates the tropical total column ozone. In our model, the tropical column ozone anomaly is somewhat larger than the observed data.

The ratio of the standard deviations between the model and MOD tropical ozone anomaly is 1.6. In a sensitivity study, we therefore reduced the QBO part of the stream function by a factor of 1.6. The QBO component in the detrended stream function anomaly was calculated by a linear regression against the 30 mbar QBO index. Then we used the stream function with weakened QBO to drive our 2-D CTM. The result is shown in Figure 1.6b. The correlation coefficient between the model and MOD curves is 0.75 with a significance level of 0.3%. The detrended ozone anomaly from our model is now

closer in amplitude to the observed anomaly, while preserving the good match in phase seen in the results derived from the original stream function.

The latitudinal distribution of the total column ozone anomaly from 1979 to 2002 is plotted in Figure 1.7. The 2-D CTM (Figure 1.7b) reproduces the seasonal and IAV of the MOD (Figure 1.7a) well, although there is some overestimation of the amplitude of variations in the tropics. There is an obvious QBO signal in the ozone anomaly from the 2-D CTM at the equator, which begins to propagate to high latitude in the winter and spring seasons.

EOF Results of the Total Column Ozone From the 2-D CTM

PCA is applied to the detrended, deseasonalized and filtered total column ozone anomaly from the 2-D CTM. The filter is chosen to obtain a full signal from periods above 15 months and no signal from periods below 12.5 months. The first two EOFs, shown in Figure 1.8 and Figure 1.9, capture over 84% of the total variance of the filtered data. The first EOF, Figure 1.8a, captures 74% of the variance and displays a structure attributable to the QBO. It is asymmetric about the equator and oscillates about nodes at 15°N and 19°S. The values show range from a high of 11.6 Dobson units (DU) to a low of –5 DU. The magnitude of this mode is larger than that of the first EOF pattern of the zonal mean MOD. The associated principal component time series, 2-D CTM PC1, is plotted in Figure 1.9a against the PC1 of the zonal mean MOD and the 30 mbar QBO index; it shows strong correlations with these indices (see Table 1.1). The power spectral

estimate of PC1, Figure 1.9b, shows a strong peak at 28 months. The characteristics of this EOF are consistent with the modulation of the meridional circulation by the QBO as discussed in Section 1.4.

The second EOF, capturing 10.8% of the variance, is a tilted plane oscillating about a node at the equator (Figure 1.8b). Values range from 3 DU in the north to –3.5 DU in the south. It is similar to the third EOF pattern of the zonal mean MOD. In Figure 1.9c, 2-D CTM PC2 is shown against the PC3 of the zonal mean MOD. The correlation between these two time series is good (see Table 1.1). The power spectral estimate of the associated PC2 has a dominant peak at 20 months, characteristic of the interaction between the QBO and annual cycles.

1.6 Conclusions

We use a 2-D model to study the signals of QBO and QBO-AB in ozone. The NCEP2 dynamical fields are used to calculate the monthly mean meridional circulation on isentropic surfaces from 1979 to 2002. The isentropic stream function is then interpolated to pressure surfaces to drive the Caltech/JPL 2-D CTM. The 2-D CTM successfully simulates the seasonal and IAV of ozone in the tropics. The phase and amplitude of the QBO signal in the total column ozone in the tropics are captured by the model. The magnitude of the QBO signal is somewhat larger in the model than in the data. The model also simulates the QBO-AB well. The first two EOFs of the detrended, deseasonalized, and filtered total column ozone anomaly from the model capture over

84% of the total variance. The first EOF explains 74% of the variance, and displays a structure attributable to the asymmetric QBO with a mean period of approximately 28 months. The second EOF, capturing 10.8% of the variance, is related to the approximately 20-month QBO-AB. All of these signals found in the model ozone are close to those in MOD. The successful simulation of the IAV of the total column ozone in the 2-D CTM suggests that the NCEP2 data have captured the bulk of IAV in the tropics.

Since the 2-D meridional stream function cannot capture the longitudinal variation of the ENSO signal, no clear ENSO signal is found in the simulated total column ozone results. Future work will use a 3-D isentropic model to simulate the ENSO signal in the total column ozone. Similarly, since the decadal signal is only weakly present in our stream function, the simulated total column ozone does not show a decadal signal in the leading EOFs. Further work is also in progress to elucidate the detailed mechanism of the origin of QBO-AB and to extend these results to higher latitudes. In view of the obvious need to account for the natural IAV of ozone [see *Newchurch et al*., 2003], it is important to extend this type of analysis to global ozone.

1.7 Appendix

The material in this appendix provides information on the transformed Eulerian-mean (TEM) circulation and correlation coefficients between monthly mean column ozone from MOD and model.

Transformed Eulerian-mean circulation

For the quasi-geostrophic approximation, the residual velocity is defined by [*Andrew et al*., 1987]

$$\overline{v^*} = \overline{v} - \rho_0^{-1}\partial(\rho_0 \overline{v'\theta'} / \theta_{0z}) / \partial z$$

$$\overline{w^*} = \overline{w} + \partial(\overline{v'\theta'} / \theta_{0z}) / \partial y$$

where v and w are the meridional and vertical velocity, ρ_o is the density, θ is the potential temperature, θ_{oz} is the vertical derivative of potential temperature. The over bar and prime denote the zonal average and its deviation from zonal mean, respectively. A residual stream function for the TEM circulation can be determined by

$$\overline{v^*} = -\partial\overline{\psi^*} / \partial z \, , \, \overline{w^*} = \partial\overline{\psi^*} / \partial y \, .$$

The resulting residual meridional circulation in the stratosphere is shown in Figure 1.10.

Correlation Coefficients

Correlation coefficients and significance levels between monthly mean column ozone from MOD and model over the period from 1979 to 2002 are shown in the Figure 1.11. The correlation coefficients are high in most areas and are significant. The

correlations are poor in the summer high latitudes and a narrow band around 15°N. Both of regions have a weak QBO signals. The northern summer is weak since there is only a weak summer Brewer-Dobson circulation for the QBO to modulate. The subtropic band is weak for it is the node of the ozone QBO signal. The correlation coefficients are small in the high latitude of the southern hemisphere (SH). This is primarily due to the poor quality of the meridional wind in the NCEP/DOE Reanalysis 2 data set in the SH. In addition, we do not include the heterogeneous chemistry in the model. This will cause some biases in the spring of the polar region.

1.8 References

Allen, M., Y. L. Yung, and J. W. Waters, Vertical transport and photochemistry in the terrestrial mesosphere and lower thermosphere (50-120 km), *J. Geophys. Res.*, *86*, 3617-3627, 1981.

Andrews, D. G., J. R. Holton, C. B. Leovy, *Middle Atmosphere Dynamics*, Academic Press: Orlando, FL, 1987.

Austin, J., J. R. Knight, and N. Butchart, Three-dimensional chemical model simulations of the ozone layer: 1979-2015, *Quart. J. Roy. Meteorol. Soc.*, *126*, 1533-1556, 2000.

Bartels, J., D. Peters, and G. Schmitz, Climatological Ertel's potential-vorticity flux and mean meridional circulation in the extratropical troposphere – lower stratosphere, *Ann. Geophys.*, *16*, 250-265, 1998.

Baldwin, M. P., *et al*., The Quasi-Biennial Oscillation, *Rev. Geophys.*, *39*, 179-229, 2001.

Camp, C. D., M. S. Roulston, and Y. L. Yung, Temporal and spatial patterns of the interannual variability of total ozone in the tropics, *J. Geophys. Res.*, *108*, art. no. 4643, 2003.

DeMore, W. B., *et al*., Chemical kinetics and photochemical data for use in stratospheric modeling, *Evaluation No. 12, JPL Pub. 97-4*, Jet Propulsion Laboratory (Pasadena), 1997.

Devore, J. L., *Probability and Statistics for Engineering and the Sciences*, 1st ed., 640 pp., Brooks/Cole, Monterey, Calif., 1982.

Fleming, E. L., C. H. Jackman, J. E. Rosenfield, and D. B. Considine, Two-dimensional model simulations of the QBO in ozone and tracers in the tropical stratosphere, *J. Geophys. Res., 107*, art. no. 4665, 2002.

Fusco, A. C., and M. L. Salby, Interannual variations of total ozone and their relationship to variations of planetary wave activity, *J. Clim., 12*, 1619-1629, 1999.

Hadjinicolaou, P., A. Jrrar, J. A. Pyle, and L. Bishop, The dynamically-driven long-term trend in stratospheric ozone over northern mid-latitudes, *Quart. J. Roy. Meteorol. Soc*., *128*, 1393-1412, 2002.

Hasebe, F., Quasi-Biennial Oscillations of ozone and diabatic circulation in the equatorial stratosphere, *J. Atmos. Sci.*, 51, 729-745, 1994.

Held, I. M., and T. Schneider, The surface branch of the zonally averaged mass transport circulation in the troposphere, *J. Atmos. Sci., 56*, 1688-1697, 1999.

Holton, J. R., P. H. Haynes, and M. E. McIntyre, A. R. Douglass, R. B. Rood, and L. Pfister, Stratosphere-troposphere exchange. *Rev. Geophys., 33***,** 403–439, 1995.

Hood, L. L., J. P. McCormack, and K. Labitzke, An investigation of dynamical contributions to midlatitude ozone trends in winter, *J. Geophys. Res.*, *102*, 13079-13093, 1997.

Huesmann, A. S., and M. H. Hitchman, The stratospheric quasi-biennial oscillation in the NCEP reanalyses: Climatological structures, *J. Geophys. Res., 106*, 11859-11874, 2001.

Huesmann, A. S., and M. H. Hitchman, The 1978 shift in the NCEP reanalysis stratospheric quasi-biennial oscillation, *Geophys. Res. Lett., 30*, doi:10.1029/2002GL016323, 2003.

Johnson, D. R., The forcing and maintenance of global monsoonal circulations – An isentropic analysis, *Adv. Geophys., 31*, 43-316 1989.

Jones, D. B. A., H. R. Schneider, and M. B. McElroy, Effects of the quasibiennial oscillation on the zonally averaged transport of tracers, *J. Geophys. Res., 103*, 11235-11249, 1998.

Juckes, M. N., I. N. James, and M. Blackburn, The influence of Antarctica on the momentum budget of the southern extratropics. *Quart. J. Roy. Meteor. Soc., 120*, 1017–1044, 1994.

Kalnay, E., *et al.*, The NCEP/NCAR 40-year reanalysis project, *Bull. Amer. Meteor. Soc., 77*, 437-471, 1996.

Kinnersley, J. S., Seasonal asymmetry of the low- and middle-latitude QBO circulation anomaly, *J. Atmos. Sci., 56*, 1140-1153, 1999.

Kinnersley, J. S., and K. K. Tung, Mechanisms for the extratropical QBO in circulation and ozone, *J. Atmos. Sci., 56*, 1942-1962, 1999.

Kistler, R., *et al*., The NCEP-NCAR 50-year reanalysis: Monthly means CD-ROM and documentation, *Bull. Amer. Meteor. Soc., 82*, 247-267, 2001.

Ko, M. K. W., *et al*., A zonal mean model of stratospheric tracer transport in isentropic coordinates – numerical simulations for nitrous oxide and nitric acid, *J. Geophys. Res., 90*, 2313-2329, 1985.

Mahlman, J. D., D. G. Andrews, D. L. Hartmann, T. Matsuno and R. G. Murgatroyd, Transport of trace constituents in the stratosphere, *Dynamics of the Middle Atmosphere*, J. R. Holton and T. Matsuno, Eds., Terra Scientific, 387-416, 1984.

McPeters, R., *et al*., NIMBUS-7 Total Ozone Mapping Spectrometer (TOMS) data products user's guide, NASA Tech. Rep., 1996.

Morgan, C. G., M. Allen, M. C. Liang, R. L. Shia, G. A. Blake, and Y. L. Yung, Isotopic fractionation of nitrous oxide in the stratosphere: Comparison between model and observations, *J Geophys. Res.*, In press, 2003. Preprint available from website http://yly-mac.gps.caltech.edu/ under "N_2O_JGR".

Newchurch, M. J., E. S. Yang, D. M. Cunnold, G. C. Reinsel, and J. M. Zawodny, Evidence for slowdown in stratospheric ozone loss: first stage of ozone recovery. *J. Geophys. Res., 108*, art. no. 4507, 2003.

Pawson, S., and M. Fiorino, A comparison of reanalyses in the tropical stratosphere. Part 1: Thermal structure and the annual cycle, *Clim. Dyn., 14*, 631-644, 1998.

Pawson, S., and M. Fiorino, A comparison of reanalyses in the tropical stratosphere. Part 2: The quasi-biennial oscillation, *Clim. Dyn., 14*, 645-658, 1998.

Pawson, S., and M. Fiorino, A comparison of reanalyses in the tropical stratosphere. Part 3: Inclusion of the pre-satellite data era, *Clim. Dyn., 15*, 241-250, 1999.

Plumb, R. A., and R. C. Bell, A model of the Quasi-Biennial Oscillation on an equatorial beta-plane, *Q. J. R. Meteor. Soc., 108*, 335-352, 1982.

Politowicz, P. A., and M. H. Hitchman, Exploring the effects of forcing quasi-biennial oscillations in a two-dimensional model, *J. Geophys. Res., 102*, 16481-16497, 1997.

Prather, M. J., Numerical advection by conservation of 2nd-order moment, *J. Geophys. Res*., *91*, 6671-6681, 1986.

Press, W., S. Teukolsky, W. Vetterling, and B. Flannery, *Numerical Recipes in Fortran 77: The Art of Scientific Computing*, 2nd ed., 933 pp., Cambridge Univ. Press, New York, 1992.

Randel, W. J., and J. B. Cobb, Coherent variations of monthly mean total ozone and lower stratospheric temperature, *J. Geophys. Res., 99*, 5433–5447, 1994.

Randel, W. J., F. Wu, and D. J. Gaffen, Interannual variability of the tropical tropopause derived from radiosonde data and NCEP reanalysis, *J. Geophys. Res*., *12*, 15509-15523, 2000.

Randel, W. J., F. Wu, R. Swinbank, J. Nash, and A. O'Neill, Global QBO circulation derived from UKMO stratospheric analyses, *J. Atmos. Sci., 56*, 457-474, 1999.

Shia, R. L., Y. L. Yung, M. Allen, R. W. Zurek, and D. Crisp, Sensitivity study of advection and diffusion coefficients in a 2-dimensional stratospheric model using excess ^{14}C data, *J. Geophys. Res*., *94*, 18467-18484, 1989.

Shia, R. L., Y. L. Ha, J. S. Wen, and Y. L. Yung, Two-dimensional atmospheric transport and chemistry model – numerical experiments with a new advection algorithm, *J. Geophys. Res*., *95*, 7467-7483, 1990.

Shiotani, M., Annual, quasi-biennial, and El Niño-Southern Oscillation (ENSO) time-scale variations in equatorial total ozone, *J. Geophys. Res*., 97, 7625– 7633, 1992.

Stevermer, A., and E. C. Weatherhead, Detecting recovery in vertically-resolved ozone records, AGU, A11C-04, p.74, 2001.

Summers, M. E., D. E. Siskind, J. T. Bacmeister, R. R. Conway, S. E. Zasadil, and D. F. Strobel, Seasonal variation of middle atmospheric CH_4 and H_2O with a new chemical-dynamical model**,** *J. Geophys. Res., 102***,** 3503-3526, 1997.

Tung, K. K., Modeling of tracer transport in the middle atmosphere, *Dynamics of the Middle Atmosphere*, J. R. Holton and T. Matsuno, Eds., Terra Scientific, 417-444, 1984.

Tung, K. K., Nongeostrophic theory of zonally averaged circulation. Part I: Formulation, *J. Atmos. Sci.,43,* 2600-2618, 1986.

Tung, K. K., and H. Yang, Global QBO in circulation and ozone, Part I: Reexamination of observational evidence, *J. Atmos. Sci., 51,* 2699– 2707, 1994a.

Tung, K. K., and H. Yang, Global QBO in circulation and ozone, Part II: A simple mechanistic model, *J. Atmos. Sci., 51,* 2708– 2721, 1994b.

WMO (World Meteorological Organization), Scientific Assessment of Ozone Depletion: 2002, *Global Ozone Research and Monitoring Project—Report No. 47*, 498 pp., Geneva, 2003.

Yang, H., K. K. Tung, and E. Olaguer, Nongeostrophic theory of zonally averaged circulation. 2. Eliassen-Palm Flux divergence and isentropic mixing coefficient, *J. Atmos. Sci., 47*, 215-241, 1990.

Table 1.1. Correlations (Lag = 0) and Maximum Cross Correlations of the Stream Function and Modeled Total Column Ozone PCs with Various Indices. The numbers in parentheses denote significance levels. Units of lag are month. Positive (negative) lags correspond to the PC time series leading (trailing) the indices.

		QBO (30mb)	QBO-AB (PC3 of Zonal Mean MOD)	PC1 of Zonal Mean MOD
Stream Function	PC1	-0.46 (12.5%), Lag=0 -0.82 (0.4%), Lag=4		
	PC2		0.52 (3.1%), Lag=0 0.65 (0.4%), Lag=2	
	PC3	-0.58 (7.3%), Lag=0 -0.81 (0.7%), Lag=–3		
Modeled Total Column Ozone	PC1	0.87 (0.2%), Lag=0 0.91 (0.1%), Lag=1		0.81 (0.3%), Lag=0 0.86 (0.1%), Lag=–1
	PC2		0.50 (1.6%), Lag=0 0.50 (1.6%), Lag=0	

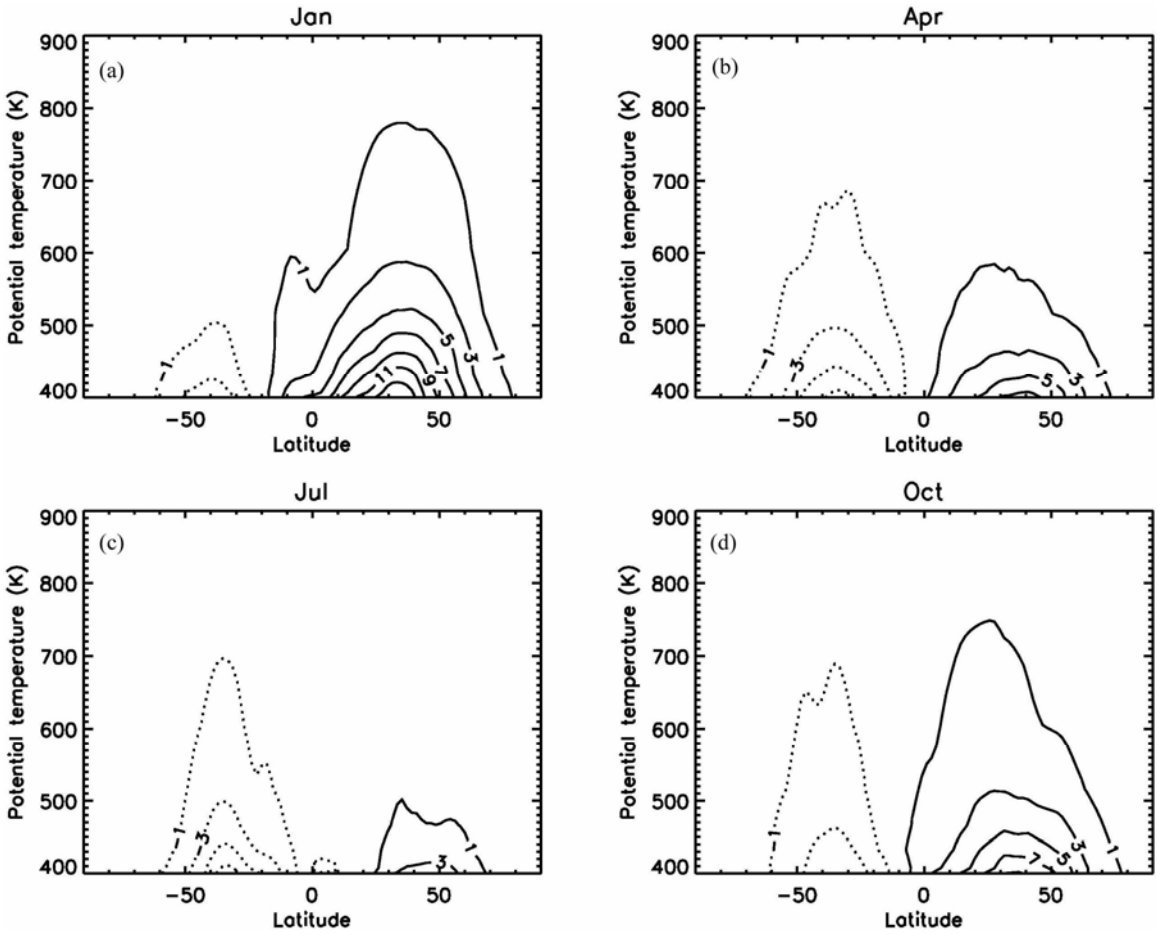

Figure 1.1: Stratospheric isentropic stream function in 1985. (a) January, (b) April, (c) July, and (d) October. Units are 10^9 kg/s.

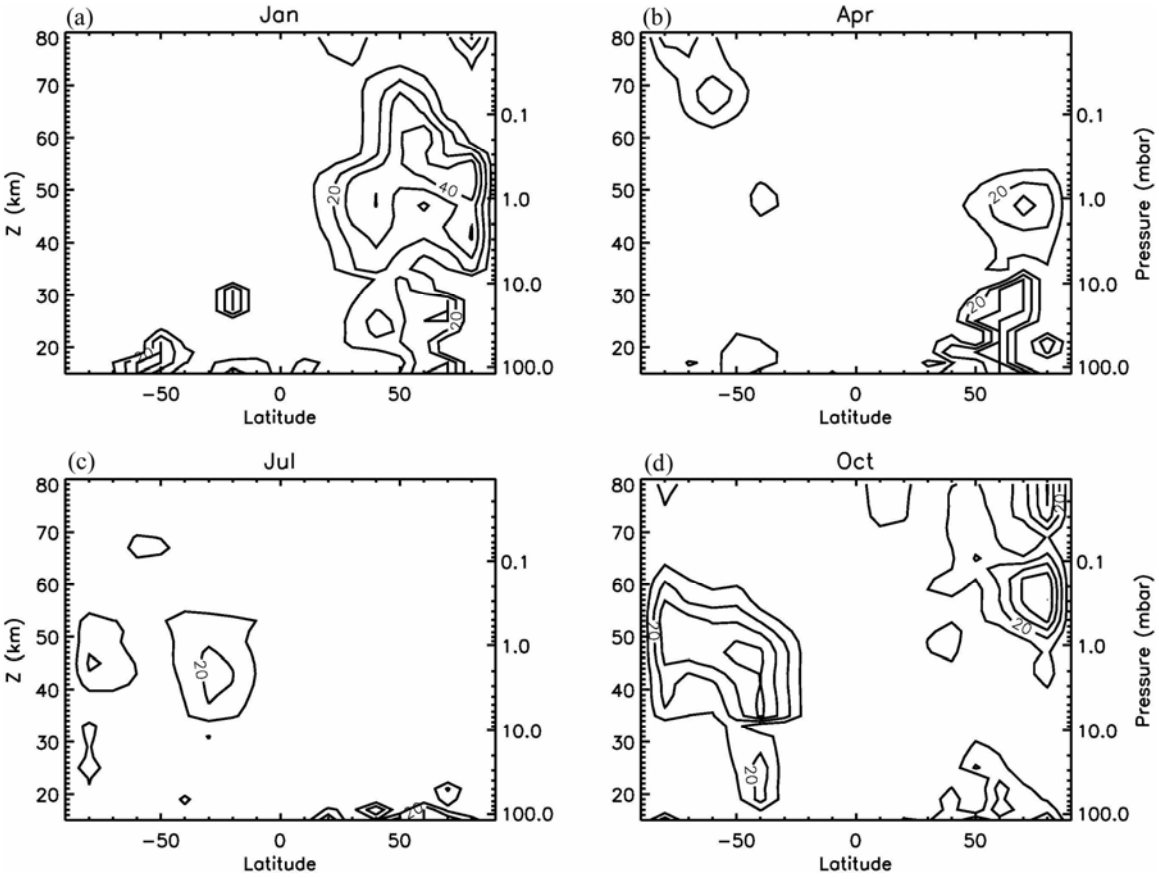

Figure 1.2: Isentropic mixing coefficient K_{yy} interpolated to the pressure surfaces in 1985. (a) January, (b) April, (c) July, and (d) October. Units are 10^5 m^2/s.

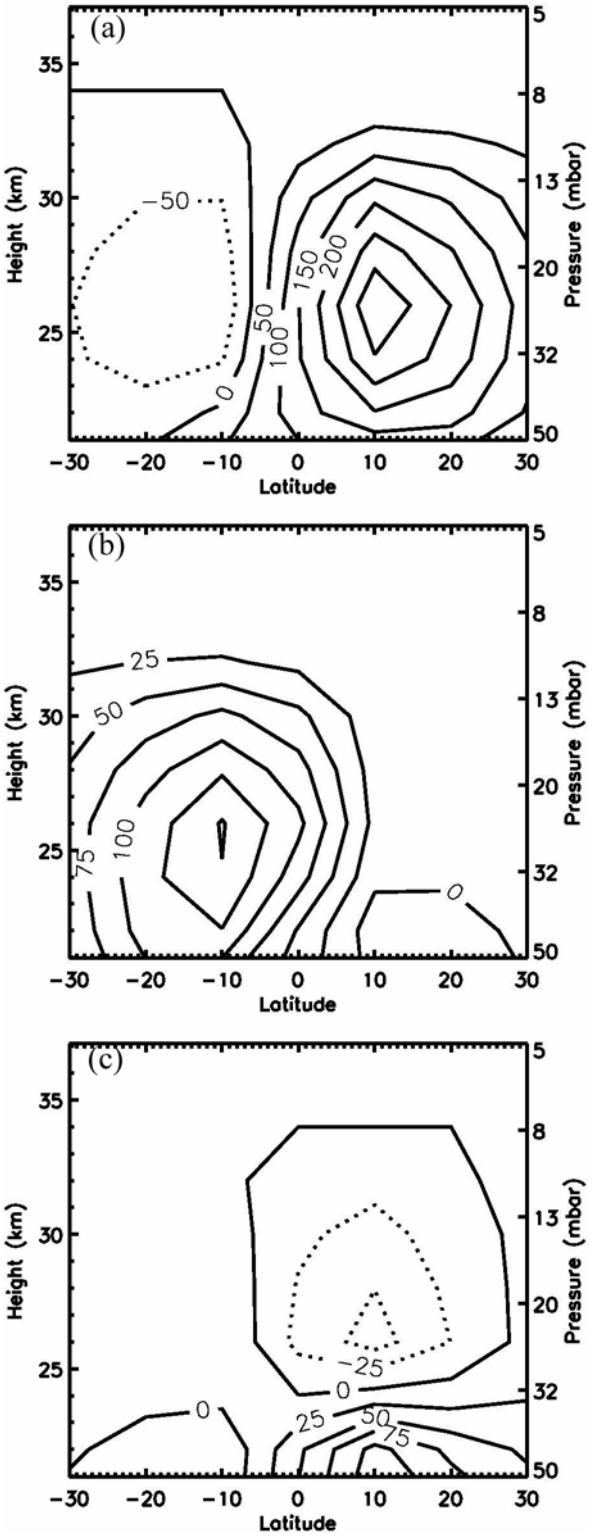

Figure 1.3: First three spatial EOF patterns of the pressure surface stream function. Units are m^2/s.

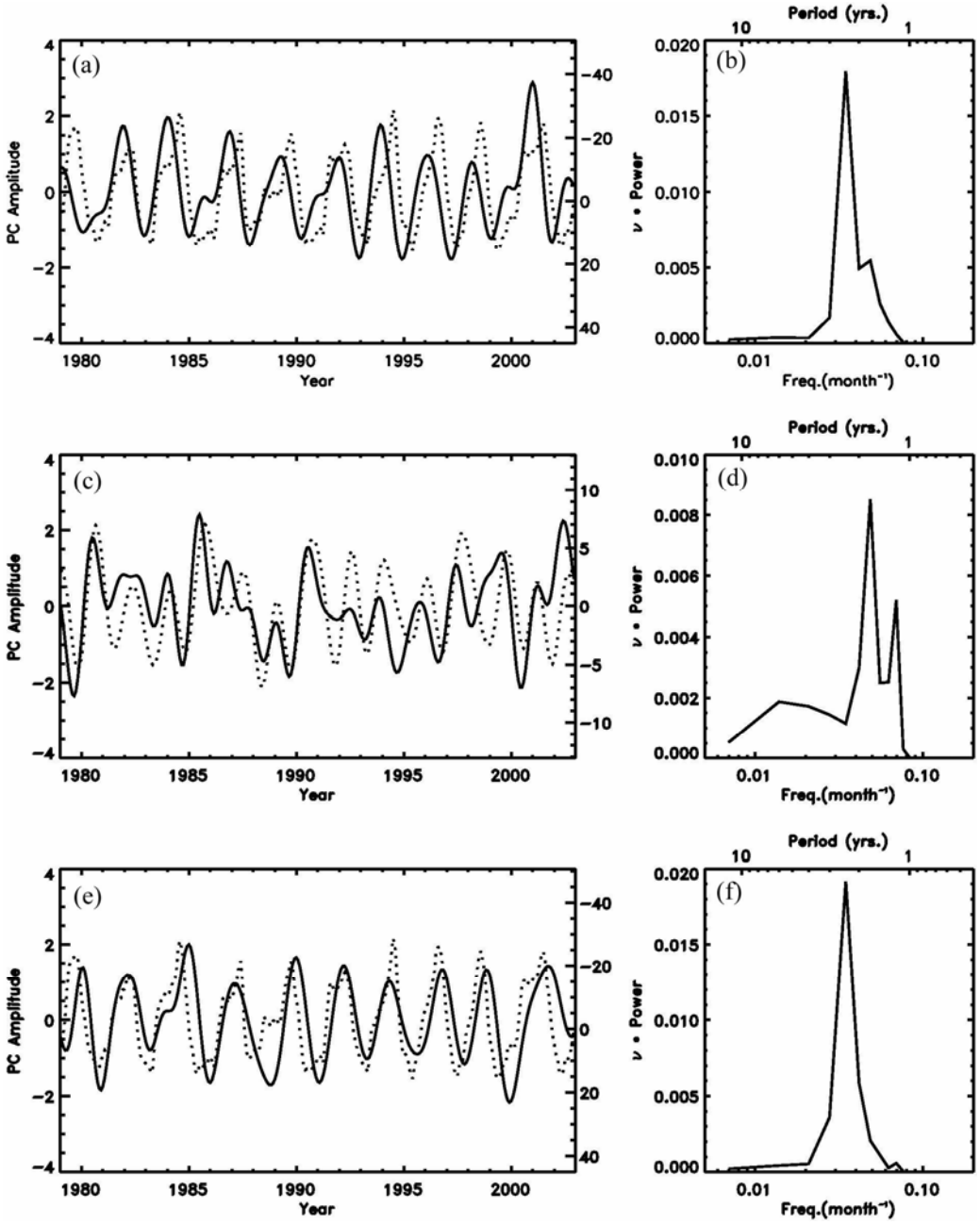

Figure 1.4: PC time series (left column) and spectra (right column) for the first three EOFs of the stream function. PCs (solid line) are shown along with an appropriate index (dotted line). (a) PC1 and inverted 30 mbar QBO index, (c) PC2 and constructed QBO-AB index (PC3 of the zonal mean MOD), (e) PC3 and inverted 30 mbar QBO index.

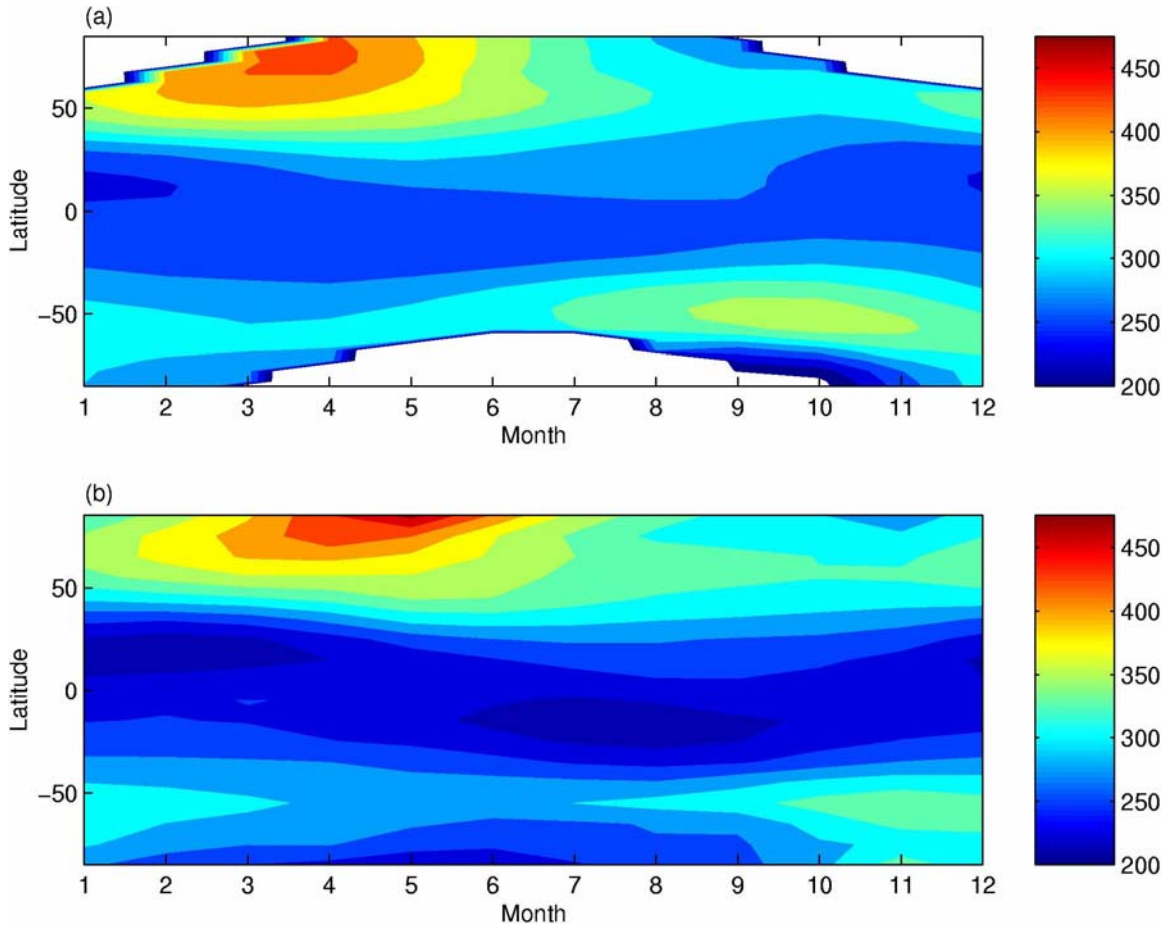

Figure 1.5: (a) 1979-2002 mean of MOD, (b) 1979-2002 mean of total column ozone from 2-D model.

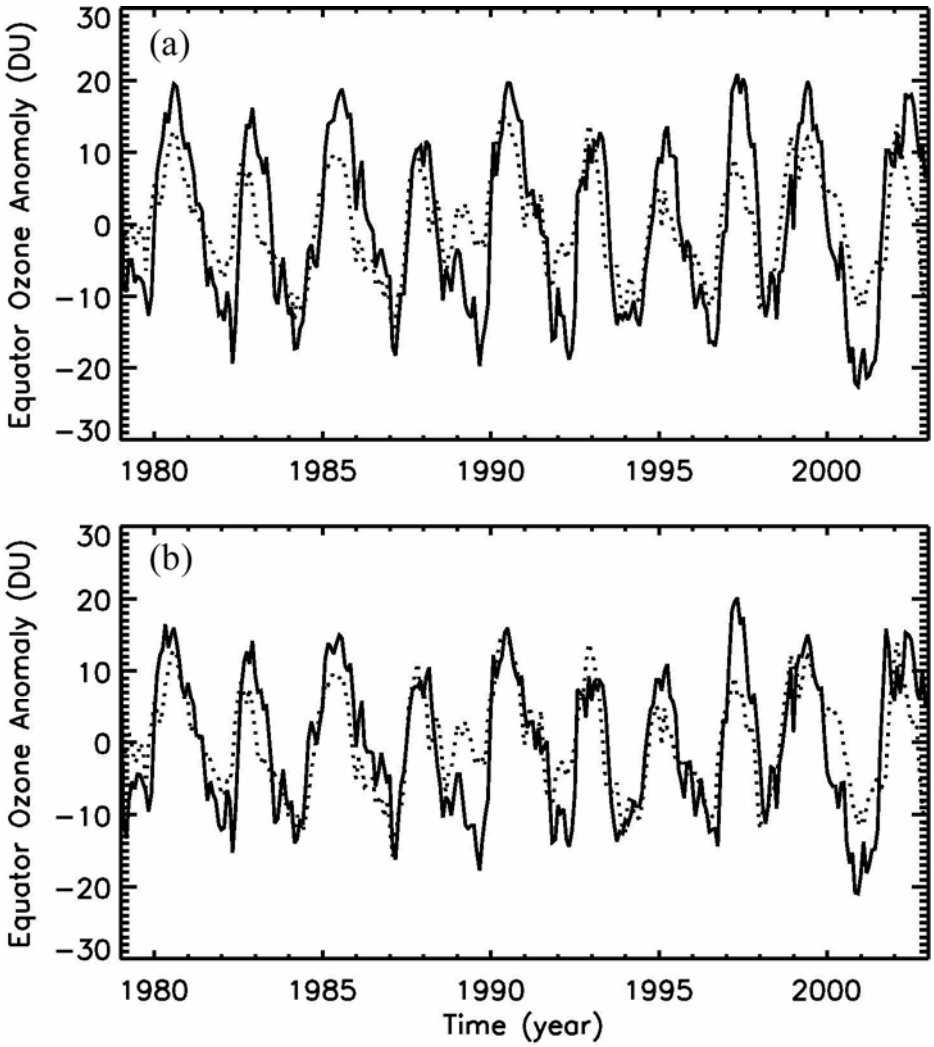

Figure 1.6: Equatorial detrended ozone anomaly from the 2-D Caltech/JPL CTM (solid line), driven by (a) the original stream function, (b) the stream function in which the QBO component was reduced by a factor of 1.6. Both results are compared to the equatorial detrended ozone anomaly from MOD (dotted line).

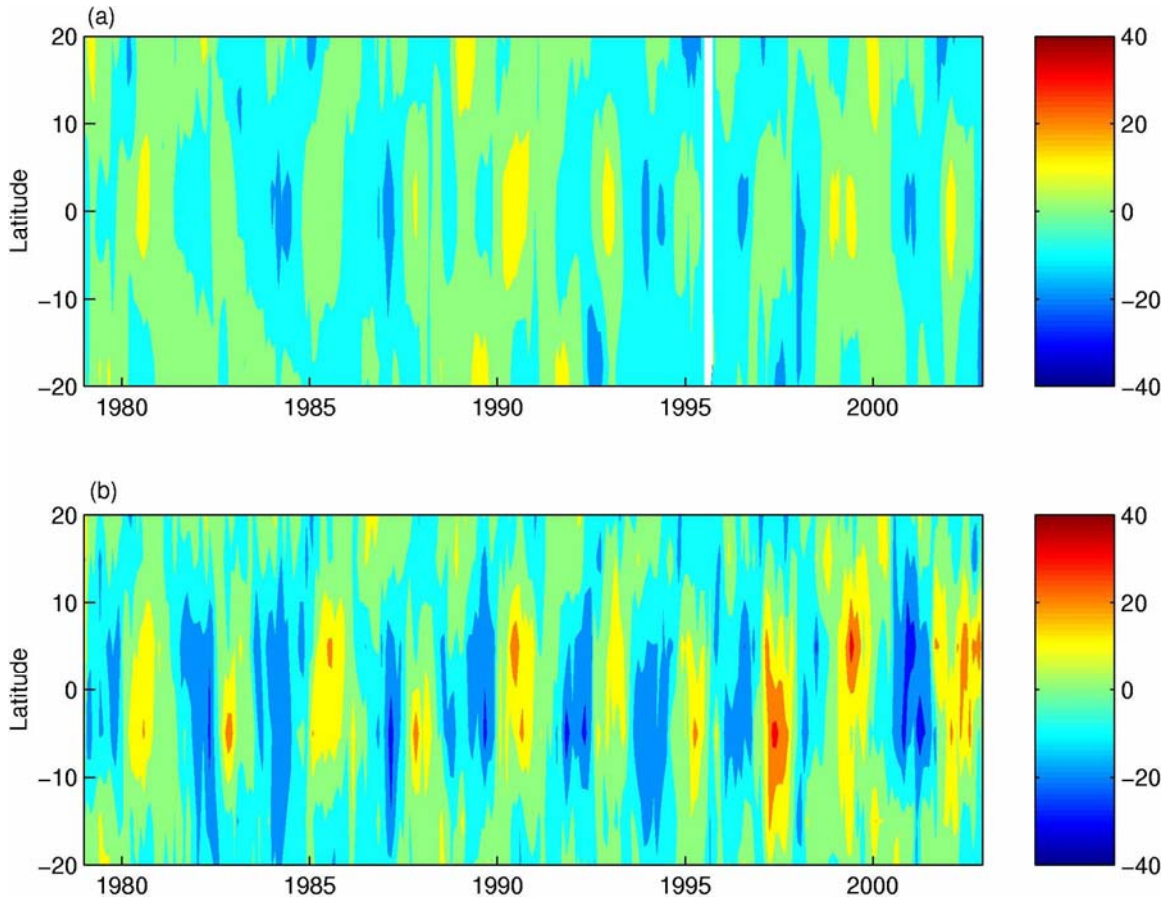

Figure 1.7: Latitude distribution of ozone anomaly from (a) MOD, (b) 2-D CTM driven by the original stream function.

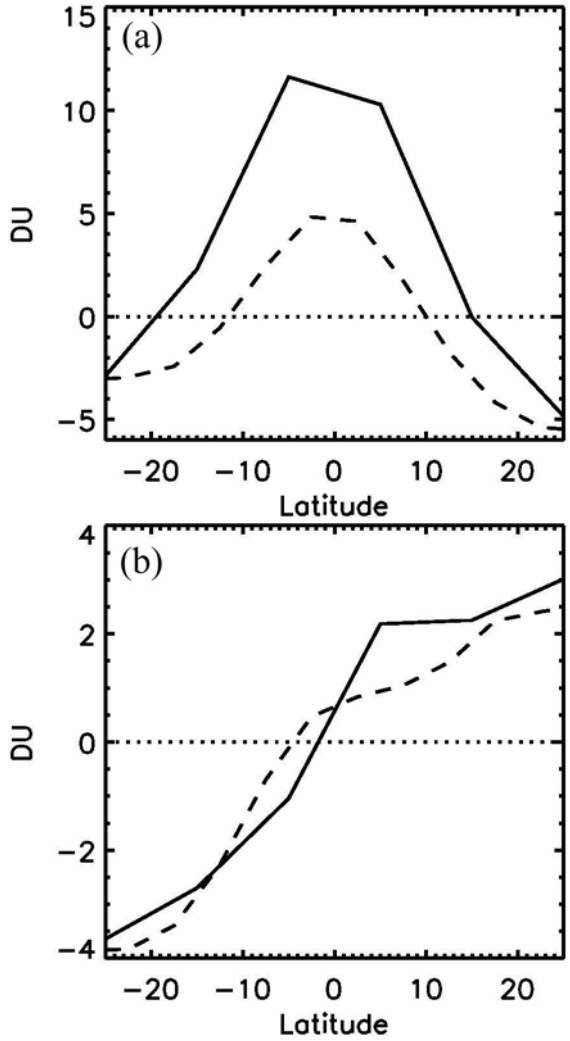

Figure 1.8: Spatial EOF patterns of the total column ozone. (a) First spatial EOF pattern of the total column ozone from 2-D CTM (solid line) and first spatial EOF pattern of the zonal mean MOD (dashed line), (b) Second spatial EOF pattern of the total column ozone from 2-D CTM (solid line) and third spatial EOF pattern of the zonal mean MOD (dashed line).

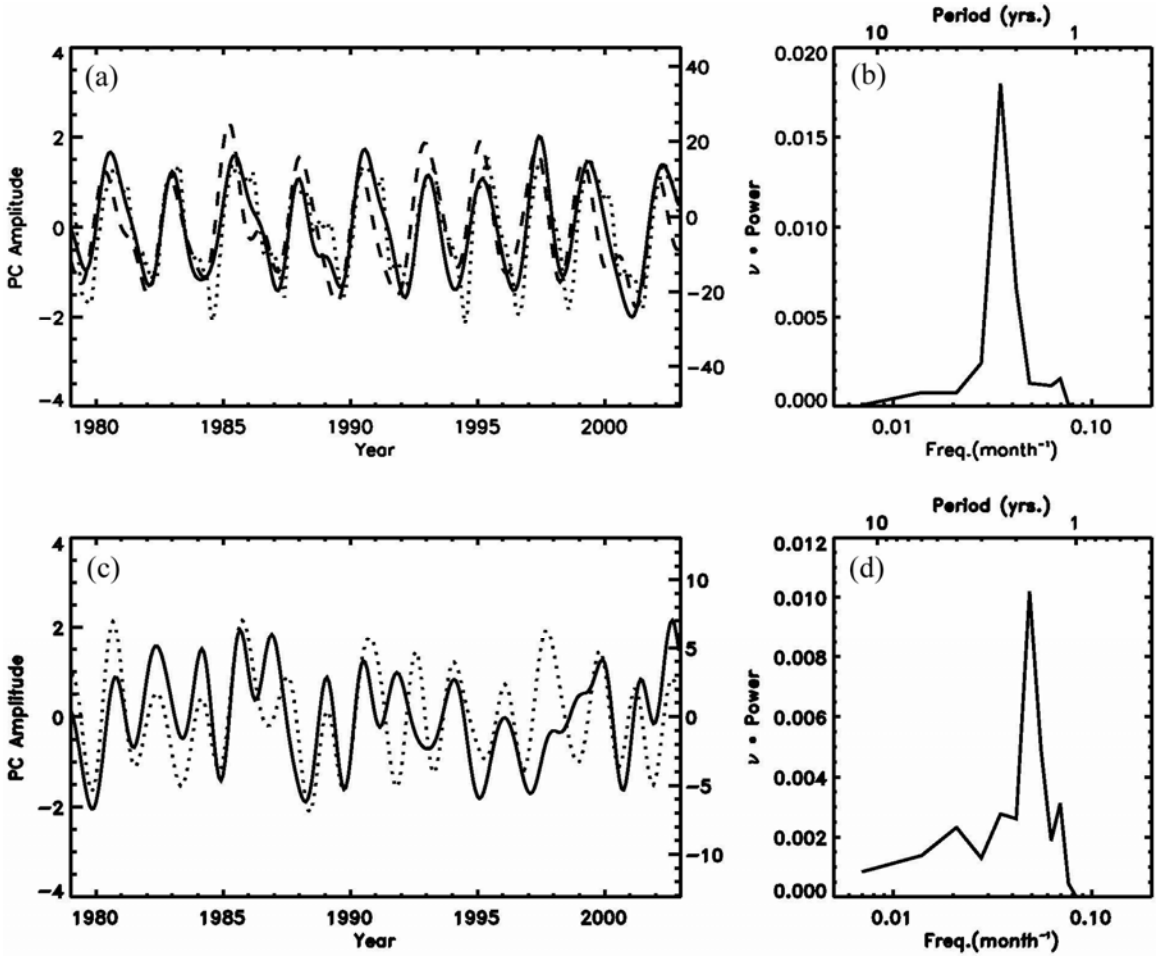

Figure 1.9: PC time series (left column) and spectra (right column) for the first two EOFs of the total column ozone from 2-D model. PCs are shown along with an appropriate index. (a) PC1 of the 2-D CTM ozone (solid line), PC1 of the zonal mean MOD (dashed line), and 30 mbar QBO index (dotted line), (c) PC2 of the 2-D CTM ozone (solid line) and PC3 of the zonal mean MOD (dashed line).

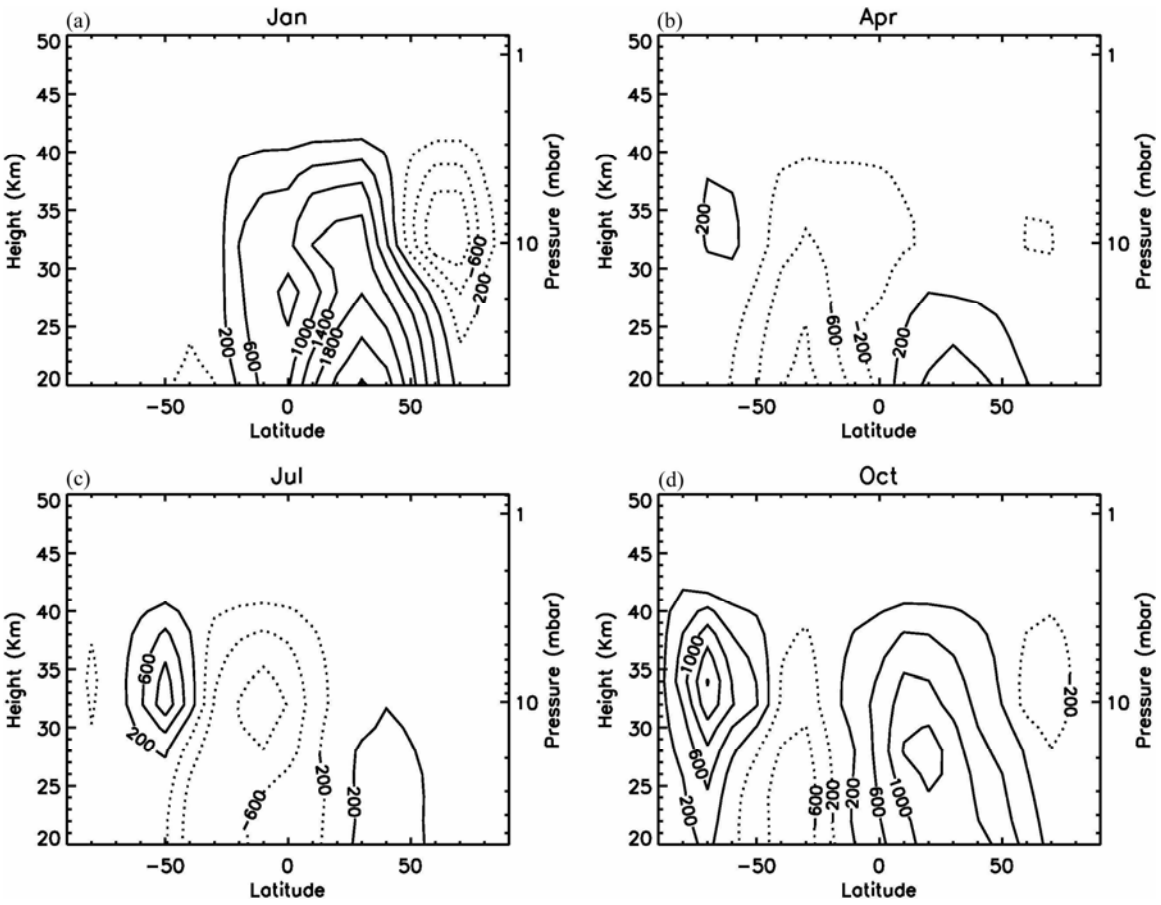

Figure 1.10: Stratospheric Transport Eulerian mean (TEM) stream function in 1985. (a) January, (b) April, (c) July, and (d) October. Units are m^2/s.

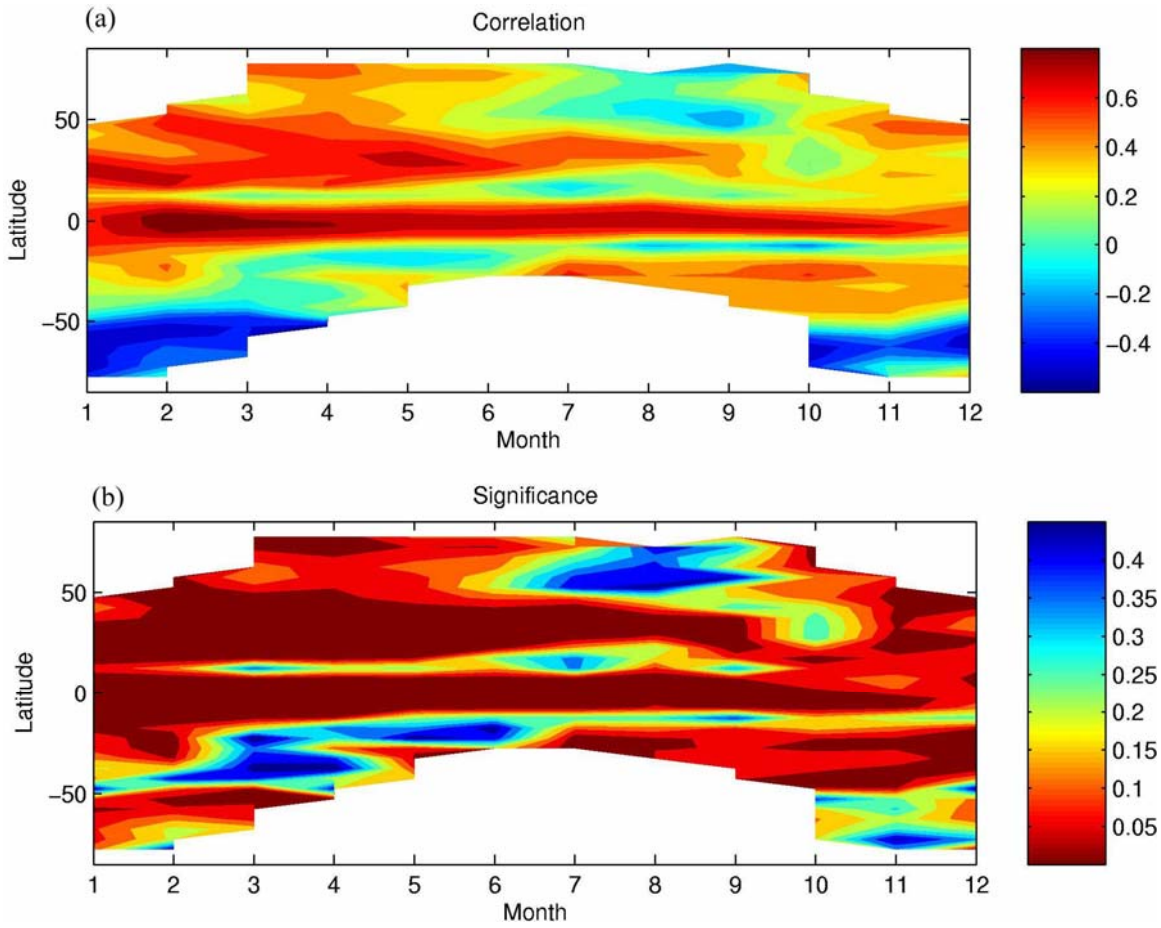

Figure 1.11: (a) Correlation coefficients between monthly mean column ozone from MOD and model over the period from 1979 to 2002, (b) Significance levels of the correlation coefficients.

Chapter 2: Spatial Patterns and Mechanisms of the Quasi-biennial Oscillation-Annual Beat of Ozone

2.1 Abstract

An idealized two-dimensional (2-D) chemistry and transport model (CTM) is used to investigate the spatial patterns of, and mechanism for, the QBO-annual beat (QBO-AB) signal in ozone in the tropics and subtropics. Principal component analysis (PCA) is applied to the detrended, deseasonalized and filtered total column ozone anomaly from the standard model. The first two empirical orthogonal functions (EOFs) capture over 98.5% of the total variance. The first EOF, accounting for 70.3% of the variance, displays a structure attributable to the approximately symmetric QBO with a period of 28 months. The second EOF, capturing 28.2% of the variance, is related to the QBO-AB around 20 months. An extended EOF analysis reveals the characteristic pattern of the downward propagation of QBO and upward propagation of QBO-AB. The model results are compared to those from the Merged Ozone Data (MOD). Sensitivity experiments indicate that the QBO-AB is produced primarily as a result of the dynamical QBO-AB in the mean meridional circulation and by the interaction between the QBO and the annual cycle in transport, each contributing roughly equally to the forcing of QBO-AB. The interaction between the QBO in the transport fields and the annual cycle in chemistry plays a minor role.

2.2 Introduction

The quasi-biennial oscillation (QBO; See Table 1 for list of acronyms) is the dominant interannual variability in the tropical stratosphere. It is primarily an oscillation in zonal winds in the stratosphere between downward propagating easterly and westerly phases, with a period of 22-32 months [*Reed et al*., 1961; *Veryard and Ebdon*, 1961; See extensive review by *Baldwin et al*., 2001]. There have been numerous observational studies of the QBO in the zonal wind, temperature, and ozone [e.g., *Angell and Korshover*, 1970; *Oltmans and London*, 1982; *Hasebe*, 1983; *Zawodny and McCormick*, 1991; *Pawson and Fiorino*, 1998; *Randel et al*., 1999]. The mechanism by which the QBO modulates the ozone abundance in the stratosphere is well known [*Plumb and Bell*, 1982; *Baldwin et al*., 2001]. When the QBO is in the westerly (easterly) phase, there is anomalous descending (upwelling) motion in the tropical stratosphere and anomalous upwelling (descending) motion in the subtropical stratosphere. This results in more (less) ozone at the equator in the westerly (easterly) QBO phase [*Gray and Dunkerton*, 1990; *Tung and Yang*, 1994a; *Hasebe*, 1994; *Randel and Cobb*, 1994]. The QBO also induces large variations in ozone in the extra-tropical stratosphere through its modulation of the vertical propagation of planetary Rossby waves [*Holton and Tan* 1980; *Dunkerton and Baldwin*, 1991] and through the QBO-induced meridional circulation (QBO-MMC) [*Kinnersley and Tung*, 1999; *Ruzmaikin et al.*, 2005].

An outstanding deficiency in our understanding of the QBO in ozone is associated with the mechanism responsible for the QBO-related harmonics that have been detected in stratospheric ozone. Consider a multiplicative model

$$(1 + a\sin\omega_A t)(1 + b\sin\omega_Q t) = 1 + a\sin\omega_A t + b\sin\omega_Q t + ab(\sin\omega_A t)(\sin\omega_Q t),$$

where ω_A and ω_Q are the frequencies of the annual cycle and the QBO. The nonlinear term produces the sum and difference frequencies through the trigonometric identity

$$(\sin\omega_A t)(\sin\omega_Q t) = \frac{1}{2}\cos(\omega_A - \omega_Q)t - \frac{1}{2}\cos(\omega_A + \omega_Q)t .$$

As a result, the QBO and annual cycles will produce beat frequencies with periods of approximately 20 and 8.6 months, which was first found in the total column ozone data obtained by TOMS in the tropics and extra-tropics [*Tung and Yang*, 1994a; *Tung and Yang*, 1994b]. These frequencies have also been observed in the power spectra of angular momentum and planetary Rossby wave forcing in the stratosphere [*Baldwin and Tung*, 1994]. Using version 7 merged ozone data (MOD), *Camp et al.* [2003] carried out a principal component analysis (PCA) of the temporal and spatial patterns of the interannual variability of the total column ozone in the tropics from 1979 to 2002. They found that the first four empirical orthogonal functions (EOFs) captured over 93% of the variance of the detrended and deseasonalized data on interannual timescales. The PC associated with the third EOF (which accounted for 15% of the variance) had a dominant peak around 20 months (referred to as the QBO-annual beat (QBO-AB) hereafter). The spatial pattern is a zonally symmetric, north-south tilted plane centered at the equator. A weaker signal at about 8 months (QBO-AB′ hereafter) was also found in MOD. At present, a mechanistic understanding of the origin of these harmonics is still lacking.

Such an understanding is critical to accurately account for the large QBO-induced interannual variability in ozone when trying to quantify the impact of human activity on ozone in the stratosphere.

Using a two-dimensional (2-D) model, *Jones et al*. [1998b] successfully reproduced the QBO beat frequencies in stratospheric ozone. They did not, however, perform a detailed analysis of the mechanism responsible for the beat in the model. More recently, *Jiang et al*., [2004] were able to simulate the QBO and the QBO-AB signals in column ozone from 1979 to 2002 using a 2-D chemical transport model (CTM) driven by transport fields derived from the National Centers for Environmental Prediction (NCEP) — Department of Energy Reanalysis 2. Here, we extend the analysis of *Jiang et al*. [2004], using the 2-D model of *Jones et al*. [1998a,b], to investigate the spatial pattern (latitude-altitude) of, and the mechanism for, the QBO-AB of ozone in the stratosphere. The reason for using the Jones model is as follows. The QBO signal in *Jiang et al.* [2004] has a broad power spectrum, making it difficult to isolate the QBO from the QBO-AB. The situation will improve with a longer record. In the model of *Jones et al*. [1998a,b] the parameterized QBO forcing produces an oscillation with a fixed period of ~28 months. There are no other sources of interannual variability in this idealized model. It is therefore a better tool to determine the mechanisms for producing the QBO-AB in ozone. The model of *Jones et al*. [1998a,b], however, does not account for the QBO modulation of planetary wave breaking, which is responsible for the QBO in ozone in the extra-tropical stratosphere. We therefore focus here on understanding the mechanism responsible for the QBO-AB in ozone in the tropical and subtropical stratosphere.

There are three possible mechanisms for the QBO-AB signal in column ozone. In the chemical tracer continuity equation, the interaction between the QBO and the annual cycle in the Brewer-Dobson circulation (BDC) and in the photochemical sources and sinks will both contribute to the QBO-AB [*Gray and Dunkerton*, 1990]. In addition, the mean meridional circulation (MMC) will possess a QBO-AB signal as a result of the interaction of the QBO and the annual cycle in the advection terms of the momentum equation in the tropics. This QBO-AB signal in the transport will also produce a QBO-AB signal in column ozone. However, it is unclear which is the predominant mechanism. We propose to test the different mechanisms through a series of sensitivity experiments listed in Table 2.

2.3 Modeling Ozone in the Tropics and Subtropics

2.3.1 Modeling Results

The 2-D model is described in detail in [*Jones et al.*, 1998b] and [*Schneider et al.*, 2000]. It has a horizontal resolution of 5° from pole-to-pole and a vertical resolution of 2 km from the surface to 80 km. It is a fully interactive primitive equation model in which the heating rates are calculated from model-derived ozone in the stratosphere. The model includes a comprehensive treatment of stratospheric chemistry. The effects of planetary wave breaking are specified as annually varying eddy diffusion coefficients K_{yy} based on *Newman et al.* [1986, 1988]. The QBO in zonal wind is reproduced in the model using mainly the parameterization of *Gray and Pyle* [1989] for the deposition of Kelvin and

Rossby-gravity wave momentum in the tropical zonal wind. The Rossby-gravity wave dissipation is adopted from the formulation of *Holton and Lindzen* [1972].

In the analysis presented here, we employ an offline version of the model, driven by the transport fields archived from a 50-year simulation of the fully interactive model. The total column ozone climatology and the QBO ozone anomalies from 30 years simulation are shown in Figure 2.1. The annual cycle of the modeled ozone column abundance is consistent with observations. The QBO anomaly in ozone is calculated by removing the monthly mean annual cycle from the original total column ozone abundances. The model provides a good simulation of the QBO signal in the ozone columns. The amplitude of the ozone anomaly is ~7 Dobson unit (DU). Estimates of the magnitude of the tropical anomaly range from about 6 DU by *Hasebe* [1983] to about 9 DU by *Zawodny and McCormick* [1991]. Using a least squares fit to the anomalies in column ozone, *Tung and Yang* [1994a] suggested that the amplitude of the QBO anomaly in middle and high latitudes is about 6 DU, about a quarter of the amplitude of the unfiltered anomaly.

To investigate the magnitude of the QBO-AB and QBO-AB′, we apply Bandpass filters A and B to the column ozone from the 2-D CTM and MOD. The details of the Bandpass filters A and B, and other similarly constructed filters used in this study are presented in Table 3. Bandpass filters A and B are desired to retain the signals of QBO-AB and QBO-AB′. Because the QBO-AB is not a strict oscillation around 20 months in the MOD and model, signal will be compensated through averaging over pure 20 months

cycle. Thus the QBO-AB is averaged over 18 and 14 events for the model and MOD, respectively, when the QBO-AB signal reaches maximum at 17.5° N. Similar approach is applied to isolate the QBO-AB′ from the model and MOD. Mean QBO-AB and QBO-AB′ of 2-D CTM and MOD are shown in Figure 2.2. The magnitude of the QBO-AB in the 2-D CTM (solid line) is a little smaller than that in the MOD (dashed line). The magnitude of the QBO-AB′ in the model is similar to that in the MOD. The amplitude of the QBO-AB is about 2-3 times larger than that of the QBO-AB′ from the 2-D CTM and MOD. The reason will be given in section 2.4.1.

2.3.2 PCA of Ozone Column Abundance

PCA is applied to the detrended, deseasonalized and filtered total column ozone anomaly from the 2-D CTM. Lowpass filter A is chosen to obtain a full signal from periods above 15 months and no signal from periods below 12.5 months. The first two EOFs capture 98.5% of the total variance of the filtered data, as shown in Figure 2.3. The fractions of variance for the leading EOFs are listed in Table 4. The first EOF captures 70.3% of the variance, and displays a structure similar to the QBO. It is approximately symmetric about the equator and oscillates about nodes at 10° N and 11° S. The values range from a high of 3 DU to a low of –2 DU. The magnitude of this mode is smaller than that of the first EOF pattern of the zonal mean MOD [*Jiang et al.*, 2004]. The associated principal component time series, PC1, is plotted in Figure 2.3b. The power spectral estimate of PC1, Figure 2.3c, shows a strong peak at 28 months. The phase of PC1 does not match the PC1 from the zonal mean MOD, because the observed QBO has a much broader spectral band around 28 months than that in the model. Ozone is

transported to the polar region by the BDC. During the QBO westerly (easterly) phase, the BDC is weak (strong). Therefore the tropical total column ozone will increase (decrease), while the opposite will occur at higher latitudes.

The second EOF, capturing 28.2% of the variance, oscillates about a node at the equator. Values range from 1.4 DU in the north to –1.6 DU in the south. It is similar to the third EOF pattern of the zonal mean MOD [*Jiang et al.*, 2004]; however, the magnitude is smaller than that in the zonal mean MOD. The power spectral estimate of the associated PC2 has a dominant peak around 20 months, suggesting that this EOF reflects the interaction of the annual cycle with the QBO signal.

2.3.3 Extended EOF Analysis of Ozone Mixing Ratio

To study the interannual variability in the vertical distribution of ozone, particularly its spatial-temporal structure, we apply Extended EOF (EEOF) [*Weare and Nasstrom*, 1982] to the deseasonalized ozone volume-mixing ratio (VMR) from the 2-D CTM. For this analysis, time is lagged –15 months to +14 months. The main advantage of EEOF analysis over PCA analysis in this case is that we can extract modes that exhibit systematic co-variability in space and time, such as propagating "waves" (e.g., *Waliser et al.*, 2003). Note that since EEOF modes are constrained in both space and time, the dominant modes typically do not capture as much overall variance as for a regular PCA. In this case, the first four EEOFs, shown in Figure 2.4, capture 79.6% of the total variance.

The first two EEOFs capture 24.3% and 23.6% of the variance, respectively, and represent the QBO. Their spatial patterns and PCs are in quadrature. PC1 and PC2, plotted in Figure 2.4b and 2.4e, respectively, have maximum cross-correlation (=0.98) at -7 months, which represents a complete period of about 28 months and is consistent with the power spectral estimate shown in Figures 2.4c and 2.4f. The third and fourth EEOF modes account for 16.1% and 15.6% of the variance, respectively, and correspond to the QBO-AB. Their spatial patterns and PCs are also in quadrature. PC3 and PC4, plotted in Figures 2.4h and 2.4k, have a maximum cross-correlation (=0.97) at 5 months. It is consistent with the power spectral estimates in Figures 2.4i and 2.4l, displaying a dominant period of about 20 months.

To illustrate the propagation of the QBO and QBO-AB, respectively, we reconstruct the data using only the first two EEOF modes (i.e., $PC_1 \times EEOF_1 + PC_2 \times EEOF_2$), and then separately using only third and fourth EEOF modes (i.e. $PC_3 \times EEOF_3 + PC_4 \times EEOF_4$). Figure 2.5 shows these constructed data along the equator for the QBO mode, and at 12.5° N and 12.5° S for the QBO-AB mode. There is downward propagation of the ozone QBO as a result of the downward propagation of the dynamical QBO. In contrast, the ozone QBO-AB propagates upward. The ozone QBO-AB in 12.5° N has opposite sign to that in 12.5° S. The reason for the upward propagation of the QBO-AB will be given in section 2.4.1. The downward propagation speed of the QBO is about 0.6 km/month in the region of 20-36 km. The upward propagation speed of the QBO-AB is about 1.2 km/month in the region of 28-36 km. The downward propagation of the QBO in the ozone VMR is similar to that found in *Politowicz and*

Hitchman [1997]. Using the diabatic-forcing method in their 2-D model, they also found that QBO in the deseasonalized and filtered ozone VMR propagates downward with a speed of 1 km/month in the region of 20-39 km. However, the authors did not find the QBO-AB.

2.3.4 Comparison With Observations

To investigate the propagation characteristics of QBO and QBO-AB in the observed ozone data, we apply EEOF analysis to the deseasonalized, detrended, and filtered ozone VMR from version 8 MOD [*Wellemeyer et al.*, 2004]. Bandpass filter C is used to retain the QBO and QBO-AB signals. The first four EEOFs capture 63.1% of the total variance. The first EEOF, shown in Figure 2.6a, represents the QBO, accounting for 23.4% of the variance. The power spectral estimate of the PC1 shows a broad peak around 28 months. The spatial pattern of the first EEOF demonstrates that less (more) ozone is transported to the high latitudes in the westerly (easterly) phase of QBO. The second EEOF accounts for 21.8% of the variance and represents the QBO too. PC1 and PC2 have a maximum cross-correlation (=0.93) at 7 months. The third and fourth EEOFs, shown in Figure 2.6g and 2.6j, represent the asymmetric QBO-AB, accounting for 9.5% and 8.4% of the variance respectively. PC1 and PC2 have a maximum cross-correlation (=0.92) at 5 months. The power spectra of PC3 and PC4 display dominant peak around 20 months. There is also small peak around QBO in the power spectra of PC3 and PC4.

The propagations of the QBO and QBO-AB are shown in Figure 2.7. The downward propagation of the ozone QBO is similar to that in the model, although the

propagation is weak in the lower stratosphere. This is because the QBO signal in the MOD has a broader spectral peak than that in the model, thus the signal is more complex. Unlike the idealized model, the length of the QBO phases in the MOD changes from year to year. We also find the upward propagation of the ozone QBO-AB in the MOD as in the model. The sign of the ozone QBO-AB is opposite in the different hemispheres. Because there is also a QBO signal in the third and fourth modes, the amplitude of the constructed signal from the third and fourth modes does not represent the real amplitude of the QBO-AB, which can explain why the amplitude is larger in the south than that in the north. The downward propagation speed of the QBO is about 1 km/month in the region of 32-43 km. The upward propagation speed of the QBO-AB is about 1.3 km/month in the same region.

The spatial patterns of the first and second EEOFs in the model ozone VMR are similar to the first two modes from singular-value decomposition (SVD) between the ozone VMR from SAGE II and the QBO zonal winds [*Randel and Wu*, 1996]. SVD for the two fields involves the covariance of two fields. As a result, the analysis of two fields by SVD will exhibit the highest temporal covariance between the two fields. Since the QBO is the dominant signal in the QBO zonal winds, they only find the QBO signal in ozone VMR. The QBO-AB was not found in their two-field SVD results.

2.4 Mechanisms for Generating QBO-AB

2.4.1 Theory of Harmonics

We follow *Gray and Dunkerton* [1990] in the treatment of the interaction between the QBO and the annual cycle in column ozone. The continuity equation for the tracers in the model can be written as

$$\frac{\partial \chi}{\partial t} + \bar{v}\frac{\partial \chi}{\partial y} + \bar{w}\frac{\partial \chi}{\partial z} = (P - L) + \vec{\nabla} \cdot K\vec{\nabla}\chi \qquad (1)$$

where χ is the mixing ratio, $\bar{v}$ and $\bar{w}$ are the mean meridional and vertical velocities, *P* and *L* represent photochemical production and loss rates, respectively, and *K* is the "eddy diffusion" coefficient, representing mixing by planetary waves.

Multiplying Equation (1) by the density ρ and taking the vertical integral, we can approximately obtain

$$\frac{\partial C}{\partial t} + \bar{v}\frac{\partial C}{\partial y} = \int_0^\infty \rho(P - L)dz + \overline{\vec{\nabla} \cdot K\vec{\nabla}C} \qquad (2)$$

where $C = \int_0^\infty \rho\,\chi\,dz$ is the column ozone. The nonlinear advection term, $\bar{v}\frac{\partial C}{\partial y}$, implies that the initial harmonics can interact to form new harmonics with frequencies equal to the sum or the difference of any pair of initial frequencies.

We can explore the details of these harmonics by expanding the meridional velocity into its seasonal and QBO-dependent components

$$\bar{v} = v_0 + v_A \exp(i\omega_A t) + v_Q \exp(i\omega_Q t) + v_{AQ}^{+} \exp[i(\omega_A + \omega_Q)t] + v_{AQ}^{-} \exp[i(\omega_A - \omega_Q)t] \qquad (3)$$

where the subscripts *A* and *Q* denote annual and quasi-biennial harmonics, v_A and v_Q are the amplitudes associated with the annual and quasi-biennial harmonics, v_{AQ}^{+} and v_{AQ}^{-} are the amplitudes associated with the sum and difference between the annual and quasi-biennial harmonics. Similarly, we can express the ozone column, C, as

$$C = C_0 + C_A \exp(i\omega_A t) + C_Q \exp(i\omega_Q t) + C_{AQ}^{+} \exp[i(\omega_A + \omega_Q)t] + C_{AQ}^{-} \exp[i(\omega_A - \omega_Q)t] + \ldots \quad (4)$$

where C_A and C_Q are the amplitudes associated with the annual and quasi-biennial oscillations for the column ozone, C_{AQ}^{+} and C_{AQ}^{-} are the amplitudes associated with the two beat frequencies. The photochemical production and loss rates can also be written as

$$(P - L) = (P - L)_0 + S_A \exp(i\omega_A t) \quad (5)$$

where S_A is the amplitude associated with the annual cycle of the photochemical production and loss rates.

In the previous section, we found that the QBO-AB propagates upward and the amplitude of the QBO-AB is larger than that of QBO-AB′. Assuming the annual cycle signal does not propagate, the interaction between the annual cycle and the propagating QBO gives:

$$\sin(\omega_A t)\sin(\omega_Q t - \frac{\omega_Q}{W_Q} z) = \frac{1}{2}\left\{\cos[(\omega_A - \omega_Q)t + \frac{\omega_Q}{W_Q} z] - \cos[(\omega_A + \omega_Q)t - \frac{\omega_Q}{W_Q} z]\right\} \quad (6)$$

where W_Q is the phase speed of the QBO, t is time, and z is height. Thus the phase speeds of the QBO-AB and QBO-AB′ are separately

$$W_{AB} = -\frac{\omega_A - \omega_Q}{\omega_Q} W_Q \text{ and } W_{AB'} = \frac{\omega_A + \omega_Q}{\omega_Q} W_Q \tag{7}$$

Since the QBO propagates downward, $W_Q < 0$, the phase speed of the QBO-AB is positive (upward) and the phase speed of the QBO-AB′ is negative (downward).

To investigate the ozone response to the QBO-AB and QBO-AB′ signals, we also need to consider the lifetime of O_3. Consider a heuristic model with pure sinusoidal forcing [*Camp et al.*, 2001]:

$$\frac{dy(t)}{dt} = -\frac{y(t)}{\tau} - \frac{F(t)}{\tau}; \quad F(t) = A_0 \sin(\omega t - \frac{\omega}{W} z), \tag{8}$$

where $y(t)$ is O_3 VMR, τ is the lifetime of the O_3, and $F(t)$ is the sinusoidal forcing with period of 20 or 8 months. The loss of O_3 is non-linear so this is an approximate description. Define $\tan\phi = \omega\tau$, the solution to Equation (8) is:

$$y(t) = \left(y(0) - \frac{A_0 \sin(\omega z / W + \phi)}{\sqrt{1+\omega^2\tau^2}} \right) e^{-t/\tau} - \frac{A_0 \sin(\omega t - \frac{\omega}{W} z - \phi)}{\sqrt{1+\omega^2\tau^2}}, \tag{9}$$

where $y(0)$ is the value of y at $t = 0$. Ignoring the first transient term, the sensitivity of the response of O_3 to the oscillatory forcing is

$$\alpha = \frac{\|y(t)\|}{\|F(t)\|} = \frac{1}{\sqrt{1+\omega^2\tau^2}}, \tag{10}$$

Because the lifetime of ozone is long with respect to loss in the lower stratosphere where most of the column resides, we have $\omega\tau >> 1$ and $\alpha \approx \frac{1}{\omega\tau}$. Therefore, the response of ozone to the QBO-AB is about $\frac{\omega_A + \omega_Q}{\omega_A - \omega_Q} \approx 2.5$ times larger than that of QBO-AB′.

2.4.2 Sensitivity Experiments A, B, and C

To understand how the QBO-AB signal in column ozone, $C_{AQ}^{-} \exp[i(\omega_A - \omega_Q)t]$, is generated, we consider three possible mechanisms. First, the QBO-AB in the transport fields, $v_{AQ}^{-} \exp[i(\omega_A - \omega_Q)t]$, will produce a signal with a 20-month period in ozone. Second, the QBO and the annual cycle from the transport fields will interact to produce a QBO-AB in the 2-D CTM. Finally, the interaction between the QBO in the transport and the annual cycle in the ozone chemistry will generate a QBO-AB. To determine the contributions of the three mechanisms in producing the QBO-AB signal in column ozone we have performed a series of sensitivity experiments.

In experiment A, Bandpass filter A is applied to the transport fields for extracting the QBO-AB signal, $v_{AQ}^{-} \exp[i(\omega_A - \omega_Q)t]$. In this experiment we turn off the annual cycle in the photochemical production and loss rates (see Eq. 5). As a result, shown in Figure 2.8a, there is no annual cycle in the total column ozone climatology from this 30-year model run. The ozone anomaly, shown in Figure 2.8b, displays a 20-month period characteristic of the QBO-AB. PCA is applied to the detrended and lowpass filtered total

column ozone anomaly. The first leading mode, shown in Figure 2.9, captures 97.4% of the total variance, representing the QBO-AB signal. This EOF is a tilted plane; values range from 1 DU in the north to –0.8 DU in the south. The magnitude is smaller than that of the second EOF in Figure 2.3d. The power spectral estimate of the associated PC has a dominant peak around 20 months, indicating that the ozone QBO-AB in this experiment is a direct result of the original QBO-AB signal in the transport fields. EEOF analysis is applied to the deseasonalized ozone VMR from experiment A. The first two modes, together accounting for 98% of the variance, correspond to the QBO-AB. We reconstruct the data using the first two EEOF modes. The 12.5° N $PC_1 \times EEOF_1 + PC_2 \times EEOF_2$ displays the upward propagation of the QBO-AB.

In experiment B we retain the annual and QBO cycles in the transport fields by applying Bandpass filters D and E. There is no annual cycle in the chemical terms. The climatology of the 30-year total column ozone and the ozone anomaly are shown in Figure 2.10. There is an annual cycle in the ozone, which is due to the annual cycle in the transport fields, $v_A \exp(i\omega_A t)$. PCA is applied to the detrended, deseasonalized and filtered total column ozone anomaly. The first EOF represents the QBO. The second EOF, shown in Figure 2.11, captures 26.4% of the total variance and represents the QBO-AB signal. The values of this EOF range from 1 DU in the north to –1 DU in the south. The magnitude of this EOF is comparable to the first EOF from experiment A. The ozone QBO-AB in this experiment is the result of the interaction between the QBO and annual signals from the transport fields in the 2-D CTM. EEOF is applied to the deseasonalized ozone VMR from experiment B. The third and fourth modes correspond to the QBO-AB,

accounting for 14.2% and 13.3% of the variance, respectively. The $PC_3 \times EEOF_3 + PC_4 \times EEOF_4$ at 12.5° N also displays the upward propagation of the QBO-AB.

Finally, we examine the interaction between the QBO and the annual cycle in the chemistry in experiment C by applying bandpass filter E to the transport fields to retain only the QBO signal, $v_Q \exp(i\omega_Q t)$. The annual cycle is retained in the photochemical production and loss rates, $S_A \exp(i\omega_A t)$. As shown in Figure 2.12a, there is an annual cycle in the ozone climatology, which represents the change of photochemical production and loss rates by the annual march of solar heating. The ozone anomaly, shown in Figure 2.12b, has the QBO and QBO-AB signals. We applied PCA to the detrended, deseasonalized and filtered total column ozone anomaly. The first two EOFs correspond to the QBO. The third mode, shown in Figure 2.13, captures 2% of the total variance and represents the QBO-AB. Values of this EOF range from 0.2 DU in the north to –0.19 DU in the south, significantly smaller than that in experiments A and B. This suggests that the interaction between the QBO in the transport fields and the annual cycle in the chemistry model makes the smallest contribution to the ozone QBO-AB signal. The QBO-AB signal is too weak in ozone VMR from the experiment C, and does not appear in the leading EEOFs.

To further investigate the magnitude of the QBO-AB signal in column ozone, we multiply the PC and EOF corresponding to the column ozone QBO-AB in each model experiment. Since the QBO-AB is an asymmetric mode, we average the product of the

PC and EOF from 0° to 30° N. The results, shown in Figure 2.14, confirm that the magnitude of the ozone QBO-AB in experiments A and B is comparable. The ozone QBO-AB signal in experiment C is the smallest. We then summed the product of the PC and EOF corresponding to the QBO-AB signal at 12.5° N from all three experiments. In Figure 2.15, the sum (dotted line) is compared against the QBO-AB signal from the standard model shifted forward by three months (solid line). These two curves match well. The three-month phase shift is mostly due to the Fourier filters applied to the original transport fields [*Tung and Yang*, 1994a].

2.5 Conclusions

We have used an idealized 2-D CTM [*Jones et al.*, 1998] to study the spatial-temporal pattern of and the mechanisms responsible for producing QBO-AB in the stratospheric ozone. The model produces a QBO in the ozone with a period of 28 months. The amplitude of the modeled QBO anomalies of ozone in the tropics is about 7 DU, in agreement with observations [*Hasebe*, 1983; *Zawodny and McCormick*, 1991]. PCA was applied to the detrended, deseasonalized, and filtered total column ozone anomaly from the standard model. The first two EOFs capture over 98.5% of the total variance. The first EOF explains 70.3% of the variance, and is identified with the approximately symmetric QBO with a period of 28 months. The second EOF, capturing 28.2% of the variance, is the asymmetric QBO-AB with a period of 20 months, arising from the interaction between the QBO and the annual cycle. EEOF analysis of the deseasonalized model ozone VMR illustrates that the ozone QBO and QBO-AB are vertical propagating

features. The QBO propagates downward, in agreement with previous analysis. However, the QBO-AB propagates upward as a result of the interaction between the BDC and QBO. We also found similar propagations of the ozone QBO and QBO-AB in the MOD.

Sensitivity experiments were performed to isolate the mechanism primarily responsible for the QBO-AB signal in total column ozone. Our analysis indicate that the interaction between the QBO signal in the transport fields and the annual cycle in the chemistry play a minor role in generating the QBO-AB in ozone in the model. We found that the dynamical QBO-AB in the MMC and the interaction between the QBO and the annual cycle in the transport fields provide comparable contributions to the QBO-AB in ozone. The idealized model employed here is not able to match the observed QBO phase. In future work we will investigate the details of the phase relationship between the ozone anomalies and the QBO in zonal wind by relaxing the model zonal winds to match observed tropical winds, to reproduce the interannual variability of the QBO in the model. Extension of the model to higher latitudes is also being planned.

This work constitutes an advance beyond the work of *Camp et al*. [2003] and *Jiang et al*. [2004] in elucidating the non-linear interaction between the QBO and the annual cycle, primarily the BDC. It is a tribute to the high quality of the MOD data that we can now extract a second order signal that is less than 1% of the bulk signal. This allows us to sensitively probe nonlinear interactions between the different physical processes in the atmosphere. It is desirable to extend our data analysis and modeling to investigate related non-linear interactions such as that between QBO and the solar cycle

[*Labitzke and Vanloon*, 1988; *Hamilton*, 2002; *Salby and Callaghan*, 2000]. Longer records and improvements in measurements will provide the necessary data to test critical components of our model.

2.6 References:

Angell, J.K., and J. Korshover, Quasi-Biennial, Annual, and Semiannual Zonal Wind and Temperature Harmonic Amplitudes and Phases in Stratosphere and Low Mesosphere of Northern Hemisphere, *Journal of Geophysical Research*, *75* (3), 543-&, 1970.

Baldwin, M.P., L.J. Gray, T.J. Dunkerton, K. Hamilton, P.H. Haynes, W.J. Randel, J.R. Holton, M.J. Alexander, I. Hirota, T. Horinouchi, D.B.A. Jones, J.S. Kinnersley, C. Marquardt, K. Sato, and M. Takahashi, The quasi-biennial oscillation, *Reviews of Geophysics*, *39* (2), 179-229, 2001.

Baldwin, M.P., and K.K. Tung, Extra-tropical QBO signals in angular-momentum and wave forcing, *Geophysical Research Letters*, *21* (24), 2717-2720, 1994.

Camp, C.D., M.S. Roulston, A.F.C. Haldemann, and Y.L. Yung, The Sensitivity of Tropospheric Methane to the Interannual Variability in Stratospheric Ozone, *Chemosphere-Global Change Science*, *3*, 147-156, 2001.

Camp, C.D., M.S. Roulston, and Y.L. Yung, Temporal and spatial patterns of the interannual variability of total ozone in the tropics, *Journal of Geophysical Research-Atmospheres*, *108* (D20), 2003.

Dunkerton, T.J., and M.P. Baldwin, Quasi-Biennial Modulation of Planetary-Wave Fluxes in the Northern-Hemisphere Winter, *Journal of the Atmospheric Sciences*, *48* (8), 1043-1061, 1991.

Gray, L.J., and T.J. Dunkerton, The role of the annual cycle in the Quasi-Biennial Oscillation of ozone, *Journal of the Atmospheric Sciences, 47* (20), 2429-2451, 1990.

Gray, L.J., and J.A. Pyle, A two-dimensional model of the Quasi-Biennial Oscillation of ozone, *Journal of the Atmospheric Sciences, 46* (2), 203-220, 1989.

Hamilton, K., On the quasi-decadal modulation of the stratospheric QBO period, *Journal of Climate, 15* (17), 2562-2565, 2002.

Hasebe, F., Interannual variations of global total ozone revealed from Nimbus 4-Buv and Ground-based observations, *Journal of Geophysical Research-Oceans and Atmospheres, 88* (NC11), 6819-6834, 1983.

Hasebe, F., Quasi-Biennial Oscillations of ozone and diabatic circulation in the equatorial stratosphere, *J. Atmos. Sci.*, 51, 729-745, 1994.

Holton, J.R., and R.S. Lindzen, Updated theory for Quasi-Biennial Cycle of tropical stratosphere, *Journal of the Atmospheric Sciences, 29* (6), 1076-1080, 1972.

Holton, J.R., and H.C. Tan, The Influence of the Equatorial Quasi-Biennial Oscillation on the Global Circulation at 50 Mb, *Journal of the Atmospheric Sciences, 37* (10), 2200-2208, 1980.

Jiang, X., C.D. Camp, R. Shia, D. Noone, C. Walker, and Y.L. Yung, Quasi-biennial oscillation and quasi-biennial oscillation-annual beat in the tropical total column ozone: A two-dimensional model simulation, *Journal of Geophysical Research-Atmospheres, 109* (D16), 2004.

Jones, D.B.A., An analysis of the mechanisms for the QBO in ozone in the tropical and subtropical stratosphere, Ph.D. Thesis, 1998a.

Jones, D.B.A., H.R. Schneider, and M.B. McElroy, Effects of the quasi-biennial oscillation on the zonally averaged transport of tracers, *Journal of Geophysical Research-Atmospheres*, *103* (D10), 11235-11249, 1998b.

Kinnersley, J.S., and K.K. Tung, Mechanisms for the extratropical QBO in circulation and ozone, *Journal of the Atmospheric Sciences*, *56* (12), 1942-1962, 1999.

Labitzke, K., and H. Vanloon, Associations between the 11-Year Solar-Cycle, the QBO and the Atmosphere 1. The Troposphere and Stratosphere in the Northern Hemisphere in Winter, *Journal of Atmospheric and Terrestrial Physics*, *50* (3), 197-206, 1988.

Newman, P.A., M.R. Schoeberl, and R.A. Plumb, Horizontal mixing coefficients for two-dimensional chemical-models calculated from National Meteorological Center Data, *Journal of Geophysical Research-Atmospheres*, *91* (D7), 7919-7924, 1986.

Newman, P.A., M.R. Schoeberl, R.A. Plumb, and J.E. Rosenfield, Mixing rates calculated from potential vorticity, *Journal of Geophysical Research-Atmospheres*, *93* (D5), 5221-5240, 1988.

Oltmans, S.J., and J. London, The Quasi-Biennial Oscillation in Atmospheric Ozone, *Journal of Geophysical Research-Oceans and Atmospheres*, *87* (NC11), 8981-8989, 1982.

Pawson, S., and M. Fiorino, A comparison of reanalyses in the tropical stratosphere. Part 2: The quasi-biennial oscillation, *Climate Dynamics*, *14* (9), 645-658, 1998.

Plumb, R.A., and R.C. Bell, A model of the Quasi-Biennial Oscillation on an equatorial Beta-plane, *Quarterly Journal of the Royal Meteorological Society*, *108* (456), 335-352, 1982.

Politowicz, P.A., and M.H. Hitchman, Exploring the effects of forcing quasi-biennial oscillations in a two-dimensional model, *Journal of Geophysical Research-Atmospheres*, *102* (D14), 16481-16497, 1997.

Randel, W.J., and J.B. Cobb, Coherent variations of monthly mean total ozone and lower stratospheric temperature, *J Geophys. Res. -Atmos*, *99*, 5433-5447, 1994.

Randel, W.J., and F. Wu, Isolation of the ozone QBO in SAGE II data by singular-value decomposition, *Journal of the Atmospheric Sciences*, *53* (17), 2546-2559, 1996.

Randel, W.J., F. Wu, R. Swinbank, J. Nash, and A. O'Neill, Global QBO circulation derived from UKMO stratospheric analyses, *Journal of the Atmospheric Sciences*, *56* (4), 457-474, 1999.

Reed, R.J., Rasmusse.La, W.J. Campbell, and D.G. Rogers, Evidence of a downward-propagating, annual wind reversal in equatorial stratosphere, *Journal of Geophysical Research*, *66* (3), 813-818, 1961.

Ruzmaikin, A., J. Feynman, X. Jiang, and Y.L. Yung, The extratropical signature of the Quasi-Biennial Oscillation, *Journal of Geophysical Research*, in press, 2005.

Salby, M., and P. Callaghan, Connection between the solar cycle and the QBO: The missing link, *Journal of Climate*, *13* (14), 2652-2662, 2000.

Schneider, H.R., D.B.A. Jones, M.B. McElroy, and G.Y. Shi, Analysis of residual mean transport in the stratosphere 1. Model description and comparison with satellite data, *Journal of Geophysical Research-Atmospheres*, *105* (D15), 19991-20011, 2000.

Tung, K.K., and H. Yang, Global QBO in circulation and ozone. 1. Reexamination of observational evidence, *Journal of the Atmospheric Sciences*, *51* (19), 2699-2707, 1994a.

Tung, K.K., and H. Yang, Global QBO in circulation and ozone. 2. A simple mechanistic model (Vol 51, Pg 2708, 1994), *Journal of the Atmospheric Sciences*, *51* (22), 3365-3365, 1994b.

Veryard, R.G., and R.A. Ebdon, Fluctuations in tropical stratospheric winds, *Meteorology Magazine*, *90*, 125-143, 1961.

Waliser, D.E., K.M. Lau, W. Stern, and C. Jones, Potential predictability of the Madden-Julian oscillation, *Bulletin of the American Meteorological Society*, *84* (1), 33-50, 2003.

Weare, B.C., and J.S. Nasstrom, Examples of Extended Empirical Orthogonal Function Analyses, *Monthly Weather Review*, *110* (6), 481-485, 1982.

Wellemeyer, C., P.K. Bhartia, S. Taylor, W. Qin, and C. Ahn, Version 8 Total Ozone Mapping Spectrometer (TOMS) Algorithm, *Proceedings of the XX Quadrenniel Ozone Symposium*, edited by C. Zerefos, International Ozone Commission, Athens, Greece, 635-636, 2004.

Zawodny, J.M., and M.P. McCormick, Stratospheric Aerosol and Gas Experiment-Ii Measurements of the Quasi-Biennial Oscillations in Ozone and Nitrogen-Dioxide, *Journal of Geophysical Research-Atmospheres*, *96* (D5), 9371-9377, 1991.

Table 2.1: List of Acronyms

2-D: Two-dimensional
3-D: Three-dimensional
BDC: Brewer-Dobson circulation
CTM: Chemistry and transport model
DU: Dobson unit
EEOF: Extended empirical orthogonal function
EOF: Empirical orthogonal function
MMC: Mean meridional circulation
MOD: Merged ozone data
PCA: Principal component analysis
QBO: Quasi-biennial oscillation
QBO-AB: QBO-Annual Beat, around 20 months
QBO-AB′: QBO-Annual Beat, around 8 months
QBO-MMC: QBO-induced meridional circulation
VMR: Volume mixing ratio
ω_A: Frequency of the annual cycle
ω_Q: Frequency of QBO

Table 2.2 Description of Model Runs in Sensitivity Studies.

Model Run	Description
Standard model	Offline-version of the 2-D model using the parameterized QBO circulation. Annual cycle in the temperature field.
Experiment A	Only the QBO-AB signal is kept in the transport fields. No annual cycle in the chemistry.
Experiment B	Only the annual cycle and QBO are kept in the transport fields. No annual cycle in the chemistry.
Experiment C	Only the QBO signal is kept in the transport fields. Annual cycle in the chemistry.

Table 2.3 Frequency Filters[a] used in the models.

Filter	Period Windows (months)	
	Passed	Blocked
Lowpass A	(15, max)	(0, 12.5)
Bandpass A	(18, 22.5)	(0, 17) and (24, max)
Bandpass B	(7.7, 8.7)	(0, 7.3) and (9.1, max)
Bandpass C	(15, 37)	(0, 12.5) and (50, max)
Bandpass D	(11, 13)	(0,10.5) and (14, max)
Bandpass E	(26.5, 33)	(0, 24) and (38, max)

[a]Passed ranges correspond to frequencies unaltered by the spectral window. Stopped ranges correspond to frequencies completely blocked. Frequencies in the transition intervals are damped; the spectral windows used are convolutions of a Hanning window and a step function. Max is 600 months.

Table 2.4 The Fractions of Variance Explained by EOFs.

	EOF1	EOF2	EOF3	EOF4
PCA on the column O_3 from the standard model	70.3%	28.2%		
EEOF on the O_3 VMR from the standard model	24.3%	23.6%	16.1%	15.6%
EEOF on the bandpass filtered O_3 VMR from MOD	23.4%	21.8%	9.5%	8.4%
PCA on the column O_3 from the experiment A	97.4%			
PCA on the column O_3 from the experiment B	67.5%	26.4%		
PCA on the column O_3 from the experiment C	90.4%	6.5%	2%	

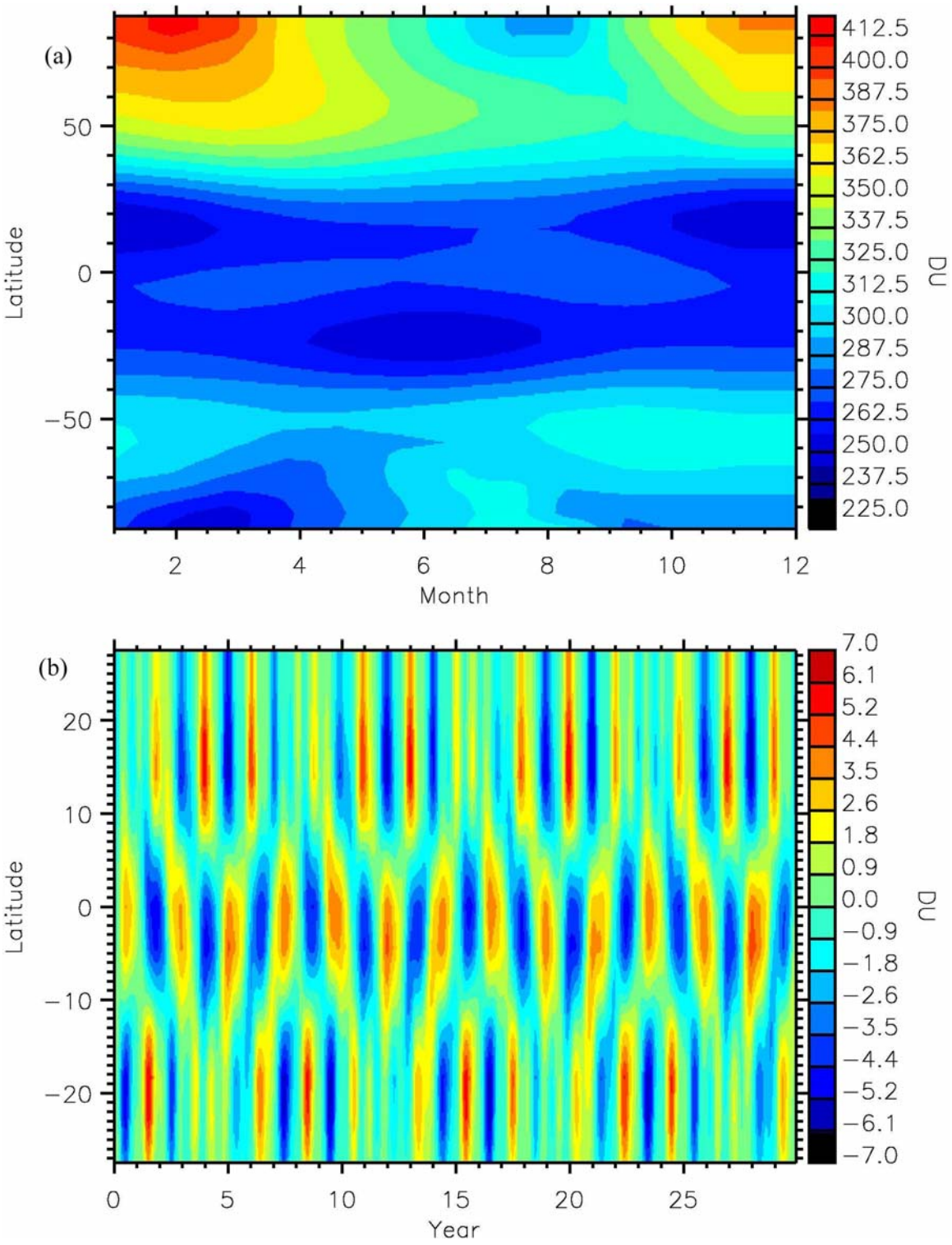

Figure 2.1: (a) Climatology and (b) anomaly of the total column ozone for the standard model.

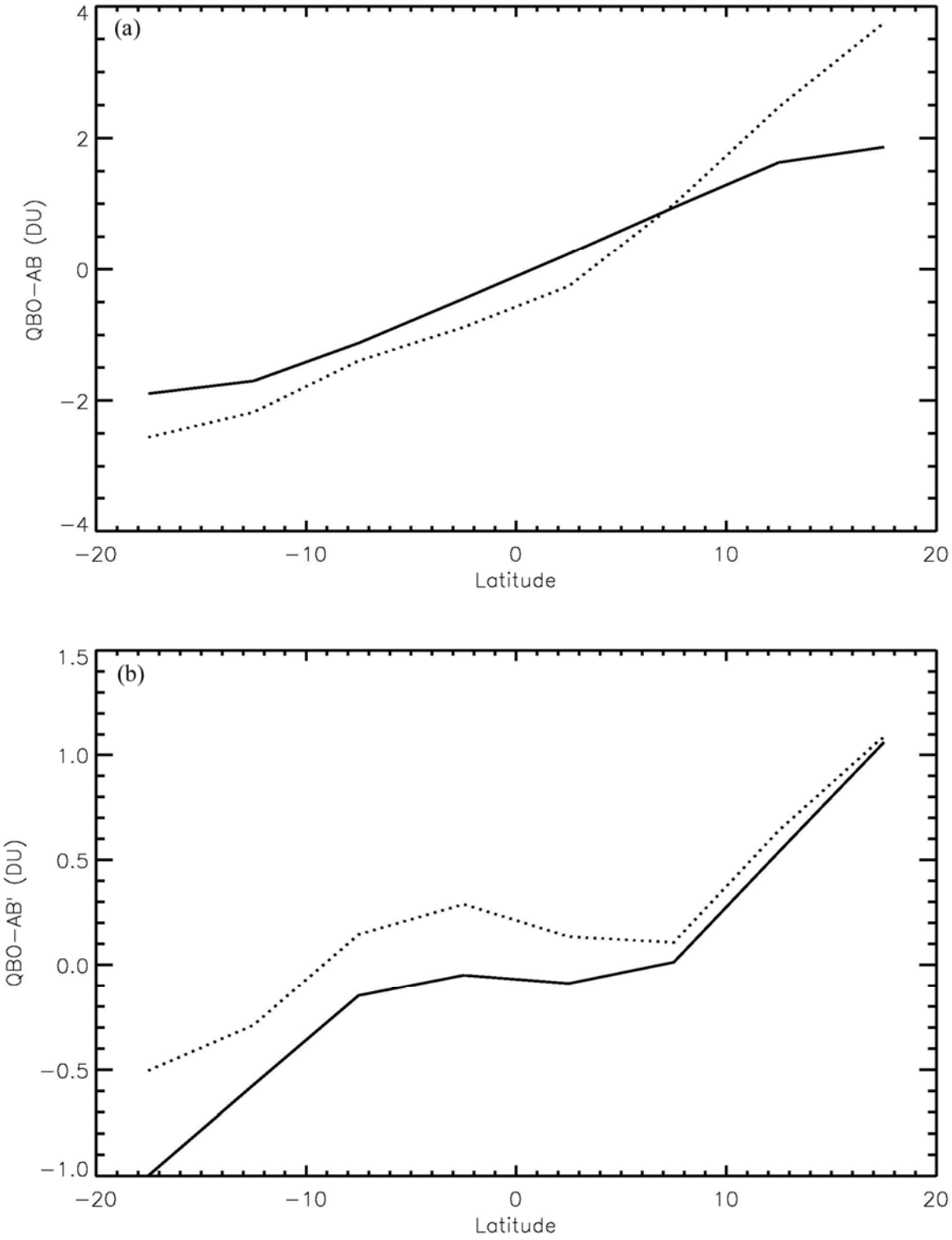

Figure 2.2: (a) Ozone QBO-AB and (b) QBO-AB′ signals from 2-D CTM (solid line) and MOD (dashed line).

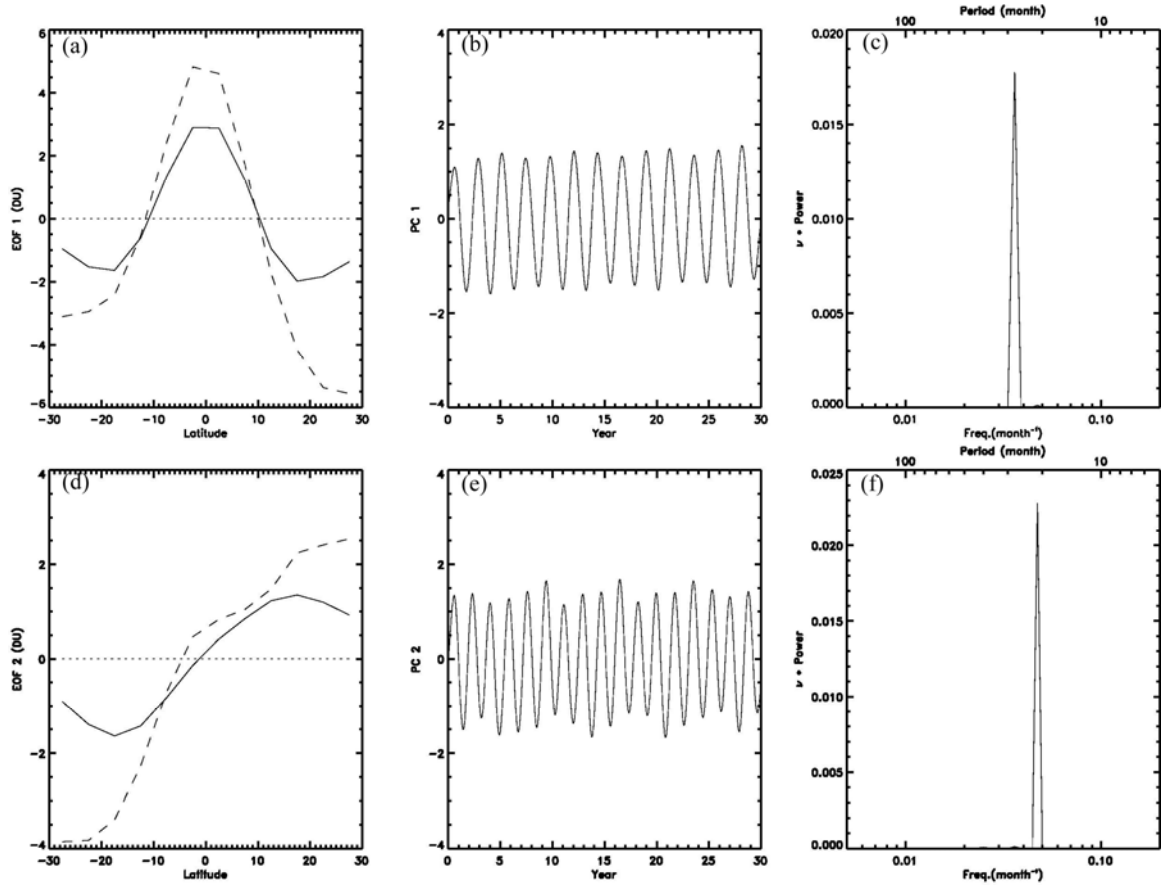

Figure 2.3: Spatial EOF patterns (left column), PC time series (middle column) and spectra (right column) for the first two EOFs of the total column ozone from the standard model. The solid line is the EOF patterns from the standard model. The dash line is the EOF patterns from the zonal mean MOD. Units of EOFs are DU. (a) EOF_1, (b) PC_1, (c) Spectrum for PC_1, (d) EOF_2, (e) PC_2, and (f) Spectrum for PC_2.

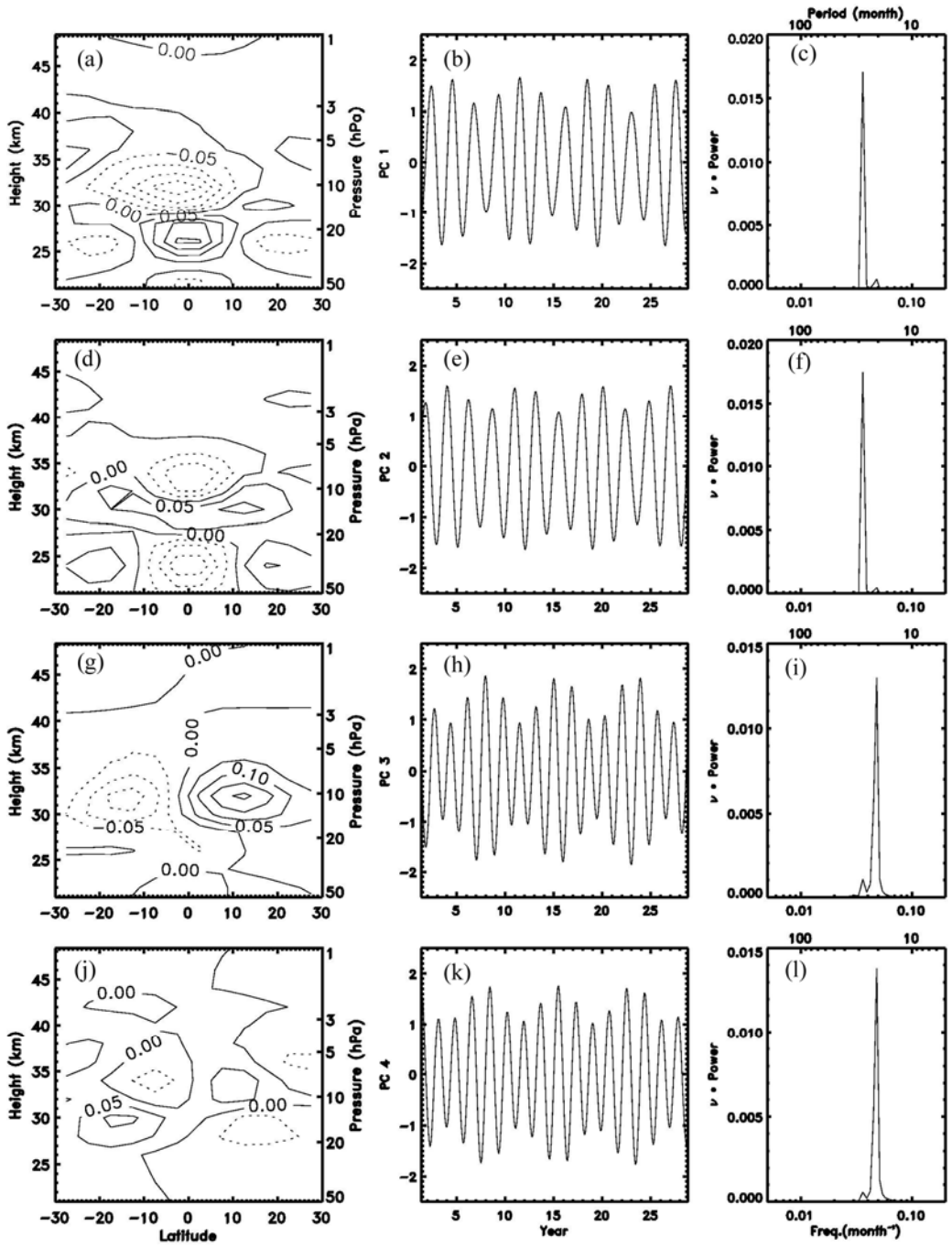

Figure 2.4: Spatial EEOF patterns (left column), PC time series (middle column) and spectra (right column) for the first four Extended EOFs at lag = 0 of the ozone VMR from the standard model. Units of EEOFs are ppmv. (a, b, c) $EEOF_1$, PC_1, and Spectrum for PC_1. (d, e, f) $EEOF_2$, PC_2, and Spectrum for PC_2. (g, h, i) $EEOF_3$, PC_3, and Spectrum for PC_3. (j, k, l) $EEOF_4$, PC_4, and Spectrum for PC_4.

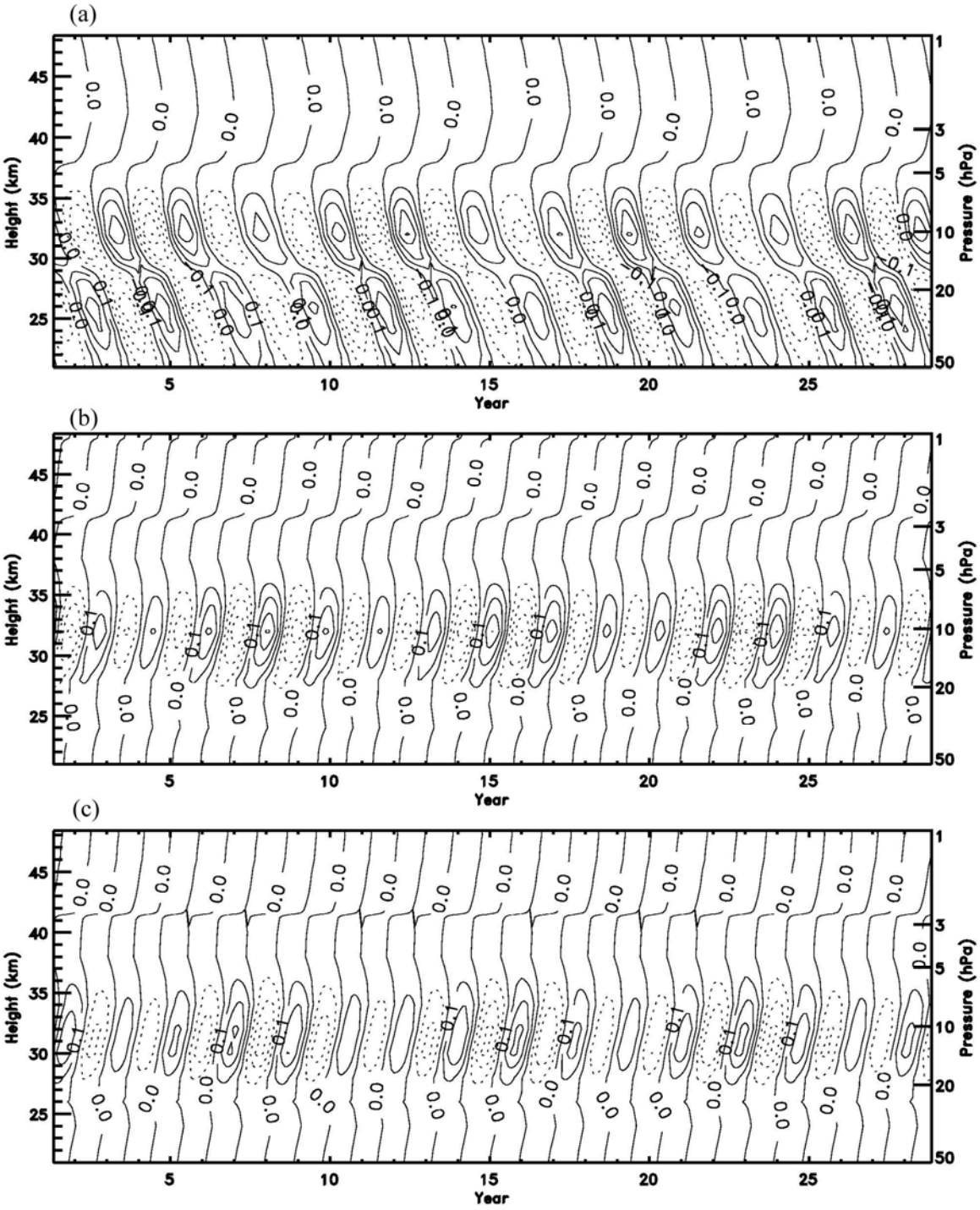

Figure 2.5: (a) $PC_1 \times EEOF_1 + PC_2 \times EEOF_2$ at equator, (b) $PC_3 \times EEOF_3 + PC_4 \times EEOF_4$ at 12.5° N, and (c) $PC_3 \times EEOF_3 + PC_4 \times EEOF_4$ at 12.5° S obtained at lag = 0 from the ozone VMR from the standard model. Units are ppmv.

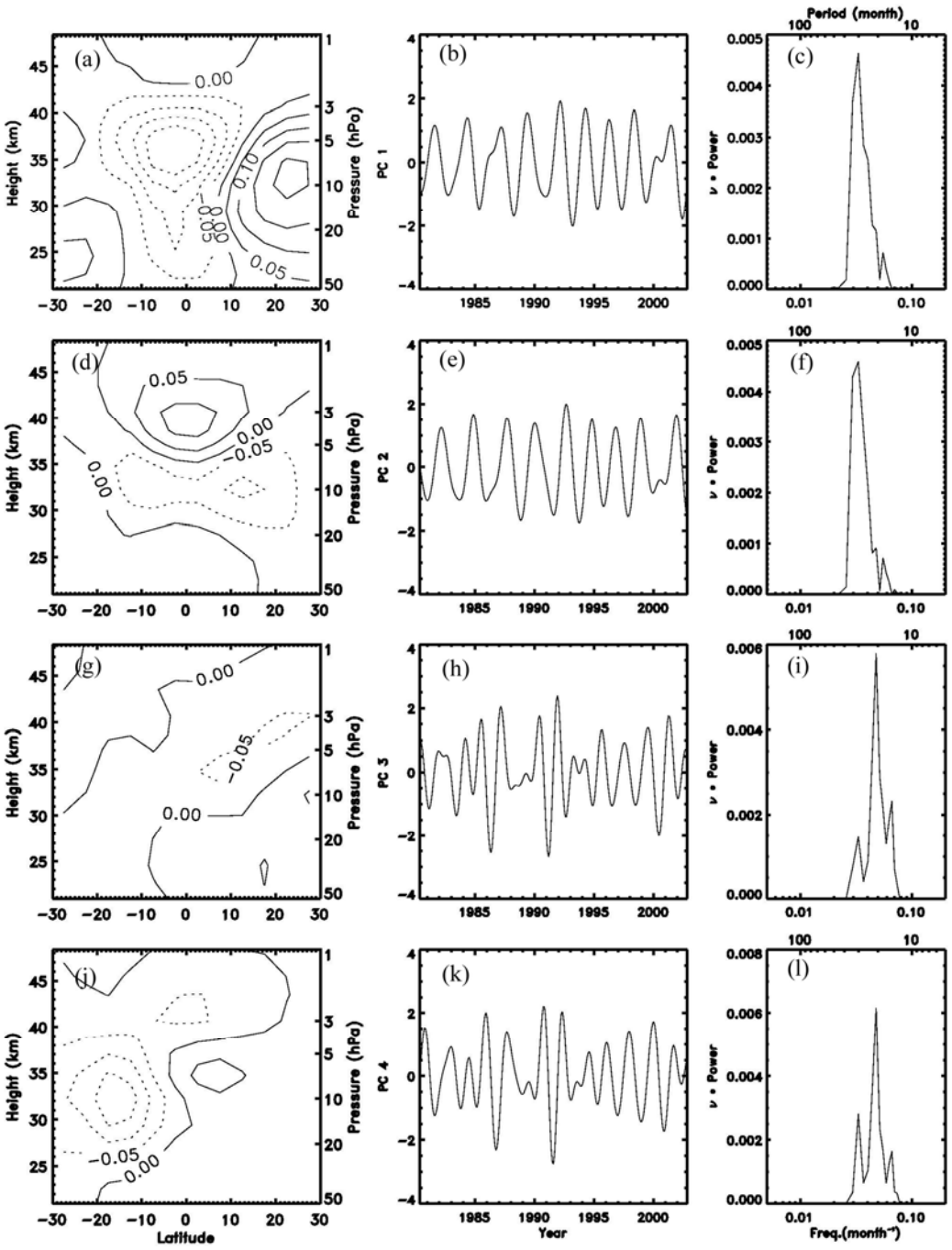

Figure 2.6: Spatial EEOF patterns (left column), PC time series (middle column) and spectra (right column) for the first four Extended EOFs at lag = 0 of the bandpass filtered ozone VMR from MOD. Units of EEOFs are ppmv. (a, b, c) $EEOF_1$, PC_1, and Spectrum for PC_1. (d, e, f) $EEOF_2$, PC_2, and Spectrum for PC_2. (g, h, i) $EEOF_3$, PC_3, and Spectrum for PC_3. (j, k, l) $EEOF_4$, PC_4, and Spectrum for PC_4.

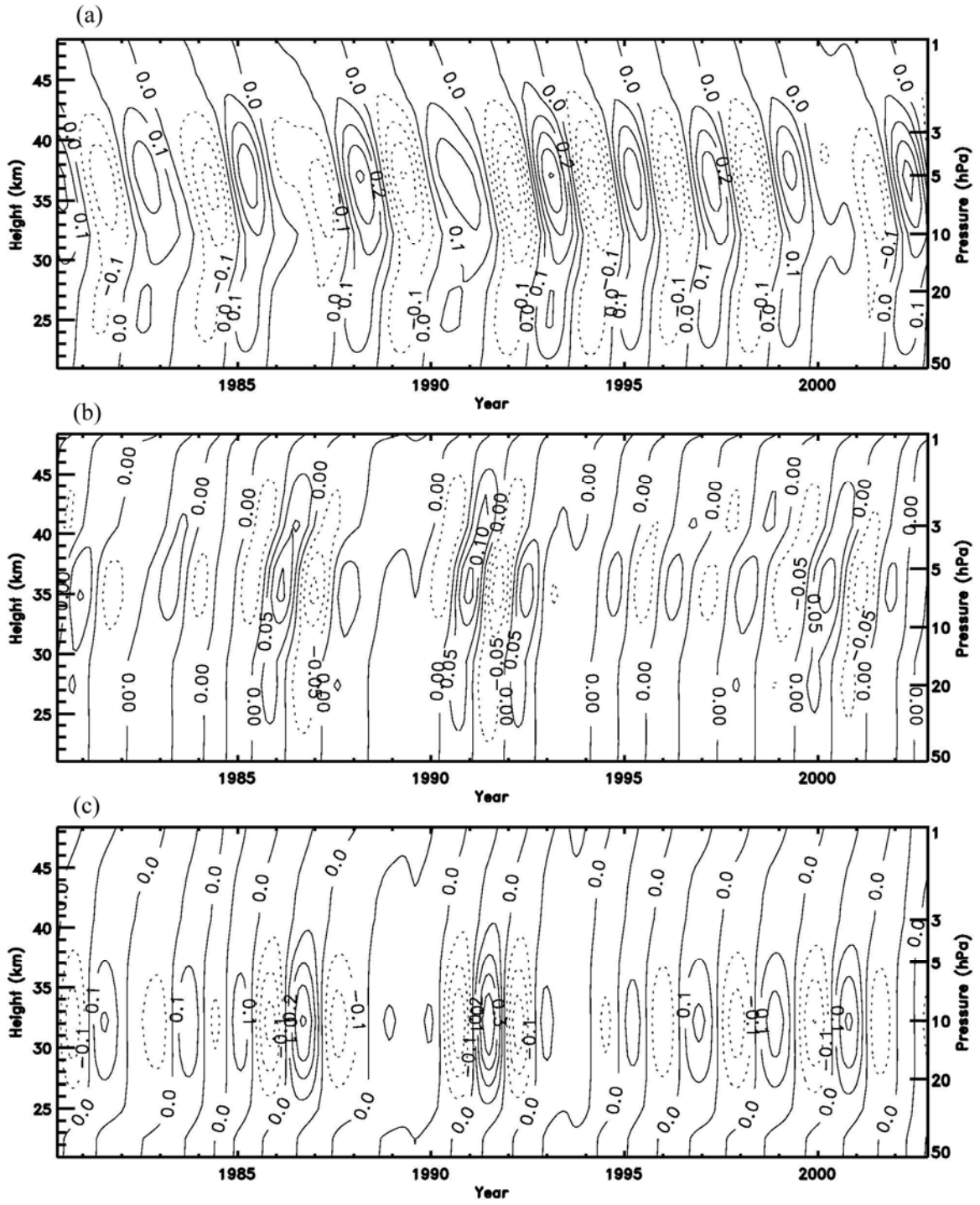

Figure 2.7: (a) $PC_1 \times EEOF_1 + PC_2 \times EEOF_2$ at equator, (b) $PC_3 \times EEOF_3 + PC_4 \times EEOF_4$ at 12.5° N, and (c) $PC_3 \times EEOF_3 + PC_4 \times EEOF_4$ at 12.5° S obtained at lag = 0 from the bandpass filtered ozone VMR from MOD. Units are ppmv.

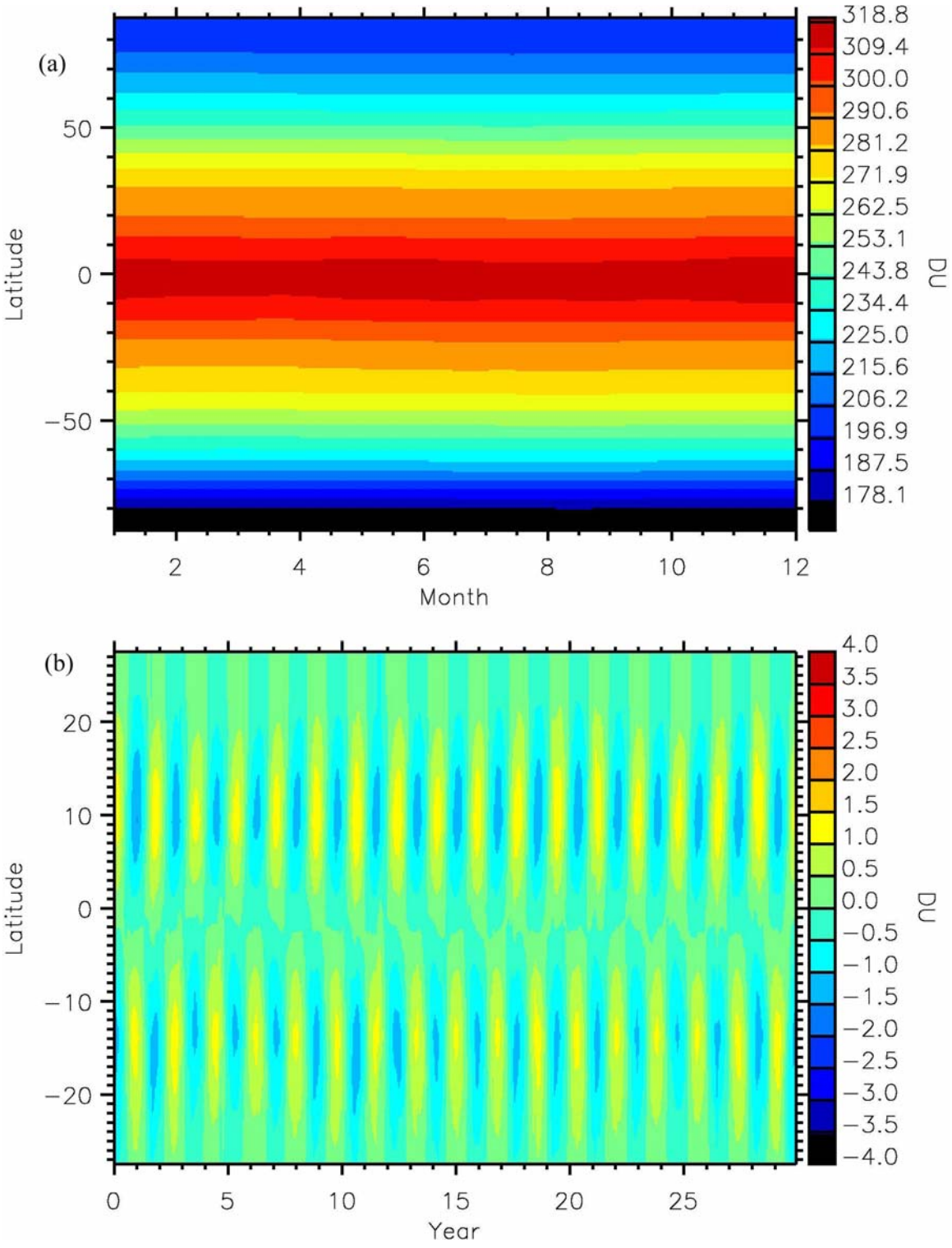

Figure 2.8: (a) Climatology and (b) anomaly of the total column ozone for experiment A.

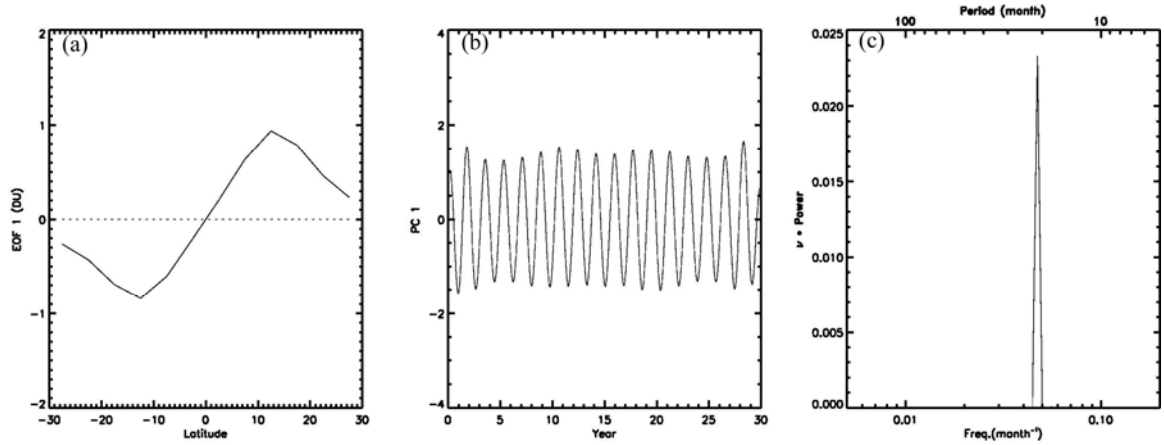

Figure 2.9: Spatial EOF patterns (left column), PC time series (middle column) and spectra (right column) for the first EOF of the total column ozone from experiment A. Units of EOFs are DU.

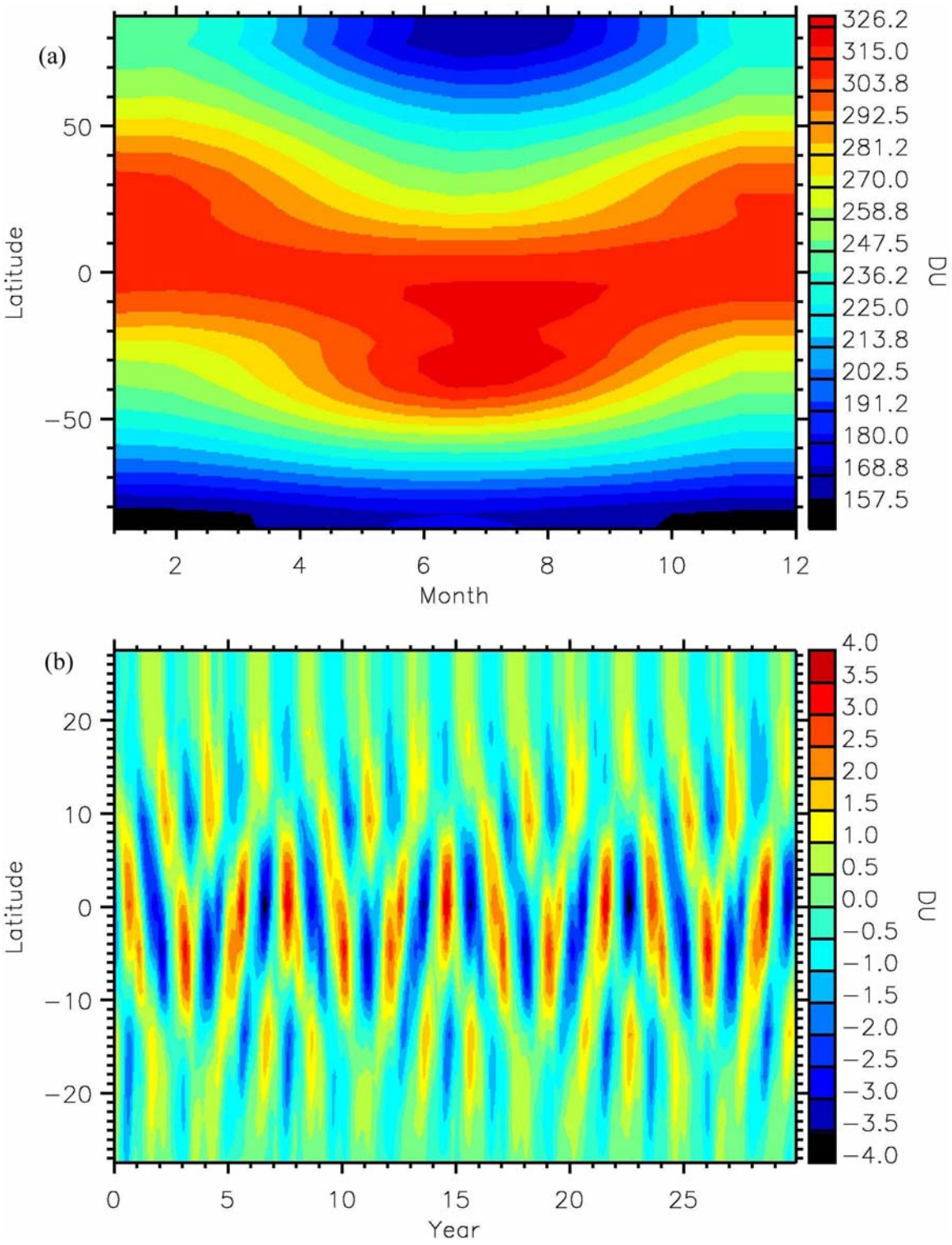

Figure 2.10: (a) Climatology and (b) anomaly of the total column ozone for experiment B.

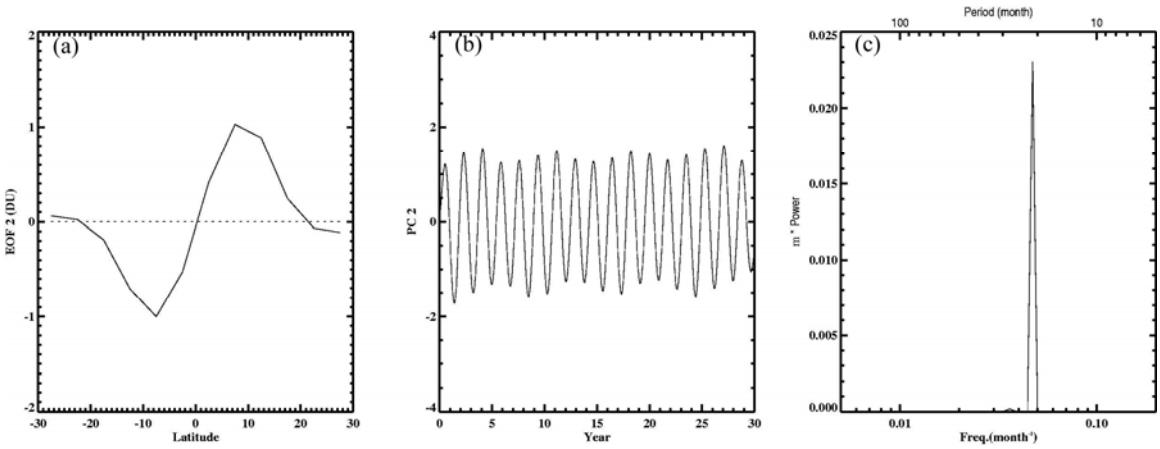

Figure 2.11: Spatial EOF patterns (left column), PC time series (middle column) and spectra (right column) for the second EOF of the total column ozone from experiment B. Units of EOFs are DU.

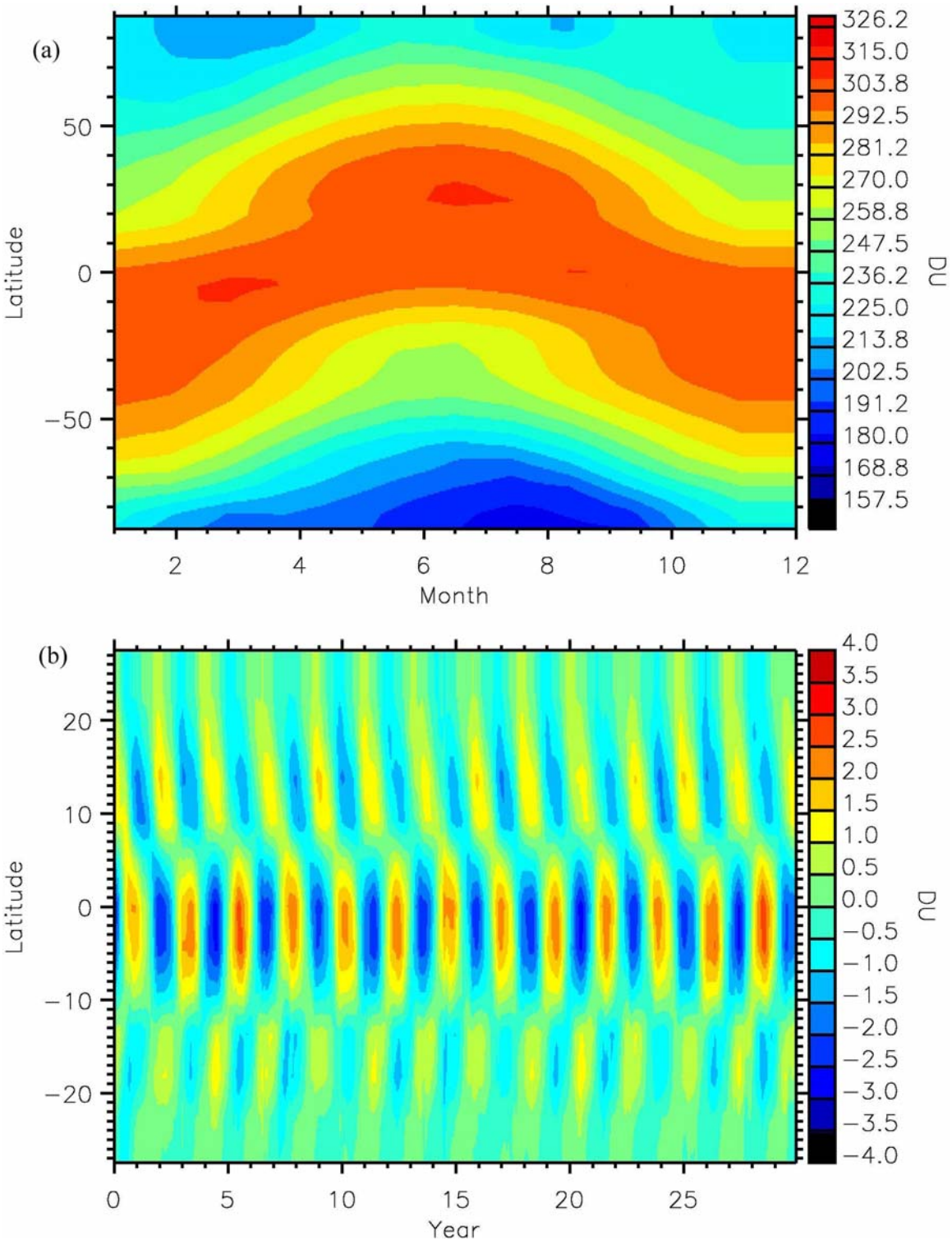

Figure 2.12: (a) Climatology and (b) anomaly of the total column ozone for experiment C.

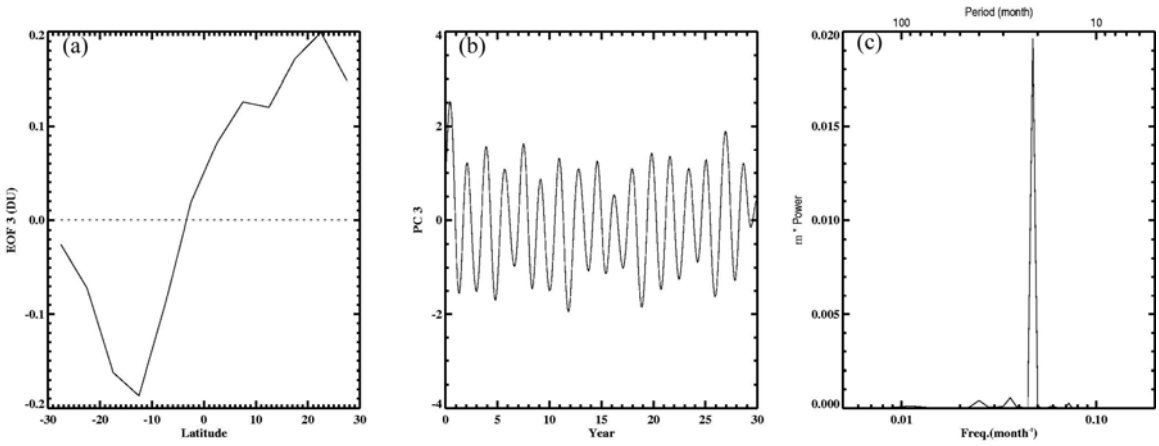

Figure 2.13: Spatial EOF patterns (left column), PC time series (middle column) and spectra (right column) for the third EOF of the total column ozone from experiment C. Units of EOFs are DU.

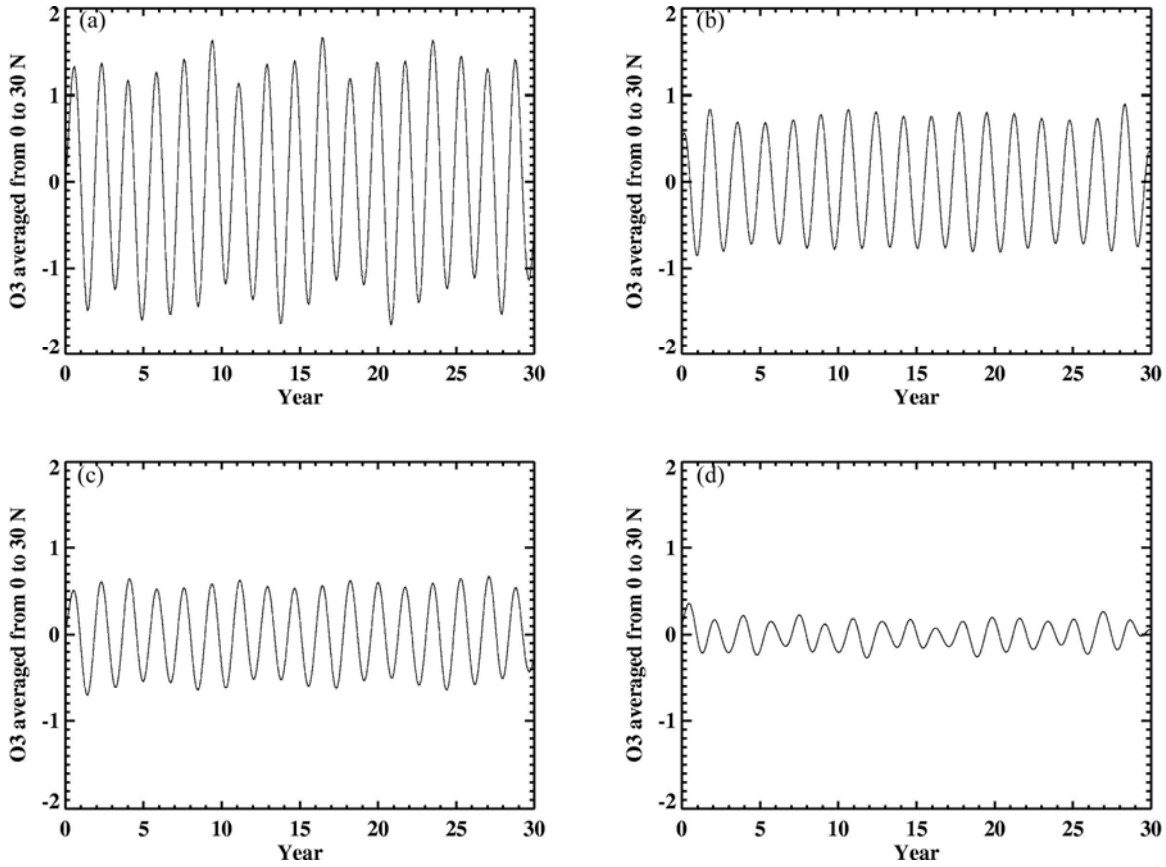

Figure 2.14: Product of the PC and EOF corresponding to the QBO-AB signal averaged from 0° to 30° N. (a) $PC_2 \times EOF_2$ of column ozone anomaly in the standard model, (b) $PC_1 \times EOF_1$ of column ozone anomaly in experiment A, (c) $PC_2 \times EOF_2$ of column ozone anomaly in experiment B, (d) $PC_3 \times EOF_3$ of column ozone anomaly in experiment C. Units are DU.

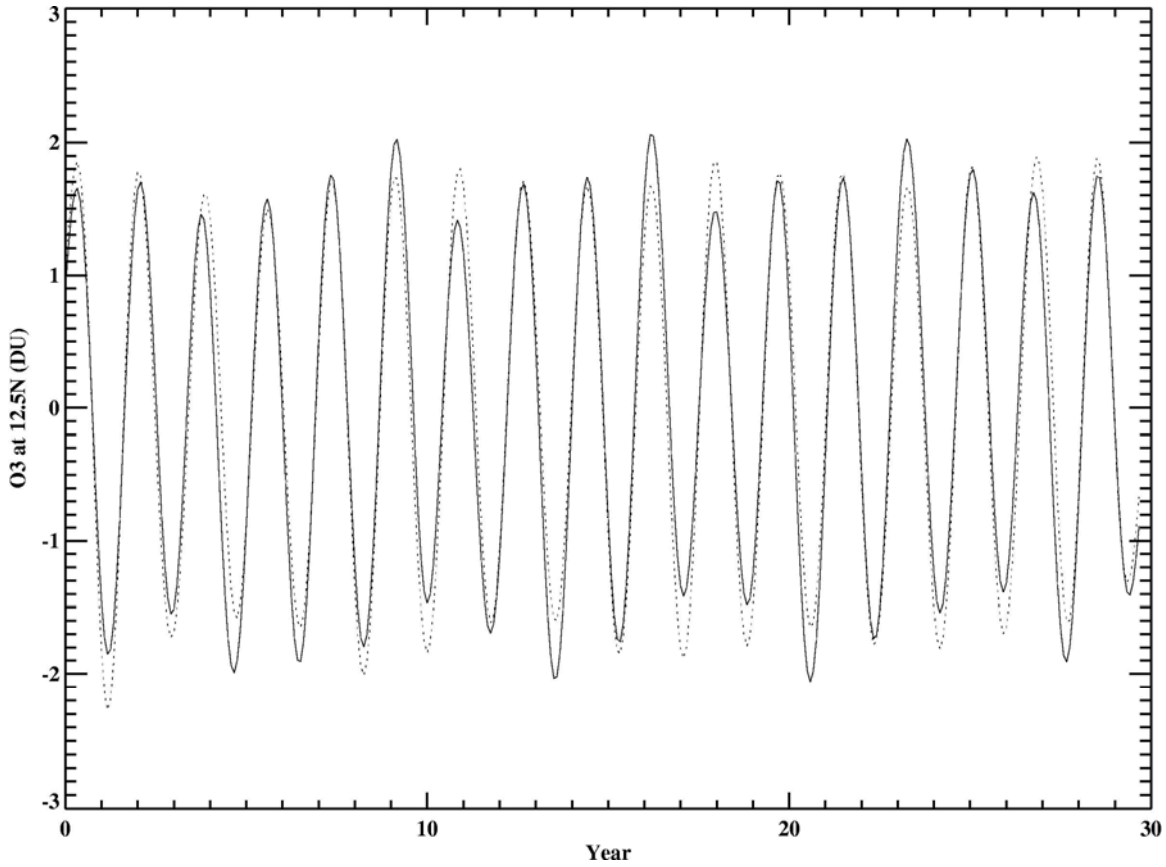

Figure 2.15: Comparison between the QBO-AB in the standard model (solid line) and the sum of the QBO-AB in experiments A, B, and C (dotted line). The QBO-AB signal is derived from the product of the PC and EOF corresponding to the QBO-AB. Units are DU.

Chapter 3: Interannual Variability and Trend in High Latitude Stratospheric Ozone

3.1 Abstract

We apply principal component analysis (PCA) to the total column ozone data from the combined Merged Ozone Data and European Center for Medium-Range Weather Forecasts assimilated ozone from Jan 1979 to Aug 2002. The interannual variability (IAV) of high-latitude O_3 in each hemisphere is characterized by four main modes. Attributable to dominant dynamical effects, these four modes account for nearly 60% of the total ozone variance in the northern hemisphere (NH) and 75% of that in the southern hemisphere (SH).

In both hemispheres, the first two leading modes are nearly zonally symmetric and represent the connections to the Annular Modes and the Quasi-Biennial Oscillation. The latter two modes exhibit in-quadrature, wavenumber-1 structures that represent the displacement of the polar vortex in response to planetary waves. In the NH, these combined modes have preferred extrema locations that suggest fixed topographical and land-sea thermal forcing of the involved planetary waves. Such stationary forcing is not apparent in the SH modes. Similar spatial patterns and trends are simulated by the Goddard Earth Observation System, Version 4 (GEOS-4) chemistry-climate model (CCM). To relate the results to the atmospheric dynamics, similar decompositions are performed for geopotential thicknesses between 30 hPa and 100 hPa. The results reveal close connections between the IAV of ozone and that of the atmospheric dynamics. The decreasing O_3 trends in both hemispheres are captured in the first mode and are

successfully reproduced by the GEOS-4 CCM. However, the model overestimates the trend in the NH, especially after 1997.

3.2 Introduction

Dynamics can strongly modulate the interannual variability (IAV) of stratospheric ozone [*Fusco and Salby,* 1999; *Hood and Soukharev,* 2003; *Randel et al.,* 2002] and dynamical feedbacks associated with climate change may consequently delay ozone recovery [*Shindell et al.,* 1999; *Austin et al.,* 2000; *Weatherhead et al.,* 2000]. Consequently, ozone recovery is difficult to detect since total column ozone exhibits strong IAV associated with dynamics and climate change. A primary motivation for studying the IAV of column ozone is to separate the anthropogenic perturbations of the ozone layer from natural variability (See, for example, *World Meteorological Organization (WMO)* [2002]).

Using rotated principal component analysis, *Eder et al*. [1999] studied column O_3 from 1980 to 1992. They identified 14 contiguous sub-regions, accounting for more than 70% of the column ozone variance from 65°S to 65°N. The time series associated with these sub-regions reveal significant periodicities on semi-annual, annual, and quasi-biennial oscillations (QBO). *Camp et al*. [2003] found that in the tropics, 93% of total column ozone IAV could be explained by four modes whose structures are attributable to the QBO, the interaction between the QBO and the annual cycle (QBO-AB), the El Niño–Southern Oscillation (ENSO), and the solar cycle. Based on both observational and modeling studies, evidence reveals a trend in total column ozone over northern mid-latitudes [*Hood and Soukharev*, 2003]. However, quantifying this trend accurately is difficult due to the large ozone IAV.

The principal IAV modes of stratospheric ozone and their relationship to dynamical influences can offer clues to improve our understanding of ozone variability and its connection to (and interaction with) climate changes at high latitudes. To date, extensions of principal component analysis (PCA) to the northern hemisphere (NH) and southern hemisphere (SH) are hampered by the fact that the most comprehensive Merged Ozone Data (MOD) set [*McPeters*, 1996] lacks O_3 data in the polar night region.

Here, we report a new analysis, based on a combination of MOD and the assimilated data from the European Centre for Medium-Range Weather Forecasts (ECMWF) [*Dethof and Holm*, 2004; *Simmons et al.*, 1999; Uppala *et al*., 2005]. The ECMWF O_3 data are assimilated from Jan 1979 to Dec 1988 and from Jan 1991 to Aug 2002. Ozone observations by Total Ozone Mapping Spectrometers (TOMS) and Solar Backscattered Ultraviolet (SBUV) instruments are assimilated. Post-processed data are available on a $2.5^{\circ}\times2.5^{\circ}$ latitude-longitude grid [*Uppala et al*., 2005]. Similar analysis is also applied to the model column O_3 results from a chemistry-climate model (GEOS-4 CCM) based on the Goddard Earth Observation System, Version 4 general circulation model and a stratospheric chemistry code [*Bloom et al*., 2005; *Stolarski et al.*, 2006a]. To relate the results to atmospheric dynamics, similar decompositions are performed for geopotential thickness (GPT) between 30 hPa and 100 hPa. GPT is computed from geopotential heights from the National Center for Environmental Prediction — Department of Energy Reanalysis 2 (NCEP2) [*Kalnay et al*., 1996; *Kistler et al*., 2001]. This layer roughly includes the bulk of the ozone layer and has been shown to exhibit strong correlation with ozone column in the tropics [*Camp et al.*, 2003]. The resolution of

the data is also $2.5^{\circ}\times2.5^{\circ}$. Using these analyses, we can explore the connections between the ozone and atmospheric dynamics.

In Section 3.2, the data sets and methodology are described. The results for PCA of the column ozone are discussed in Section 3.3. In Section 3.4, the results of PCA of the NCEP2 GPT are shown and compared to the ozone results. Section 3.5 contains our conclusion and final remarks. In the appendix, we provide information on the validation of O_3 data, PCA of ECMWF assimilated O_3, statistical significance of spectral peaks in the power spectrum, analysis of the Arosa O_3 record, and cylindrical projections, zonal mean, and t-statistics of the leading modes.

3.3 Data Sets and Methodology

In this chapter, we have used four data sets: O_3 data from MOD [*McPeters et al*., 1996], ECMWF assimilated O_3 and potential vorticity (PV), Arosa O_3 data, and NCEP2 GPT data. All data are the monthly mean data. To extract the spatio-temporal patterns of O_3 IAV, we apply PCA [*Richman*, 1986; *Preisendorfer*, 1988; *Thompson and Wallace*, 2000; *Camp et al.*, 2003] to the deseasonalized and weighted column O_3 data from MOD, which spans from Jan 1979 to Aug 2002. Seasonal cycles for each time series are removed; cycles are determined by taking averages for each month independently. The resolution of the MOD is $5^{\circ}\times10^{\circ}$ (latitude-longitude) and the regions we studied are from 10° N/S to 90° N/S for the NH/SH analysis. Missing data in the polar night are filled by the assimilated data from ECMWF. The assimilated data are very similar to the MOD data where they overlap. The ECMWF O_3 has good agreement with the radiosonde O_3

data in the polar region after 1979 except that the ECMWF O_3 at the South Pole is slightly high in Oct [*Dethof and Holm*, 2004]. During the years of 1989 and 1990 when the ECMWF assimilated O_3 were not available, ECMWF PV was used as a proxy for O_3 based on a mapping method [*Manney et al.*, 1999]. Details of validating the ECMWF assimilated O_3 and proxy data are shown in Figs. 3.12–3.14 in the appendix.

PCA [*Richman*, 1986; *Preisendorfer*, 1988; *Thompson and Wallace*, 2000; *Camp et al.*, 2003] provides a decomposition of a multivariate dataset into orthogonal spatial patterns, known as empirical orthogonal functions (EOF), with associated time-dependent amplitude, known as principal component time series (PC). The EOFs are the eigenfunctions of the covariance matrix of the dataset sorted by the decreasing values of associated eigenvalues. Since these eigenvalues represent the variance captured by each EOF, PCA guarantees that the leading *n* EOFs capture more of the total variance of the dataset than any other *n* orthogonal vectors. However, PCA is not a scale-independent method. Therefore, it is necessary to weight each element of the covariance matrix by the area it represents; *i.e.*, scale each time series by square root of area, $\sqrt{\cos\theta}$ (where θ is the latitude), prior to constructing the covariance matrix. The PCA decomposition of the scaled, deseasonalized column-ozone anomaly, Ω_A, can be represented as:

$$\Omega_A(t,\theta,\varphi) = \sum_i p_i(t)\, e_i(\theta,\varphi), \qquad (1)$$

where t is time, φ is longitude, p_i is i^{th} PC, e_i is the i^{th} EOF, and the summation is over all the eigenfunctions with eigenvalues arranged in descending order. In order to recover the spatial patterns for the original (unscaled) ozone anomaly, we perform a multiple linear

regression for each grid point (θ,φ), using as predictors the PC time series, $p_i(t)$, determined from the scaled PCA of Eq. (1) [*Baldwin and Dunkerton*, 1999]; *i.e.*,

$$\Omega(t,\theta,\varphi)=\sum_{i=1}^{n} C_i(\theta,\varphi)\, p_i(t) + R_n(\theta,\varphi), \qquad (2)$$

where $\Omega(t,\theta,\varphi)$ is the deseasonalized (unscaled) O_3 anomaly fields. The resulting linear regression coefficients, $C_i(\theta,\varphi)$, are the spatial patterns of the ozone variability associated with the i^{th} PC time series, $p_i(t)$. R_n is the residual of regression. In this study only four modes are used; *i.e.*, in Eq. (2), n=4. It should be noted that the resulting spatial patterns, $C_i(\theta,\varphi)$, are no longer mutually orthogonal; the PC time series remain mutually orthogonal.

3.4 PCA of Column O_3

3.4.1 Results for Column O_3 in the NH

The four leading modes account for 30.4, 15.9, 7.1 and 6.5% of the total variance. Together, they account for 59.9% of the total variance of O_3. Details of the leading modes are listed in Table 1. The spatial patterns of the O_3 anomalies regressed upon their leading PCs are shown in Fig. 3.1. The polar projection, cylindrical projection, and zonal mean of the regression coefficients are shown in Fig. 3.16 in the appendix. The first two modes are approximately zonally symmetric. The first mode represents a hemispheric change in O_3, in the sense that if PC1>0 ozone is low over the entire NH, with a larger anomaly in the polar region. The second mode has a see-saw structure, so that low O_3 in the polar region occurs with higher values in the mid-latitudes. As illustrated below, these two

modes are related to the Northern Hemisphere Annual Mode (NAM) [*Thompson and Wallace,* 1998] and QBO [*Baldwin et al.,* 2001]. The third and fourth modes are zonally asymmetric. Their eigenvalues are sufficiently similar that their patterns represent a wavenumber-1 distribution in quadrature. Physically, the wavenumber-1 structure can be visualized as the wobbling and displacement of the polar vortex in response to planetary waves. Similar results were obtained from analyses of the ECMWF assimilated O_3 data. *Thompson and Wallace* [2000] only regressed the column ozone in Mar (NH) and Nov (SH) upon the standardized monthly time series of the annualar modes. In this chapter, we study the column ozone data from Jan. 1979 to Aug. 2002 in greater detail and reveal that there are symmetric and asymmetric modes in the column ozone, which do not appear in the previous studies.

Further insights into the first four modes are gained by examining the temporal signature in the PCs. The temporal behavior of PC1 in NH is shown in Fig. 3.2a. For comparison, we overlay the NAM Index as a dotted line. The NAM Index is the PC associated with the first leading mode, capturing 29% of the total variance, for the geopotential height at 100 hPa from Jan 1979 to Aug 2002 [*Baldwin and Dunkerton*, 1999; *Thompson and Wallace,* 2000]. The correlation between the detrended PC1 and detrended NAM index is 0.53 (0.1% significance level). Linear trends have been removed from PC1 and NAM index before calculating the correlation. The significance statistics for correlations were generated by a Monte Carlo method [*Press et al.,* 1992]. A distribution of correlations was generated by determining the correlations of three thousand isospectral surrogate time series with the relevant indices. This distribution was

transformed into an approximately normal distribution by the Fisher transformation [*Devore*, 1982]. The significance level of the actual correlation within the normal distribution was then determined. The El Chichon and Pinatubo eruptions happened in Apr 1982 and Jun 1991, respectively. PC1 are positive after these two events, which suggest there are ozone depletions after the volcano eruptions in the NH. These results are consistent with results in *Zerefos et al*. [1994] and *Coffey* [1996].

The power spectrum of the detrended PC1 (Fig. 3.2b) reveals a significant peak at 3.5 years (42 months, denoted by P). The other significant spectral peaks are attributed to the QBO (28 months, Q), the QBO-AB (21 months, Q_1) [*Camp et al.*, 2003; *Tung and Yang*, 1994a; *Tung and Yang*, 1994b], the residual annual cycle (A) and the Semi-Annual Oscillation (6 months, A_1) [*Gray and Pyle*, 1986]. Since the annual cycle has a broad power spectrum, there is some residual annual cycle left after removing the monthly mean from the data. The statistical significance of signals in a power spectrum is obtained by comparing the amplitude of a spectral peak to the red noise spectrum (see appendix for details). Because the spatial pattern of the first mode (Fig. 3.1a) is negative, the positive (negative) trend in PC1 (Fig. 3.2a) represents the declining (increasing) trend in ozone. The secular variation in PC1 from 1979 to 1997 displays the declining trend in ozone reported by *Fusco and Salby* [1999; see their Fig. 1] and Chapter 3 in *World Meteorological Organization (WMO)* [2002]. However, we note that the trend has been absent since 1997. The warmer winter of 1998/1999 would contribute to the downward trend in the PC1 in the later years [*Newman et al.*, 1997; *WMO*, 2002].

To confirm the spectral peaks, we analyzed the Arosa monthly mean column O_3, which is the longest O_3 record (from Aug 1931 to Dec 2002). Details are shown in Fig. 3.15 in the appendix. The peaks P and Q_1 are smaller than 1% significance level (see Fig. 3.15c). The mechanism for the 3.5-year signal is currently not known, and will be investigated in the future.

The spectral power of the detrended PC2 is shown in Fig. 3.2d. It reveals significant peaks related to the QBO-AB (Q_1), the Biennial Oscillation (B), and the Semi-Annual Oscillation (A_1). There is also a peak around 8 months (Q_1'), arising also from the interaction between QBO and the annual cycle [*Tung and Yang*, 1994a; *Jiang et al*., 2005]. The Biennial Oscillation has been previously identified in stratospheric potential vorticity by *Baldwin and Dunkerton* [1998]. *Scott and Haynes* [1998] found the biennial oscillation is in the winter evolution, with alternately dynamically disturbed and dynamically quiescent winters.

The time series of PC3 and PC4 in NH are shown in Figs. 3.3a and c. The corresponding power spectra are given in Figs. 3.3b and d. Most of the variability is at short periods (less than a year), associated with internal variability. There is evidence for a signal at the decadal period in PC3. The maxima and minima of modes 3 and 4 are stationary, as seen by the histogram for the longitudes at which the maxima of the combined pattern for modes 3 and 4 [i.e., $p_3(t)C_3(\theta, \varphi) + p_4(t)C_4(\theta, \varphi)$] occur (Fig. 3.3e). Note that the preferred longitudes are 95°, 185°, 275°, and 335°, approximately coinciding with the nodal points in the modes 3 and 4 in Figs. 3.1c and d. This suggests that the

wobbling/displacement motion is driven by planetary waves associated with topography and land-sea thermal contrasts in the NH. Episodic strong upward burst of stationary wave activity and interference with traveling planetary waves can conceivably produce a strong displacement of the polar vortex core that subsequently wobbles [*McIntyre*, 1982; *Salby and Garcia*, 1987]. The displaced vortex about the pole can retain its identity for an extended period of time, giving rise to column ozone anomalies depicted in modes 3-4 and possibly sudden warmings [*Leovy et al.*, 1985].

3.4.2 Results for Column O_3 in the SH

In the SH, the first four modes (Fig. 3.4) account for 43.9, 13.7, 9.8 and 7.4% of the variance, cumulatively explaining over 74.8% of the variance of O_3 (see Table 1). The first mode is zonally symmetric and strongly resembles the first mode in the NH; it is associated with the Southern Hemisphere Annual Mode (SAM) [*Thompson and Wallace*, 2000]. The second mode in the SH (Fig. 3.4b) has some resemblance to its NH counterpart, in that it describes a see-saw between high and middle latitudes, changing sign at approximately 60° S but the meridional gradients at the vortex edge are weaker in the SH, where the high-latitude minimum is displaced from the Pole. The last two modes are zonally asymmetric and they represent a wavenumber-1 structure similar to the NH.

Fig. 3.5a shows PC1 (solid line) in SH. For comparison, we also show the SAM index (dotted line). The correlation between the detrended PC1 and detrended SAM index is 0.45 (significant at the 0.1% level). The power spectrum (Fig. 3.5b) of the detrended PC1 reveals significant peaks at the residual annual cycle (A), 20 months (Q_1)

and 6 months (A_1). The trend of PC1 is much larger than that of SAM. It suggests that the negative ozone trend in the SH cannot be accounted for by dynamics, and is mostly due to chemical loss. The volcano effect for the PC1 in the SH is not obvious. The El Chichon aerosols remained mostly north of the equator, thus there was less ozone depletion in the SH [*Pollack et al*., 1983; *Zerefos et al*., 1994]. Although there is considerable amount of Pinatubo aerosols that moved to the SH mid-latitude; the ozone depletion signal is very small [*Zerefos et al*., 1994; *Coffey*, 1996] and may be embedded in the large natural variability. The spectral estimate of the detrended PC2 reveals significant peaks at the residual annual cycle (A), and around 20 months (Q_1), 28 months (Q), and 9 months. The time series of PC3 and PC4 are shown in Figs. 3.6a and c. The power spectra of the detrended PC3 and PC4 display peaks at shorter periods. There are also significant peaks around 20 (Q_1), and 28 months (Q) for PC3 and significant peak around 24 months (B) for PC4. The maxima and minima of modes 3 and 4 are not stationary, as seen by the histogram for the longitudes at which the maxima of the combined pattern for modes 3 and 4 (Fig. 3.6e). Hence, while these latter two modes may represent the wobbling and displacement of the polar vortex in response to planetary waves, results shown in Fig. 3.6e suggest that these waves are not stationary in phase, as observed in the NH case (Fig. 3.3e).

3.4.3 Comparison with a 3-D Chemistry-Climate Model

Similar analysis is also applied to the column O_3 in the GEOS-4 CCM [*Stolarski et al*., 2006b]. The underlying GEOS-4 general circulation model is described in *Bloom et al.* [2005]. The chemistry module [*Douglass et al*., 2003; *Stolarski et al*., 2006a] is

implemented on-line in the general circulation model, with feedback of O_3, H_2O, CO_2, CH_4, N_2O, CFC-11, and CFC-12 into the radiation module. At the lower boundary, sea surface temperature and sea ice are prescribed from observations compiled by *Rayner et al*. [2003], along with time-dependent World Meteorological Organization/United Nations Environment Programme (WMO/UNEP) and Intergovernmental Panel on Climate Change/Special Report on Emissions Scenarios (IPCC/SRES) surface mixing ratios for chemically active and greenhouse gases. The model was run for 55 years (1951-2004) at $2^o \times 2.5^o$ (latitude by longitude) with 55 layers between the surface and about 80km. Neither the solar cycle nor volcanic aerosol variations were included in the model and it does not capture a QBO (see *Horinouchi et al.*, 2003), so these sources of ozone variability are all absent from the simulation.

The results from the GEOS-4 CCM are from Jan 1951 to Dec 2004. For comparison, we select the same period as that in the combined MOD and ECMWF column O_3. The first mode for the model O_3 in the NH captures 31.8% of the total variance. The spatial pattern of the first mode in the NH and the associated PC1 time series are shown in Fig. 3.7a and 3.7b. It is zonally symmetric and the sign is negative in the whole region, which is similar to that from the combined MOD and ECMWF column O_3. The trend for the PC1 of the model O_3 in the NH is 0.092 ± 0.042 /yr, which is larger than the trend for the PC1 (0.056 ± 0.042 /yr) in the combined O_3. The main reason is that after 1997 the combined O_3 shows a negative trend whereas the model trend is much less. The reason could be due to misalignment of random IAV in the model compared to observations, or due to the absence of low-frequency climate changes (such as the solar

cycle) in the model. The spatial pattern of the first mode and the PC1 time series in the SH are shown in Fig. 3.7c and 3.7d. The first mode in the SH, capturing 59.5% of the total variance, is also zonally symmetric and the minimum value is lower than that in the NH. The spatial pattern is similar as that in the observed O_3. The trend for the PC1 of the model O_3 in the SH is 0.1±0.042 /yr, which is close to the trend for the PC1 (0.093±0.042 /yr) of the combined O_3 in the SH.

The second, third, and fourth modes for the model O_3 in the NH capture 9.1%, 7.8%, and 6.0% of the total variances, respectively. The spatial patterns for these modes are similar to those in the combined O_3 data in the NH. For the model O_3 in the SH, the second, third, and fourth modes account for 9.9%, 9.0%, and 5.8% of the total variances. The spatial patterns for these modes are also similar to those in the SH combined O_3 data.

3.5 PCA of Geopotential Thicknesses

For comparison to the structures in dynamical variables in the stratosphere, similar analyses are performed on the GPT of the 30-100 hPa layer in the NCEP2 analyses. The 30 hPa level is near the region of maximum ozone density within the column. As ozone is the principal absorber of solar UV radiation in the stratosphere, an increase in the ozone concentration would give rise to the stratospheric heating rate and temperature. Near 100 hPa, the temperature is dynamically controlled and is expected to be insensitive to ozone heating. However, near 30 hPa the temperature is partly controlled by radiative heating. Therefore increasing (decreasing) the ozone amount in the lower stratosphere will induce thermal expansion (contraction) of the air column

between 30 and 100 hPa (See Section 3.4.3 for quantitative relation). As presented below, thickness variations are probably caused by a combination of the direct effect by dynamical processes and an indirect effect by chemical species such as ozone as an intermediary [*Camp et al.*, 2003].

3.5.1 Results for GPT in the NH

Fig. 3.8 shows the spatial patterns of the first four leading modes of the NCEP2-layer data from 10° N to 90° N. These four modes capture over 78% of the variance, as summarized in Table 1. The polar projection, cylindrical projection, and zonal mean of the regression coefficients are shown in Fig. 3.18 in the appendix. The first, third, and fourth modes show the similar structures as the first, third and fourth ozone modes in NH (Fig. 3.1). As in the ozone analyses, the first mode is related to the NAM mode. The first mode (Fig. 3.8a), capturing 32.3% of the total variance, is negative in the polar region and positive in the subtropics. The change of sign occurs at about 60° N. In contrast, the first mode for O_3 column (Fig. 3.1a) does not change sign. The difference may be because the atmospheric circulation does not have the same influence on the GPT as that on the ozone. The third mode and fourth mode capture 15% and 12.4% of the total variance, which are larger than the variances for the ozone field. It represents the wavenumber-1 component in the layer thickness. In the time domain, PC1, PC3, and PC4 from the layer thickness have good correlation with the corresponding PCs in column ozone, with correlation coefficients of 0.49, 0.79 and 0.71, respectively. The significance levels are smaller than 1% for all three cases. The spectrum of the detrended PC1 (Fig. 3.9b) shows a peak at 3.5 years, but the signal is weaker than that from the ozone PC1

(Fig. 3.2b). Figs. 3.9f and 3.9h show the spectra of detrended PC3 and PC4. Most signals are at high frequencies as in the ozone case (Figs. 3.3b and 3.3d).

The second mode of the layer thickness is different from the second mode in the ozone. The GPT anomalies in the NH (Fig. 3.8b) are negative in almost all regions, except for a small positive area over Northern Europe. The latter is not statistically significant. In contrast, the spatial pattern of the second mode of O_3 column (Fig. 3.1b) is approximately symmetric around the pole. The power spectral estimate of the PC2 (Fig. 3.9d) has peaks around 2, 4-5, and 8 years. Although the Biennial Oscillation (B) appears here and in PC2 of O_3 column (Fig. 3.2d), there is more power in the low-frequency peaks. It is beyond the scope of this work to explain the difference here. We can speculate that O_3 and GPT are sensitive to different physical and chemical processes. For example, GPT anomaly can be forced by stationary topographical waves [see Lin, 1982; Chapter 5 and Fig. 5.6 in Andrews *et al*. 1987]. The trend for the GPT second mode is possibly related to the stratospheric cooling by the greenhouse effect. On the other hand, O_3 is preferentially destroyed by catalytic chemistry when the polar vortex gets unusually cold [Rex *et al*., 2004].

3.5.2 Results for GPT in the SH

The first four modes of the NCEP2-layer data from 10° S to 90° S are shown in Fig. 3.10. These four modes capture over 80% of the variance. The first, third, and fourth modes show similar structures as the first, third and fourth ozone modes in SH. The first mode, capturing 29% of the total variance, is related to the SAM. The third and fourth

modes capture 18.9% and 10.3% of the total variance, respectively. They represent the wavenumber-1 component in the GPT. The PC1, PC3, and PC4 time series for the layer thickness are highly correlated with the corresponding PCs in the SH ozone, with correlation coefficients of 0.55, 0.4 and 0.71, respectively. The significance levels are below 1% for all three cases. The spectrum of the detrended PC1 (Fig. 3.11d) shows peaks around 20 months (Q_1) and 8 months (Q_1'). Figs. 3.11f and 3.11h show the spectra of detrended PC3 and PC4. Most signals are at high frequencies.

As in the NH case, the second mode, capturing 22.4% of the total variance, is not similar to the second mode in the ozone. The second mode of GPT anomalies in the SH has a node around 55° S; that for O_3 column has a node around 60° S. The power spectral estimate of PC2 has a peak at 8 years, which is absent from the PC2 for column O_3. As in NH, we conclude that the second modes of GPT and column O_3 do not match.

3.5.3 Ozone Effect on Temperature

Ozone is a radiatively active molecule and has direct impact on temperature, and hence GPT, in the stratosphere. To investigate the effect of ozone on temperature, MODTRAN [*Berk et al*., 1989], the Air Force PL/Geophysics Directorate moderate spectral resolution background radiance and transmission model, is used to calculate the radiative heating rates. The MODTRAN calculations are based on a 0-3000 cm^{-1} spectral for the infrared heating rates. For the shortwave heating rates, the calculation is based on a 5000-50000 cm^{-1} spectral interval. We use three model atmospheres to test the results: tropical atmosphere, mid-latitude summer, and sub-arctic winter. The effects on the net

heating rates, after adding 10 DU to the stratosphere ozone, are approximately equal to the effect after decreasing the temperature by 1 K between 10 and 100 hPa. This result is consistent with that obtained by *McElroy et al*. [1974]. From the hydrostatic balance and ideal gas law, we can obtain that a change in the temperature of 1 K corresponds to an approximately 35 m change in GPT.

3.6 Conclusions

The extensive use of PCA resolves the high latitude ozone into zonally symmetric and asymmetric (wavenumber-1) modes (Figs. 3.1 and 3.4), with connections to Annular Modes (NAM and SAM), QBO, QBO-annual Beat, Biennial Oscillation, Semi-annual Oscillation, annual cycle and solar cycle. The structures of these patterns appearing in the ozone record are similar to those in the GEOS-4 CCM and NCEP2 GPT, although there are some discrepancies between column O_3 and GPT in mode 2. The characteristics of the leading modes are summarized in Table 1. The first symmetric mode captures about 30% and 44 % of the total variance in the NH and SH, respectively. The cause of the difference may be the smaller forcing by topographical and land-ocean thermal contrast in the SH than that in the NH. The upward trend in PC1 of ozone in the NH is partly related to the positive trend in the vortex in the 1980s. The trend appears to reverse itself after 1997. A similar trend is seen in PC1 for SH, however, there is no sign of return. In addition, the ozone trend is much larger than that of the SAM. This result may be due to the chemical loss of ozone that results in permanently altering the dynamics of the polar climatology of SH [*Thompson and Solomon*, 2002]. The trend and the spatial pattern for the leading mode of O_3 anomalies in both hemispheres are well captured by the GEOS-4

CCM, although the trend in the NH from the model O_3 is larger than that from the combined O_3.

If we apply the same lowpass filter to the detrended and deseasonalized O_3 data as in *Camp et al*. [2003], the total variance of the first four modes is 81.8% and 84.4% for the NH and SH, respectively. A lowpass filter is chosen to obtain a full signal from periods above 15 months and no signal from periods below 12.5 months. For comparison, the variances of ozone IAV of the leading modes account for 93% of the total variance in the tropics [*Camp et al*., 2003]. For the detrended, deseasonalized, and lowpass filtered GPT, the total variances of the first four modes are 82.3% and 85.7% for the NH and SH, respectively. The variances of the leading modes are smaller than the 97% of the total variance in the tropical layer thickness [*Camp et al*., 2003]. The reason is that there is more internal dynamics at higher latitudes [*Ma et al*., 2004].

We will briefly give heuristic reasons for the two key successes of the PCA analysis: (1) the large fraction of IAV explained by the first 4 modes, and (2) the trend projects mainly into the first mode. First, column O_3 is an approximate conservative tracer in the stratosphere, where dynamical disturbances usually originate from the troposphere. The theorem by *Charney and Drazin* [1961] states that only planetary disturbances with the longest wavelengths can propagate from the lower to the upper atmosphere. Thus, the stratosphere acts as a natural low pass filter; only the largest planetary patterns get excited. Second, physical processes that control IAV in the stratosphere exhibit different symmetry properties, allowing for their separation. The first

mode is nearly zonally symmetric; its amplitude increases from the equator to the pole consistent with the loss of O_3 being primarily driven by heterogeneous chemistry in the spring polar stratosphere [*Austin et al.*, 2000]. Averaged over a long time, the chemical loss rates are zonally symmetric. This allows a natural separation of the IAV into a largely chemically driven trend and dynamically driven variability.

The identification of the physical processes responsible for generating the leading modes of IAV is still preliminary. Our results can be divided into two categories. In the first category, the mechanisms of the QBO, QBO-AB, and SAO are well known. In the second category, the physical mechanisms for the 3.5-year signal and Biennial Oscillation are not well known and will be investigated with the modeling study in future. Global climate change (e.g., changes in NAM and SAM) could impact the ozone layer by modulating the transport of ozone-rich air from lower latitudes. Variations in vortex dynamics induce changes in ozone loss by heterogeneous chemistry [*Austin et al*., 2000; *Rex et al.*, 2004]. Since ozone is radiatively coupled to atmospheric dynamics, such a close linkage opens up possibilities for a synergistic interaction between ozone change and climate variability, as first suggested by *Shindell et al*. [1999].

One of the most important implications in this work is that the pattern of ozone is dominated by a few fundamental modes. By analogy with climate changes, it is possible that ozone changes, natural or anthropogenic, only change the occurrence frequencies but not the structure of the fundamental modes [*Corti et al.*, 1999]. The Goddard GEOS-4

chemistry-climate model can simulate the ozone trend reasonably well. It remains a challenge to simulate realistically the dynamical IAV of ozone.

3.7 Appendix

The material in this appendix provides information on the validation of O_3 data, principal component analysis (PCA) of European Centre for Medium-Range Weather Forecasts (ECMWF) assimilated O_3, statistical significance of spectral peaks in the power spectrum, analysis of the Arosa O_3 record, and cylindrical projections, zonal mean, and t-statistics of leading modes.

3.7.1 Validation of O_3 Data

The ECMWF O_3 data are assimilated from Jan 1979 to Dec 1988 and from Jan 1991 to Aug 2002. Retrievals from TOMS and SBUV instruments on various satellites are directly assimilated. During the years of 1989 and 1990 when the ECMWF assimilated O_3 was not available, ECMWF potential vorticity was used as a proxy for O_3 in the polar night regions. A simple mapping method is used [*Manney et al*., 1999]. First, we choose similar winters as those in 1989 and 1990 by the Annular Mode indices. The details are listed in Table A1. The data for PV and O_3 (originally on pressure surfaces) are interpolated to isentropic surfaces using a linear interpolation scheme described by *Held and Schneider* [1999]. Then the relation between PV and O_3 is fitted to a fourth-order polynomial. O_3 values in 1989 and 1990 are calculated from PV using this polynomial fit. Finally, we interpolate the O_3 data from the isentropic surfaces back to the pressure surfaces. O_3 abundances in the troposphere are set to climatological values. ECMWF assimilated O_3 are compared to the MOD at different latitudes in Fig. 3.12. It agrees well with the MOD. In the polar region, the radiosonde O_3 data are compared with

the combined MOD and ECMWF assimilated O_3 data in Fig. 3.13 and Fig. 3.14. The combined O_3 data agree well with the radiosonde data, although the ozone hole is not deep enough at the South Pole in October.

3.7.2 Statistical Significance of Signals in Power Spectrum

The statistical significance of signals in a power spectrum is obtained by comparing the amplitude of a spectral peak to the red noise spectrum. The red noise spectrum used in constructing null hypothesis for significance is the spectrum associated with the autocorrelation function, ρ [*Gilman et al.*, 1963]. Here, ρ is the average of one-lag autocorrelation and the square-root of the two-lag autocorrelation. The red noise spectrum associated with the autocorrelation function is

$$L(h,\rho,M) = \frac{1-\rho^2}{1-2\rho\cos(\frac{h\pi}{M})+\rho^2}$$

where h is frequency and M is the maximum lag [*Gilman et al*., 1963]. The 10%, 5%, and 1% significance level for the power spectrum are found using F-statistics to compare the spectrum to the red noise spectrum.

3.7.3 3.5-year Signal in Arosa O_3

The longest record of column O_3 measurement is that at Arosa (46.8° N, 9.7° E) in Switzerland. Fig. 3.15a shows Arosa monthly mean column O_3 data and 3rd order polynominal trend from Aug 1931 to Dec 2002. The deseasonalized and detrended monthly O_3 anomalies are shown in Fig. 3.15b. The power spectrum of Fig. 3.15b and a statistical significance test of the peaks are given in Fig. 3.15c. The 3.5 years and 20

months signals are below the 1% significance level. The decadal cycle is below 5% significance level. See Fig. 3.2b in the chapter for the meaning of the letters above the spectral peaks in Fig. 3.15.

3.7.4 Cylindrical Projections, Zonal Mean, and t-statistics of Leading Modes

The polar projection, the cylindrical projection, and the zonal mean of the leading two modes for the combined MOD and ECMWF O_3 anomalies are shown in Figs. 3.16–3.17. Similar results for the 30 hPa to 100 hPa geopotential height (GPT) layer thickness anomalies are shown in Figs. 3.18–3.19. The first modes of O_3 anomalies in both hemispheres are negative. The second modes of O_3 anomalies in the NH and SH have a node at approximately 60° N and 60° S, respectively. The first modes of GPT anomalies are negative in the polar region and positive in the subtropical region in both hemispheres. The second mode of GPT anomalies in the NH is negative in almost all regions, except for a small positive area in North Europe, which is not statistic significant. The second mode of GPT anomalies in the SH has a node around 55° S.

The associated t-statistics for the regression coefficients of O_3 and GPT anomalies are calculated. For the regression coefficients, β_k, the t-statistic is defined by $t_k = \left|\beta_k / Se(\beta_k)\right|$. $Se(\beta_k)$ is the 1-sigma uncertainty estimates for the β_k. The result is statistically significant when t_k is larger than certain value t_0. Given the number of degrees of freedom, t_0 can be found from the t-distribution table. t_0 with a 5%

significance level varies around 2. t_k of O_3 and GPT anomalies are larger than 2 in most areas. This suggests that the results are statistically significant in most areas.

3.8 References

Andrews, D.G., J.R. Holton, and C.B. Leovy, *Middle atmosphere dynamics*, 489 pp., Academic Press, 1987.

Austin, J., J.R. Knight, and N. Butchart, Three-dimensional chemical model simulations of the ozone layer: 1979-2015, *Quarterly Journal of the Royal Meteorological Society*, *126*, 1533-1556, 2000.

Baldwin, M.P., and T.J. Dunkerton, Biennial, quasi-biennial, and decadal oscillations of potential vorticity in the northern stratosphere, *Journal of Geophysical Research-Atmospheres*, *103* (D4), 3919-3928, 1998.

Baldwin, M.P., and T.J. Dunkerton, Propagation of the Arctic Oscillation from the stratosphere to the troposphere, *Journal of Geophysical Research-Atmospheres*, *104* (D24), 30937-30946, 1999.

Baldwin, M.P., L.J. Gray, T.J. Dunkerton, K. Hamilton, P.H. Haynes, W.J. Randel, J.R. Holton, M.J. Alexander, I. Hirota, T. Horinouchi, D.B.A. Jones, J.S. Kinnersley, C. Marquardt, K. Sato, and M. Takahashi, The quasi-biennial oscillation, *Reviews of Geophysics*, *39* (2), 179-229, 2001.

Berk, A., L. S. Bernstein, and D. C. Robertson, MODTRAN: A moderate resolution model for LOWTRAN 7, pp. 38, AFGL, 1989.

Bloom, S., *et al*., The Goddard Earth Observation System Data Assimilation System, GEOS DAS Version 4.0.3: Documentation and Validation, NASA TM-2005-104606, *26*, 166pp, 2005.

Camp, C.D., M.S. Roulston, and Y.L. Yung, Temporal and Spatial Patterns of the Interannual Variability of Total Ozone in the Tropics, *Journal of Geophysical Research-Atmospheres*, *108* (D20), art. no. 4643, 2003.

Charney, J. G., and P. G. Drazin, Propagation of Planetary-Scale Disturbances from Lower into Upper Atmosphere, *Journal of Geophysical Research*, *66*, 83-109, 1961.

Coffey, M.T., Observations of the impact of volcanic activity on stratospheric chemistry, *Journal of Geophysical Research*, *101*, 6767-6780, 1996.

Corti, S., F. Molteni, and T.N. Palmer, Signature of recent climate change in frequencies of natural atmospheric circulation regimes, *Nature*, *398* (6730), 799-802, 1999.

Dethof, A., and E.V. Holm, Ozone assimilation in the ERA-40 reanalysis project, *Quarterly Journal of the Royal Meteorological Society*, *130* (603), 2851-2872, 2004.

Devore, J.L., *Probability and Statistics for Engineering and the Science*, 640 pp., Brooks/Cole, Monterey, Calif., 1982.

Douglass, A. R., *et al*., Evaluation of transport in the lower tropical stratosphere in a global chemistry and transport model, *Journal of Geophysical Research-Atmospheres*, *108*, 2003.

Eder, B.K., S.K. LeDuc, and J.E. Sickles II, A climatology of total ozone mapping spectrometer data using rotated principal component analysis, *Journal of Geophysical Research-Atmospheres*, *104* (D3), 3691-3709, 1999.

Fusco, A.C., and M.L. Salby, Interannual variations of total ozone and their relationship to variations of planetary wave activity, *Journal of Climate, 12* (6), 1619-1629, 1999.

Gray, L.J., and J.A. Pyle, The Semiannual Oscillation and Equatorial Tracer Distributions, *Quarterly Journal of the Royal Meteorological Society, 112* (472), 387-407, 1986.

Hood, L.L., and B.E. Soukharev, Quasi-decadal variability of the tropical lower stratosphere: The role of extratropical wave forcing, *Journal of the Atmospheric Sciences*, *60* (19), 2389-2403, 2003.

Horinouchi, T., S. Pawson, K. Shibata, U. Langematz, E. Manzini, M.A. Giorgetta, F. Sassi, R.J. Wilson, K.P. Hamilton, J. de Grandpré, A.A. Scaife, Tropical Cumulus Convection and Upward Propagating Waves in Middle Atmospheric GCMs, *Journal of the Atmospheric Sciences*, *60*, 2765-2782, 2003.

Jiang, X., D.B.A. Jones, R. Shia, D.E. Waliser, and Y.L. Yung, Spatial patterns and mechanisms of the Quasi-biennial oscillation-annual beat of ozone, *Journal of Geophysical Research*, Accepted, 2005.

Kalnay, E., M. Kanamitsu, R. Kistler, W. Collins, D. Deaven, L. Gandin, M. Iredell, S. Saha, G. White, J. Woollen, Y. Zhu, M. Chelliah, W. Ebisuzaki, W. Higgins, J. Janowiak, K.C. Mo, C. Ropelewski, J. Wang, A. Leetmaa, R. Reynolds, R. Jenne, and D. Joseph, The NCEP/NCAR 40-year reanalysis project, *Bulletin of the American Meteorological Society*, *77* (3), 437-471, 1996.

Kistler, R., E. Kalnay, W. Collins, S. Saha, G. White, J. Woollen, M. Chelliah, W. Ebisuzaki, M. Kanamitsu, V. Kousky, H. van den Dool, R. Jenne, and M. Fiorino,

The NCEP-NCAR 50-year reanalysis: Monthly means CD-ROM and documentation, *Bulletin of the American Meteorological Society, 82* (2), 247-267, 2001.

Leovy, C.B., C.R. Sun, M.H. Hitchman, E.E. Remsberg, J.M. Russell, L.L. Gordley, J.C. Gille, and L.V. Lyjak, Transport of ozone in the middle stratosphere: Evidence for planetary wave breaking, *Journal of the Atmospheric Sciences, 42* (3), 230-244, 1985.

Lin, B.D., The Behavior of Winter Stationary Planetary-Waves Forced by Topography and Diabatic Heating, *Journal of the Atmospheric Sciences, 39* (6), 1206-1226, 1982.

Ma, J., D.W. Waugh, A.R. Douglass, S.R. Kawa, P.A. Newman, S. Pawson, R. Stolarski, and S.J. Lin, Interannual variability of stratospheric trace gases: The role of extratropical wave driving, *Quarterly Journal of the Royal Meteorological Society, 130* (602), 2459-2474, 2004.

Manney, G.L., H.A. Michelsen, M.L. Santee, M.R. Gunson, F.W. Irion, A.E. Roche, and N.J. Livesey, Polar vortex dynamics during spring and fall diagnosed using trace gas observations from the Atmospheric Trace Molecule Spectroscopy instrument, *Journal of Geophysical Research-Atmospheres, 104* (D15), 18841-18866, 1999.

McElroy, M.B., S.C. Wofsy, J.E. Penner, and McConnel.Jc, Atmospheric Ozone - Possible Impact of Stratospheric Aviation, *Journal of the Atmospheric Sciences, 31* (1), 287-303, 1974.

McIntyre, M.E., How well do we understand the dynamics of stratospheric warmings?, *Journal of the Meteorological Society of Japan, 60* (1), 37-65, 1982.

McPeters, R., *et al*., Nimbus-7 Total Ozone Mapping Spectrometer (TOMS) data products user's guide, *NASA Tech. Rep*., 1996. Data are available from http://code916.gsfc.nasa.gov/Public/Analysis/merged/.

Newman, P.A., J.F. Gleason, R.D. McPeters, and R.S. Stolarski, Anomalously low ozone over the Arctic, *Geophysical Research Letters, 24* (22), 2689-2692, 1997.

Pollack, J.B., O.B. toon, and E.F. Danielsen, The El Chichon volcanic cloud: An introduction, *Geophysical Research Letters, 10*, 989-992, 1983.

Preisendorfer, R. W. *Principal component analysis in meteorology and oceanography*. Elsevier Science, 425 pp**,** 1988.

Press, W., S. Teukolsky, W. Vetterling, and B. Flannery, *Numerical Recipes in Fortran 77: The Art of Scientific Computing*, 933 pp., Cambridge Univ. Press, New York, 1992.

Randel, W.J., F. Wu, and R. Stolarski, Changes in column ozone correlated with the stratospheric EP flux, *Journal of the Meteorological Society of Japan, 80* (4B), 849-862, 2002.

Rayner, N. A., *et al*., Global analyses of sea surface temperature, sea ice, and night marine air temperature since the late nineteenth century, *Journal of Geophysical Research-Atmospheres*, *108*, 2003.

Richman, M. B., Rotation of principal components, *Journal of Climatology*, *6* (3), 293-335, 1986.

Rex, M., R.J. Salawitch, P. von der Gathen, N.R.P. Harris, M.P. Chipperfield, and B. Naujokat, Arctic ozone loss and climate change, *Geophysical Research Letters*, *31* (4), 2004.

Salby, M.L., and R.R. Garcia, Vacillations Induced by Interference of Stationary and Traveling Planetary-Waves, *Journal of the Atmospheric Sciences, 44* (19), 2679-2711, 1987.

Scott, R.K., and P.H. Haynes, Internal interannual variability of the extratropical stratospheric circulation: The low-latitude flywheel, *Quarterly Journal of the Royal Meteorological Society, 124* (550), 2149-2173, 1998.

Shindell, D.T., R.L. Miller, G.A. Schmidt, and L. Pandolfo, Simulation of recent northern winter climate trends by greenhouse-gas forcing, *Nature, 399* (6735), 452-455, 1999.

Simmons, A.J., A. Untch, C. Jakob, P. Kallberg, and P. Unden, Stratospheric water vapour and tropical tropopause temperatures in ECMWF analyses and multi-year simulations, *Quarterly Journal of the Royal Meteorological Society, 125* (553), 353-386, 1999.

Stolarski, R.S., A.R. Douglass, S.E. Steenrod, S. Pawson, Trends in Stratospheric Ozone: Lessons Learned from a 3D Chemical Transport Model, *Journal of the Atmospheric Sciences, 63,* 1028-1041, 2006a.Stolarski, R.S, A.R. Douglass, M. Gupta, P.A. Newman, S. Pawson, M.R. Schoeberl, J.E. Nielsen, and P.K. Bhartia, Dynamic Feedback due to Ozone Changes in the Antarctic Stratosphere, *Submitted to Geophysical Research Letters*, 2006b.

Thompson, D.W.J., and S. Solomon, Interpretation of recent Southern Hemisphere climate change, *Science, 296* (5569), 895-899, 2002.

Thompson, D.W.J., and J.M. Wallace, The Arctic Oscillation signature in the wintertime geopotential height and temperature fields, *Geophysical Research Letters, 25* (9), 1297-1300, 1998.

Thompson, D.W.J., and J.M. Wallace, Annular modes in the extratropical circulation. Part I: Month-to-month variability, *Journal of Climate, 13,* 1000-1016, 2000.

Tung, K.K., and H. Yang, Global QBO in Circulation and Ozone 1. Reexamination of Observational Evidence, *Journal of the Atmospheric Sciences, 51* (19), 2699-2707, 1994a.

Tung, K.K., and H. Yang, Global QBO in Circulation and Ozone 2. A Simple Mechanistic Model, *Journal of the Atmospheric Sciences, 51* (22), 3365-3365, 1994b.

Uppala, S. M., *et al*., The ERA-40 re-analysis, *Quarterly Journal of the Royal Meteorological Society*, *131*, 2961-3012, 2005.World Meteorological Organization (WMO), Scientific Assessment of Ozone Depletion: 2002, *WMO Report 47*, Geneva, Switzerland, 2002. Data are available from http://data.ecmwf.int/data/d/era40/.

Weatherhead, E.C., G.C. Reinsel, G.C. Tiao, C.H. Jackman, L. Bishop, S.M.H. Frith, J. DeLuisi, T. Keller, S.J. Oltmans, E.L. Fleming, D.J. Wuebbles, J.B. Kerr, A.J. Miller, J. Herman, R. McPeters, R.M. Nagatani, and J.E. Frederick, Detecting the recovery of total column ozone, *Journal of Geophysical Research-Atmospheres*, *105* (D17), 22201-22210, 2000.

World Meteorological Organization (WMO), Scientific Assessment of Ozone Depletion: 2002, *WMO Report 47*, Geneva, Switzerland, 2002.

Zerefos, C.S., K. Tourpali, and A.F. Bais, Further studies on possible volcanic signal to the ozone layer, *Journal of Geophysical Research-Atmospheres*, *99*, 25741-27746, 1994.

Table 3.1: Comparison of Leading Modes of Variability in Column O_3 and GPT in the NH and SH.

Modes	NH		SH	
	O3	GPT	O3	GPT
Fractions of variance				
1	30.4%	32.3%	43.9%	29%
2	15.9%	18.5%	13.7%	22.4%
3	7.1%	15%	9.8%	18.9%
4	6.5%	12.4%	7.4%	10.3%
Sum	59.9%	78.2%	74.8%	80.6%
Spatial pattern				
1	Symmetric	Symmetric	Symmetric	Symmetric (off pole)
2	Symmetric	Non-symmetric	Symmetric (off pole)	Symmetric (off pole)
3 4	Wave 1	Wave 1	Wave 1	Wave 1
Temporal pattern				
1	NAM + trend 3.5 yr, QBO, QBO-AB, SAO	NAM 3.5 yr, 17 months	SAM + trend QBO-AB, SAO	SAM+trend QBO-AB, 8 months
2	BO, QBO-AB, SAO	BO, 4-5yr, 8yr, trend	QBO, QBO-AB	8 yr
3	Stochastic	Stochastic	Stochastic, QBO, QBO-AB	Stochastic
4	Stochastic	Stochastic	Stochastic, BO	Stochastic

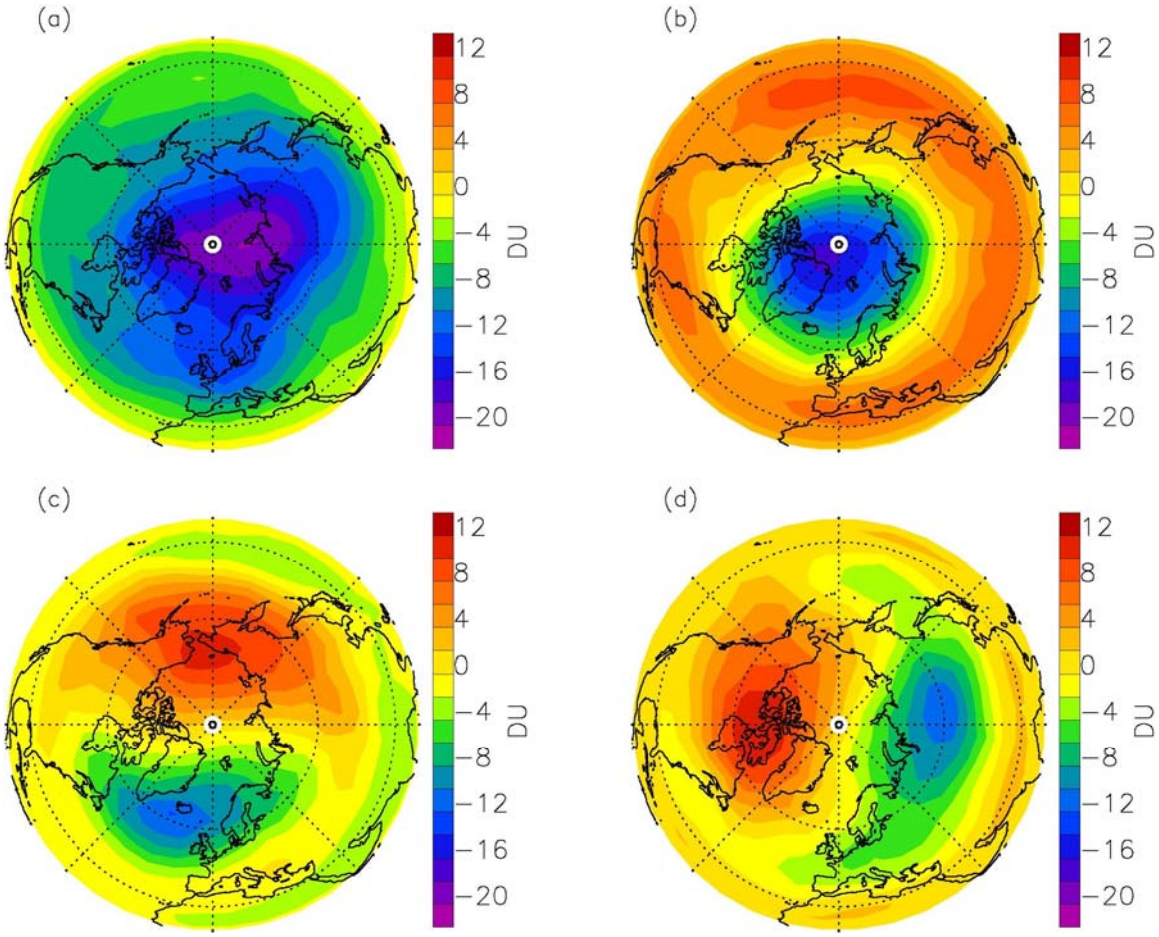

Figure 3.1: The spatial patterns of the O_3 anomalies regressed upon the leading PCs in the NH. Units are DU. The first four modes explain 30.4, 15.9, 7.1, 6.5% of the total variance, respectively.

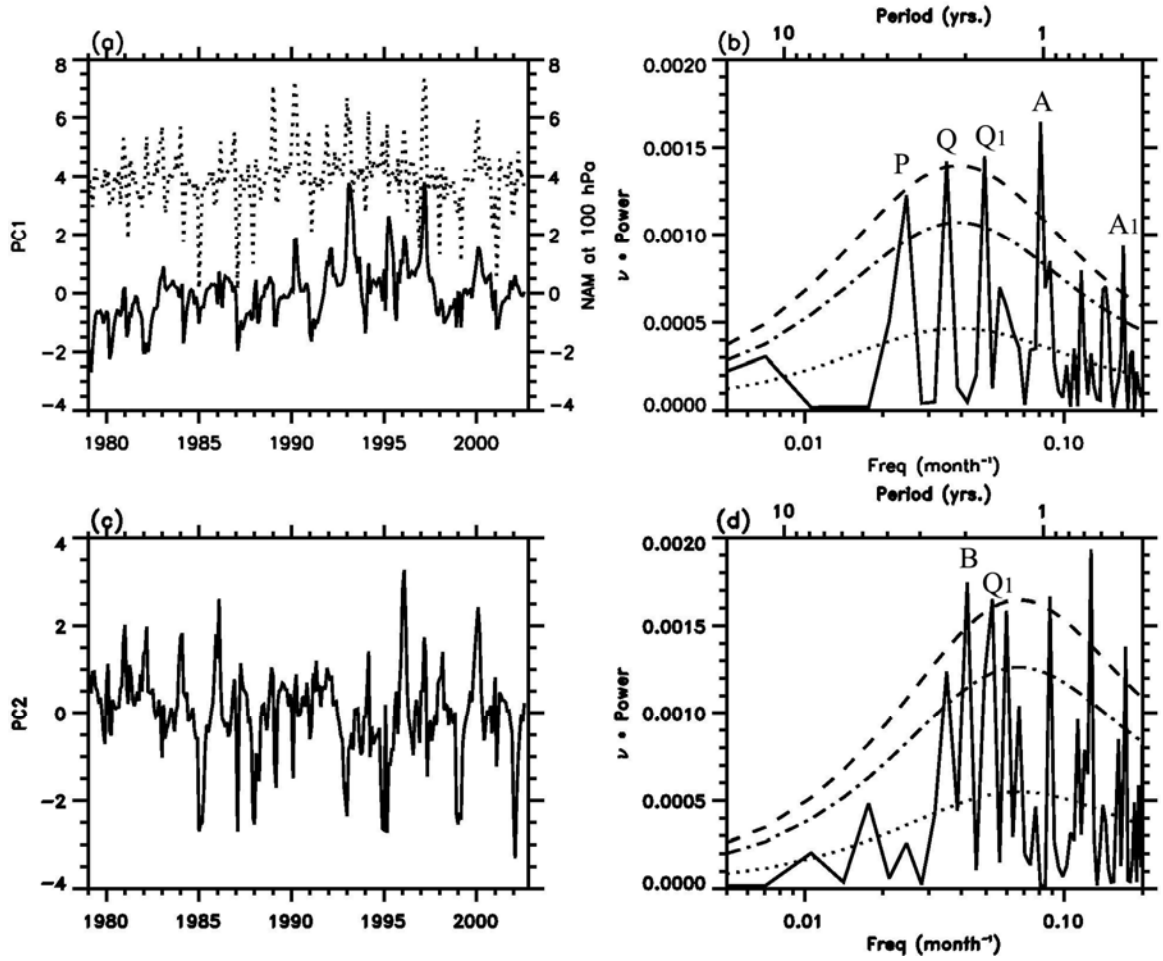

Figure 3.2: (a) PC1 (Solid) and NAM index at 100 hPa shifted upward by 4 (Dotted). The correlation is 0.53 (0.1% significance level). (b) Power spectral estimate of detrended PC1 (Solid), red noise spectrum (Dotted), 10% and 5% significance level (Dashed). P, Q, Q_1, A, and A_1 denote the 3.5-year signal, QBO, QBO-AB, residue seasonal cycle, and SAO respectively. (c) PC2. (d) Power spectral estimate of detrended PC2 (Solid), red noise spectrum (Dotted), 10% and 5% significance level (Dashed). B denotes the BO.

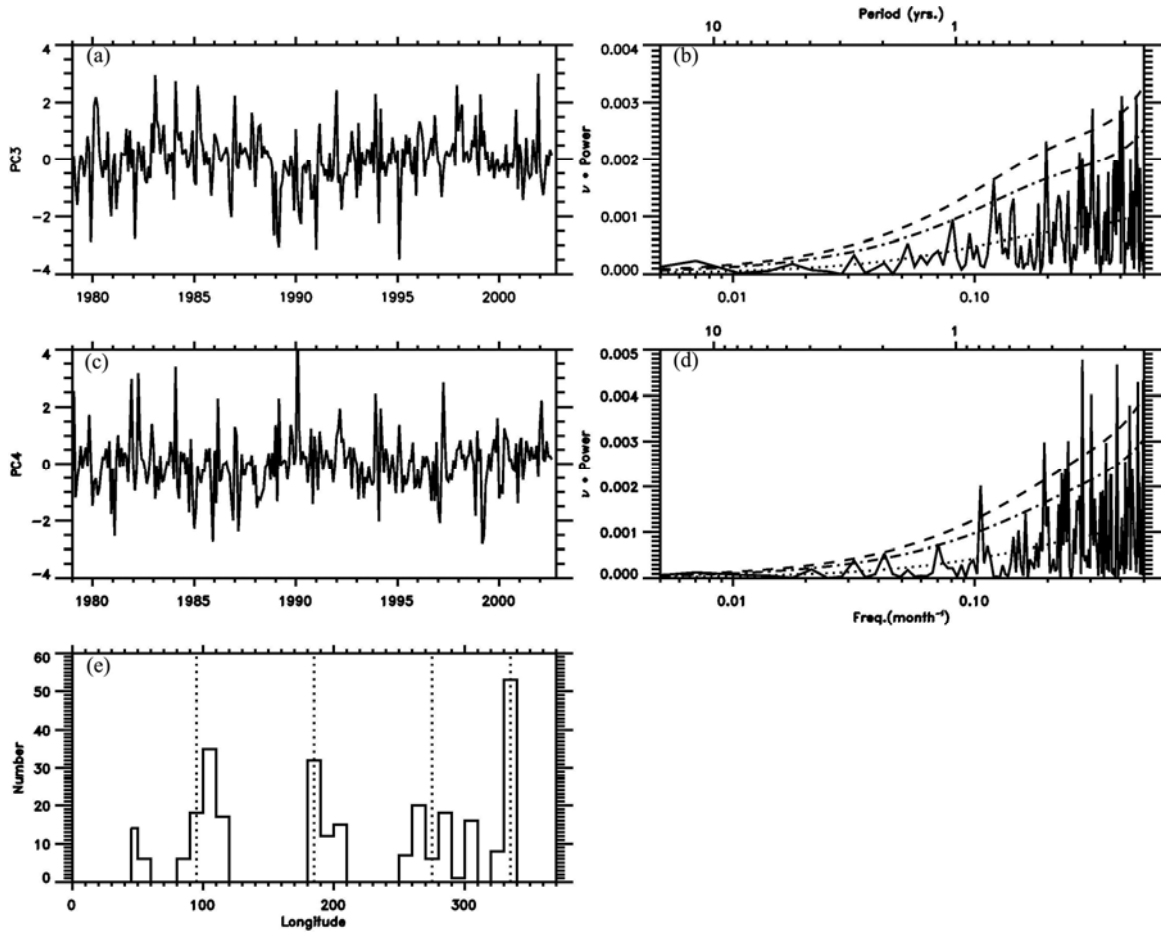

Figure 3.3: (a) PC3. (b) Power spectrum of detrended PC3 (Solid), red noise spectrum (Dotted), 10% and 5% significance level (Dashed). (c) PC4. (d) Power spectrum of detrended PC4 (Solid), red noise spectrum (Dotted), 10% and 5% significance level (Dashed). (e) Histogram of the maximum longitude of $p_3(t)C_3(\theta, \varphi) + p_4(t)C_4(\theta, \varphi)$. Dotted lines represent the nodal points in the modes 3 and 4 in Figs. 3.1c and d.

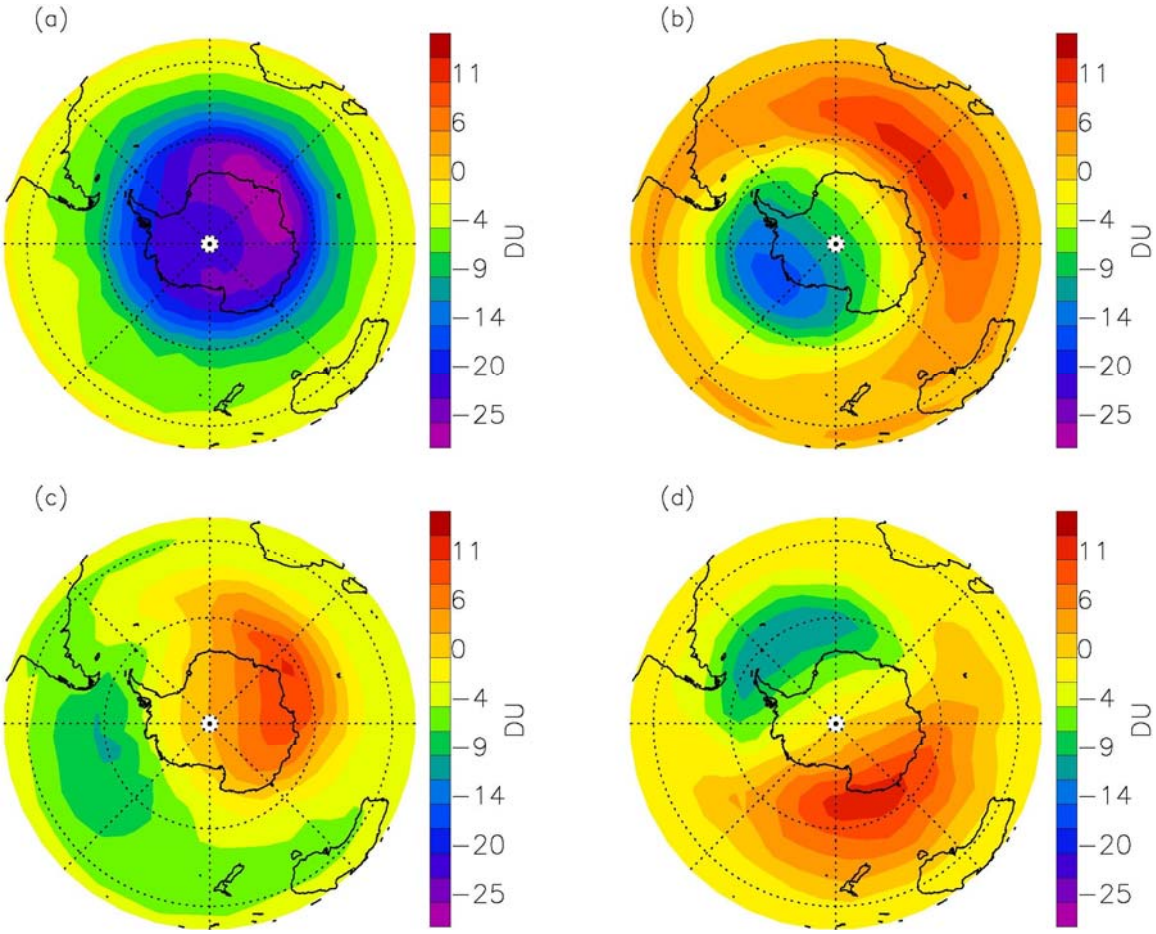

Figure 3.4: The spatial patterns of the O_3 anomalies regressed upon the leading PCs in the SH. Units are DU. The first four modes explain 43.9, 13.7, 9.8 and 7.4% of the total variance, respectively.

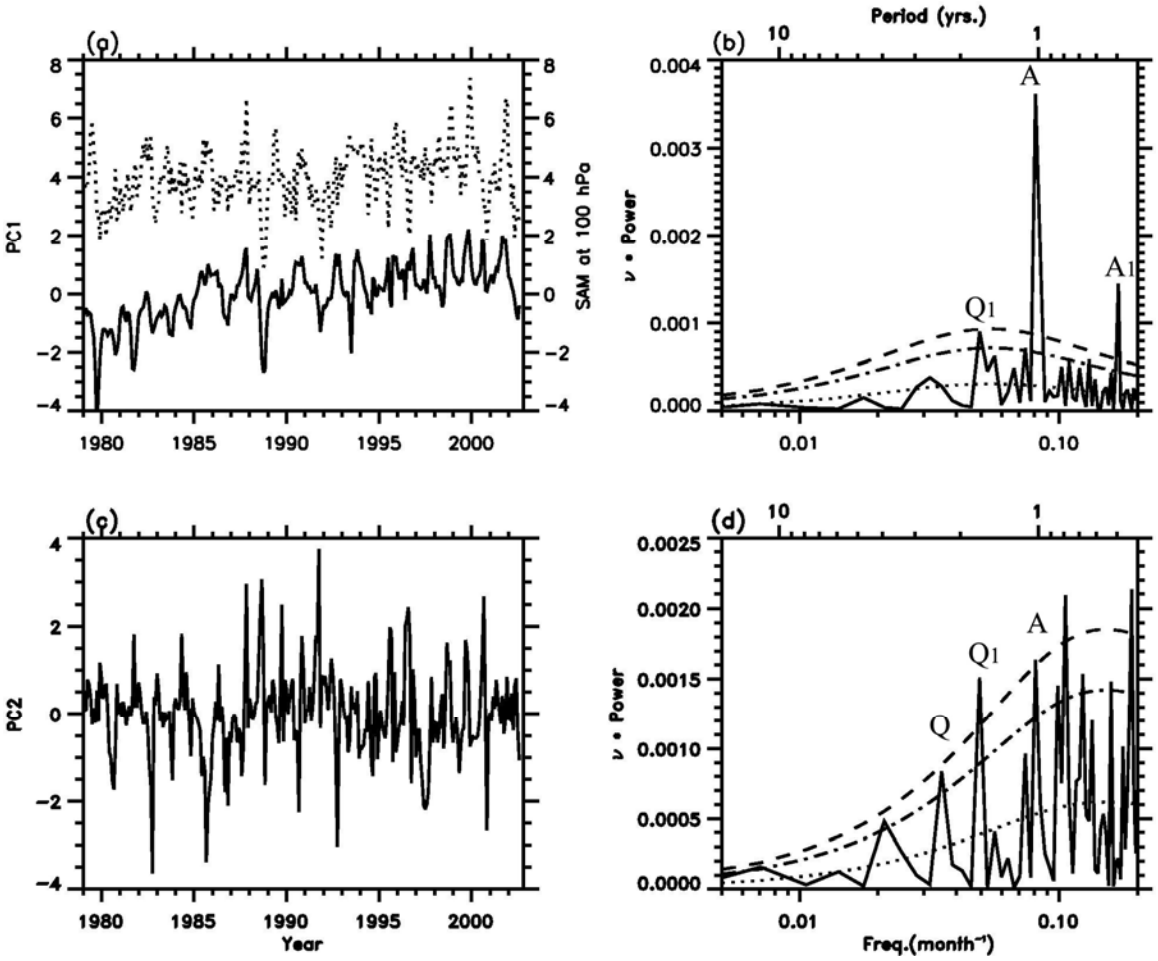

Figure 3.5: (a) PC1 (Solid) and SAM index at 100 hPa shifted upward by 4 (Dotted). The correlation is 0.45 (0.1% significance level). (b) Power spectral estimate of detrended PC1 (Solid), red noise spectrum (Dotted), 10% and 5% significance level (Dashed). (c) PC2. (d) Power spectral estimate of detrended PC2 (Solid), red noise spectrum (Dotted), 10% and 5% significance level (Dashed). In (b) and (d), the letters above the spectral peaks have the same meaning as in Fig. 3.2b.

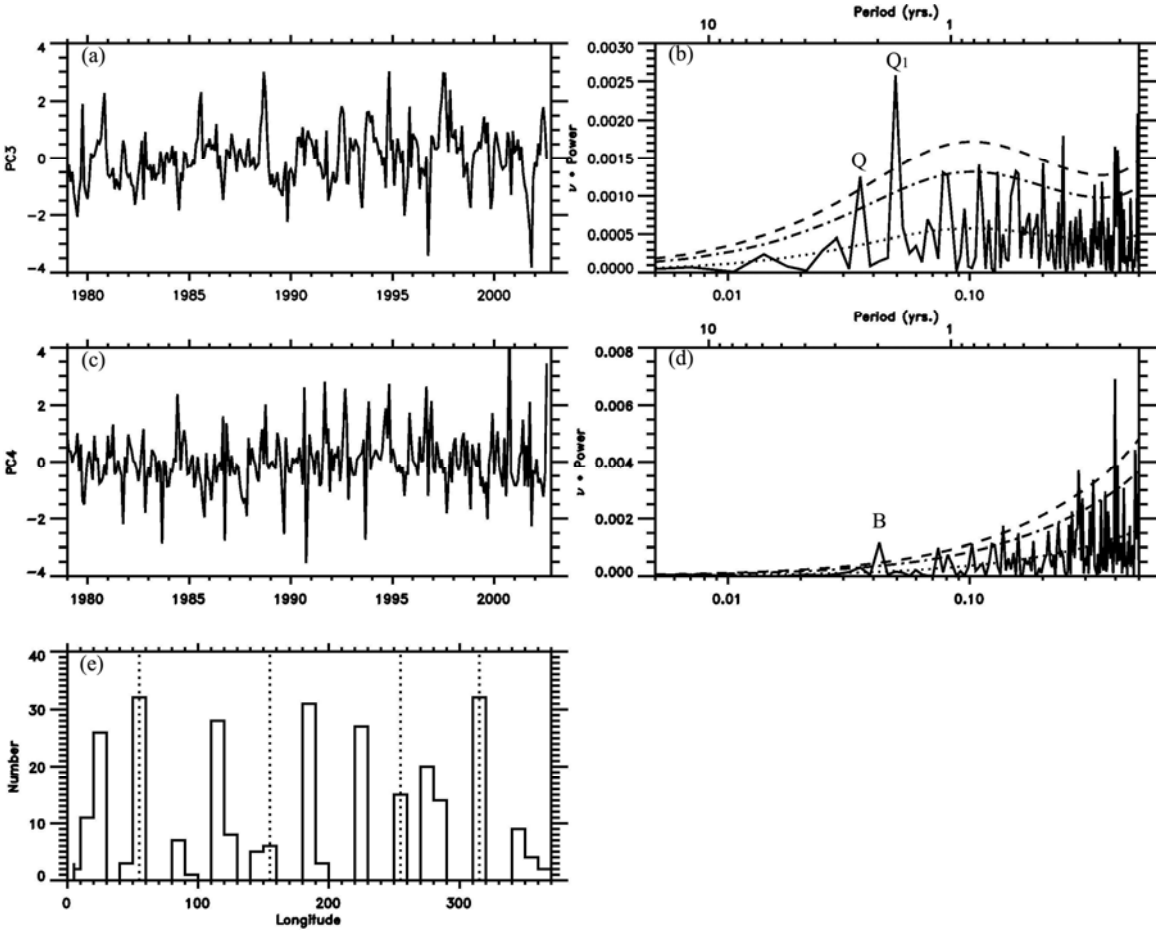

Figure 3.6: (a) PC3. (b) Power spectrum of detrended PC3 (Solid), red noise spectrum (Dotted), 10% and 5% significance level (Dashed). (c) PC4. (d) Power spectrum of detrended PC4 (Solid), red noise spectrum (Dotted), 10% and 5% significance level (Dashed). (e) Histogram of the maximum longitude of $p_3(t)C_3(\theta, \varphi) + p_4(t)C_4(\theta, \varphi)$. Dotted lines represent the nodal points in the modes 3 and 4 in Figs. 3.4c and d.

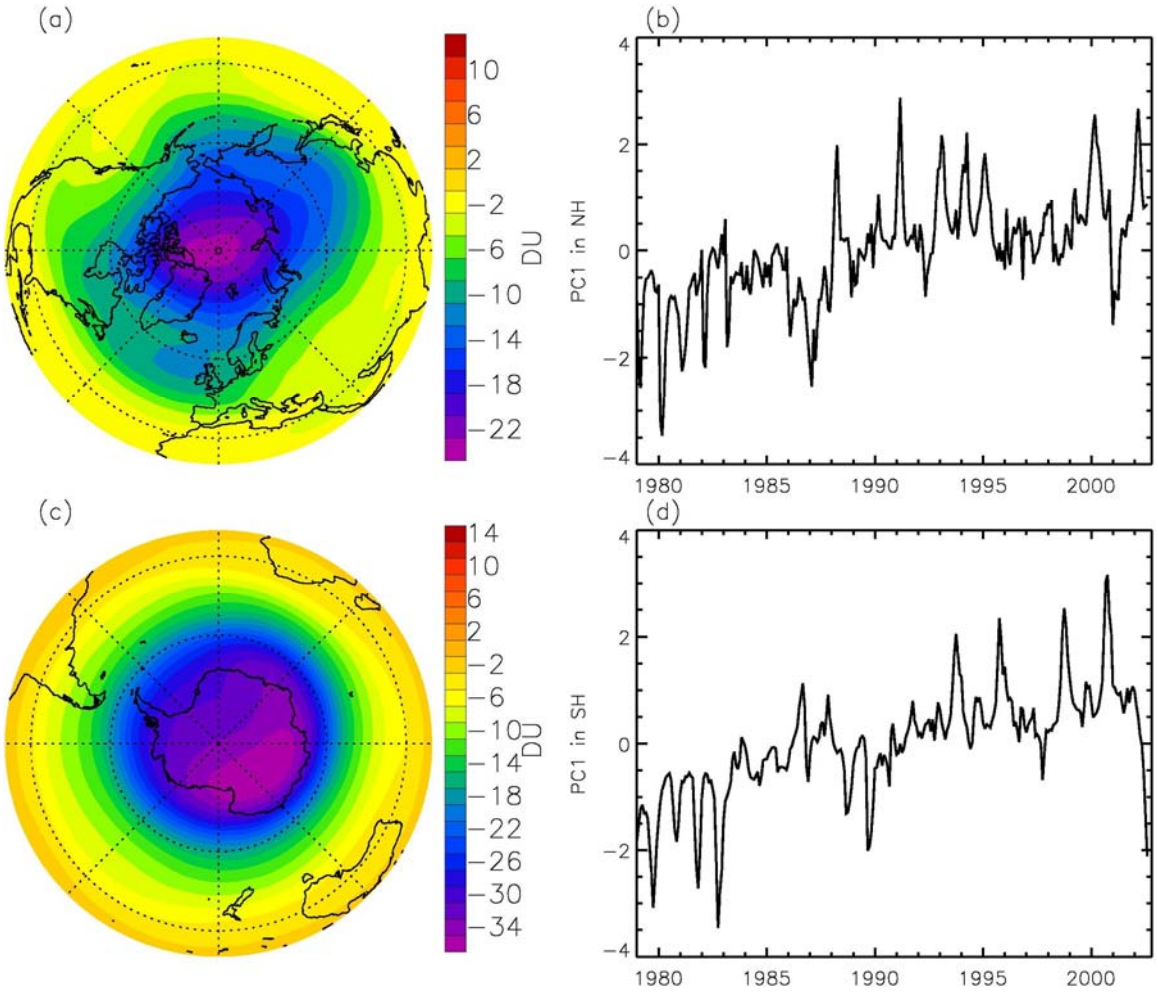

Figure 3.7: (a) The spatial pattern of the model O_3 anomalies regressed upon the leading PC1 in the NH. Units are DU. The first mode explains 31.8% of the total variance. (b) PC1 of the model O_3 in the NH. (c) The spatial pattern of the model O_3 anomalies regressed upon the leading PC1 in the SH. Units are DU. The first mode explains 59.5% of the total variance. (d) PC1 of the model O_3 in the SH.

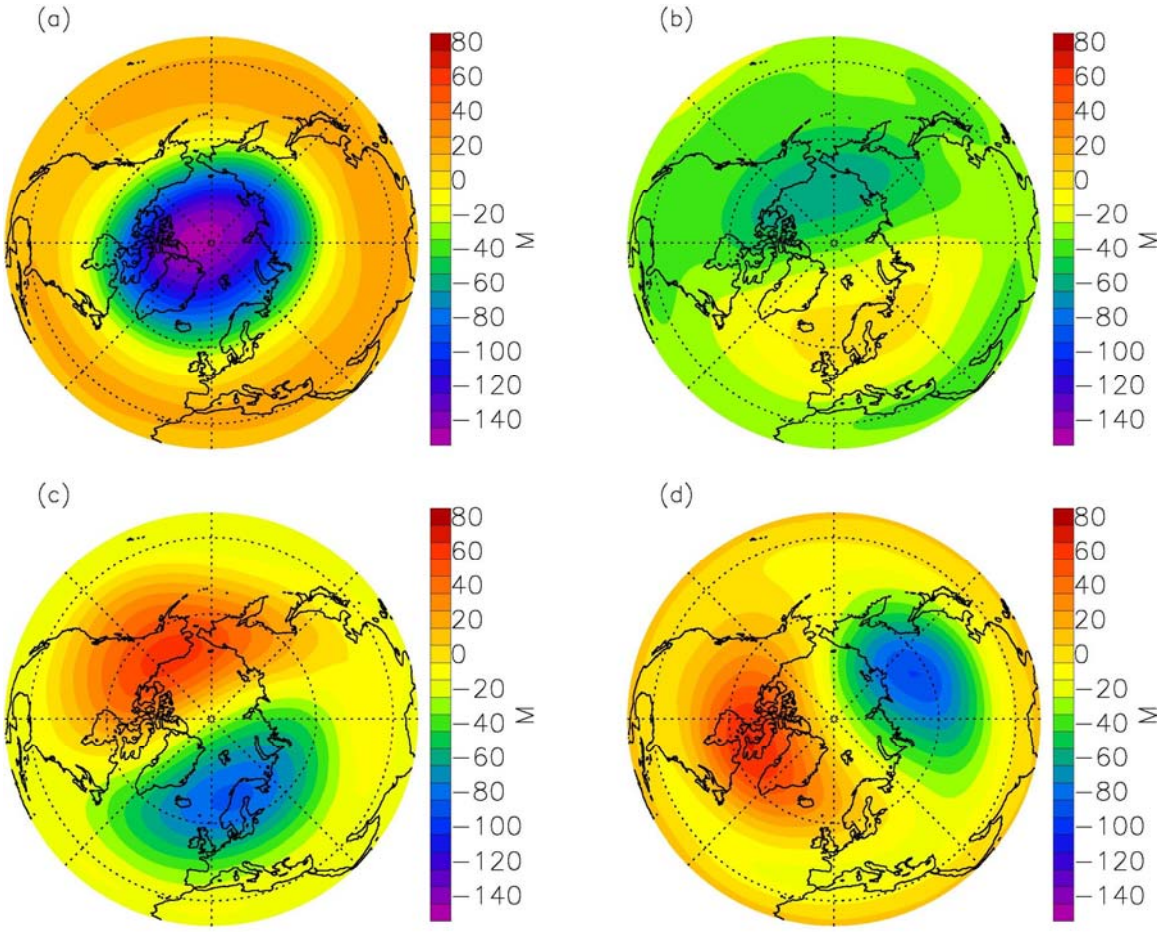

Figure 3.8: The spatial patterns of the 30 hPa to 100 hPa layer thickness anomalies regressed upon the leading PCs in the NH. Units are m. The first four modes explain 32.3, 18.5, 15, 12.4% of the total variance, respectively.

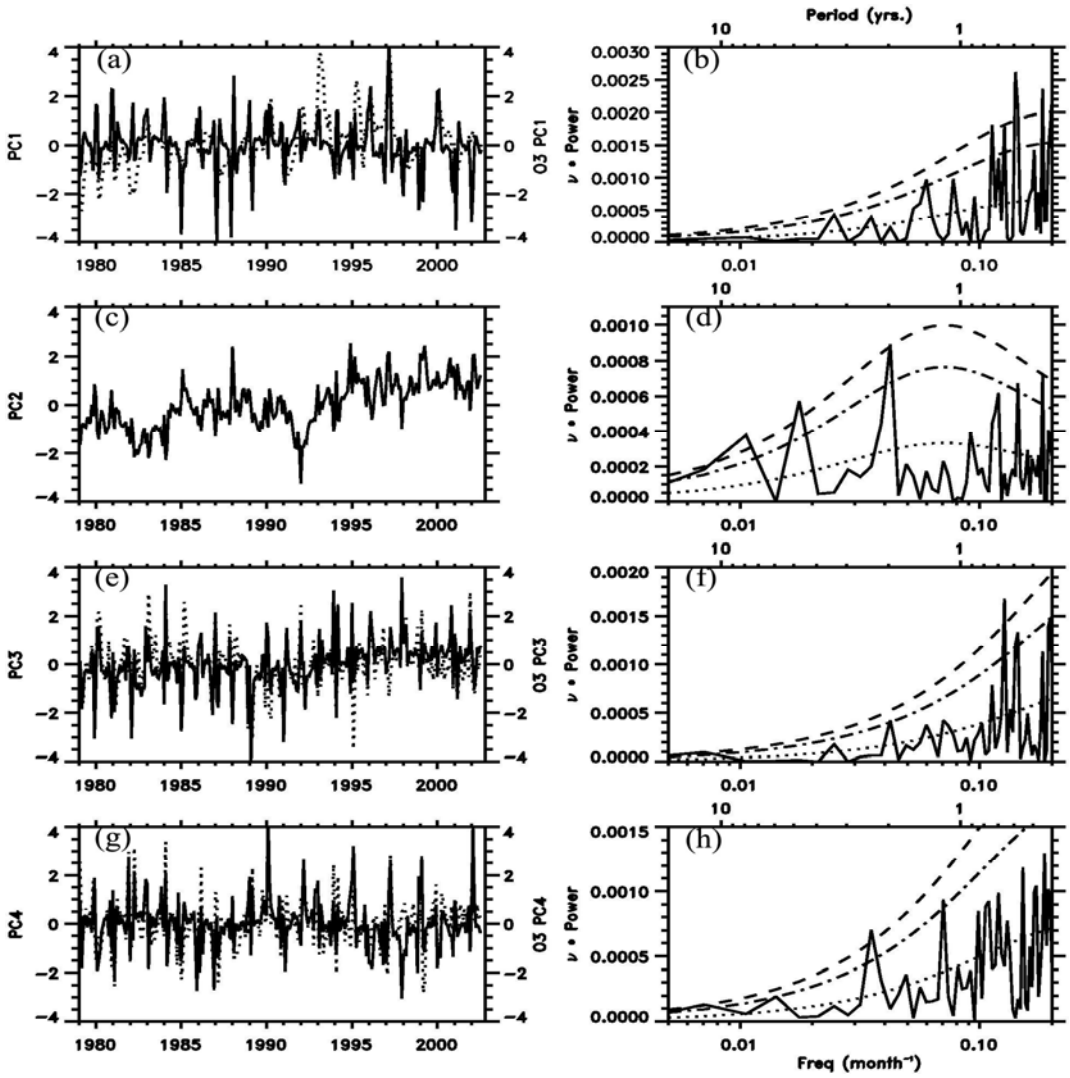

Figure 3.9: (a) Layer thickness PC1 (Solid) and O_3 PC1 (Dotted) in NH. The correlation is 0.49 (0.1% significance level). (b) Power spectral estimate of detrended PC1 (Solid), red noise spectrum (Dotted), 10% and 5% significance level (Dashed). (c) Layer thickness PC2 in NH. (d) Power spectral estimate of detrended PC2 (Solid), red noise spectrum (Dotted), 10% and 5% significance level (Dashed). (e) Layer thickness PC3 (Solid) and O_3 PC3 (Dotted) in NH. The correlation is 0.79 (0.1% significance level). (f) Power spectral estimate of detrended PC3 (Solid), red noise spectrum (Dotted), 10% and 5% significance level (Dashed). (g) Layer thickness PC4 (Solid) and O_3 PC4 (Dotted) in

NH. The correlation is 0.71 (0.1% significance level). (h) Power spectral estimate of detrended PC4 (Solid), red noise spectrum (Dotted), 10% and 5% significance level (Dashed).

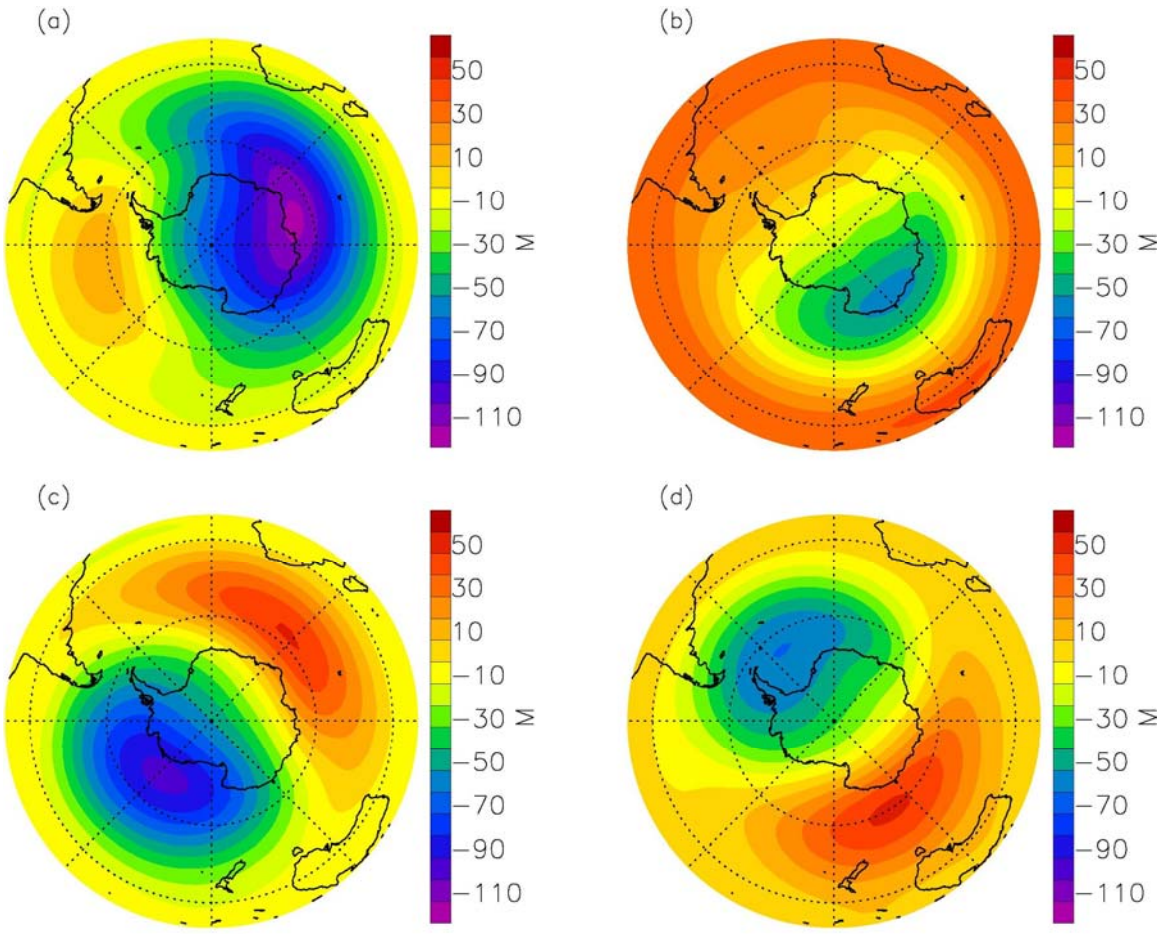

Figure 3.10: The spatial patterns of the 30 hPa to 100 hPa layer thickness anomalies regressed upon the leading PCs in the SH. Units are m. The first four modes explain 29, 22.4, 18.9, 10.3% of the total variance, respectively.

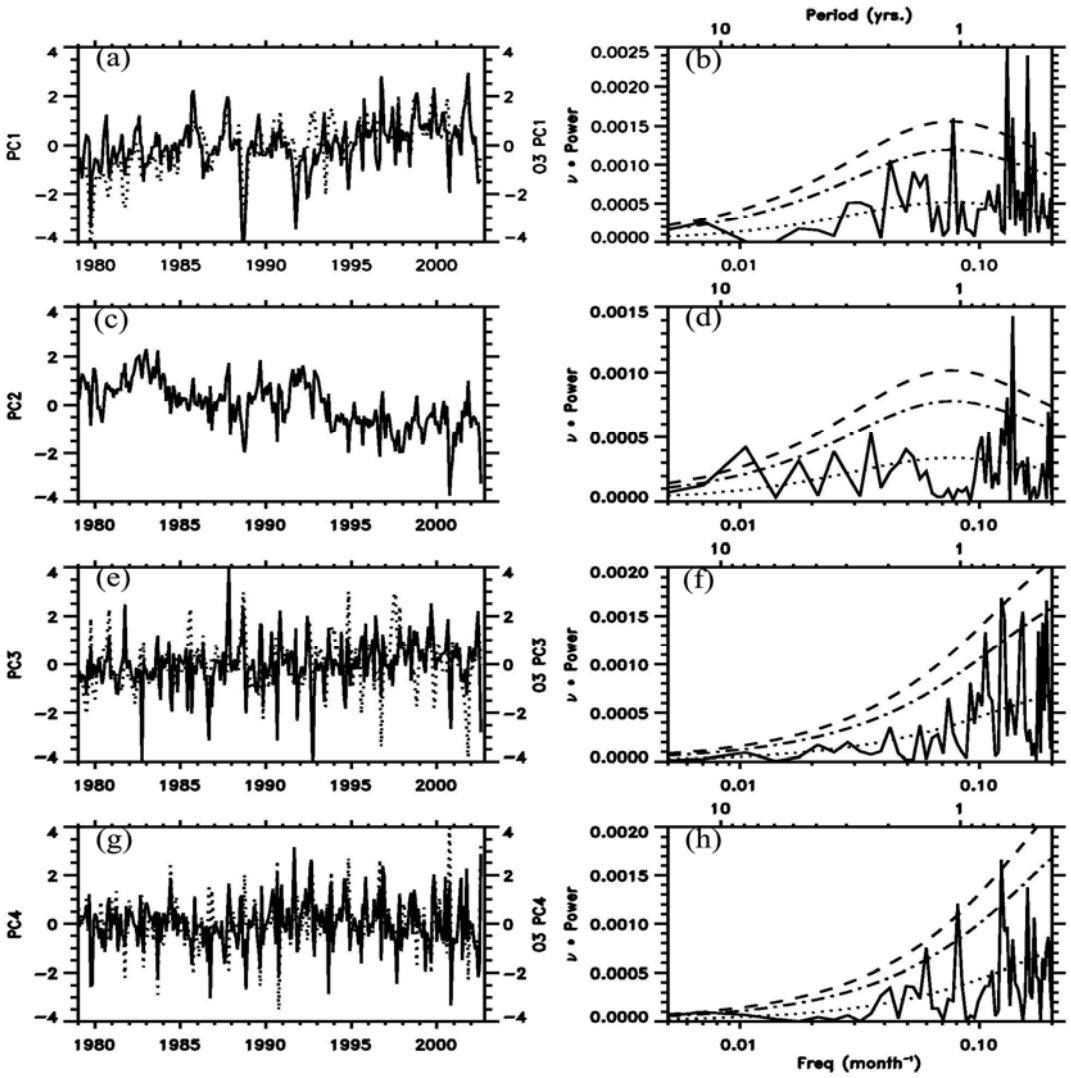

Figure 3.11 (a) Layer thickness PC1 (Solid) and O_3 PC1 (Dotted) in SH. The correlation is 0.55 (0.1% significance level). (b) Power spectral estimate of detrended PC1 (Solid), red noise spectrum (Dotted), 10% and 5% significance level (Dashed). (c) Layer thickness PC2 in SH. (d) Power spectral estimate of detrended PC2 (Solid), red noise spectrum (Dotted), 10% and 5% significance level (Dashed). (e) Layer thickness PC3 (Solid) and O_3 PC3 (Dotted) in SH. The correlation is 0.40 (0.1% significance level). (f) Power spectral estimate of detrended PC3 (Solid), red noise spectrum (Dotted), 10% and 5% significance level (Dashed). (g) Layer thickness PC4 (Solid) and O_3 PC4 (Dotted) in

SH. The correlation is 0.71 (0.1% significance level). (h) Power spectral estimate of detrended PC4 (Solid), red noise spectrum (Dotted), 10% and 5% significance level (Dashed).

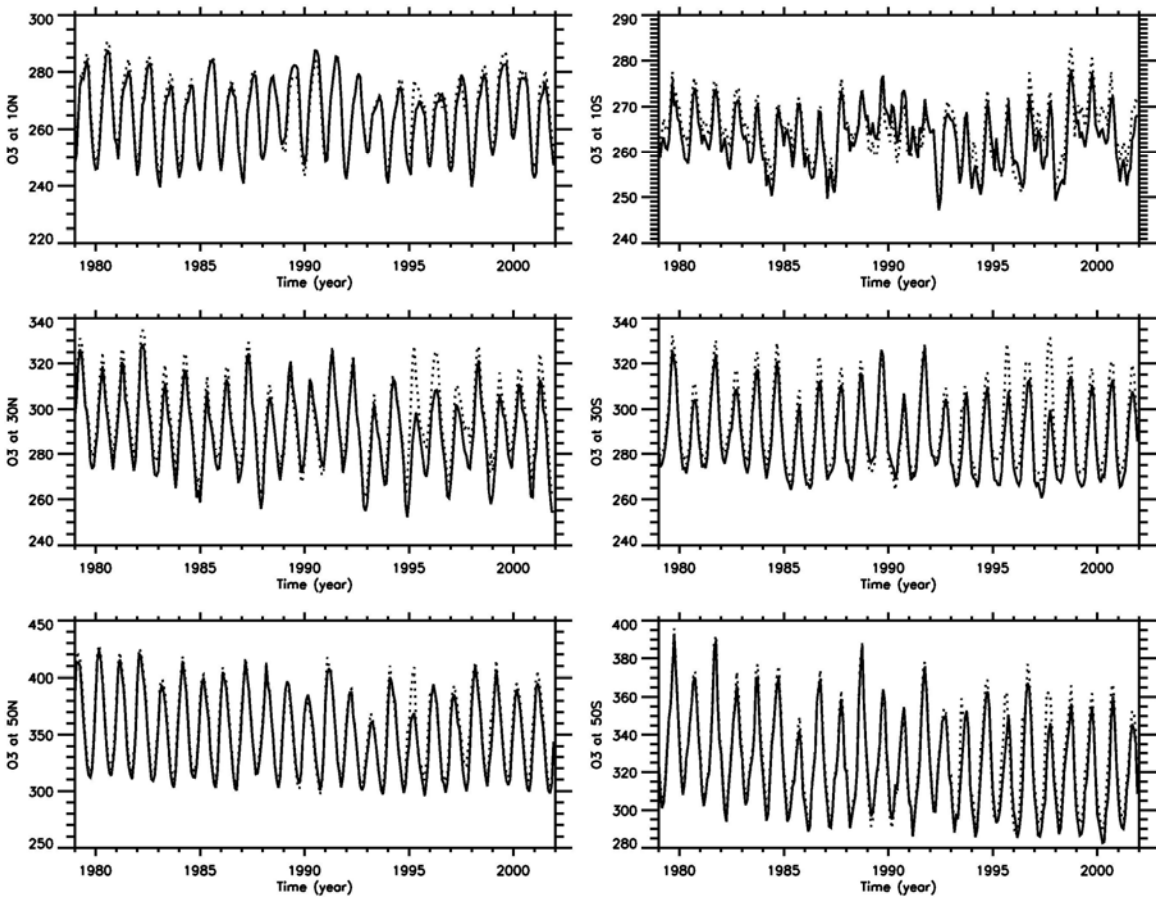

Figure 3.12: Comparison of the ECMWF O_3 (Dotted) with MOD (Solid).

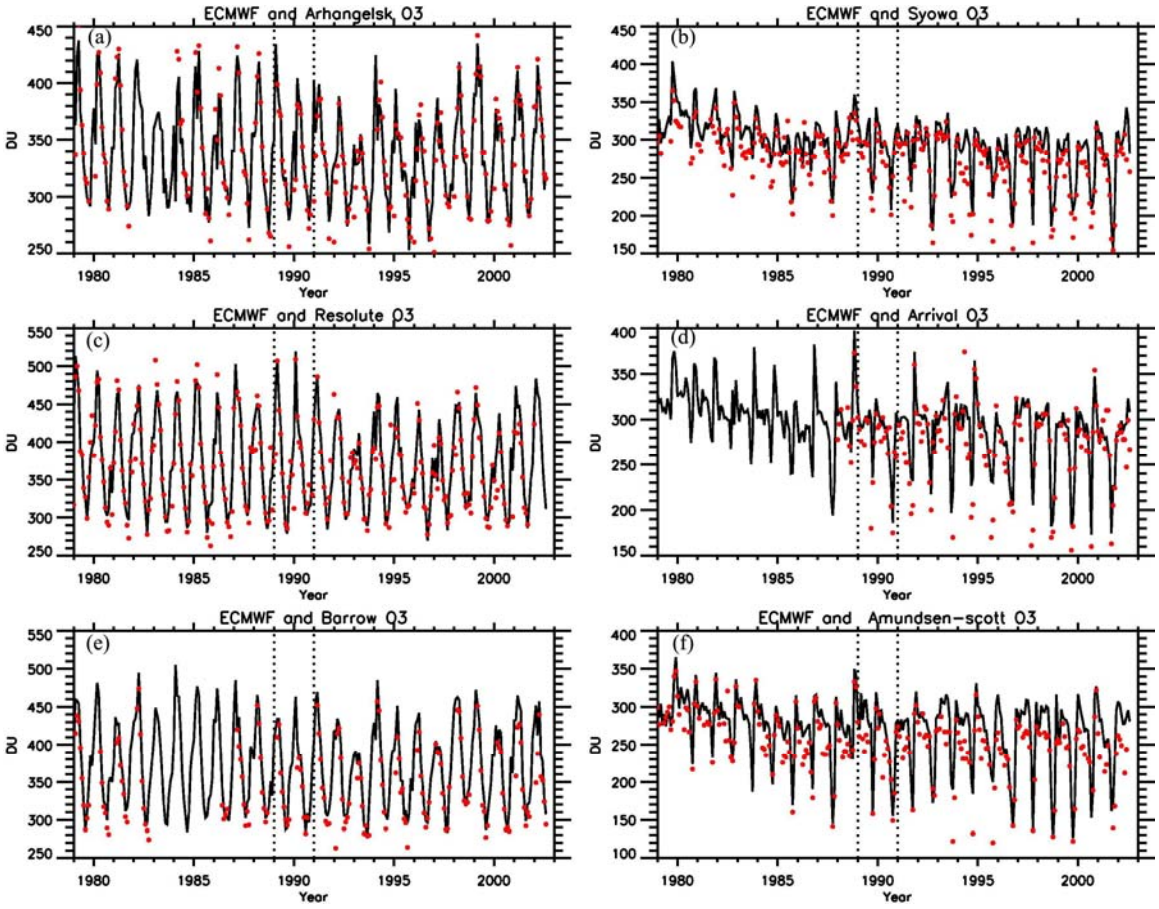

Figure 3.13: Comparison of the combined MOD and ECMWF assimilated O_3 (Solid) with the radiosonde ozone data (Red Dots) in the polar region. Arhangelsk O_3 is at 64.58° N, 40.5° E. Resolute O_3 is at 74.72° N, 94.98° W. Barrow O_3 is at 71.32° N, 156.6° W. Syowa O_3 is at 69° S, 39.58° E. Arrival O_3 is at 77.83° S, 166.67° E. Amudsen-scott O_3 is at 89.98° S, 24.8° W.

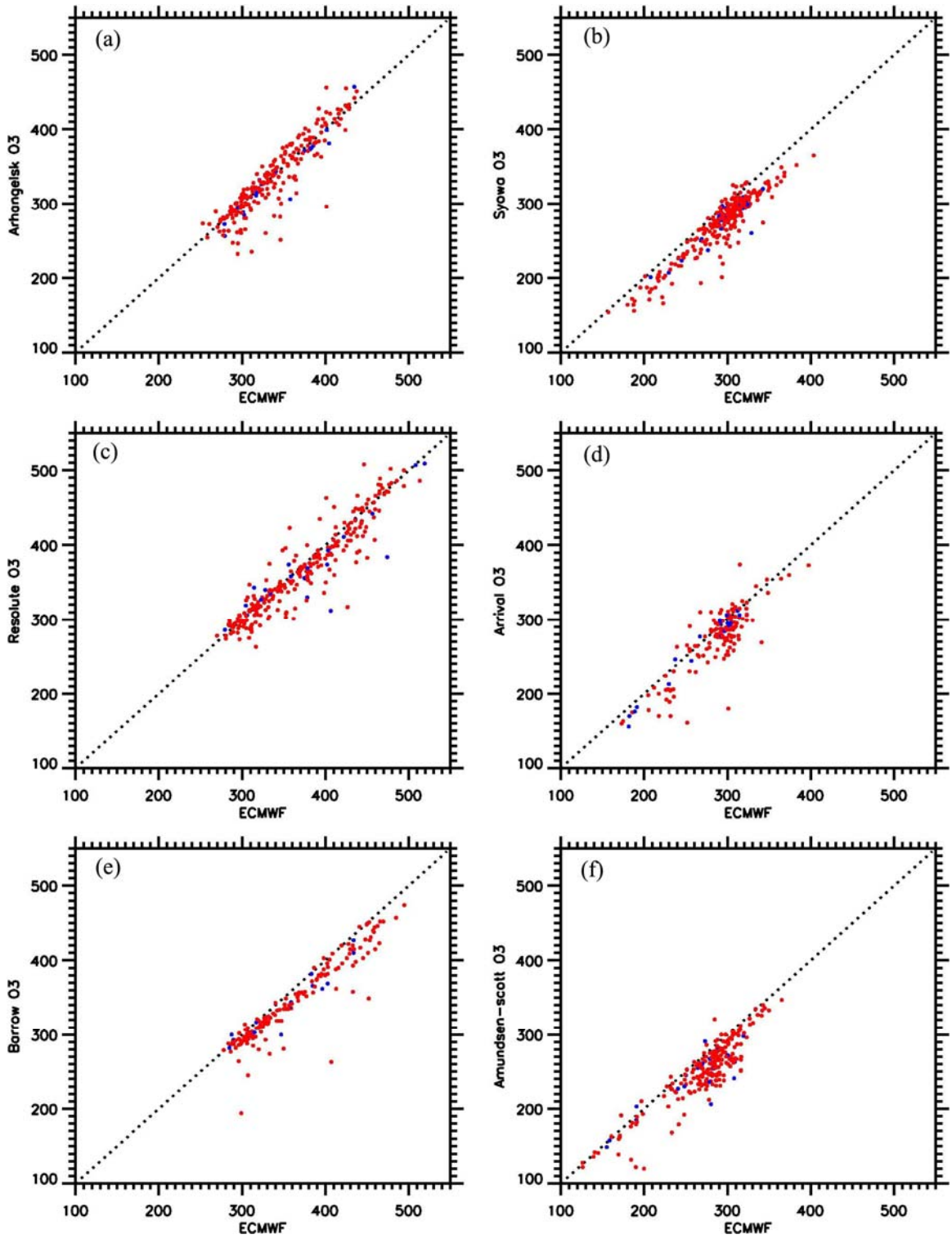

Figure 3.14: The combined MOD and ECMWF assimilated O_3 versus the radiosonde ozone data in the polar region. The blue dots are the data in 1989 and 1990. The slope of the dotted line is 1.

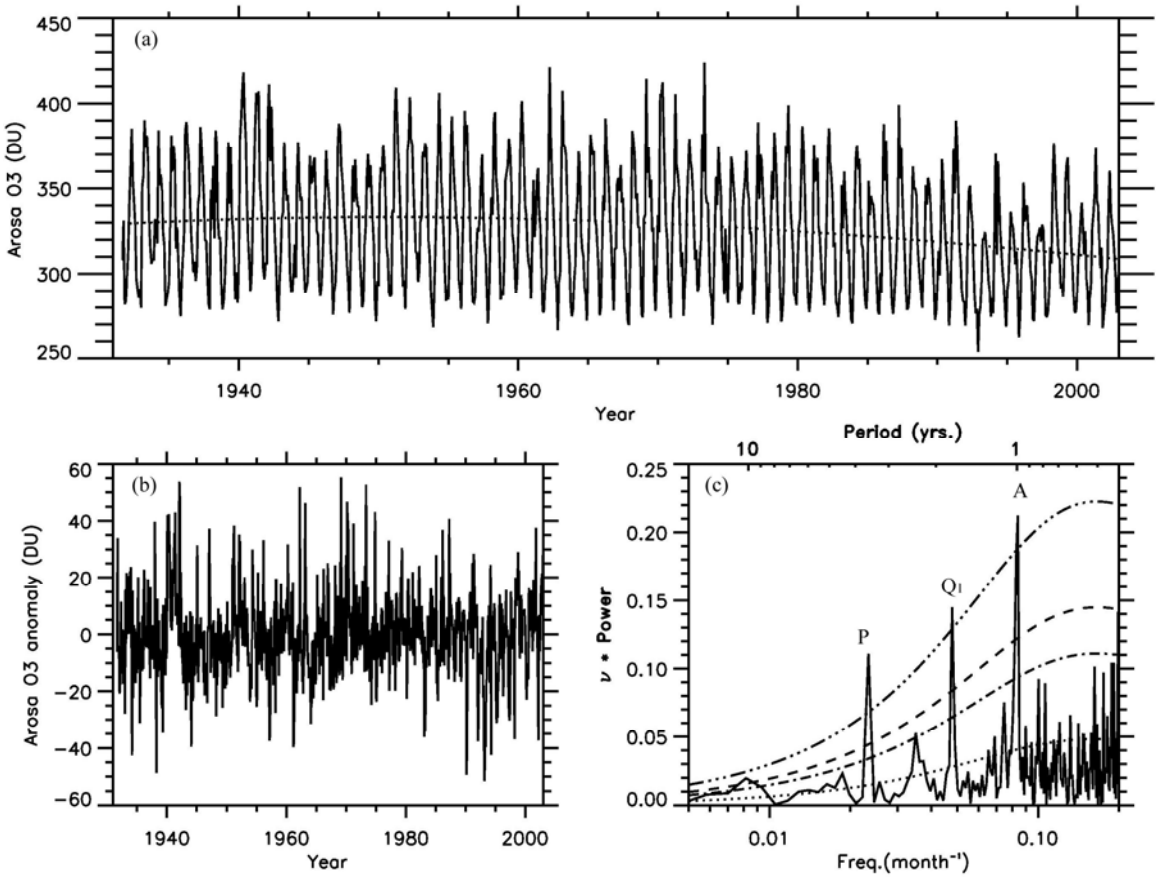

Figure 3.15: (a) Arosa O_3 (Solid) from Aug 1931 to Dec 2002 and trend (Dotted). Units are DU. (b) Deseasonalized and detrended Arosa O_3 anomaly from Aug 1931 to Dec 2002. Units are DU. (c) Power spectrum of deseasonalized and detrended Arosa O_3 anomaly (Solid), red noise spectrum (Dotted), 10%, 5%, and 1% significance level (Dashed). Arosa O_3 is at 46.8° N, 9.7° E.

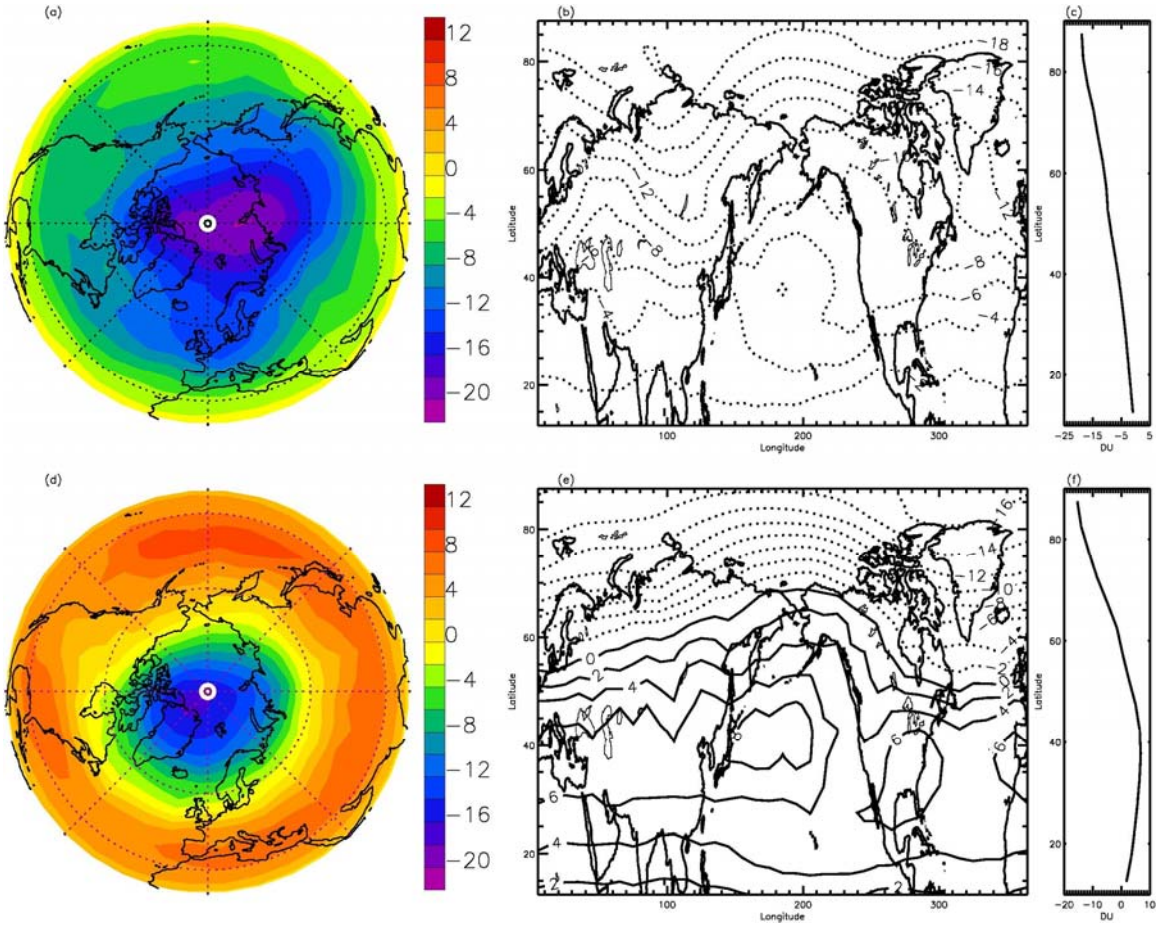

Figure 3.16: The first and second modes of the combined MOD and ECMWF O_3 anomalies in the NH. (a), (d) polar projection maps; (b), (e) cylindrical projection maps; (c), (f) meridional profile of zonally averaged modes.

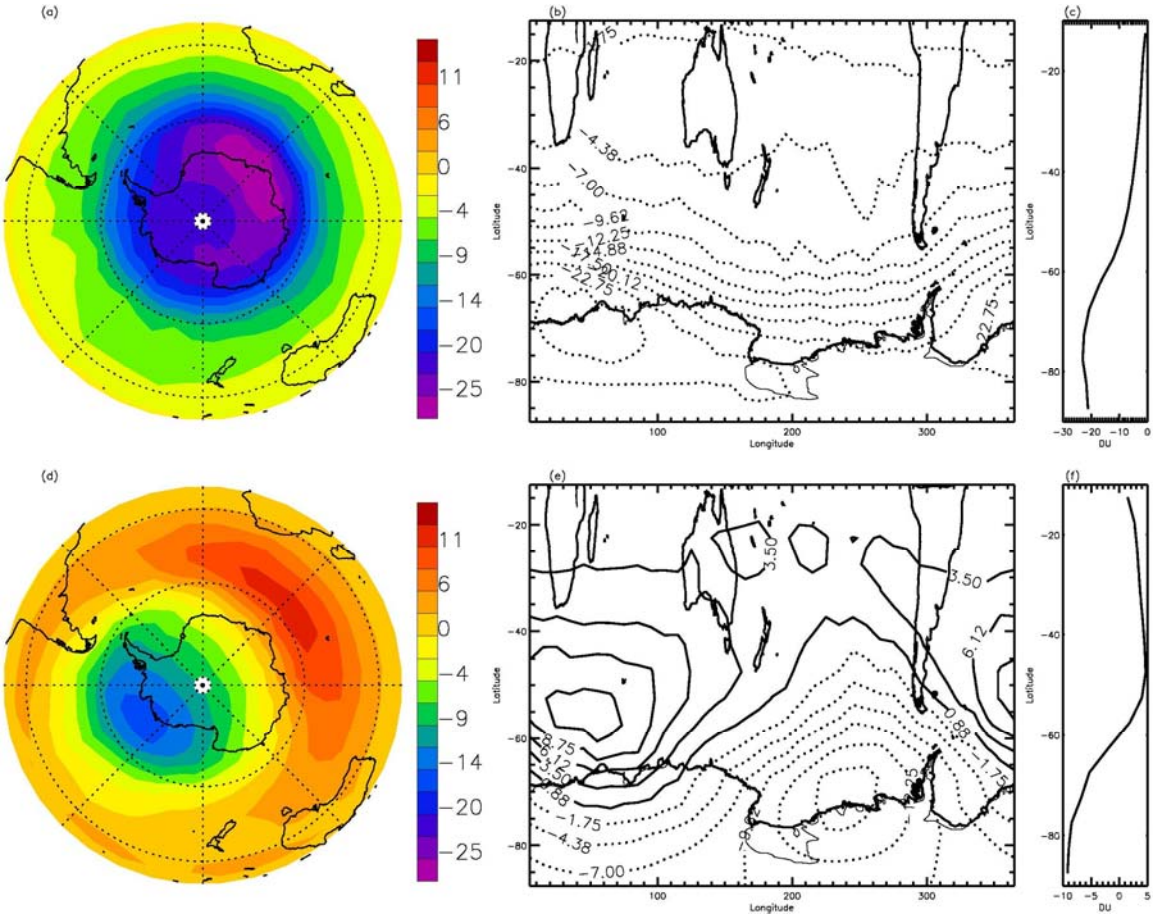

Figure 3.17: The first and second modes of the combined MOD and ECMWF O_3 anomalies in the SH. (a), (d) polar projection maps; (b), (e) cylindrical projection maps; (c), (f) meridional profile of zonally averaged modes.

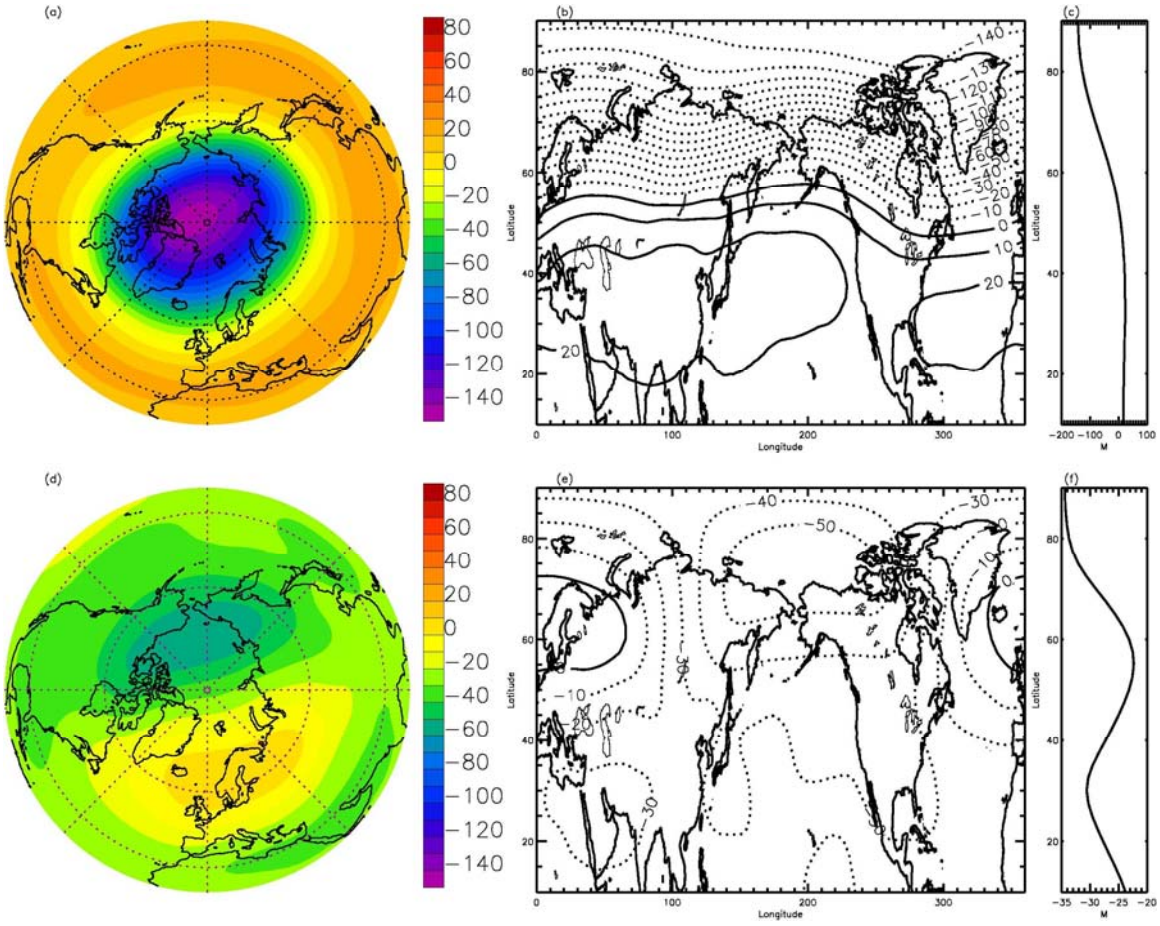

Figure 3.18: The first and second modes of the 30 hPa to 100 hPa layer thickness anomalies in the NH. (a), (d) polar projection maps; (b), (e) cylindrical projection maps; (c), (f) meridional profile of zonally averaged modes.

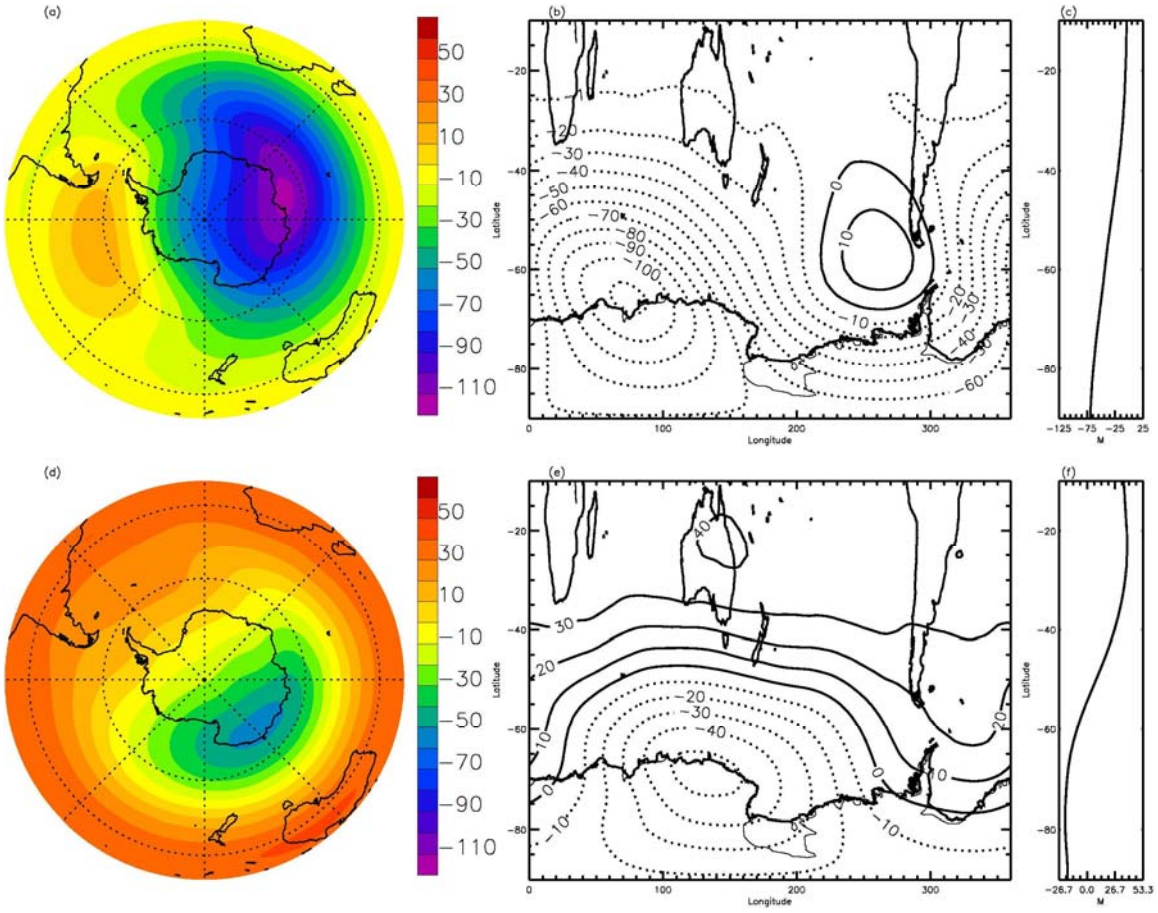

Fig. 3.19: The first and second modes of the 30 hPa to 100 hPa layer thickness anomalies in the SH. (a), (d) polar projection maps; (b), (e) cylindrical projection maps; (c), (f) meridional profile of zonally averaged modes.

Chapter 4: El Niño-Southern Oscillation in Tropical Stratospheric Ozone

4.1 Abstract

We apply principal component analysis (PCA) to the stratospheric column ozone and tropopause pressure simulated by the Goddard Earth Observation System, Version 4 (GEOS-4) chemistry-climate model (CCM) from January 1951 to December 2004 in the tropics. The model was forced by observed sea surface temperature and sea ice at the surface. The first mode for the stratospheric column ozone, capturing 65.8% of the total variance, is related to the El Niño-Southern Oscillation (ENSO). The spatial pattern of the first mode is similar to the ENSO signal in the column ozone observed by Total Ozone Mapping Spectrometer (TOMS) instrument from Nov 1978 to Apr 1993. However, there are some discrepancies for the model ozone in the southern hemisphere. There is also a clear ENSO signal in the tropical tropopause in the chemistry-climate model, which may be the cause for the ENSO signal in the stratospheric ozone.

4.2 Introduction

El Niño corresponds to times when sea surface temperature (SST) anomalies in the Niño-3 region (5º N-5º S, 150º-190º W) exceed 0.5 ºC or when SST anomalies in the Niño-3.4 region (5º N-5º S, 170º-120º W) exceed 0.4 ºC [*Trenberth*, 1997]. The atmospheric component tied to El Niño is called "Southern Oscillation". The phenomenon where the atmosphere and ocean are coupled together is referred as The El Niño-Southern Oscillation (ENSO). In the El Niño event, there are warm SST anomalies in the central and eastern equatorial Pacific and along the coast of South America [*Bjerknes*, 1966; *Quinn et al*., 1978]. Associated with it, it will lead to a larger seesaw of sea level pressure between the eastern and western tropical Pacific [*Walker and Bliss*, 1932; *Trenberth and Shea*, 1987]. The normal easterly winds in the central equatorial Pacific will become weaker [*Brooks and Braby*, 1921; *Harrison and Giese*, 1991]. There will be an eastward shift of the deep atmospheric convection and rainfall into the central tropical Pacific [*Rasmusson and Wallace*, 1983].

In addition to influence the SST, surface pressure, winds, and convection, ENSO will also influence the column ozone abundance. *Bojkov* [1987] first found low column ozone anomalies in the middle and high latitudes within a few months after the El Niño episodes. *Shiotani* [1992] studied the asymmetric ENSO signal in column ozone by removing the zonal means. *Kayano* [1997] carried out an empirical orthogonal function (EOF) study of the ozone between 70º N and 70º S; and found that the first two modes are related to ENSO. Recently, *Camp et al*. [2003] used the column ozone observed by Total Ozone Mapping Spectrometer (TOMS) and revealed that there is ENSO signal in

the fourth mode of the column ozone in the tropical region. For the El Niño periods, there are negative column ozone anomalies in the eastern tropical Pacific and positive ozone anomalies in the western Pacific. The influence of ENSO on column ozone can be mostly explained by the variation of tropopause height caused by convections [*Schubert and Munteanu*, 1988; *Shiotani*, 1992; *Hasebe*, 1993].

In this paper, we will investigate the ENSO signal in the tropopause pressure and stratospheric column ozone simulated by the Goddard Earth Observation System, Version 4 (GEOS-4) chemistry-climate model (CCM).

4.3 GEOS-4 Chemistry-climate Model

The GEOS-4 general circulation model includes: version3 of the Community Climate Model (CCM3) with the addition of a finite-volume dynamical core; version 2 of the Community Land Model (CLM2); the Physical-space Statistical Analysis System (PSAS); and an interactive retrieval system (iRET) for assimilating TOVS radiance data [*Bloom et al.*, 2005]. The chemistry module [*Douglass et al*., 2003; *Stolarski et al*., 2006] is implemented on-line in the general circulation model, with feedback of O_3, H_2O, CO_2, CH_4, N_2O, CFC-11, and CFC-12 into the radiation module. At the lower boundary, sea surface temperature and sea ice are prescribed from observations compiled by *Rayner et al*. [2003], along with time-dependent World Meteorological Organization/United Nations Environment Programme (WMO/UNEP) and Intergovernmental Panel on Climate Change/Special Report on Emissions Scenarios (IPCC/SRES) surface mixing ratios for chemically active and greenhouse gases. The model was run for 55 years (1951-

2004) at 2º× 2.5º (latitude by longitude) with 55 layers between the surface and about 80km. Neither the solar cycle nor volcanic aerosol variations were included in the model and it does not capture a QBO (see *Horinouchi et al.*, 2003), so these sources of ozone variability are all absent from the simulation. The results from the GEOS-4 CCM are from Jan 1951 to Dec 2004.

4.4 ENSO Signals in Sea Surface Temperature and TOMS Column Ozone

The National Oceanic and Atmospheric Administration (NOAA) extended reconstructed sea surface temperature are used in this study, which is a similar SST data used to force the GEOS-4 chemistry-climate model. The data sets are monthly mean data constructed using the most recently available comprehensive ocean-atmosphere data set (COADS). The data are provided by the NOAA-CIRES climate diagnostics center. For comparison to the results from ozone and tropopause height, we choose the data from Jan 1951 to Dec 2004.

The mean annual cycle is determined by evaluating the mean value for each month independently. We remove the annual cycle and linear trend from the SST. Then to isolate the interannual variability (IAV) from higher frequency oscillations, a spectral filter is applied to the SST anomaly. The filter is constructed to obtain a full signal from periods above 15 months and no signal from periods below 12.5 months. This filter will be used for all data in this chapter hereafter. Principal component analysis (PCA) [*Preisendorfer,* 1988] is then performed on the filtered SST anomaly.

The first mode of the SST captures about 48.8% of the total variance. The spatial pattern, shown in Fig. 4.1a, reveals the structure related to the ENSO; which is similar to the spatial pattern in *Trenberth et al*. [2002]. For negative amplitudes of this mode, which correspond to the El Niño events, there are warm temperature anomalies in the central and eastern Pacific and cold temperature anomalies in the western Pacific. As a result, the convection will move eastward to the central Pacific. PC1 of the SST (solid line) is plotted against the lowpass filtered SOI index (dotted line) in Fig. 4.1b. The SOI index is defined as the sea level pressure anomaly between Tahiti and Darwin. The same lowpass filter is also applied the SOI index. PC1 of the SST correlates well with the lowpass filtered SOI index. The correlation coefficient and significance level between the two time series is 0.88 (0.1%), and are listed in Table 4.1. The power spectrum of PC1 for SST, shown in Fig. 4.1c, reveals peaks around 4-5 years.

Camp et al. [2003] had applied PCA to the detrended, lowpass-filtered column ozone data by Total Ozone Mapping Spectrometer (TOMS) instrument from Nov 1978 to Apr 1993. They found an ENSO signal in the fourth mode of column ozone, which is shown in Fig. 4.2a in this chapter. PC4 (solid line) is plotted along with SOI index (dotted line) and PC1 of SST (dashed line) in Fig. 4.2b. It correlates well with the other two indices. The power spectrum of PC4 for TOMS ozone reveals peaks at 2-6 years.

4.5 PCA of Tropopause Pressure and Stratospheric Column Ozone

Similarly, we apply the PCA to the detrended, deseasonalized, and lowpass-filtered tropopause pressure from the GEOS-4 chemistry-climate model in the tropical

region. The first mode of the tropopause pressure captures about 33.9% of the total variance. The spatial pattern is shown in Fig. 4.3a. For the negative amplitudes of this mode, corresponding to El Niño events, there are low-pressure anomalies in the central and eastern Pacific as a result of the warmer surface temperature, and high-pressure anomalies in the western Pacific. In the positive amplitude of this mode, La Niña events, there are low-pressure anomalies in the western Pacific and high-pressure anomalies in the central and eastern Pacific.

PC1 of the tropopause pressure (solid line) is plotted against the lowpass filtered SOI index (Dotted line) and PC1 for SST (dashed line) in Fig. 4.3b. PC1 for the tropopause pressure correlates well with the other two indices. The correlation coefficients and significance levels between the three time series are listed in Table 4.1. In the El Niño year, negative SOI and PC1, there is increased convection in the central Pacific, which will raise the tropopause pressure. In the La Niña year, the condition is opposite. The power spectrum for the PC1 of the tropopause pressure reveals peak around 17 months and 5 years.

Finally, we apply the PCA to the detrended, deseasonalized, and lowpass-filtered stratospheric column ozone from GEOS-4 chemistry-climate model. The first mode of the stratospheric column ozone captures about 65.8% of the total variance. The spatial pattern, shown in Fig. 4.4a, reveals the structure related to the ENSO. It is very similar to the ENSO spatial pattern in the TOMS column ozone data in *Camp et al*. [2003], although there are some discrepancies in the southern hemisphere. There is a double-

ridged symmetric structure with ridges at 15º N, 10º S. The value is relatively low in the western Pacific; and relatively high in the eastern Pacific. Since there is no QBO and solar cycle simulated in the model, the ENSO is the dominant interannual variability (IAV) for the tropical ozone.

PC1 of the model stratospheric column ozone (solid line) is plotted against the lowpass filtered SOI index (dotted line) and PC1 of the SST (dashed line) in Fig. 4.4b. The three time series correlate well. The correlation coefficient between ozone PC1 and SOI index is 0.48 (0.1%). The correlation coefficient between ozone PC1 and SST PC1 is 0.52 (0.1%). During El Niño years, negative SOI, warmer surface temperature in the central and eastern Pacific will raise the tropopause height. It will bring ozone-poor air from the troposphere to stratosphere. As a result, stratsospheric column ozone will decrease more in the central and eastern Pacific. During La Nina years, i.e., positive SOI, the opposite will occur, causing a relative increase in stratospheric column ozone over the central and eastern Pacific. The power spectrum for the PC1 of the model stratospheric column ozone reveals peak around 17 months and 2-5 years.

4.6 Conclusion

In this chapter, we have studied the ENSO signal in the tropical stratospheric column ozone and tropical tropopause pressure in the GEOS-4 chemistry-climate model from Jan 1951 to Dec 2004. The first modes in the model stratospheric column ozone and tropopause pressure capture 65.8% and 33.9% of the total variances, respectively. They are related to ENSO. The PC1 for the first modes in the model stratospheric column

ozone and tropopause pressure correlate well with the SOI index and leading PC time series for the SST. The spatial pattern of the first mode for the model stratospheric column ozone is similar to the ENSO signal in the TOMS column ozone, although there are some discrepancies for the ozone in the southern hemisphere. It can be improved in the future with tropospheric chemistry included in the chemical module of the GEOS-4 chemistry-climate model.

4.7 References

Bjerknes, J., A possible response of the atmospheric Hadley circulation to anomalies of ocean temperature, *Tellus, 18*, 820-829, 1966.

Bloom, S., *et al*., The Goddard Earth Observation System Data Assimilation System, GEOS DAS Version 4.0.3: Documentation and Validation, NASA TM-2005-104606, *26*, 166pp, 2005.

Bojkov, R.D., The 1983 and 1985 anomalies in ozone distribution in perspective, *Mon. Weather Rev*., *115*, 2187-2201, 1987.

Brooks, C.E.P., and H.W. Braby, The clash of the trades in the Pacific, *Q. J. R. Meteorol. Soc.*, *47*, 1-13, 1921.

Camp, C.D., M.S. Roulston, and Y.L. Yung, Temporal and Spatial Patterns of the Interannual Variability of Total Ozone in the Tropics, *Journal of Geophysical Research-Atmospheres*, *108* (D20), art. no. 4643, 2003.

Devore, J. L., *Probability and Statistics for Engineering and the Sciences*, 1st ed., 640 pp., Brooks/Cole, Monterey, Calif., 1982.

Douglass, A. R., *et al*., Evaluation of transport in the lower tropical stratosphere in a global chemistry and transport model, *Journal of Geophysical Research-Atmospheres*, *108*, 2003.

Harrison, D.E., and B.S. Giese, Episodes of surface westerly winds as observed from islands in the western tropical Pacific, J. *Geophys. Res., 96 suppl*., 3221-3237, 1991.

Hasebe, F., A global analysis of the fluctuations in total ozone, II, Non-stationary annual oscillation, quasi-biennial oscillation, and long-term variations in total ozone, *J. Meteorol. Soc., Jpn*, *58*, 104-117, 1980.

Horinouchi, T., S. Pawson, K. Shibata, U. Langematz, E. Manzini, M.A. Giorgetta, F. Sassi, R.J. Wilson, K.P. Hamilton, J. de Grandpré, A.A. Scaife, Tropical Cumulus Convection and Upward Propagating Waves in Middle Atmospheric GCMs, *Journal of the Atmospheric Sciences, 60*, 2765-2782, 2003.

Kayano, M.T., Principal modes of the total ozone on the Southern Oscillation timescale and related temperature variations, *J. Geophys. Res*., *102* (D22), 25797-25806, 1997.

Preisendorfer, R. W. *Principal component analysis in meteorology and oceanography*. Elsevier Science, 425 pp**,** 1988.

Press, W., S. Teukolsky, W. Vetterling, and B. Flannery, *Numerical Recipes in Fortran 77: The Art of Scientific Computing*, 933 pp., Cambridge Univ. Press, New York, 1992.

Quinn, W.H., et al., Historical trends and statistics of the Southern Oscillation, El Niño, and Indonesian droughts, *Fish. Bull*., *76*, 663-678, 1978.

Rasmusson, E.M., and J.M. Wallace, Meteorological aspects of the El Niño/Southern Oscillation, *Sicence*, *220*, 1195-1202, 1983.

Rayner, N. A., *et al*., Global analyses of sea surface temperature, sea ice, and night marine air temperature since the late nineteenth century, *Journal of Geophysical Research-Atmospheres*, *108*, 2003.

Schubert, S.D., and M.J. Munteanu, An analysis of tropopause pressure and total ozone correlations, *Mon. Weather Rev*., 116, 569-582, 1988.

Shiotani, M., Annual, quasi-biennial, and El Niño-Southern Oscillation (ENSO) timescale variations in equatorial total ozone, *J. Geophys. Res*., *97* (D7), 7625-7633, 1992.

Stolarski, R.S., A.R. Douglass, S.E. Steenrod, S. Pawson, Trends in Stratospheric Ozone: Lessons Learned from a 3D Chemical Transport Model, *Journal of the Atmospheric Sciences, 63,* 1028-1041, 2006.

Trenberth, K.E., and D. Shea, On the evolution of the Southern Oscillation, *Mon. Weather Rev*., *112*, 326-332, 1987.

Trenberth, K.E., The definition of El Niño, *Bull. Amer. Meteor. Soc*., *78*, 2771-2777, 1997.

Trenberth, K.E., J.M. Caron, D.P. Stepaniak, and S. Worley, Evolution of El Niño-Southern Oscillation and global atmospheric surface temperatures, *J. Geophys. Res*., *107* (D8), doi: 10.1029/2000JD000298, 2002.

Walker, G.T., and E.W. Bliss, World weather, V, *Mem. R. Meteorol. Soc*., *4*, 53-84, 1932.

Table 4.1: Correlations (Lag = 0) of the sea Surface Temperature, Tropopause Pressure, and Column Ozone PCs with SOI Indices. The numbers in parentheses denote significance levels.

		SOI	PC1 of SST
Sea Surface Temperature	PC1	0.88 (0.1%)	
TOMS Column Ozone	PC4	0.73 (0.3%)	0.74 (0.3%)
Model Tropopause Pressure	PC1	0.64 (0.1%)	0.72 (0.1%)
Model Stratospheric Column Ozone	PC1	0.48 (0.1%)	0.52 (0.1%)

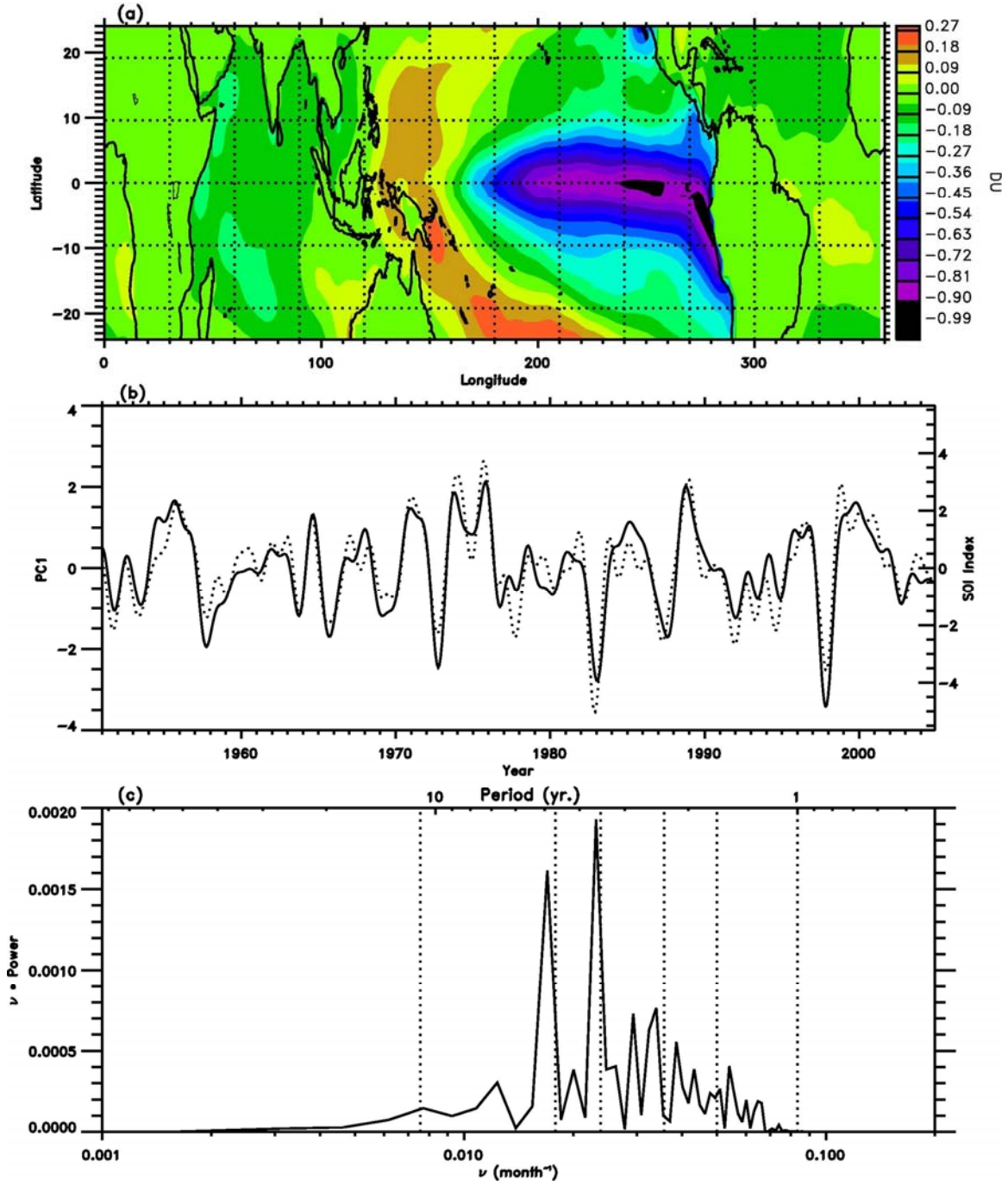

Figure 4.1: (a) The spatial pattern of the first mode for sea surface temperature in the tropics. Units are K. The first mode explains 48.8% of the total variance. (b) PC1 time series for the first mode of sea surface temperature. PC1 (solid line) is shown along with SOI index (dotted line). (c) Power spectrum of PC1.

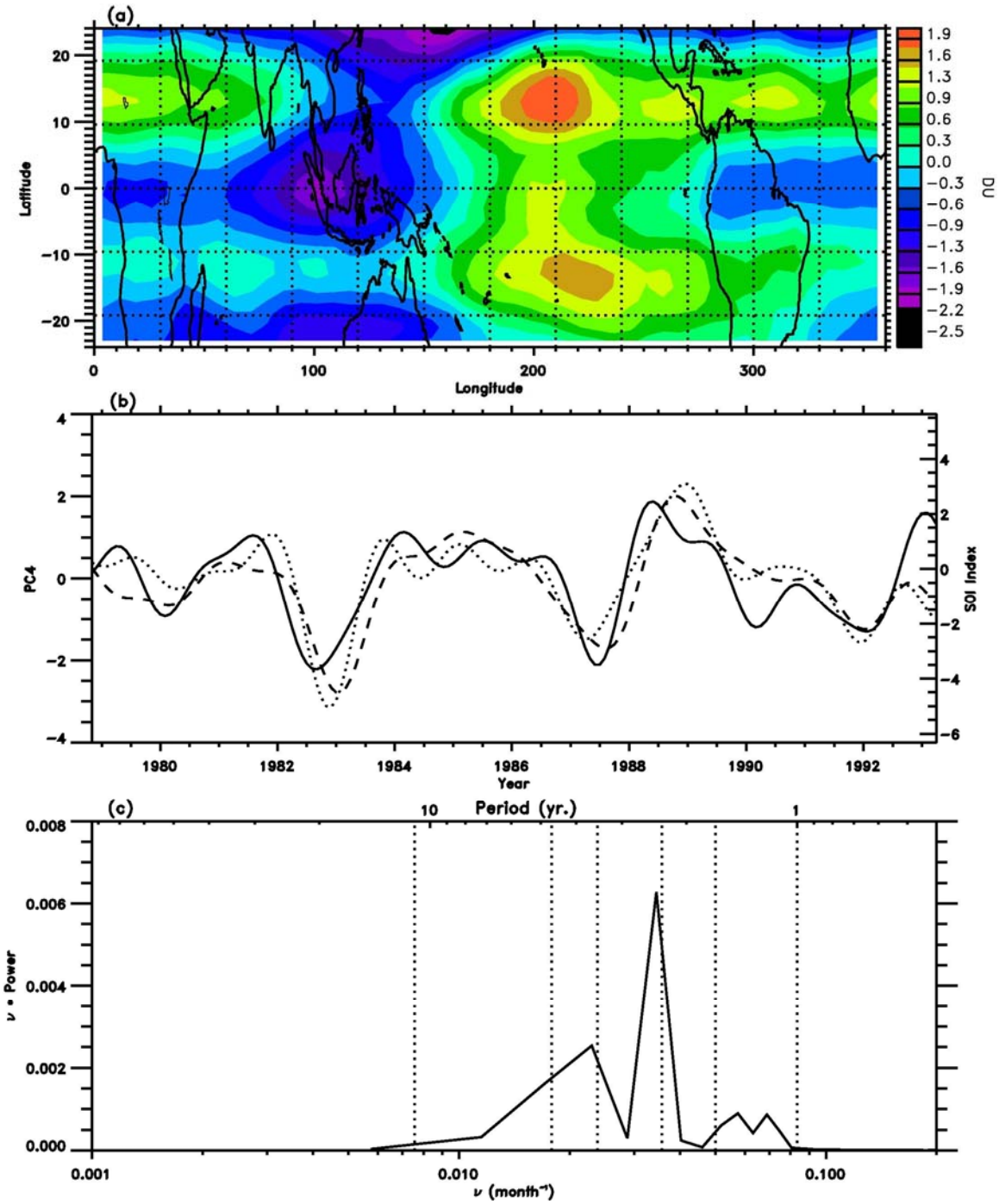

Figure 4.2: (a) The spatial pattern of the fourth mode for TOMS column ozone in the tropics. Units are DU. The fourth mode explains 3% of the total variance. (b) PC4 time series for the fourth mode of TOMS column ozone. PC4 (solid line) is shown along with SOI index (dotted line). (c) Power spectrum of PC4.

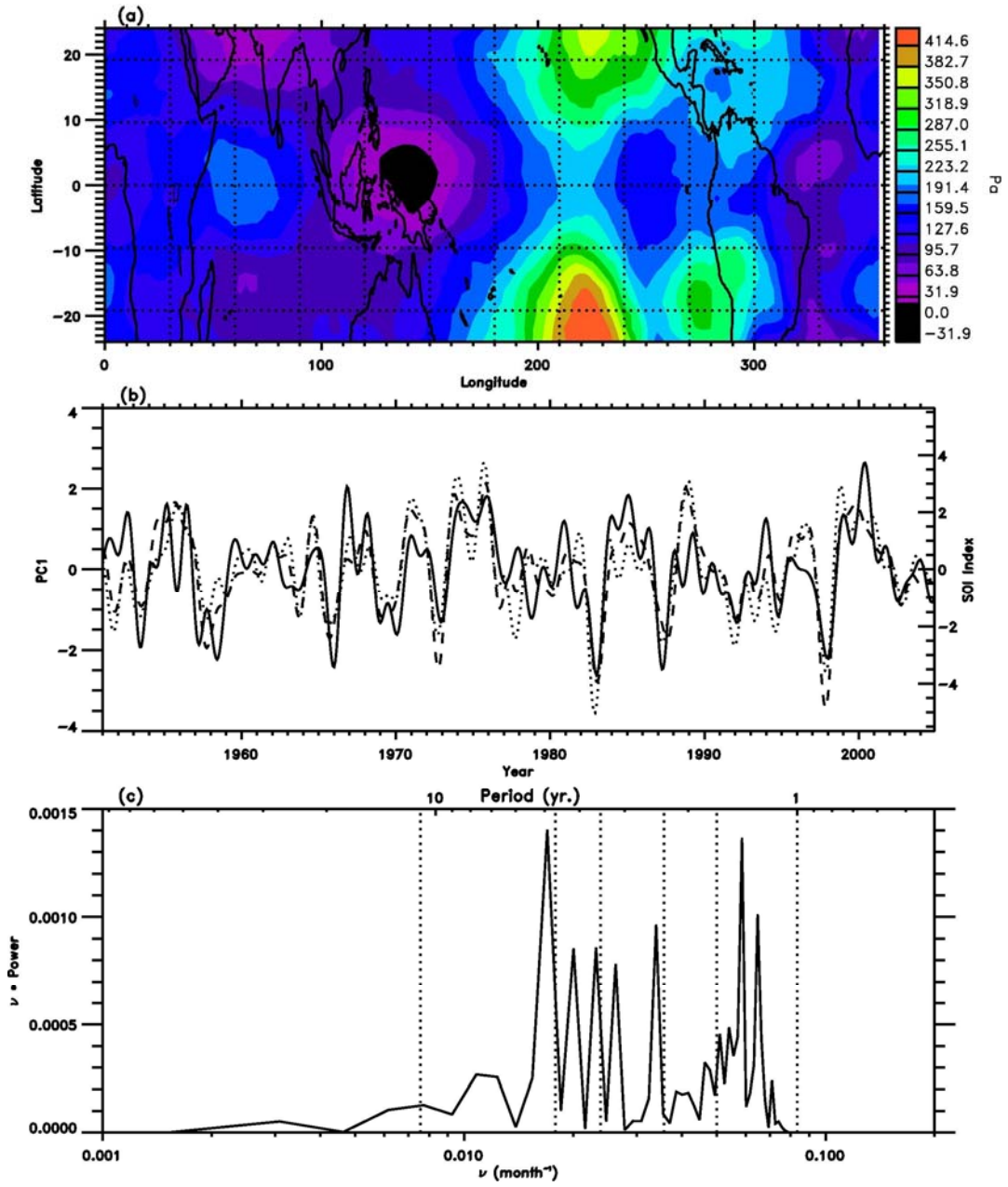

Figure 4.3: (a) The spatial pattern of the first mode for tropopause pressure from GEOS-4 chemistry-climate model in the tropics. Units are Pa. The first mode explains 33.9% of the total variance. (b) PC1 time series for the first mode of tropopause pressure. PC1 for tropopause pressure (solid line) is shown along with SOI index (dotted line) and PC1 for SST (dashed line). (c) Power spectrum of PC1.

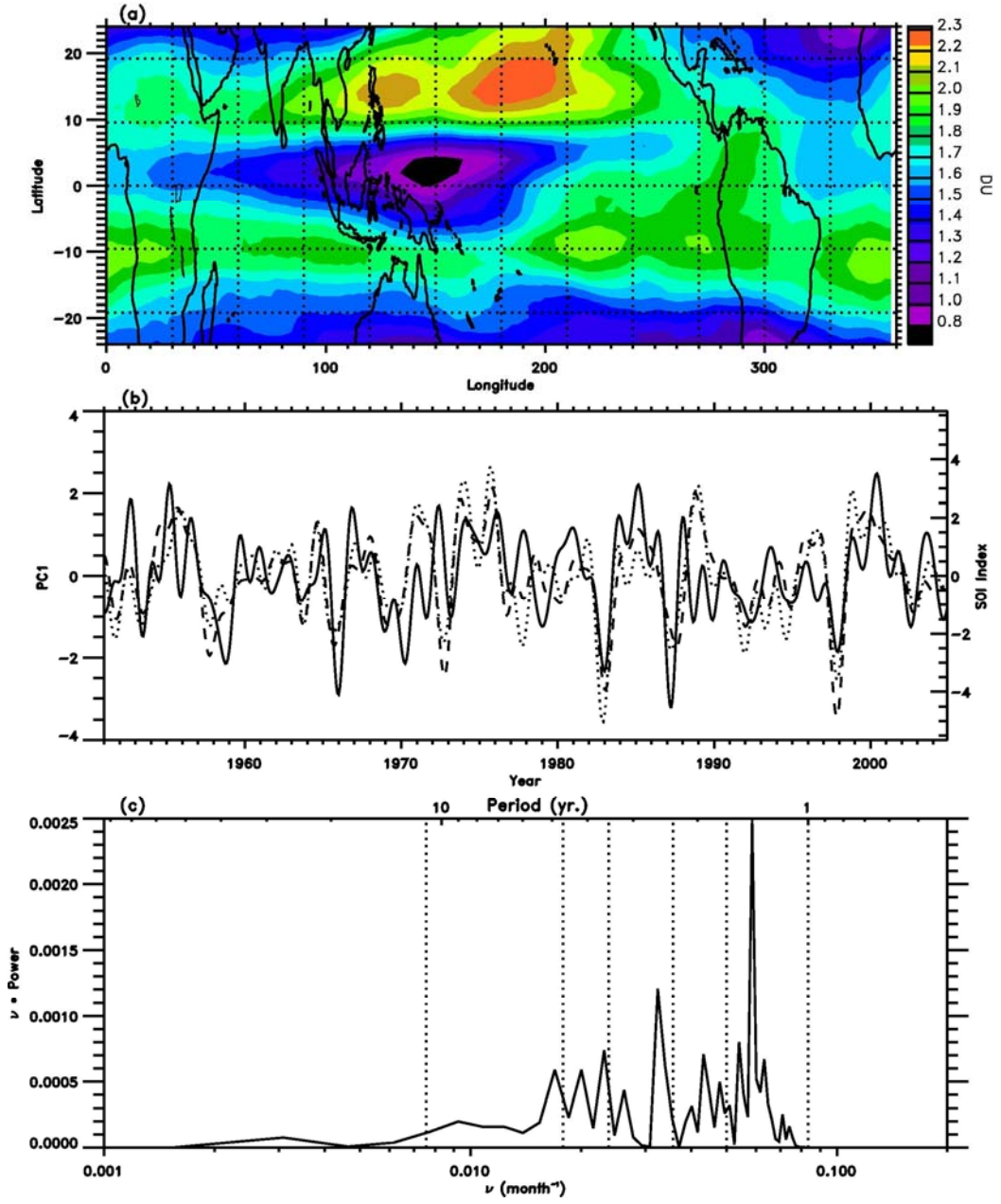

Figure 4.4: (a) The spatial pattern of the first mode for stratospheric column ozone from GEOS-4 chemistry-climate model in the tropics. Units are DU. The first mode explains 65.8% of the total variance. (b) PC1 time series for the first mode of stratospheric column ozone. PC1 for stratospheric column ozone (solid line) is shown along with SOI index (dotted line) and PC1 for SST (dashed line). (c) Power spectrum of PC1.

Chapter 5: Distinguishing Climate Change from Natural Variability in the Stratosphere

5.1 Abstract

A robust result associated with global warming of the surface and the troposphere is a concomitant cooling of the stratosphere [*Manabe and Wetheral.Rt*, 1967; *Ramaswamy, et al.*, 2001; *Ramaswamy, et al.*, 2006]. It is, however, typically very hard to separate the temperature trend due to the anthropogenic forcing from the low-frequency interannual variability (IAV). In this chapter, we apply principal component analysis (PCA) [*Camp, et al.*, 2003; *Preisendorfer*, 1988] to observations and global climate model simulations to investigate the variability of stratospheric temperature. We reveal that most (~76%) of the IAV of temperature in the northern hemisphere can be characterized by the first four principal modes. The cooling trend in the stratosphere is associated with a spatially uniform pattern of stratospheric variability, which is isolated from more common modes of natural IAV such as the Northern Annular Mode (NAM). These results are supported by a number of coupled ocean-atmosphere climate model simulations of the 20th century that were contributed to the International Panel on Climate Change's 4th Assessment Report. Given the spatial uniformity of the increased GHG forcing, this separation and identification of a spatially uniform stratospheric temperature response is not only plausible but might be expected; and provides a simple, yet useful, test for global climate models used for projecting global warming.

5.2 Stratospheric Temperature Interannual Variability in NCEP

To extract the spatio-temporal patterns of stratospheric temperature IAV, we apply PCA to the deseasonalized and area-weighted monthly mean temperature data (Ω) at 50 hPa from Jan 1958 to Dec 1999, on a $2^\circ \times 2^\circ$ latitude-longitude grid from 10° to 90° N. The data from Jan 1958 to Dec 1999 are from NCEP/NCAR Reanalysis* [*Kalnay, et al.*, 1996; *Kistler, et al.*, 2001]. The data are considered to represent the observed variability. Seasonal cycles for each time series are removed; cycles are determined by taking averages for each month independently. The deseasonalized and area weighted temperature anomaly can be represented as:

$$\Omega(t, \theta, \varphi) = \Sigma\, p_i(t) e_i(\theta, \varphi)$$

where t = time, θ = latitude, φ = longitude, $p_i = i^{th}$ time principal component (PC), $e_i = i^{th}$ spatial empirical orthogonal function (EOF), and the summation is over all the eigenfunctions with eigenvalues arranged in descending order of explained variance.

The first four leading modes account for 34.2, 16.9, 14.1 and 10.6% of the total variance, respectively. Together, they account for ~76% of the total variance of temperature anomalies. The spatial patterns of the first four leading modes are shown in Fig. 5.1. The first mode is zonally symmetric. It is negative in the polar region, and positive in the mid-latitude and tropics, with a node about 50° N. This mode can be attributed to the NAM [*Thompson and Wallace*, 1998]. The second mode is nearly

* The data from Jan 1958 to Dec 1978 are from National Centers for Environmental Prediction/National Center for Atmospheric Research (NCEP/NCAR) Reanalysis (NCEP1). The data from Jan 1979 to Dec 1999 are taken from NCEP/Department of Energy Reanalysis 2 (NCEP2). We obtain the same qualitative result if we only use NCEP1 data for the whole period. Similar results are obtained for the 50 hPa monthly mean temperature for the whole period from the European Centre for Medium-Range Weather Forecasts (ECMWF), which has a higher model top at 0.1 hPa. Data are available on a $2.5^\circ \times 2.5^\circ$ latitude-longitude grid (http://data.ecmwf.int/data/d/era40/).

uniform in sign over the whole region. It has a minimum value around –1 K that extends over most of the Northern Hemisphere (NH) and a weak maximum of about ~0.12 K centered over the Northern Atlantic Ocean. The third and fourth modes are zonally asymmetric. Their eigenvalues are similar and their patterns exhibit a wavenumber-1 distribution in quadrature. Physically, this pair of modes represents the wobbling and displacement of the polar vortex in response to planetary waves [*Jiang*, 2005].

Further insights into the first four modes are gained by an examination of the temporal signature in the PCs. The temporal behavior of PC_1 in the NH is shown in Fig. 5.2a. The correlation coefficient between the detrended PC_1 and the detrended 50 hPa NAM index, defined as the leading PC for the geopotential height at 50 hPa [*Baldwin and Dunkerton*, 1999], is 0.86, which is significant at a 0.1% significance level. The power spectrum of the detrended PC_1 reveals a significant peak around 28 months, which represents the Quasi-Biennial Oscillation (QBO) influence on the polar vortex [*Baldwin, et al.*, 2001]. The statistical significance of signals in the power spectrum is based on comparisons to a red noise spectrum [*Gilman, et al.*, 1963] with 10%, 5%, and 1% significance levels derived from F-statistics. The outstanding feature of PC_2, shown in Fig. 5.2c, is its trend of 0.55 ± 0.14 /decade. The product of the PC_2 time series with the EOF pattern in Fig. 5.1b represents the 50 hPa temperature trend over the latter half of the 20^{th} century, which amounts to about –2 K. In addition, the power spectrum of the detrended PC_2 has a significant peak at two years, which is the Biennial Oscillation (BO) [*Baldwin and Dunkerton*, 1998]. The power spectra of PC_3 and PC_4 reveal mostly high frequency signals and some weak decadal variability. The results of the above analysis

indicate that the observed negative trend in 50 hPa temperature is primarily captured by the second mode.

We have separated the temperature trend from the natural variability of the atmosphere, and in so doing, illustrated that the cooling trend is not associated with secular changes in the variability of the NAM pattern but rather associated with a more spatially uniform pattern of variability. The physical reason is similar to that discovered for the decomposition of the variability of ozone column abundance in the tropics [*Camp, et al.*, 2003], namely that the physical processes that control IAV in the stratosphere exhibit different symmetry properties, thus allowing their separation. The first (NAM) mode is zonally symmetric and restricted to the polar region. It has a node around 50° N. The second (cooling) mode is nearly zonally symmetric, but being primarily global it does not exhibit a node. The other two modes exhibit a wavenumber-1 structure and are asymmetric, making them orthogonal to the first two symmetric modes. Thus, the intrinsic symmetry properties of stratospheric temperature allow the separation of the cooling mode (~16% of the variance) from the natural variability (sum of modes 1, 3 and 4 = 59% of the variance). As a result, the statistical significance of the temperature trend based on our method is 3-σ, whereas more conventional methods that do not discriminate between trend and natural variability [*Ramaswamy, et al.*, 2001] produce trend results with only 1-σ significance.

5.3 Stratospheric Temperature Interannual Variability in Model Simulations

To more thoroughly scrutinize and understand the trend and associated pattern in

the observed temperature record, PCA had been applied to the 50 hPa, deseasonalized, and area weighted temperature data from five models contributing 20th century simulations for the Intergovernmental Panel on Climate Change (IPCC) 4th Assessment Report. These include simulations from the GFDL, UKMO, GISS, MPI, and NCAR models. The details and the vertical levels for the different models are listed in Table 5.1 in the appendix. Results from PCA applied to the models' stratospheric temperature variability are not readily comparable to those of the observed variability, particularly on a mode-by-mode basis, due to the differences in the model representations of the variability and how this variability projects onto a given model's individual PCA. However, through the use of the Procrustes Target Rotation (PTR), it is possible to linearly transform the EOF loadings into a set of loadings that are as much like a target matrix as possible – in this case is the EOFs of the NCEP/NCAR temperature data. PTR is accomplished by a least-squares fit of the loading matrix to a target matrix [*Richman and Easterling*, 1988]. In this case, we chose the first four EOFs from NCEP/NCAR 50 hPa temperature anomaly as the target matrix. Then we applied the PTR analysis on the first ten PCA modes of each model to construct the closest possible analog to the observed PCA structure. This procedure essentially projects the models' variability onto the PCA basis structure derived from the observations.

The variances for the rotated EOF (REOF) of the five models along with those from NCEP/NCAR are shown in Fig. 5.3 and Table 5.2 in the appendix. The first mode of NCEP/NCAR captures 34.2% of the total variance, while the corresponding modes in the five models account for 24.3%, 22.5%, 23.3%, 19.7%, 21.0% of the total variances

for GFDL, UKMO, GISS, MPI, and NCAR, respectively. While all models underestimate the variances of the first mode compared with that from NCEP/NCAR, two of the models, *i.e.*, GFDL and UKMO, exhibit a good depiction of the variance distribution among the four principal modes of variability. In this regard, they are likely producing a relatively good simulation of stratospheric temperature variability. The other three models, GISS, MPI, and NCAR, exhibit a relatively good distribution of variance between the first and second mode, but produce too much variance in the 3rd and 4th modes.

The spatial patterns of REOFs for the 50 hPa temperature anomalies for the five models are shown in the appendix from Figs. 5.5-5.9. As expected, these patterns are very similar to those derived from NCEP/NCAR. The PCs from the five models are shown in Figs. 5.10-5.17. PC_2 from NCEP/NCAR temperature data and the corresponding PCs from the five models are plotted in Fig. 5.4, Fig. 5.12a and Fig. 5.13a. Each model exhibits a positive trend in PC_2 that is statistically significant and in relatively good agreement with the NCEP/NCAR data, with the exception of the NCAR model which has about half the amplitude. The trends for PC_2 are 0.58, 0.68, 0.45, 0.56, and 0.28 /decade for GFDL, UKMO, GISS, MPI, and NCAR models respectively. The error bars for the trends are 0.14, 0.13, 0.13, 0.10, and 0.12 /decade, respectively. The signals associated with imposed volcanic-based aerosol variability in the GFDL, GISS, and NCAR models exhibit relatively good agreement with NCEP/NCAR, particularly for the 1991 Mt Pinatubo eruption; no volcanic aerosol forcing was imposed in the MPI and UKMO simulations. In addition, there is some decadal variability exhibited in the power

spectra for the NCEP/NCAR, GFDL, GISS, and NCAR, although the BO captured by NCEP/NCAR is not simulated in the five models. Given that 1st, 3rd and 4th modes arise from internal variability in the climate system; one would only expect or hope to find agreement in the spectral characteristics of the PCs, but not in the details of their temporal evolution. A comparison of Fig. 5.2 with Figs. 5.10, 5.11, 5.14-5.17 to a great extent bears this expectation out, at least in terms of the models' relative contributions from high versus low frequencies.

5.4 Conclusions

In conclusion, the results above illustrate a rather robust separation between the trend and natural variability of the 50 hPa temperature anomalies in 42 years of NCEP/NCAR reanalysis data. These findings indicate that, at least in terms of stratospheric temperature, the climate changes observed over the latter half of the 20th century do not appear to have a secular impact on the low-order modes of natural variability of the stratosphere, such as the NAM. Moreover, given that the NAM has been related to surface temperature variability [*Baldwin and Dunkerton*, 1999], these findings need to be examined in light of their implications for detection and attribution of NH surface temperature changes associated with global change. While the climate models examined here differ in a number of details regarding their representation of stratospheric temperature variability, namely their underestimate of the NAM (i.e. PC_1) variance and their overestimate of variance for the higher-order PCs examined (i.e. PC_3 and PC_4), it is encouraging that nearly all of them are able to capture the most fundamental modes of spatial-temporal variability. More importantly for this study is

their ability to represent the trend and its associated uniform spatial pattern in a manner that agrees qualitatively and quantitatively quite well with the observed data. Taken together, these observation and model based results help to refine the separation and quantification of natural versus anthropogenic climate signals, as well as provide a useful test for global models used for climate change projections. Additional analysis is warranted to determine if these characteristics extend to the other climate models contributing 20th century simulations for the 4th IPCC Assessment, the manner and extent that this trend and its separation from IAV extends into the modeled 21st century climate change scenarios, and what these results imply for detection and attribution of trends in NH surface temperature variability.

5.5 Appendix

The appendix provides information on the Procrustes Target Rotation (PTR) results for the different models in the IPCC fourth assessment of the 20th century climate experiment from Jan 1958 to Dec 1999.

5.5.1 Spatial REOFs From the Five Models

PTR is used to derive the rotated empirical orthogonal functions (REOFs) for the 50 hPa temperature anomalies for GFDL, UKMO, GISS, MPI, and NCAR. Results, shown in Figs. 5.5–5.9, are the spatial patterns of the REOFs. The REOFs spatial patterns are very similar to those derived from National Centers for Environmental Prediction/National Center for Atmospheric Research (NCEP/NCAR) Reanalysis, as shown in Fig. 5.1 in the chapter. The details of the models are summarized in Table 5.1. The variances for the corresponding modes in the five models are summarized in Table 5.2. The order of the REOFs in some models is different with that in NCEP/NCAR Reanalysis, for some modes are overemphasized in these models.

5.5.2 PCs Time Series, Power Spectra, and Integrated Power

PC time series, power spectra, and integrated power for the five models are plotted against those from the NCEP/NCAR in Figs. 5.10-5.17. PC_1 (black line) derived from NCEP/NCAR and the corresponding PCs in the models are plotted in Fig. 5.10a and Fig. 5.11a. The correlation coefficients between the PCs from the five models and PC_1 from NCEP/NCAR are very small, and are not statistically significant. The power spectra of these PC time series are plotted in Fig. 5.10b and Fig. 5.11b. Trends are not removed

from PCs before taking the power spectra. There is a dominant peak around Quasi-biennial Oscillation (QBO) for the PC_1 of NCEP/NCAR temperature anomalies, which are not found in the PCs from the five models. There are relatively larger ENSO signals in the GISS and NCAR models than those in the other models and NCEP/NCAR. The integrated powers over the frequency for these PCs are plotted in Fig. 5.10c and Fig. 5.11c. The integrated power from GFDL and UKMO are close to that from NCEP/NCAR in the low frequencies region with period larger than the 28 months.

PC_2 from NCEP/NCAR and the corresponding PCs from the five models are shown in Fig. 5.12a and Fig. 5.13a. The trends for the PCs from the five models are 0.58, 0.68, 0.45, 0.56, and 0.28 /decade for GFDL, UKMO, GISS, MPI, and NCAR models respectively. The trend for the PC_2 from NCEP/NCAR is 0.55 /decade. The volcano signals are well captured by GFDL, GISS, and NCAR. There are no obvious volcano signals in the other two models. The power spectra for the PC_2 from NCEP/NCAR and corresponding PCs from five models are shown in Fig. 5.12b and Fig. 5.13b. There are some decadal signals in the power spectra for the NCEP/NCAR, GFDL, GISS, and NCAR, which may relate to the volcano signal found in PCs. The ENSO signals are found in the NCAR, GISS, GFDL, and NCEP/NCAR; however, it is relatively weak in UKMO and MPI models. There is some power around QBO signal for the NCAR model. BO captured by NCEP/NCAR is not simulated in the five models. There are some signals around 20 months (QBO-AB) for the NCEP/NCAR and MPI. The integrated powers are plotted in Fig. 5.12c and Fig. 5.13c. The time series for PC_3 and corresponding PCs from the five models are shown in Fig. 5.18a and Fig. 5.19a. The power spectra for the PC_3

from NCEP/NCAR and those from five models are mostly high frequencies. There is some signal around 22 years in the PC_3 from NCEP/NCAR, which is not found in the PCs from the five models. PC_4 from NCEP/NCAR are shown with corresponding PCs from five models in Fig. 5.16a and Fig. 5.17a. Similar to PC_3, this mode is dominated by high frequency oscillations.

5.6 References:

Baldwin, M. P., and T. J. Dunkerton, Biennial, quasi-biennial, and decadal oscillations of potential vorticity in the northern stratosphere, *J. Geophys. Res.-Atmos.*, *103*, 3919-3928, 1998.

Baldwin, M. P., and T. J. Dunkerton, Propagation of the Arctic Oscillation from the stratosphere to the troposphere, *J. Geophys. Res.-Atmos.*, *104*, 30937-30946, 1999.

Baldwin, M. P., *et al*., The quasi-biennial oscillation, *Rev. Geophys.*, *39*, 179-229, 2001.

Camp, C. D., *et al*., Temporal and Spatial Patterns of the Interannual Variability of Total Ozone in the Tropics, *J. Geophys. Res.*, art. no. 4643, 2003.

Gilman, D. L., *et al*., On the Power Spectrum of Red Noise, *Journal of the Atmospheric Sciences*, *20*, 182-184, 1963.

Jiang, X., C. D. Camp, R. Shia, T. Liao, K. Jeev, V. Limpasuvan, Y. L. Yung, Interannual variability in high latitude stratospheric ozone, *Submitted to J Geophys. Res. -Atmos*, 2006.

Kalnay, E., *et al*., The NCEP/NCAR 40-year reanalysis project, *Bull. Amer. Meteorol. Soc.*, *77*, 437-471, 1996.

Kistler, R., *et al*., The NCEP-NCAR 50-year reanalysis: Monthly means CD-ROM and documentation, *Bull. Amer. Meteorol. Soc.*, *82*, 247-267, 2001.

Manabe, S., and R. T. Wetheral, Thermal Equilibrium of Atmosphere with a Given Distribution of Relative Humidity, *J. Atmos. Sci.*, *24*, 241-259, 1967.

Preisendorfer, R. W., Principal component analysis in meteorology and oceanography, 1988.

Ramaswamy, V., *et al*., Stratospheric temperature trends: Observations and model simulations, *Rev. Geophys.*, *39*, 71-122, 2001.

Ramaswamy, V., *et al*., Anthropogenic and natural influences in the evolution of lower stratospheric cooling, *Science*, *311*, 1138-1141, 2006.

Richman, M. B., and W. E. Easterling, Procrustes Target Analysis - a Multivariate Tool for Identification of Climate Fluctuations, *J. Geophys. Res.-Atmos.*, *93*, 10989-11003, 1988.

Thompson, D. W. J., and J. M. Wallace, The Arctic Oscillation signature in the wintertime geopotential height and temperature fields, *Geophys. Res. Lett.*, *25*, 1297-1300, 1998.

Table 5.1: IPCC AR4 models used in this study.

Model	Forcings	Vertical levels
US Dept. of Commerce / NOAA / Geophysical Fluid Dynamics Laboratory, GFDL-CM2.1	Well-mixed greenhouse gases, tropospheric and stratospheric ozone, sulfate aerosol direct effects, black carbon and organic carbon aerosols, land use/land cover, solar irradiance, and volcanic aerosols	24
Hadley Center for Climate Prediction and Research / Met Office, UKMO-HadCM3	Well-mixed greenhouse gases, tropospheric and stratospheric ozone, and sulfate aerosol direct and indirect effects	15
NASA / Goddard Institute for Space Studies, GISS-EH	Well-mixed greenhouse gases, tropospheric and stratospheric ozone, sulfate aerosol direct and indirect effects, black carbon and organic carbon aerosols, mineral dust, sea salt, land use/land cover, solar irradiance, and volcanic aerosols	17
Max Planck Institute for Meteorology, Hamburg, Germany, MPI	Well-mixed greenhouse gases, tropospheric and stratospheric ozone, and sulfate aerosol direct and indirect effects	16
National Center for Atmospheric Research, NCAR-CCSM3	Well-mixed greenhouse gases, tropospheric and stratospheric ozone, sulfate aerosol direct effects, black carbon aerosols, solar irradiance, and volcanic aerosols	17

Table 5.2: Corresponding REOFs for the 50 hPa Temperature Anomaly in the Five Models as EOFs From NCEP/NCAR. Fractions of Variance Explained by EOFs and REOFs are listed. Units are %.

PCA on the temperature	EOF1	EOF2	EOF3	EOF4
from the NCEP/NCAR	34.2%	16.9%	14.1%	10.6%
REOF on the temperature	REOF1	REOF2	REOF4	REOF3
from the GFDL	24.3%	16.7%	10.0%	10.1%
REOF on the temperature	REOF1	REOF2	REOF4	REOF3
from the UKMO	22.5%	16.3%	11.2%	11.3%
REOF on the temperature	REOF1	REOF4	REOF3	REOF2
from the GISS	23.3%	12.7%	16.7%	21.0%
REOF on the temperature	REOF1	REOF4	REOF2	REOF3
from the MPI	19.7%	10.1%	18.4%	13.6%
REOF on the temperature	REOF2	REOF4	REOF1	REOF3
from the NCAR	21.0%	12.5%	27.2%	18.5%

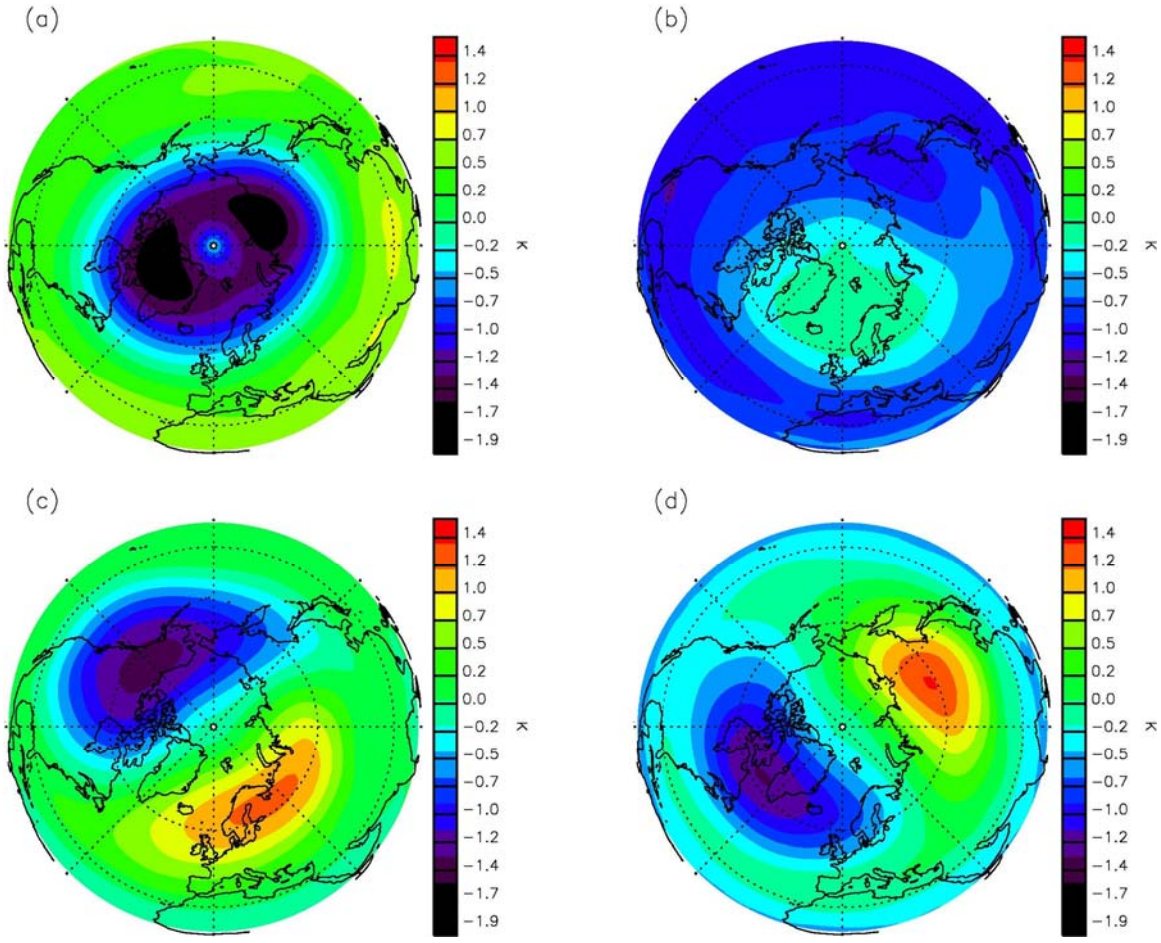

Figure 5.1: The four leading empirical orthogonal function (EOF) spatial patterns for the monthly mean NCEP/NCAR temperature anomaly in the NH from Jan 1958 to Dec 1999. Units are K. The first four modes explain 34.2, 16.9, 14.1, 10.6% of the total variance, respectively.

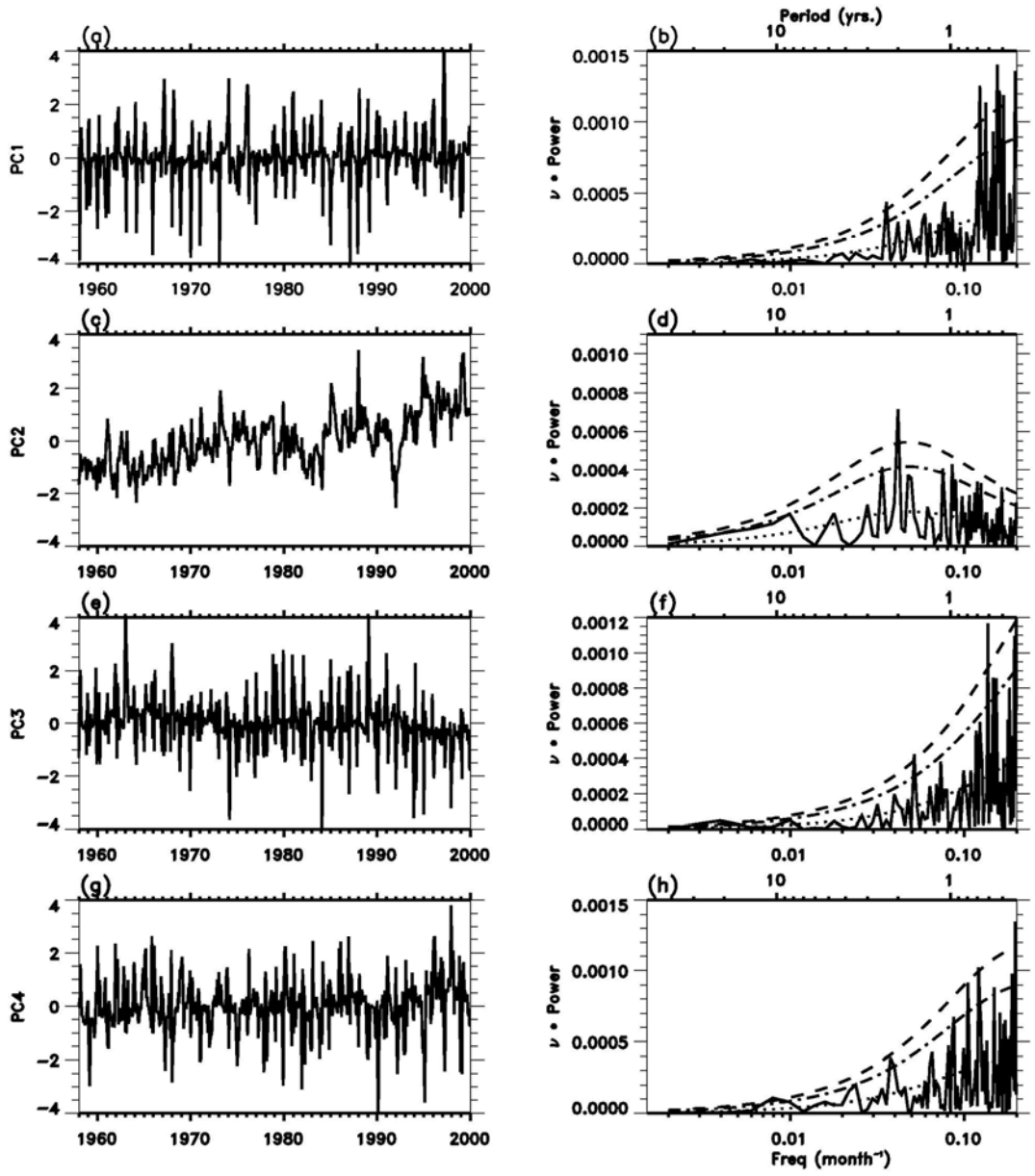

Figure 5.2: (a) PC_1 at 50 hPa. (b) Power spectral estimate of detrended PC_1 (Solid), red noise spectrum (Dotted), 10% and 5% significance level (Dashed). (c) PC_2. (d) Power spectral estimate of detrended PC_2 (Solid), red noise spectrum (Dotted), 10% and 5% significance level (Dashed). (e) PC_3. (f) Power spectrum of detrended PC_3 (Solid), red noise spectrum (Dotted), 10% and 5% significance level (Dashed). (g) PC_4. (h) Power spectrum of detrended PC_4 (Solid), red noise spectrum (Dotted), 10% and 5% significance level (Dashed).

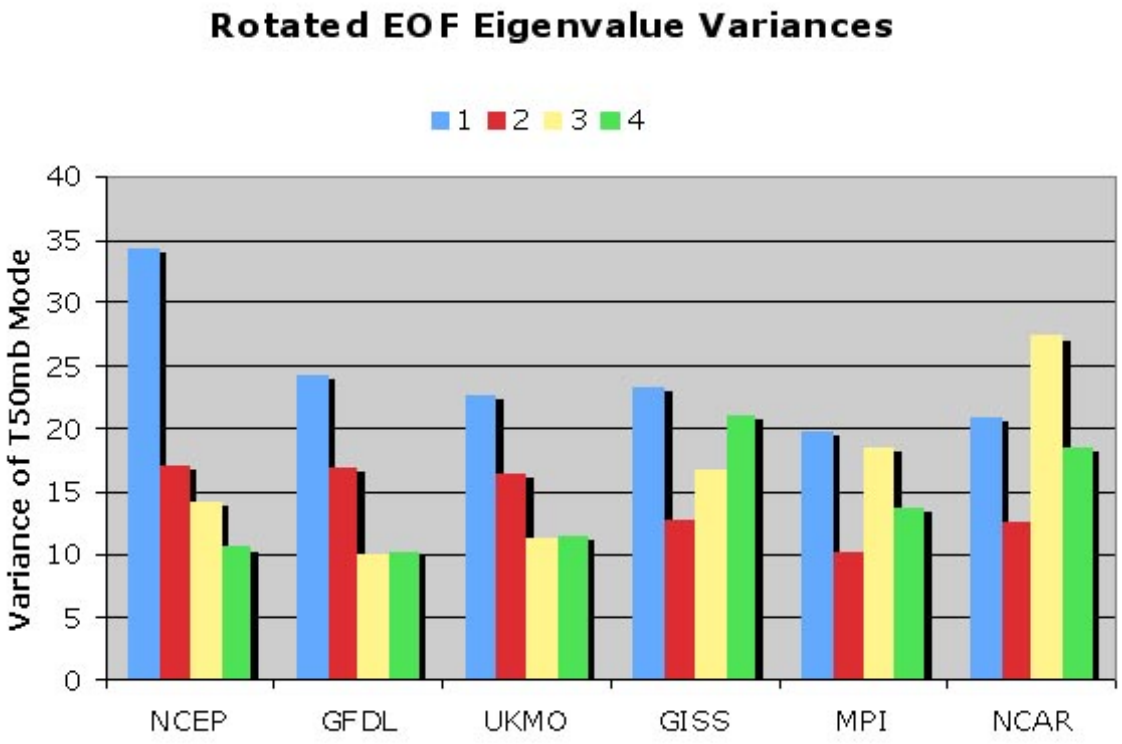

Figure 5.3: Variances of the four leading modes of variability from the observations and the GFDL, UKMO, GISS, MPI, and NCAR climate models. The data are from Jan 1958 to Dec 1999 of the 20th century simulations for the IPCC 4th assessment. The modes from models are rotated using the Procrustes Target Rotation using the modes from observations as the target. Units are %.

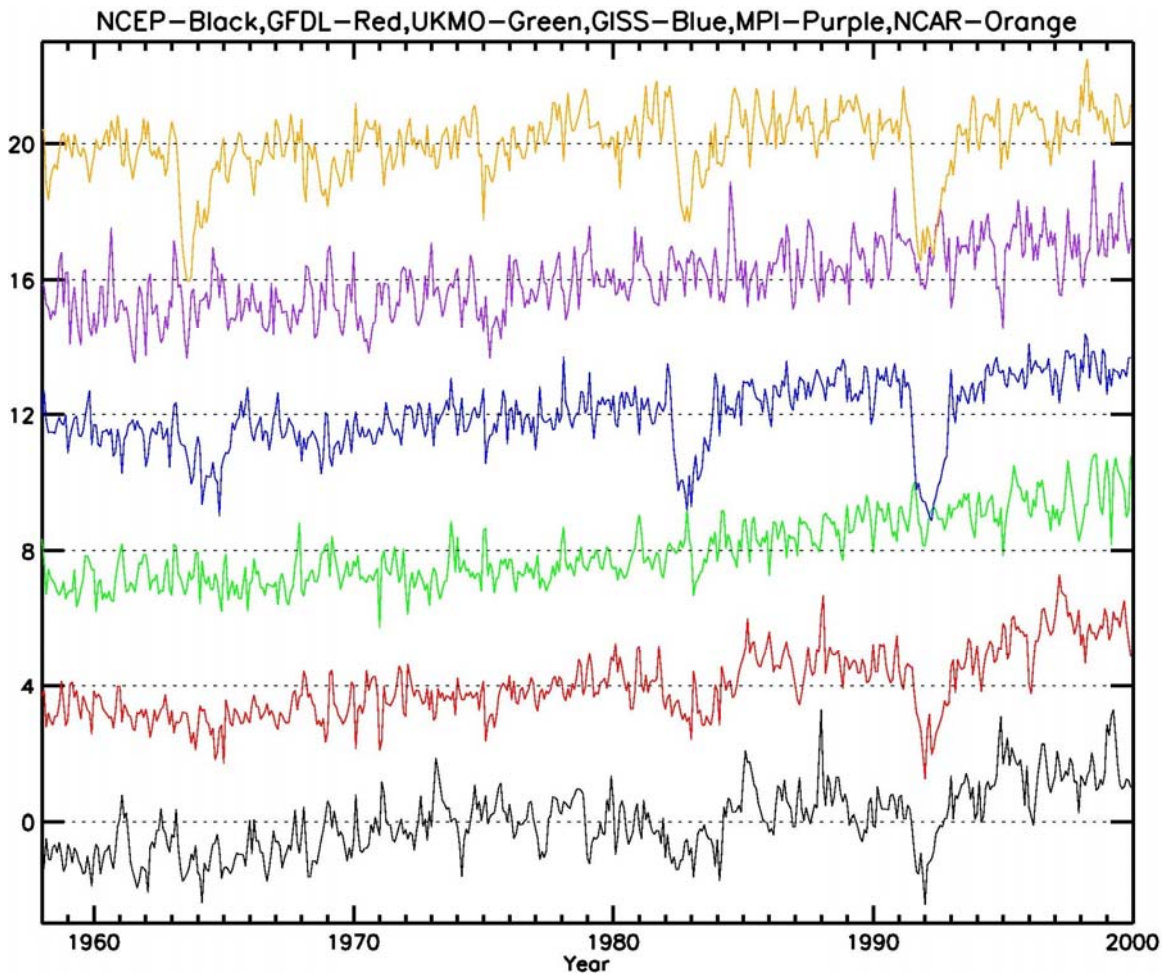

Figure 5.4: PC_2 (black line) derived from NCEP, PC_2 (red line) derived from GFDL, PC_2 (green line) derived from UKMO, PC_4 (blue line) derived from GISS, PC_4 (purple line) derived from MPI, and PC_4 (orange line) derived from NCAR. For visualization, PCs are shifted upward by 4, 8, 12, 16, and 20 for GFDL, UKMO, GISS, MPI, and NCAR, respectively.

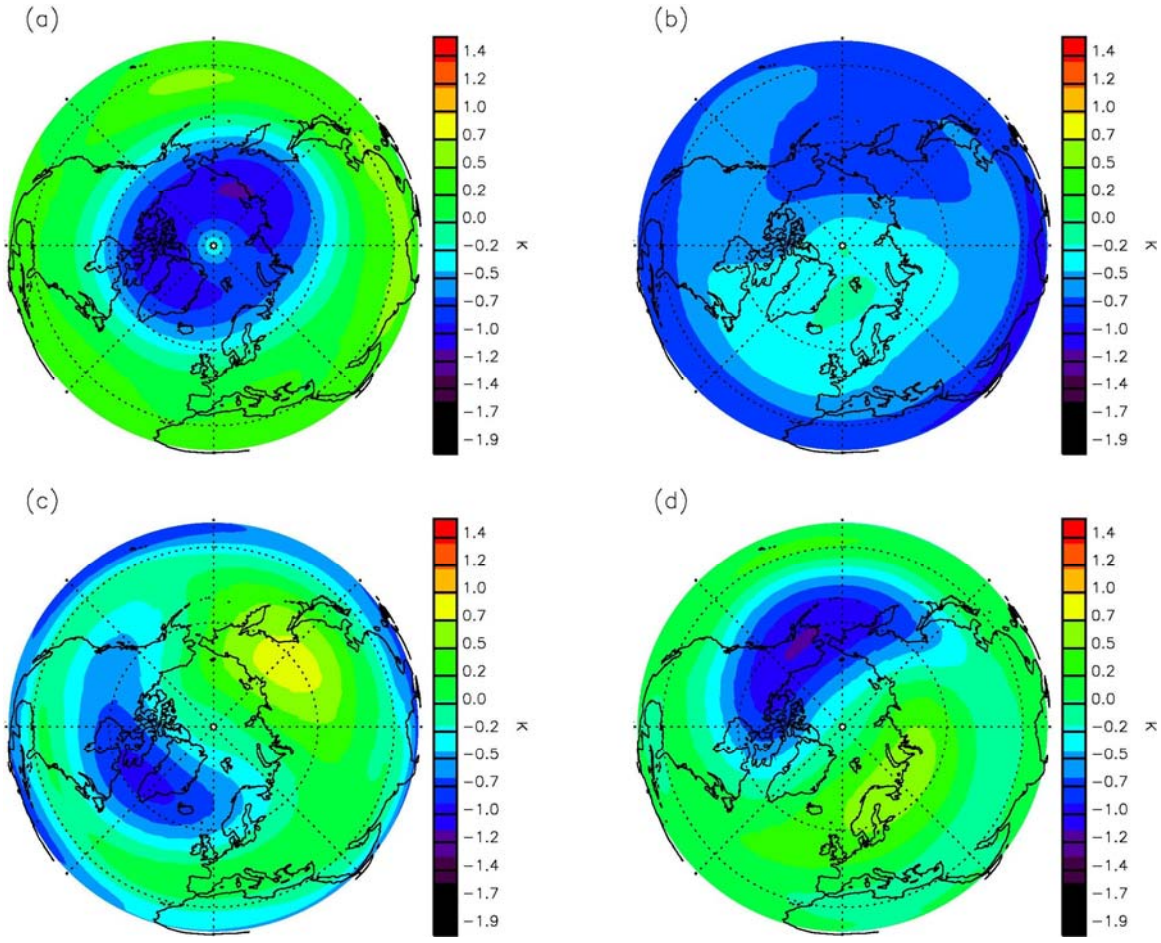

Figure 5.5: The first four leading rotated EOF spatial patterns for the monthly mean GFDL temperature anomalies in the NH from Jan 1958 to Dec 1999. Units are K. The first four modes explain 24.3, 16.7, 10.1, 10.0% of the total variance, respectively.

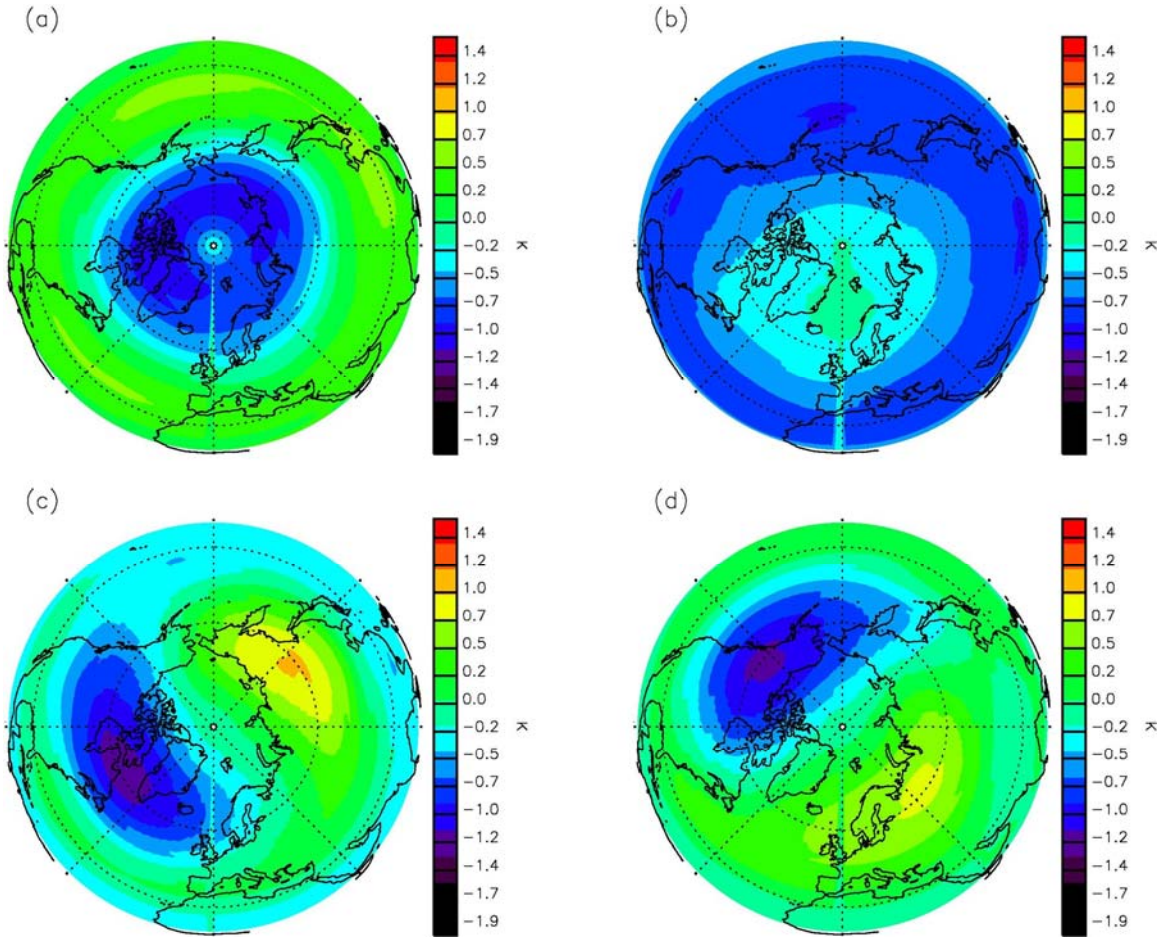

Figure 5.6: The first four leading rotated EOF spatial patterns for the monthly mean UKMO temperature anomalies in the NH from Jan 1958 to Dec 1999. Units are K. The first four modes explain 22.5, 16.3, 11.3, 11.2% of the total variance, respectively.

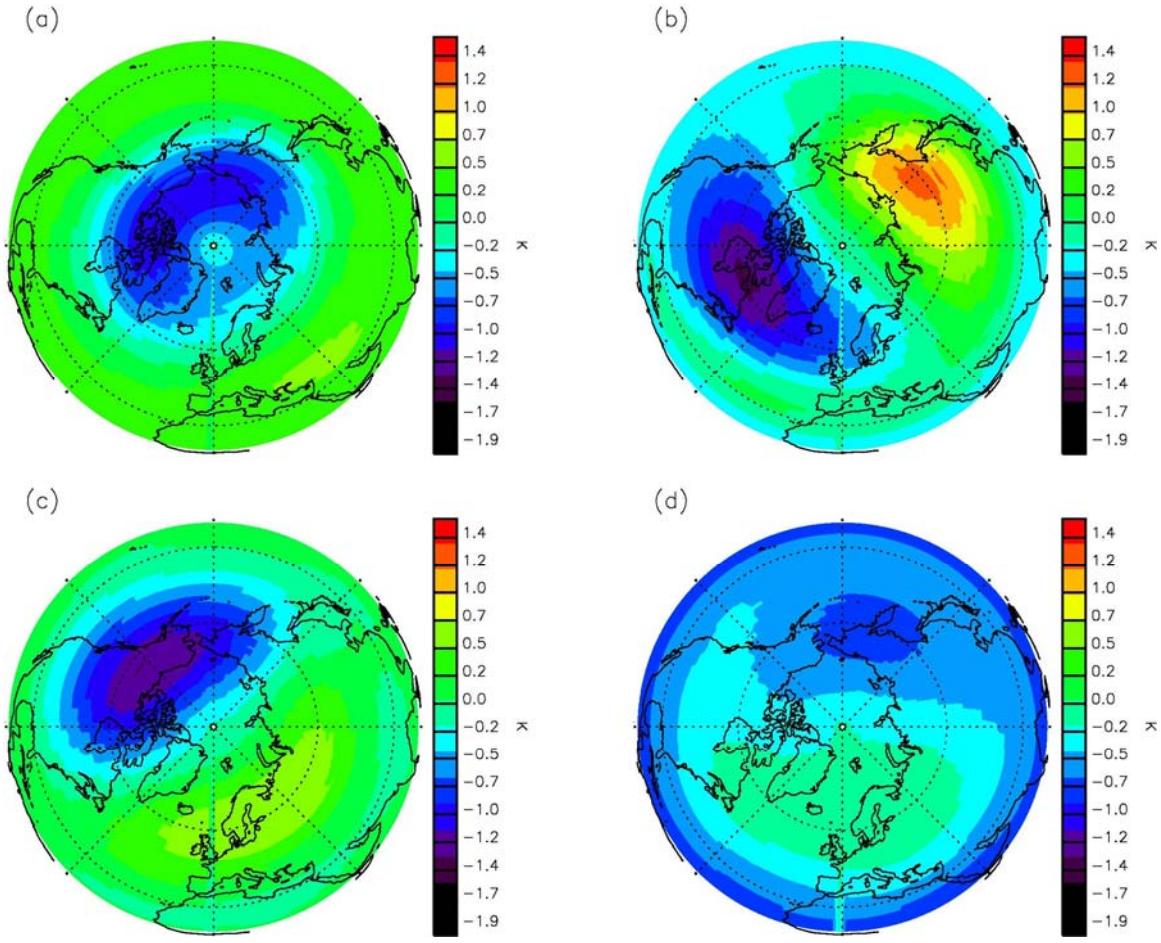

Figure 5.7: The first four leading rotated EOF spatial patterns for the monthly mean GISS temperature anomalies in the NH from Jan 1958 to Dec 1999. Units are K. The first four modes explain 23.3, 21.0, 16.7, 12.7% of the total variance, respectively.

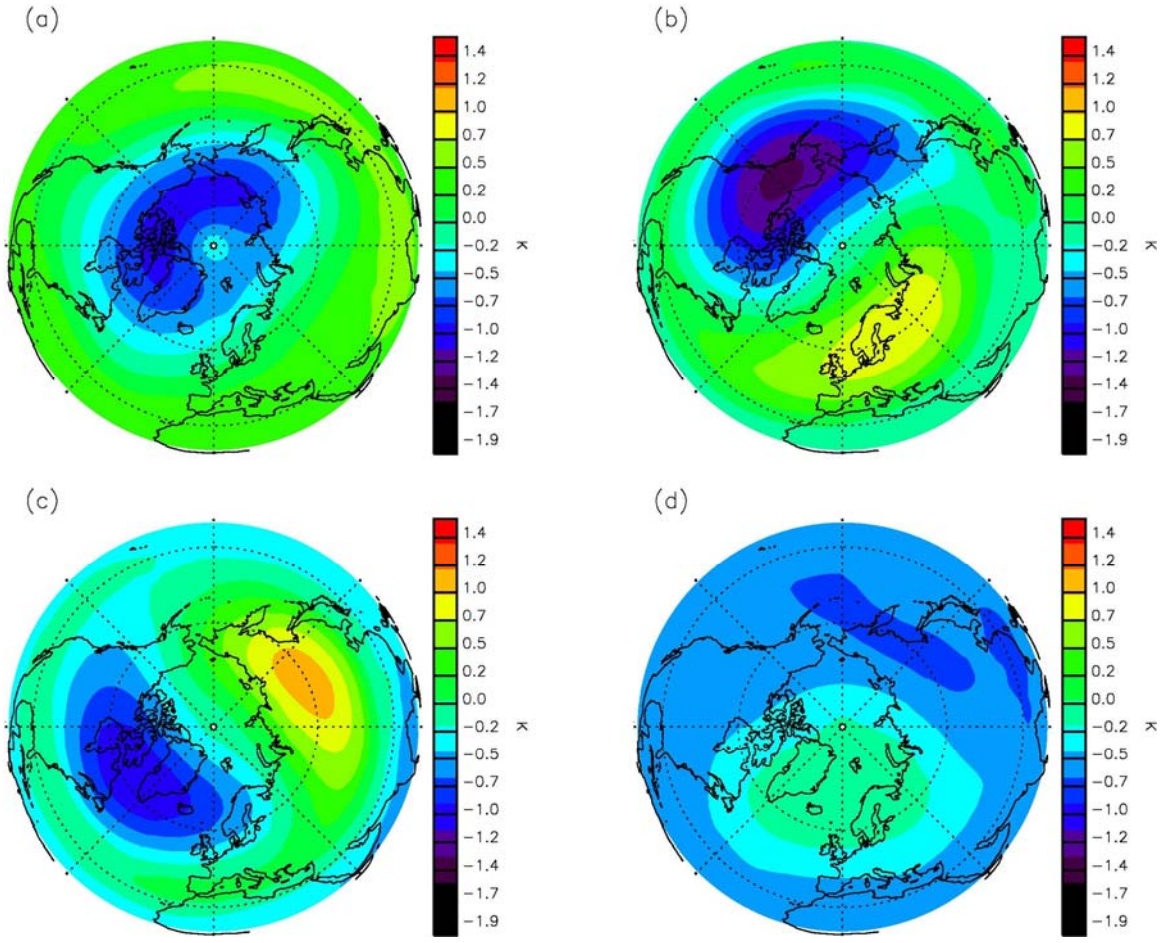

Figure 5.8: The first four leading rotated EOF spatial patterns for the monthly mean MPI temperature anomalies in the NH from Jan 1958 to Dec 1999. Units are K. The first four modes explain 19.7, 18.4, 13.6, 10.1% of the total variance, respectively.

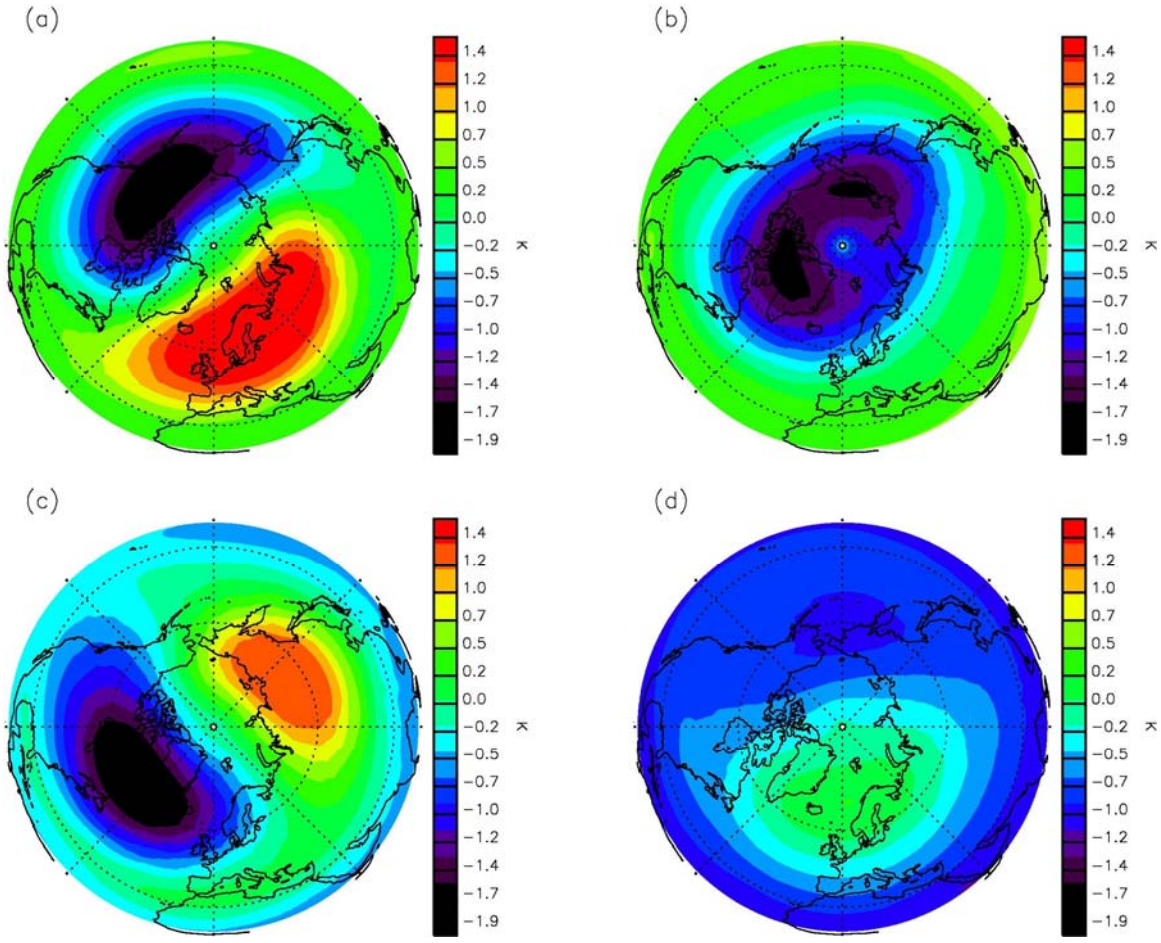

Figure 5.9: The first four leading rotated EOF spatial patterns for the monthly mean NCAR temperature anomalies in the NH from Jan 1958 to Dec 1999. Units are K. The first four modes explain 27.2, 21.0, 18.5, 12.5% of the total variance, respectively.

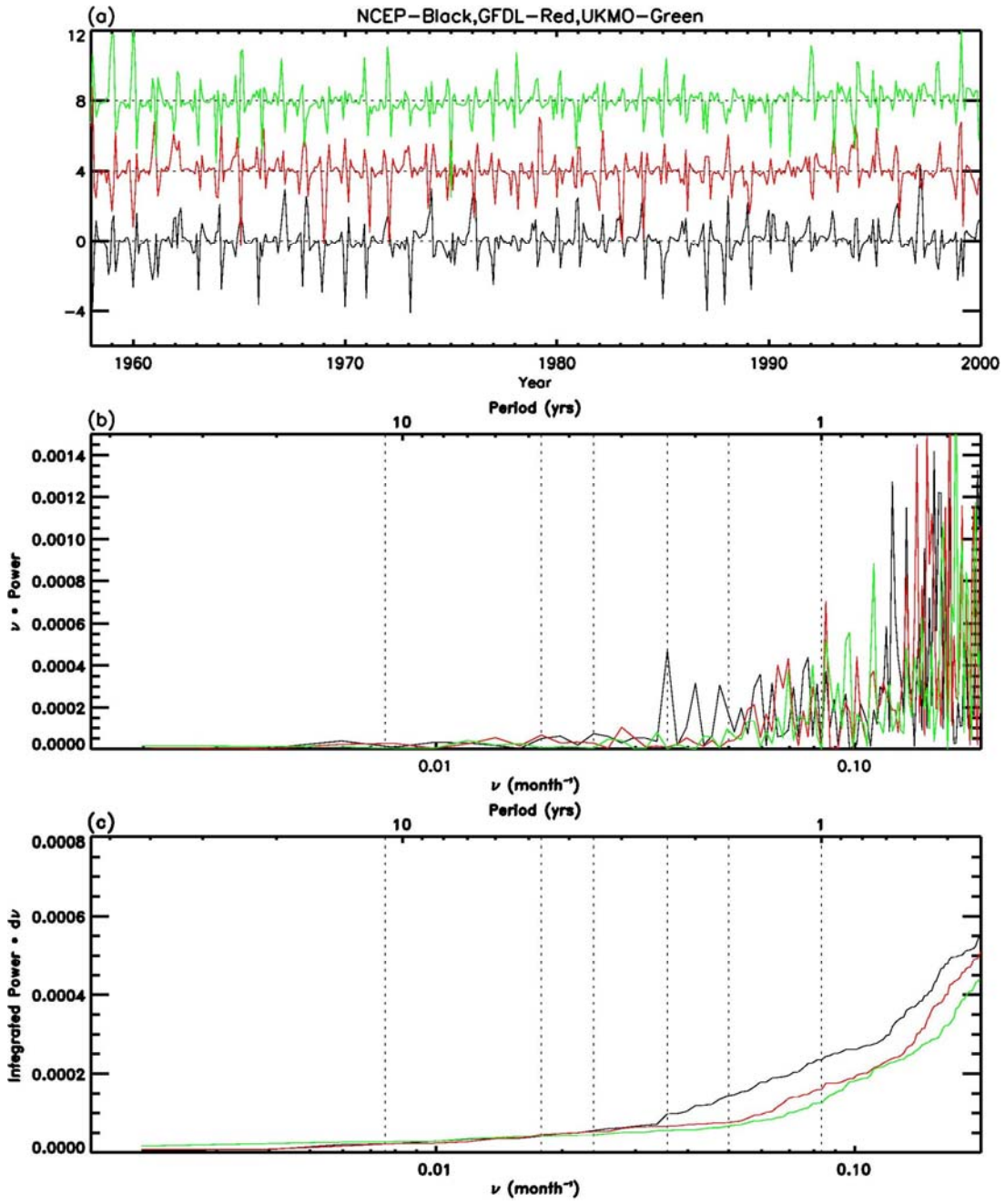

Figure 5.10: (a) PC_1 (black line) derived from NCEP/NCAR, PC_1 (red line) derived from GFDL, and PC_1 (green line) derived from UKMO. PCs are shifted upward by 4 and 8 for GFDL and UKMO, respectively. (b) Power spectra of the PC time series in (a). (c) Integrated power of the PC time series in (a).

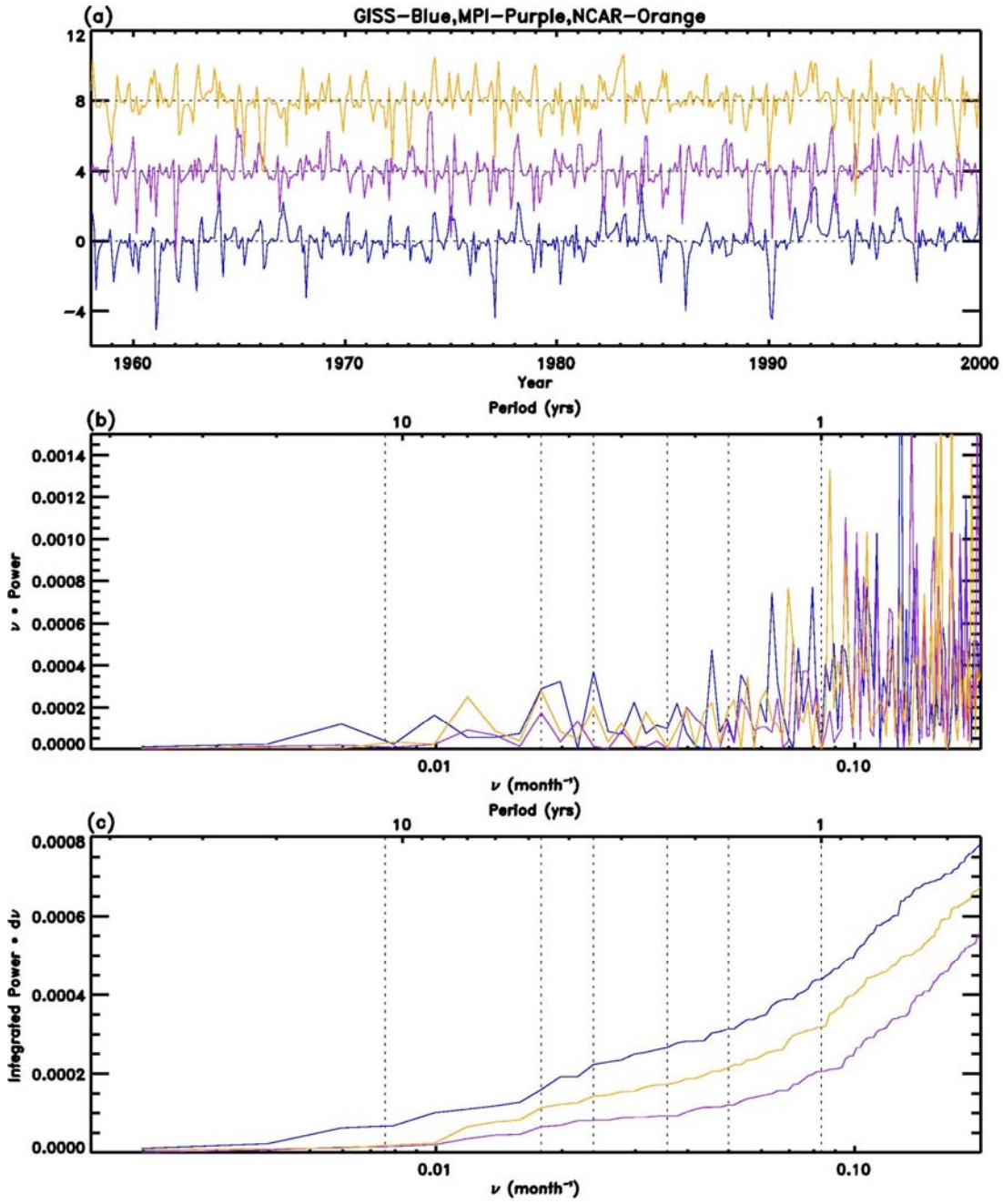

Figure 5.11: (a) PC_1 (blue line) derived from GISS, PC_1 (purple line) derived from MPI, and PC_2 (orange line) derived from NCAR. PCs are shifted upward by 4 and 8 for MPI and NCAR, respectively. (b) Power spectra of the PC time series in (a). (c) Integrated power of the PC time series in (a).

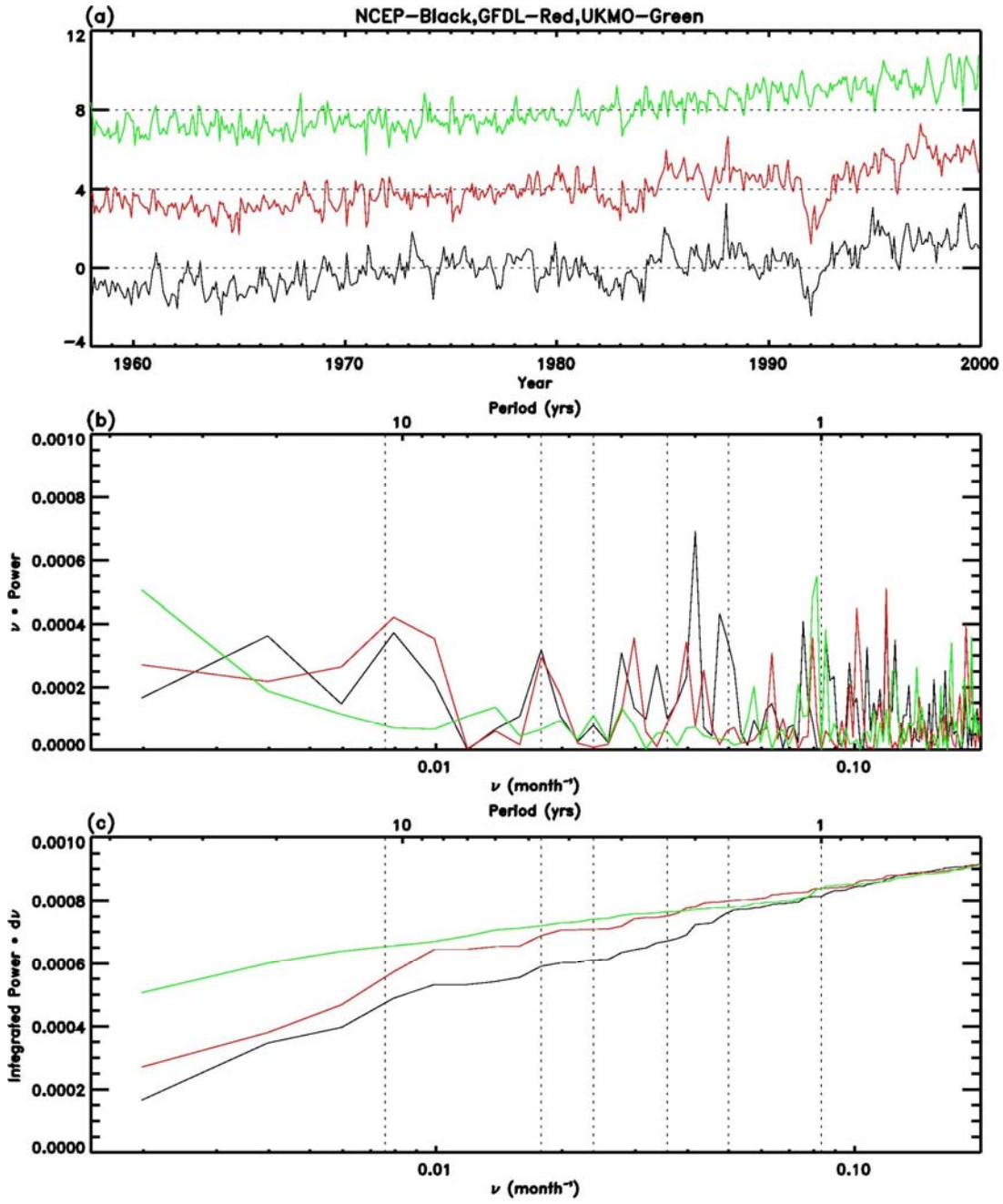

Figure 5.12: (a) PC_2 (black line) derived from NCEP/NCAR, PC_2 (red line) derived from GFDL, and PC_2 (green line) derived from UKMO. PCs are shifted upward by 4 and 8 for GFDL and UKMO, respectively. (b) Power spectra of the PC time series in (a). (c) Integrated power of the PC time series in (a).

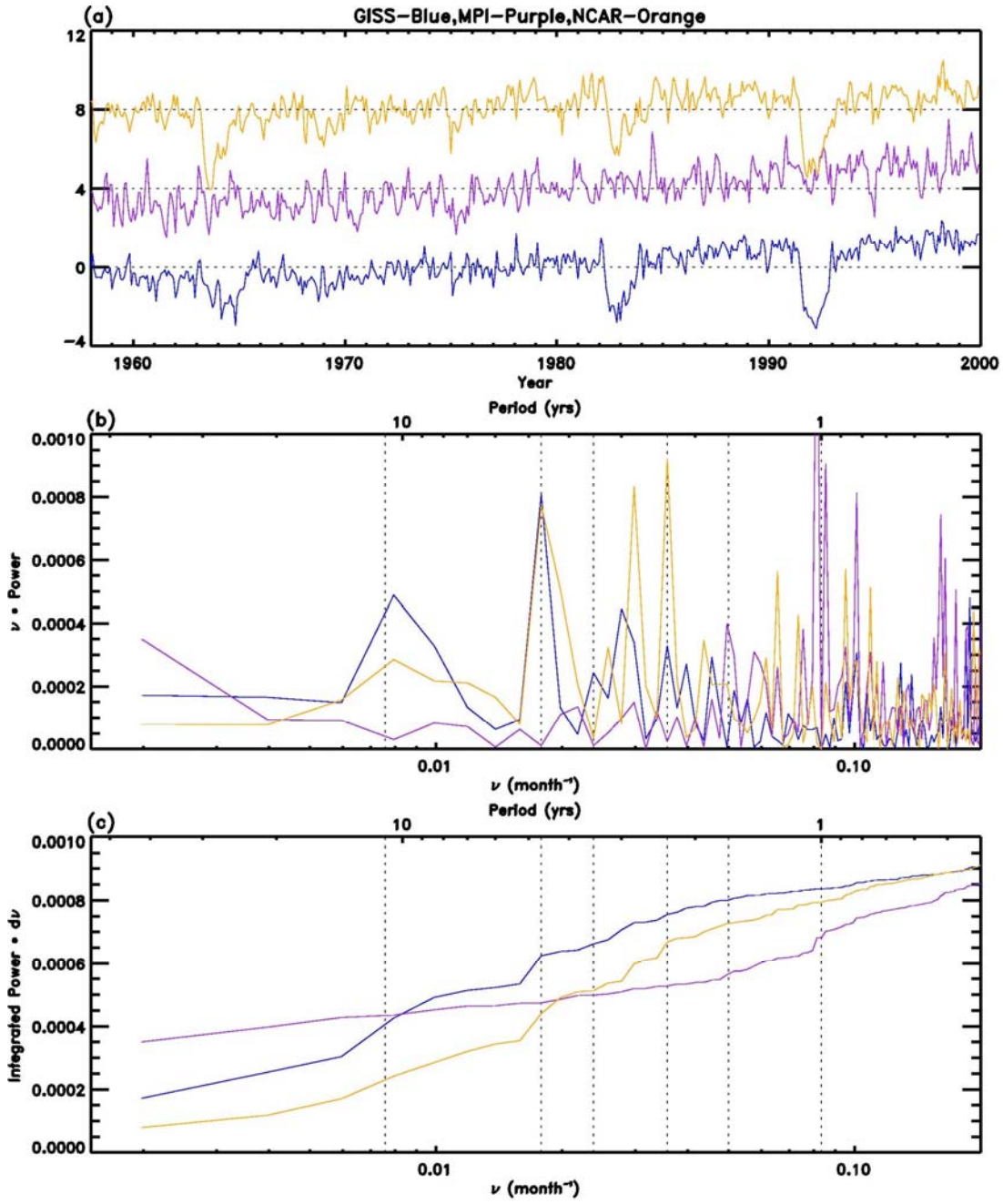

Figure 5.13: (a) PC_4 (blue line) derived from GISS, PC_4 (purple line) derived from MPI, and PC_4 (orange line) derived from NCAR. PCs are shifted upward by 4 and 8 for MPI and NCAR, respectively. (b) Power spectra of the PC time series in (a). (c) Integrated power of the PC time series in (a).

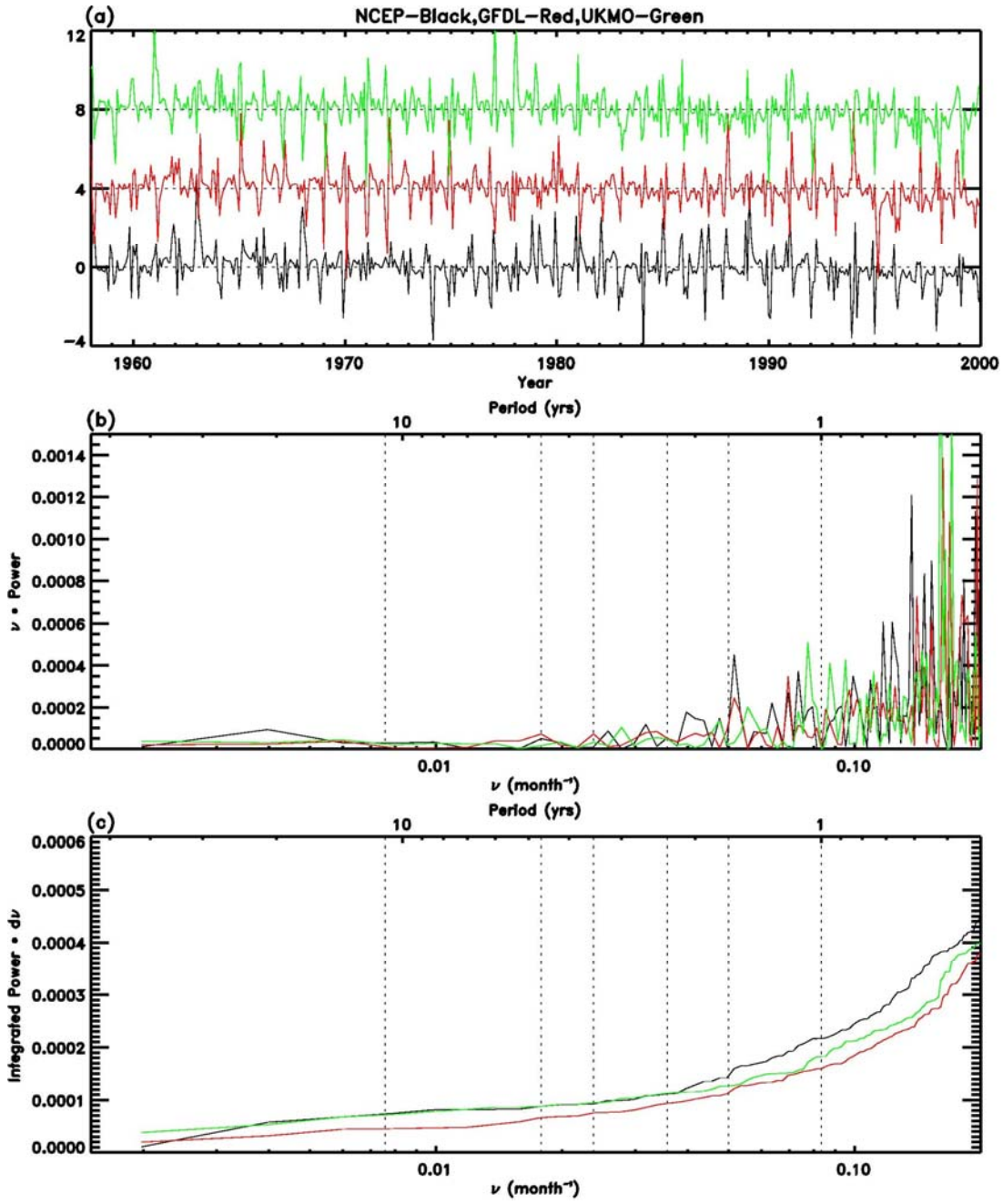

Figure 5.14: (a) PC_3 (black line) derived from NCEP/NCAR, PC_4 (red line) derived from GFDL, and PC_4 (green line) derived from UKMO. PCs are shifted upward by 4 and 8 for GFDL and UKMO, respectively. (b) Power spectra of the PC time series in (a). (c) Integrated power of the PC time series in (a).

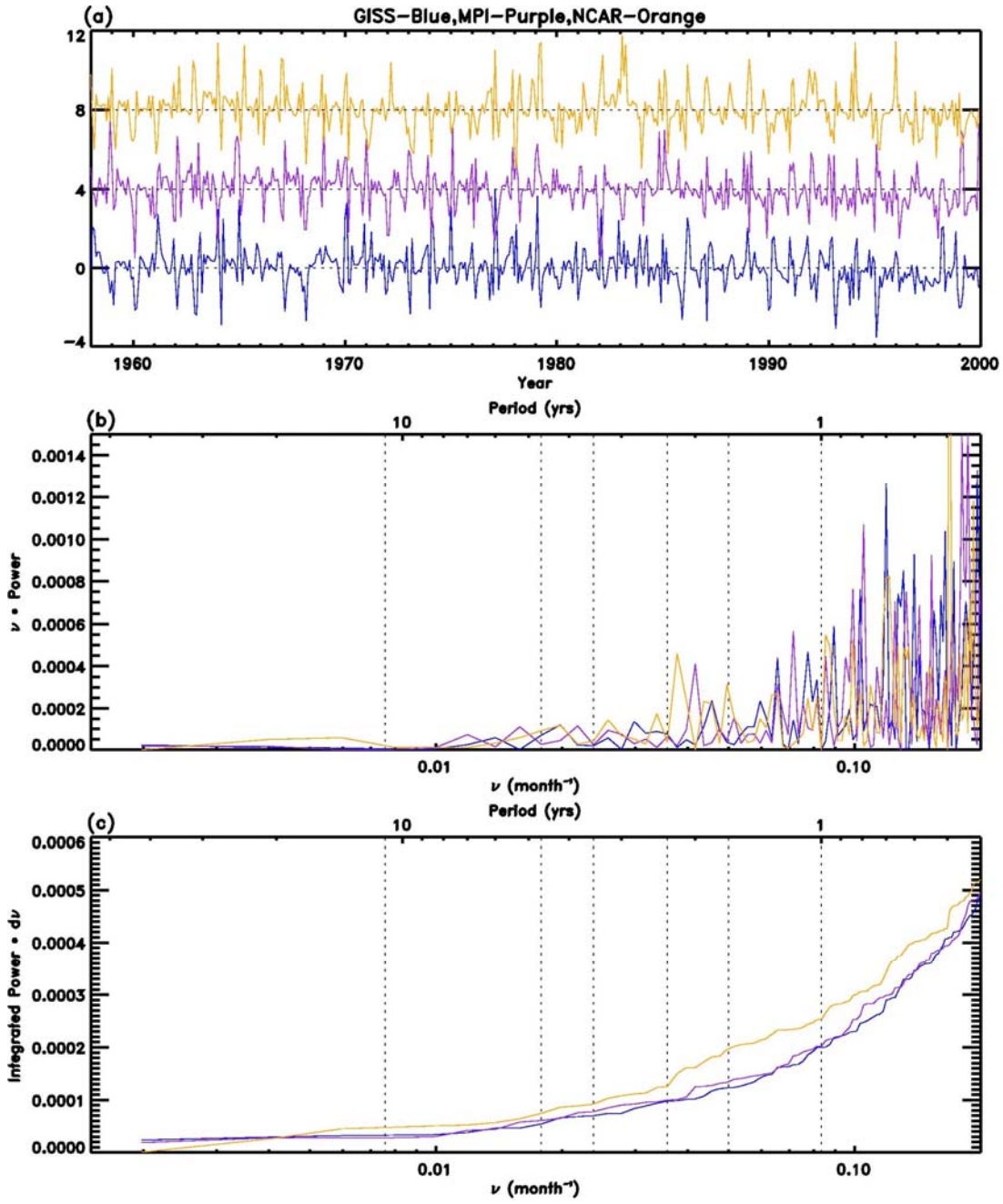

Figure 5.15: (a) PC_3 (blue line) derived from GISS, PC_2 (purple line) derived from MPI, and PC_1 (orange line) derived from NCAR. PCs are shifted upward by 4 and 8 for MPI and NCAR, respectively. (b) Power spectra of the PC time series in (a). (c) Integrated power of the PC time series in (a).

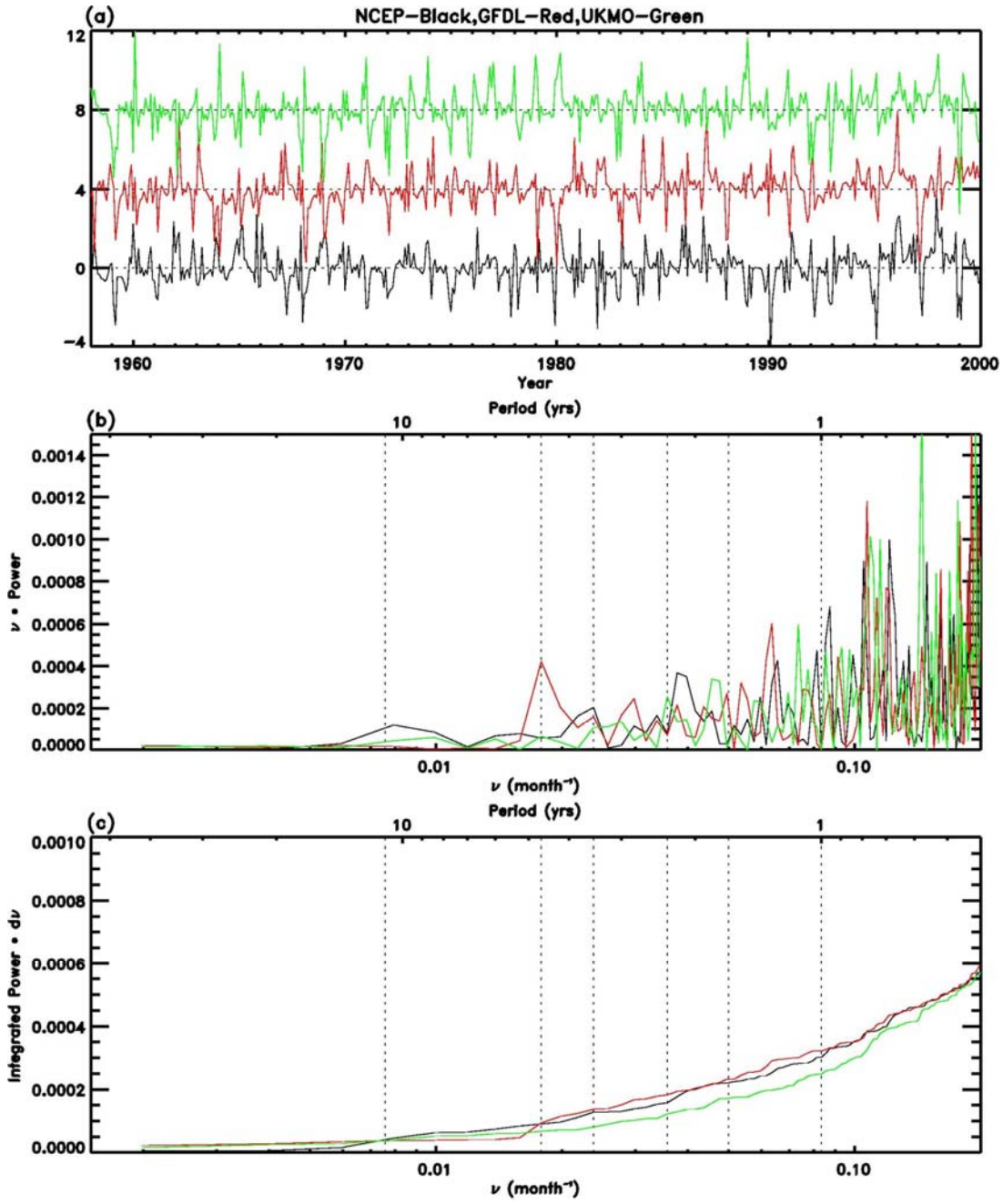

Figure 5.16: (a) PC_4 (black line) derived from NCEP/NCAR, PC_3 (red line) derived from GFDL, and PC_3 (green line) derived from UKMO. PCs are shifted upward by 4 and 8 for GFDL and UKMO, respectively. (b) Power spectra of the PC time series in (a). (c) Integrated power of the PC time series in (a).

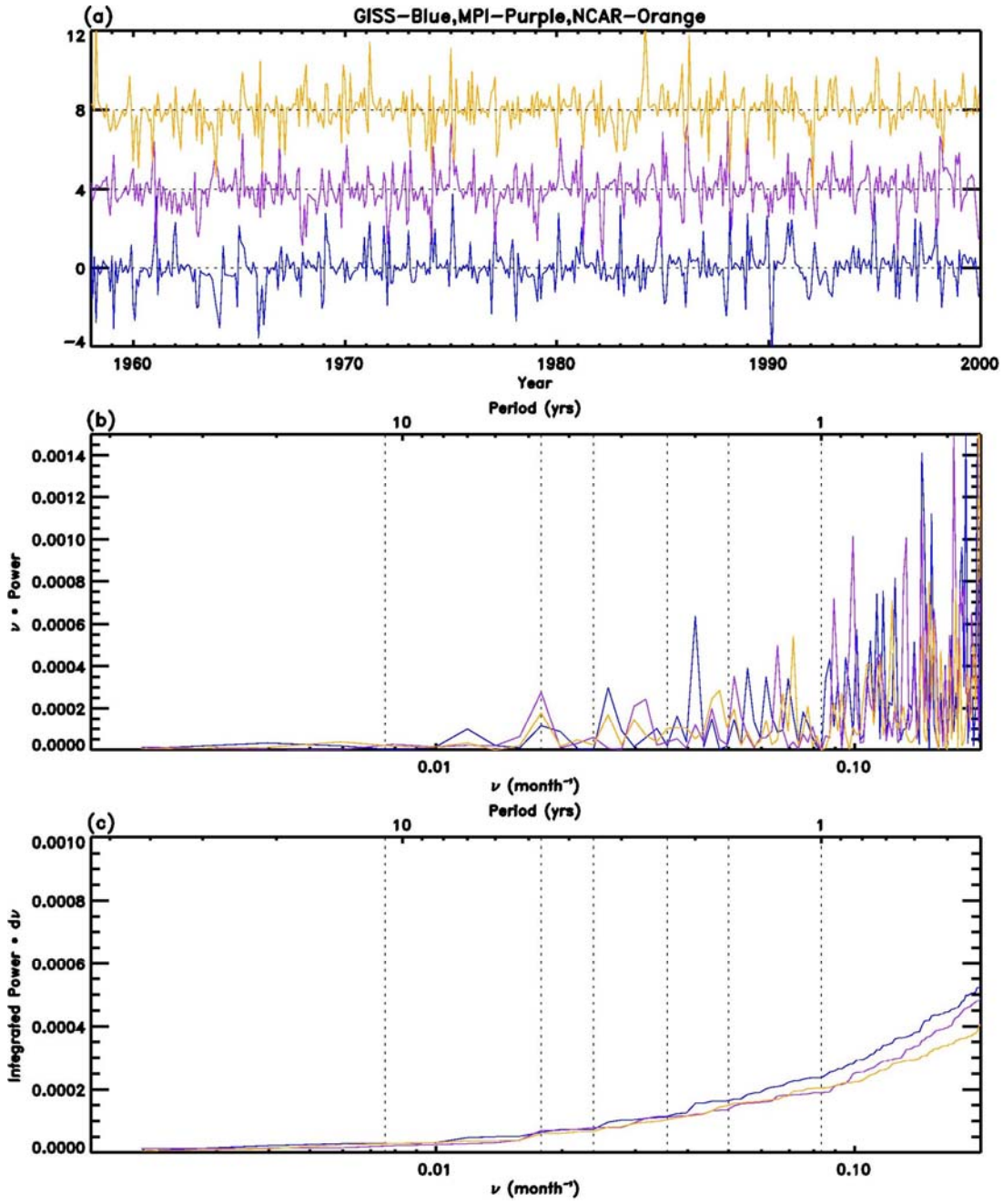

Figure 5.17: (a) PC_2 (blue line) derived from GISS, PC_3 (purple line) derived from MPI, and PC_3 (orange line) derived from NCAR. PCs are shifted upward by 4 and 8 for MPI and NCAR, respectively. (b) Power spectra of the PC time series in (a). (c) Integrated power of the PC time series in (a).

II: Seasonal Cycle of N_2O

Chapter 6: The Seasonal Cycle of N_2O: Analysis of Data

6.1 Abstract

We carried out a systematic study of the seasonal cycle and its latitudinal variation in the nitrous oxide (N_2O) data collected by National Oceanic and Atmospheric Administration-Global Monitoring Division (NOAA-GMD) and the Advanced Global Atmospheric Gases Experiment (AGAGE). In order to confirm the weak seasonal signal in the observations, we applied the multi-taper method for the spectrum analysis and imposed the criterion that the seasonal signal must be below 1% significance level. In addition, the measurement errors must be small compared with the seasonal cycle. The N_2O seasonal cycles from seven stations satisfied these criteria and were analyzed in detail. The stations are Alert (82°N, 62°W), Barrow (71°N, 157°W), Mace Head (53°N, 10°W), Cape Kumukahi (19°N, 155°W), Cape Matatula (14°S, 171°W), Cape Grim (41°S, 145°E) and South Pole (90°S, 102°W). The amplitude (peak to peak) of the seasonal cycle of N_2O varies from 0.29 ppb (parts-per-billion by mole fraction in dry air) at the South Pole to 1.15 ppb at Alert. The month at which the seasonal cycle is at a minimum varies monotonically from April (South Pole) to September (Alert). The seasonal cycle in the northern hemisphere shows the influence of the stratosphere; the seasonal cycle of N_2O in the southern hemisphere suggests greater influence from surface sources. Preliminary estimates are obtained for the magnitude of the seasonally varying sources needed to account for the observations.

6.2 Introduction

The sources of nitrous oxide (N_2O) are the microbes in nitrification and denitrification processes as well as anthropogenic activities [*Stein and Yung*, 2003]. As the nitrogen cycle has been perturbed by human activities [*McElroy et al*. 1977], the concentration of N_2O in the terrestrial atmosphere has been increasing from the pre-industrial revolution value of about 270 ppb (parts-per-billiion by mole fraction in dry air or nmol/mol) to the present value of 320 ppb [*Battle et al.*, 1996; *Thompson et al.*, 2004].

The sink of N_2O is mainly photolysis in the stratosphere with a smaller contribution from reaction with O (^1D), resulting in a very long lifetime of about 125 years for atmospheric N_2O [*Minschwaner et al*., 1993; *Volk et al*., 1997; *McLinden et al.*, 2003; *Morgan et al*., 2004]. This is the primary reason why the seasonal cycle signal in the troposphere is so small and previously clearly detectable only at Tasmania in the AGAGE network [*Prinn et al.,* 2000]. However, the long accumulation of high quality data has finally made it possible to study the seasonal cycle. The seasonal cycle of N_2O in the stratosphere is caused primarily by the seasonally varying Brewer-Dobson circulation [*Morgan et al*., 2004; *Nevison et al.,* 2004]. The seasonal cycle in the troposphere is caused partly by the mixing of N_2O-poor stratospheric air with tropospheric air in the spring of each hemisphere [*Levin et al*., 2002; *Liao et al*., 2004; *Nevison et al*., 2004]. In addition to dynamical transport, there is a seasonal cycle arising from the surface sources of N_2O. There is considerable uncertainty in the magnitude, distribution and the temporal pattern of the various natural and anthropogenic sources of N_2O [*Bouwman et al,* 1995]. Investigation of the seasonal cycle and its latitudinal

variation of the N_2O should shed light on its sources, sinks, and transport processes. In this chapter, we will carry out an analysis of surface N_2O observations.

The data and the method of analysis are described in section 2. The main results are presented in section 3, followed by conclusions in section 4.

6.3 Data and Methodology

We obtained the N_2O observation from four sources: National Oceanic and Atmospheric Administration-Global Monitoring Division (NOAA-GMD) Halocarbons and other Atmospheric Trace Species Flask Program (NOAA flask), NOAA-GMD Chromatograph for Atmosphere Trace Species (CATS), NOAA-GMD Radiatively Important Trace Species (RITS), and the Advanced Global Atmospheric Gases Experiment (AGAGE) Global Trace Gas Monitoring Network. The NOAA flask data are divided into two separate data sets, before and after 1996. The RITS data are from 1988 to 1999 and the CATS data are from 1999 to 2004 [*Thompson et al.*, 2004]. The AGAGE data are divided into three sets, ALE(1978-1986), GAGE(1985-1996), and AGAGE(1993-2003), respectively [*Prinn et al.,* 2000]. Since there are many gaps in the RITS and NOAA flask pre-1996 data, we will mainly focus on the NOAA flask post-1996, AGAGE 93-03, and CATS data. The locations of the stations in each of the measurement programs and the length of the records are listed in Table 6.1.

NOAA-GMD N_2O measurements have evolved since 1977, improving with new gas chromatographic techniques and more precise detectors. The early 1977-1995

flasks (pre-1996 data) were measured using a nitrogen carrier gas and electron capture detector coupled to a gas chromatograph (ECD-GC). Water vapor was not removed in those samples because of concern of affecting the mixing ratios of other trace gases measured (CFCs) at the parts-per-trillion. The correction varied from 0% for dry stations to almost 3% for wet stations. There was a slight CO_2 effect on the column used at the time which amounted to 0.1 ppb of N_2O per 1 ppm in the difference in CO_2 of the air sample minus that of the calibration tank. The typical corrections were from 0.1 to 2 ppb. The precisions of the pre-1996 flask data were about 1.5%. The advantage of that system was that the calibration tanks were changed only about 6 times, so there less shifts due to calibration uncertainties in the final assignment of mixing ratio. Flasks in a pair are collected at each station each week whenever possible. The frequency of in situ measurements is once an hour. The NOAA flask post-1996 data, RITS, and CATS system dried the air before sample injection, so there is no water correction. These systems have no CO_2 correction because they use an argon-methane carrier gas (P-5, 5% CH_4 in Ar), and a long Porapak Q column. The CO_2 effect is checked periodically and is undetectable in the post-1996 data and in situ measurements. The individual precisions of each analysis system depended on the station location and time. The individual precisions are given in the individual data files located at ftp://ftp.cmdl.noaa.gov/hats/n_2o. The precisions of the CATS system vary from 0.2 to 1.2 ppb, being highest at Niwot Ridge. The absolute calibration error is estimated at 1%, but the assignment of a calibration tank mixing ratio is between 0.2 and 0.4 ppb consistency with gravimetrically prepared standards from GMD. The mean offset of one method versus the next method is better than 1 ppb. By separating the N_2O detection techniques, we have eliminated the problem

of offsets to any new calibration and comparing sets with the same experimental operating parameters.

Since we are trying to extract a very weak signal from noisy data, we need an objective criterion to ensure reliable detection. Following *Liao et al*. [2004], we applied the multi-taper method (MTM) [*Ghil et al.,* 2002] to establish the existence of the N_2O seasonal cycle. MTM reduces the variance of spectral estimates by using a small set of tapers. Tapers are the specific solution to an appropriate variational problem. Averaging over the ensemble of spectra obtained by this procedure yields a better and more stable estimate than single-taper methods. The parameters of the MTM analysis must be chosen to give a good compromise between the required frequency resolution for resolving distinct signals and the benefit of reduced variance; we chose the resolution to be 2 and the number of tapers to be 3 [*Ghil et al.,* 2002; *Liao et al,* 2004]. Longer data sets permit the use of a larger number of tapers. The criterion we chose was that the seasonal cycle must be below 1% significance level.

We used the above-mentioned three data sets, NOAA flask post-1996, AGAGE 93-03, and CATS, to calculate the N_2O seasonal cycle. First, we used a 4th order polynomial to fit the trend in the monthly mean data. We compared the difference between the 4th order polynomial and the 5th order polynomial, and found no significant difference. Therefore, we used the 4th order polynomial in all subsequent work. After detrending the data by the 4th order polynomial fitting and removed the mean value, we obtain N_2O anomaly, C_{ij}, where i is the index for the month (i ranges from 1 to 12), and j

is the index for the year (j ranges from 1 to N). The units for C_{ij} are ppb. The seasonal cycle is computed by

$$S_i = \sum_{j=1}^{N} (C_{ij} / \sigma_{ij}^2)\sigma_t^2 \qquad (1)$$

where S_i is the residual monthly concentration of N_2O, σ_{ij} is the standard deviation of measurement error for the ith month and the jth year, and $\sigma_t^2 = \left[\sum_{j=1}^{N} 1/\sigma_{ij}^2\right]^{-1}$. The standard deviation, σ, for each of the 12 months is then determined by $\sigma = \sqrt{\sigma_Z^2 + \sigma_S^2}$, where σ_Z^2 and σ_S^2 are the variances for the multi-measurement errors and for the seasonal values in each month. The units for C_{ij}, S_i, and σ are ppb. The details of the error estimate are deferred to Appendix A.

As a demonstration of our methodology, we show the AGAGE data (solid line) at Mace Head (53°N, 10°W) from 1994 to 2003 and 4th order polynomial trend (dotted line) in Figure 6.1a. The residual between the raw data and the trend is shown in Figure 6.1b. The MTM power spectrum of the detrended data is shown in Figure 6.1c. There is a strong seasonal cycle (1 year) below the 1% significance level. The seasonal cycle of N_2O computed using (1) is shown in Figure 6.1d. Shaded area in Figure 6.1d represents the estimated error σ for the seasonal cycle. We also analyzed the Mace Head N_2O data as functions of time by an empirical model consisting of Legendre functions and harmonic (cos, sin) functions [*Prinn et al*., 2000] and obtained similar seasonal cycle.

6.4 Results and Discussion

The statistical significance of the seasonal cycle for the N_2O from 40 datasets listed in Table 6.1 is summarized in Table 6.2. The datasets are separated into two groups according to whether the seasonal cycle is below or above 1% significance level. There are 15 datasets with seasonal cycles that are smaller than 1% significance level. The standard deviations of measurement errors for these 15 datasets are given in brackets. The NOAA flask pre-1996 data have relatively larger measurement errors than NOAA flask post-1996, AGAGE 93-03, CATS, and RITS data. Also, when we have more than one dataset for the same location, we use the data with smaller measurement errors. After applying this criterion, seven stations, marked by asterisks in Table 6.2, are selected for detailed study. These include NOAA flask post-1996, AGAGE 93-03, and CATS. The stations with large measurement errors will be discussed in Appendix B.

The seasonal cycles of these seven datasets are shown in Figure 6.1d and Figures 6.2a-6.2f. In the northern hemisphere (NH), there are three stations. For the first two stations, Alert (ALT) and Barrow (BRW), they have positive values in winter and negative values in summer. The maxima are about 0.4 ppb in March and January, respectively. The minima are about –0.7 ppb in September. The third station in the NH is Mace Head (MHD). The maximum for MHD is 0.21 ppb in March. The minimum is –0.35 ppb in August. The MHD results are in excellent agreement with those in Figure 1a of *Nevison et al.* [2004]. If we take the average of the three NH stations, the result is consistent with Figure 4 of *Liao et al*. [2004], which used pre-1996 NOAA flask data.

The pre-1996 data was noisy, because of greater instrumental imprecision, and CO_2 and H_2O corrections that had to be applied to the original data.

In the tropics, there are two stations with significant seasonal cycles, Cape Kumukahi (KUM) and Cape Matatula (SMO). KUM has a maximum of 0.19 ppb in February, and a minimum of -0.3 ppb in June. SMO has a maximum of 0.3 ppb in January. SMO has a minimum of –0.24 ppb in June.

In the southern hemisphere (SH), there are two stations with significant seasonal cycles, Cape Grim (CGO) and South Pole (SPO). They both have positive values before February and after August. SPO has a maximum of 0.2 ppb in November and a minimum value about -0.11 ppb in April. CGO has a maximum of 0.2 ppb in December, while the minimum is –0.2 ppb in May. The CGO results are in good agreement with those shown in Figure 1c of *Nevison et al.* [2004].

Details for the seasonal amplitude and months for maximum and minimum are summarized in Table 6.3. There is a latitudinal monotonic decrease in the peak-to-peak amplitude from 1.15 ppb at Alert to 0.29 ppb at the South Pole. There appears to be a phase shift of the month of the minimum from April at the South Pole to September at Alert. For the maximum, the phase shifts from November at the South Pole to March at Alert. These results are clearly seen in Figures 6.3 and 6.4.

The 4th order polynomial N_2O trends for the seven stations are shown in Figure 6.5a. The slopes are approximately 0.76, 0.83, 0.76, 0.84, 0.80, 0.79, 0.85 ppb/yr for the seven stations from north to south. The cosine weighted averages for NH, SH and whole planet are 0.81, 0.79, and 0.80 ppb/yr, respectively. The N_2O trends are due to the anthropogenic forcing, and are approximately parallel for the seven stations. The N_2O trends in 2000, 2001, and 2002 are shown in Figure 6.5b. The cosine weighted mean for the N_2O in the NH are 315.58, 316.44, and 317.31 ppb for year 2000, 2001, and 2002. The cosine weighted mean for the N_2O in the SH are 314.95, 315.76, and 316.44 ppb for the three years. The cosine weighted mean for the global N_2O are 315.29, 316.12, and 316.91 ppb for the three years. Averaged over the three years, the N_2O concentration in the NH is higher than that in the SH by 0.73 ppb. Implications for the sources of N_2O are as follows.

The Global Emission Inventory Activities (GEIA) [*Bouwman et al,* 1995] provides a detailed global N_2O emission inventory. The data are the total emission in one year. There are nine types of sources in the inventory, including soil, ocean, post-forest clearing soil, animal excreta, industry, fossil fuel burning, biofuel burning, agriculture, and biomass burning. A hemispheric breakdown of several sources of N_2O is listed in Table 6.4. We sort the sources in four groups, each plotted by latitude in Figure 6.6. The two major sources are soil (Figure 6.6a) and ocean (Figure 6.6b), which emit 7.532 and 3.598 Tg N/yr respectively. Anthropogenic sources, including animal excreta, industry, fossil fuel burning, biofuel burning, and agriculture, are added together in Figure 6.6c. The total emission for the anthropogenic sources is 1.971 Tg N/yr. The post-forest

clearing soil and biomass burning are summed in Figure 6.6d, with total emission of 0.452 Tg N/yr. The ocean source, shown in Figure 6.6b, is mainly in the SH. In the tropics, the N_2O sources are soil, post-forest clearing soil, and biomass burning. To investigate the surface source difference between the two hemispheres, we use a two-box model by *Cicerone* [1989]. We assume the exchange time between hemispheres is 1.5 years. The rates of N_2O loss due to stratospheric processes in both hemispheres are 1/125 yr^{-1}. No soil sink is included. To account for the 0.73 ppb N_2O interhemispheric difference observed in the atmosphere, the difference of N_2O sources between NH and SH is about 4.7 Tg N/yr, which is similar to the results from *Prinn et al*. [1999]. It is larger than the GEIA estimated interhemispheric emission difference 2.657 Tg N/yr in Table 6.4.

The trends in N_2O data shown in Figure 6.5 represent annually averaged values. There are reasons to expect that the trends are seasonally dependent. In other words, the increase of N_2O may result in a change in its seasonal pattern. To investigate the seasonally varying N_2O trend, we use the data at BRW, MHD, SMO, and CGO, which have no gaps and have smaller errors than those at ALT, KUM, and SPO. For illustration, the N_2O data at MHD are shown in Figure 6.7 for June (crosses) and October (diamonds). The slope is determined by minimizing the chi-square. The N_2O trend is higher in October than in June for MHD. The N_2O trends for all months are determined in this way and are shown for the aforementioned four stations in Figure 6.8, along with error bars. For stations BRW and MHD, which are in the NH, the N_2O trends have large seasonal cycles. The peak-to-peak amplitudes are about 0.15 ppb/yr for both stations. In

the SH, the seasonal cycle for the N_2O trend is large at SMO with a peak-to-peak amplitude about 0.15 ppb/yr. The seasonal cycle for the N_2O trend is small at CGO with amplitude of 0.06 ppb/yr.

As pointed out by previous studies [*Levin et al.*, 2002; *Liao et al.*, 2004; *Nevison et al.*, 2004], the N_2O seasonal cycle in the NH may be related to the circulation in the stratosphere. The N_2O seasonal cycle in the SH may be related to the seasonal cycle in the ocean source [*Nevison et al.*, 2005]. The cause of N_2O seasonal cycle in the tropics is currently unidentified. We provide here a simple estimate that relates the seasonal cycle in N_2O concentration to its source using a heuristic model. The model describes the time evolution of the concentration of N_2O, which has a linear sink and a sinusoidal source [*Camp et al.*, 2001]:

$$\frac{dC(t)}{dt} = -\frac{C(t)}{\tau} + S(t) \tag{2a}$$

$$S(t) = (A_0 + A_1 \sin(\omega t))/\tau \tag{2b}$$

where $C(t)$ is the concentration of N_2O, τ is the lifetime of the N_2O, and $S(t)$ consists of a steady-state term and a sinusoidally varying term, ω is the frequency for the annual cycle. The solution to equation (2a) is

$$C(t) = \left[C(0) - A_0 + \frac{A_1 \sin\phi}{\sqrt{1+\omega^2\tau^2}} \right] e^{-t/\tau} + A_0 + \frac{A_1 \sin(\omega t - \phi)}{\sqrt{1+\omega^2\tau^2}} \tag{3}$$

where $C(0)$ is the initial concentration of N_2O. Because the mean lifetime of N_2O is about 125 yrs, we have $\omega\tau >> 1$. Then we get $\phi = \arctan(\omega\tau) \approx \pi/2$ and $\sqrt{1+\omega^2\tau^2} \approx \omega\tau$. Now the non-transient solution for equation (2a) can be written as

$$C(t) \approx A_0 + \frac{A_1 \sin(\omega t - \phi)}{\sqrt{1+\omega^2\tau^2}} \approx A_0 + \frac{A_1 \sin(\omega t - \pi/2)}{\omega\tau} = A_0 - \frac{A_1 \cos(\omega t)}{\omega\tau} \qquad (4)$$

From equations (2b) and (4), we note that the oscillatory parts of $S(t)$ and $C(t)$ are related by $\omega = 2\pi/T$, where T = 1 year. This result can be used to estimate the relative importance of A_0 and A_1 in the N_2O source.

Figure 6.3a suggests that the seasonal amplitude (peak to peak) consists of a roughly uniform global value of 0.5 ppb. The higher NH high latitude value of 1 ppb is partly due to the influence from the stratosphere [*Levin et al*., 2002; *Liao et al*., 2004; *Nevison et al*., 2004]. Thus, from equation (4), we have

$$\frac{2A_1}{\omega\tau} = 0.5\,ppb \qquad (5)$$

$$\frac{A_1}{\tau} = \frac{0.5\omega}{2} = 1.57\,ppb/yr = 7.54\,TgN/yr \qquad (6)$$

where we have used the conversion 1 ppb N_2O (global) equals 4.80 Tg N (see, e.g., section 4.7 of *Morgan et al*. 2004). From Table 6.4, we have the steady-state source $\frac{A_0}{\tau} = 13.55 TgN/yr$. Combining this with equation (6), we arrive at the estimate, $\frac{A_1}{A_0} = 0.56$. Therefore, the seasonally varying part of the N_2O source is as much as 50% of the steady source.

6.5 Conclusion

We have used the MTM spectrum analysis to derive a statistically significant seasonal cycle in the observed data from seven stations. Three stations are in the NH; two

are in the SH and two in the tropics (see Table 6.2). The peak-to-peak amplitude of the N_2O seasonal cycle increases with latitude from 0.29 ppb at SPO to 1.15 ppb at ALT as shown in Figure 6.3a. There are also phase shifts in the maximum and minimum month of the seasonal cycles from the SH to NH. The trends in N_2O data are also seasonally dependent. The seasonal cycles of the N_2O trends at BRW, MHD, and SMO are larger than that at CGO.

The N_2O seasonal cycle provides constraints for the N_2O surface sources. In the NH, the N_2O seasonal cycle may be influenced by the stratosphere. In the SH, the N_2O seasonal cycle may be mostly due to the ocean source. The N_2O seasonal cycle in the tropics is puzzling. We speculate that there is a much larger biomass burning and soil emission source for the tropics than in current models. Inverse modeling will be carried out to deduce the seasonal variability of the biological sources.

6.6 Appendix A: Estimation of Error in Computing the N_2O Seasonal Cycle

The estimated errors for the weighted mean of multi-measurements are discussed in this appendix. We assume Gaussian distribution of measurement errors. In section A1, the standard deviation for a case with only two measurements is discussed. In section A2, we derive the standard deviation for multiple measurements case. Finally, we discuss the estimated errors for the N_2O measurements using the results from section A1 and A2.

6.6.1 Two-measurement Case

For a two-measurement case, the probability density function (PDF) can be written as

$$f_j(x_j) \propto \exp[-(x_j - \bar{x}_j)^2 / \sigma_j^2], \quad j = 1, 2 \qquad \text{(A1)}$$

where σ_j is the standard deviation for the measurement x_j. Thus the PDF for variable $x = x_1 + x_2$ is

$$f(x) \propto \int_{-\infty}^{+\infty} f_2(x-t)\, f_1(t)\, dt \propto \int_{-\infty}^{+\infty} \exp[-(x-t-\bar{x}_2)^2 / \sigma_2^2] \exp[-(t-\bar{x}_1)^2 / \sigma_1^2]\, dt$$

$$\propto \exp\{-[x-(\bar{x}_1+\bar{x}_2)]^2 / (\sigma_1^2+\sigma_2^2)\} \qquad \text{(A2)}$$

Therefore, the mean of x is $\bar{x}_1 + \bar{x}_2$, and the standard deviation is $\sqrt{\sigma_1^2 + \sigma_2^2}$.

6.6.2 Multi-measurement Case

For multi-measurements $\{x_j\}$ with standard deviation $\{\sigma_j\}$, the PDF for variable $X = \sum_{j=1}^{N} x_j$ is

$$f(X) \propto \exp[-(X - \overline{X})^2 / \sigma_X^2], \qquad \text{(A3)}$$

where $\overline{X} = \sum_{j=1}^{N} \overline{x}_j$ and $\sigma_X = \sqrt{\sum_{j=1}^{N} \sigma_j^2}$. N is the total number of measurements.

Thus, the mean and the standard deviation for the variable $Y = \frac{1}{N} \sum_{j=1}^{N} x_j$ are separately $\overline{Y} = \frac{1}{N} \sum_{j=1}^{N} \overline{x}_j$ and $\sigma_Y = \frac{1}{N} \sqrt{\sum_{j=1}^{N} \sigma_j^2}$.

6.6.3 N_2O-measurement Case

For the N_2O measurements $\{x_j\}$ discussed in chapter, the monthly mean N_2O concentrations, $\overline{x}_j$, were measured with varying precision. Let σ_j represents the standard deviation for each measurement. We need consider the weighted value of the N_2O measurements, $Z = \sum_{j=1}^{N} (x_j / \sigma_j^2) \sigma_t^2$, where $\sigma_t^2 = \left[\sum_{j=1}^{N} 1/\sigma_j^2 \right]^{-1}$ [*Liao et al*., 2004].

From equation (A3), the PDF for variable Z can be written as

$$f(Z) \propto \exp[-(Z - \overline{Z})^2 / \sigma_Z^2], \qquad \text{(A4)}$$

where $\overline{Z} = \sum_{j=1}^{N} (\overline{x}_j / \sigma_j^2) \sigma_t^2$ and $\sigma_Z^2 = \sum_{j=1}^{N} (\sigma_t^2 / \sigma_j^2)^2 \sigma_j^2 = \sigma_t^4 \sum_{j=1}^{N} (1/\sigma_j^2) = \sigma_t^2$.

To further consider the N_2O variance due to the different seasonal values in different years, the standard deviation, σ, for the seasonal cycle of N_2O are finally determined by

$$\sigma = \sqrt{\sigma_Z^2 + \sigma_S^2}\ , \qquad \text{(A5)}$$

where σ_Z^2 is the variance for the measurement errors, $\sigma_S^2 = \frac{1}{N}\sum_{j=1}^{N}(\bar{x}_j - x_j^*)^2$ is the variance for the seasonal values in each month, and x_j^* is the mean of $\bar{x}_j$ for a particular month over all years.

6.7 Appendix B: N_2O Seasonal Cycle in the Stations With Large Measurement Errors

In Table 6.2, there are eight stations with significant seasonal cycles that are not used for detailed analysis in the main text. The measurement errors are relatively larger for these stations. For comparison purpose, we present their seasonal cycles in Figure 6.9. In the NH, there are six stations: NOAA flask pre-1996 Alert, NOAA flask pre-1996 Barrow, NOAA flask pre-1996 Mauna Loa, NOAA flask post-1996 Barrow, RITS Barrow, RITS Niwot Ridge (NWR). For these six stations, they have positive values in winter and negative value in the summer. The maxima are before May ranging from 0.12 to 1.06 ppb. The minima are after June ranging from –1.49 to -0.24 ppb. In the SH, there are two stations: NOAA flask pre-1996 Cape Grim and RITS South Pole. They both have positive values before February and after August. NOAA flask pre-1996 Cape Grim has maximum of 1.1 pb in November, while the minimum is –1.5 ppb in April. RITS South Pole has a maximum of 0.29 ppb in February and a minimum about -0.25 ppb in May. Within the large error bars, these results are consistent with those for the seven stations summarized in Figure 6.1d and Figure 6.2.

6.8 References

Battle, M., M. Bender, T. Sowers, P.P. Tans, J.H. Butler, J.W. Elkins, J.T. Ellis, T. Conway, N. Zhang, P. Lang, and A.D. Clarke, Atmospheric gas concentrations over the past century measured in air from firn at the South Pole, *Nature*, *383*, 231-235, 1996.

Bouwman, A.F., K.W. van der Hoek, and J.G.J. Oliver, Testing high-resolution nitrous oxide emission estimates against observations using an atmospheric transport model, *J. Geophys. Res., 100*, 2785-2800, 1995.

Camp, C.D., M.S. Roulston, A.F.C. Haldemann, and Y.L. Yung, The sensitivity of tropospheric methane to the interannual variability in stratospheric ozone, *Chemosphere-Global Change Science, 3*, 147-156, 2001.

Cicerone, R., Analysis of sources and sinks of atmospheric nitrous oxide (N_2O), *J. Geophys. Res., 94*, 18265-18271, 1989.

Ghil, M., M.R. Allen, M.D. Dettinger, K. Ide, D. Kondrashov, M.E. Mann, A.W. Robertson, A. Saunders, Y. Tian, F. Varadi, and P. Yiou, Advanced spectral methods for climatic time series, *Rev. Geophys., 40 (1)*, art. no. 2000RG000092, 2002.

Jaeglé, L., R.V. Martin, K. Chance, L. Steinberger, T.P. Kurosu, D.J. Jacob, A.I. Modi, V. Yoboué, L. Sigha-Nkamdjou, C. Galy-Lacaux, Satellite mapping of rain-induced nitric oxide emissions from soils, *J. Geophys. Res., 109*, art. no. 2004JD004787, 2004.

Levin, I., *et al.*, Three years of trace gas observations over the EuroSiberian domain derived from aircraft sampling — a concerted action, *Tellus, 54B*, 696-712, 2002.

Liao, T., C.D. Camp, and Y.L. Yung, The seasonal cycle of N_2O, *Geophys. Res. Lett., 31*, art. no. 2004GL020345, 2004.

McElroy, M.B., S.C. Wofsy, and Y.L. Yung, Nitrogen Cycle - Perturbations Due to Man and Their Impact on Atmospheric N_2O and O_3, *Philosophical Transactions of the Royal Society of London Series B-Biological Sciences, 277*, 159-181, 1977.

McLinden, C.A., M.J. Prather, and M.S. Johnson, Global modeling of the isotopic analogues of N_2O: Stratospheric distributions, budgets, and the O-17-O-18 mass-independent anomaly, *J. Geophys. Res., 108 (D8)*, art. no. 4233, 2003.

Minschwaner, K., R.J. Salawitch, and M.B. McElroy, Absorption of Solar-Radiation by O_2 - Implications for O_3 and Lifetimes of N_2O, $CFCL_3$, and CF_2CL_2, *J. Geophys. Res., 98* (D6), 10543-10561, 1993.

Morgan, C.G., M. Allen, M.C. Liang, R.L. Shia, G.A. Blake, and Y.L. Yung, Isotopic fractionation of nitrous oxide in the stratosphere: Comparison between model and observations, *J. Geophys. Res., 109* (D4), art. no. 2003JD003402, 2004.

Nevison, C.D., D.E. Kinnison, and R.F. Weiss, Stratospheric influences on the tropospheric seasonal cycles of nitrous oxide and chlorofluorocarbons, *Geophys. Res. Lett., 31* (20), art. no. L20103, 2004.

Nevison, C.D., R.F. Keeling, R.F. Weiss, B.N. Popp, X. Jin, P.J. Fraser, L.W. Porter, P.G. Hess, Southern Ocean ventilation inferred from seasonal cycles of atmospheric N_2O and O_2/N_2 at Cape Grim, Tasmania, *Tellus, 57B*, 218-229, 2005.

Prinn, R.G., *et al*., Atmospheric emissions and trends of nitrous oxide deduced from 10 years of ALE-GAGE data, *J. Geophys. Res., 95*, 18369-18385, 1990.

Prinn, R.G., *et al*., A history of chemically and radiatively important gases in air deduced from ALE/GAGE/AGAGE, *J. Geophys. Res., 105*, 17751-17792, 2000.

Stein, L.Y., and Y.L. Yung, Production, isotropic composition, and atmospheric fate of biologicall produced nitrous oxide, *Annual Review of Earth and Planetary Sciences, 31*, 329-356, 2003.

Thompson, T. M., *et al*., Halocarbons and other atmospheric trace species, *Climate Monitoring Diagnostics Lab. Summary Rep. 27 2002-2003*, edited by R.C. Schnell, A.-M. Buggle, and R. M. Rosson, pp. 115-135, U.S. Dept. of Commerce., Boulder, Colo, 2004.

Volk, C.M., J.W. Elkins, D.W. Fahey, G.S. Dutton, J.M. Gilligan, M. Loewenstein, J.R. Podolske, K.R. Chan, and M.R. Gunson, Evaluation of source gas lifetime from stratospheric observations, *J. Geophys. Res.*, *102* (D21), 25543-25564, 1997.

Table 6.1: Locations of stations and length of records in all measurement programs.

Measurement Program	Station Name	Latitude	Longitude	Time
NOAA flask	Alert (ALT)	82°N	62°W	2/1988-12/1995; 12/1994-8/2002
	Barrow (BRW)	71°N	157°W	9/1977-12/1995; 12/1994-10/2002
	Niwot Ridge (NWR)	40°N	106°W	8/1977-12/1995; 1/1995-10/2002
	Cape Kumukahi (KUM)	19°N	155°W	11/1995-10/2002
	Mauna Loa (MLO)	19°N	156°W	9/1977-12/1995; 1/1995-10/2002
	Cape Matatula (SMO)	14°S	171°W	10/1977-12/1995; 11/1994-10/2002
	Cape Grim (CGO)	40°S	145°E	5/1991-12/1995; 2/1995-10/2002
	South Pole (SPO)	90°S	102°W	5/1977-12/1995; 3/1995-2/2002
CATS	Barrow (BRW)	71°N	157°W	6/1998-12/2004
	Niwot Ridge (NWR)	40°N	106°W	1/2001-11/2004
	Mauna Loa (MLO)	19°N	156°W	12/1999-12/2004
	Cape Matatula (SMO)	14°S	171°W	1/1999-12/2004
	South Pole (SPO)	90°S	102°W	1/1998-12/2004
AGAGE	Mace Head (MHD)	53°N	10°W	3/1994-3/2003
	Trinidad Head	45°N	124°W	10/1995-3/2003
	Ragged Point	13°N	59°W	7/1996-3/2003
	Cape Matatula (SMO)	14°S	171°W	9/1996-3/2003
	Cape Grim (CGO)	40°S	145°E	9/1993-3/2003
RITS	Barrow (BRW)	71°N	157°W	9/1987-2/1999
	Niwot Ridge (NWR)	40°N	106°W	2/1990-8/2001
	Mauna Loa (MLO)	19°N	156°W	6/1987-4/2000
	Cape Matatula (SMO)	14°S	171°W	9/1987-4/2000
	South Pole (SPO)	90°S	102°W	1/1989-11/2000

The data are available from the following websites.

NOAA flask: ftp://ftp.cmdl.noaa.gov/hats/n2o/flasks/

CATS: ftp://ftp.cmdl.noaa.gov/hats/n2o/insituGCs/CATS/global/insitu_global_N2O

AGAGE: http://cdiac.ornl.gov/ftp/ale_gage_Agage/AGAGE/gc-md/monthly/

RITS: ftp://ftp.cmdl.noaa.gov/hats/n2o/insituGCs/RITS/.

Table 6.2: Separation of datasets into two groups according to whether the seasonal cycle is below or above 1% significance level. The standard deviations of measurement errors are given in brackets by $\frac{1}{N}\sqrt{\sum_{j=1}^{N}\sigma_j^2}$. Units are ppb. Seven stations marked by asterisks are selected for detailed study.

Data	Below 1%	Above 1%
NOAA flask pre-1996	Alert (0.267) Barrow (0.160) Mauna Loa (0.174) Cape Grim (0.289)	Niwot Ridge Cape Matatula South Pole
NOAA flask post-1996	Alert (0.062)* Barrow (0.060) Cape Kumakahi (0.047)*	Niwot Ridge Mauna Loa Cape Matatula Niwot Ridge South Pole
AGAGE 78-86	None	Mace Head Trinidad Head Ragged Point Cape Matatula Cape Grim
AGAGE 85-96	None	Mace Head Trinidad Head Ragged Point Cape Matatula Cape Grim
AGAGE 93-03	Mace Head (0.022)* Cape Matatula (0.033)* Cape Grim (0.024)*	Trinidad Head Ragged Point
CATS	Barrow (0.004)* South Pole (0.007)*	Mauna Loa Cape Matatula Niwot Ridge
RITS	Barrow (0.070) Niwot Ridge (0.182) South Pole (0.066)	Mauna Loa Cape Matatula

Table 6.3: Summary of the peak-to-peak amplitude in ppb, month of maximum and month of minimum in the seasonal cycles shown in Figure 6.1d and Figures 6.2a-6.2f.

Station	Amplitude	Maximum Month	Minimum Month
Alert	1.15	Mar	Sep
Barrow	1.06	Jan	Sep
Mace Head	0.57	Mar	Aug
Cape Kumukahi	0.50	Feb	Jun
Cape Matatula	0.55	Jan	Jun
Cape Grim	0.42	Dec	May
South Pole	0.29	Nov	Apr

Table 6.4: Sources of N_2O (in Tg N/yr). Anthropogenic sources include animal excreta, industry, fossil fuel burning, biofuel burning, and agriculture. The latitudinal distributions of the sources are plotted in Figure 6.6.

Source	NH	SH	Global
Soil	4.601	2.931	7.532
Ocean	1.546	2.052	3.598
Anthropogenic Sources	1.701	0.270	1.971
Post-forest clearing soil + Biomass burning	0.257	0.195	0.452
Total Sources	8.105	5.448	13.553

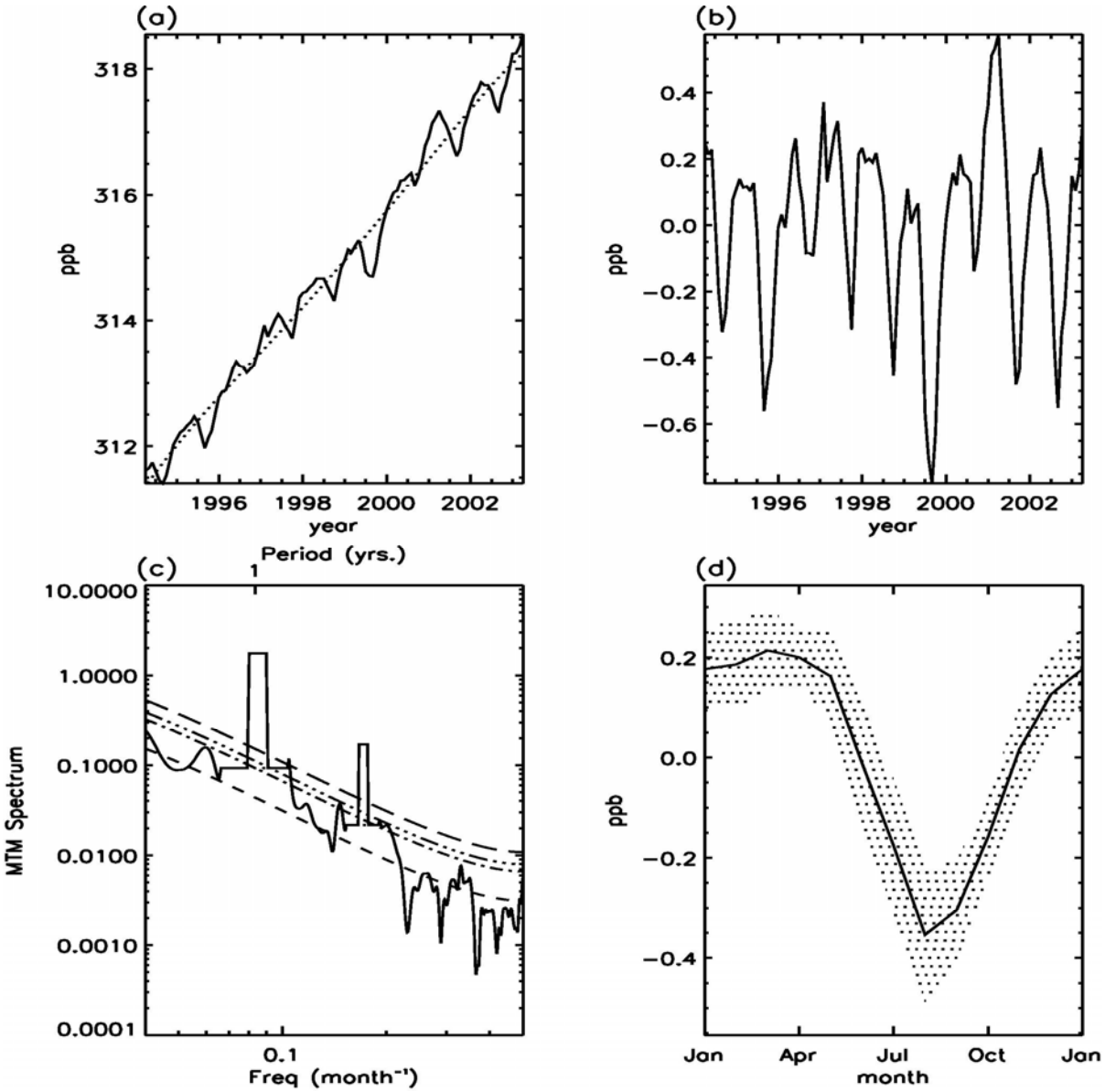

Figure 6.1: Analysis of N_2O AGAGE data at Mace Head (53°N, 10°W). (a) Raw data (Solid) and 4th order polynomial trend (Dotted). (b) Detrended data. (c) Estimate of power spectrum by multi-taper method. The dashed lines represent the median, 10%, 5%, and 1% significance level. (d) Seasonal Cycle of N_2O derived from monthly weighted means (solid line). Shaded area represents the estimated error, $\sigma = \sqrt{\sigma_Z^2 + \sigma_S^2}$, for the seasonal cycle.

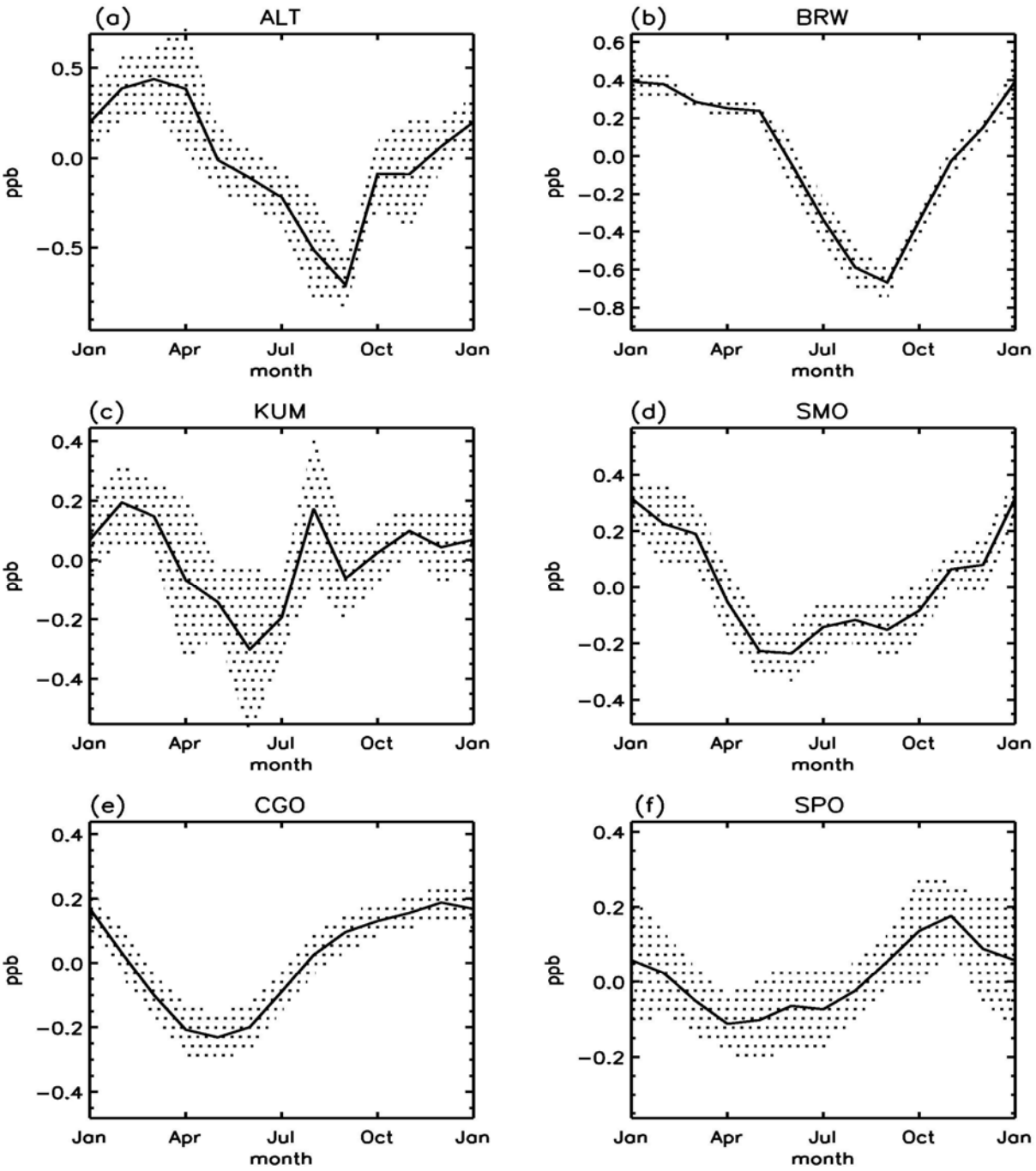

Figure 6.2: Same as Figure 6.1(d) for AGAGE, CATS, and NOAA flask data. The solid line is the seasonal cycle. Shaded area represents the estimated error of the seasonal cycle. (a) NOAA flask, Alert (82°N, 62°W). (b) CATS, Barrow (71°N, 157°W). (c) NOAA flask, Cape Kumukahi (19°N, 155°W). (d) AGAGE, Cape Matatula (14°S, 171°W). (e) AGAGE, Cape Grim (41°S, 145°E). (f) CATS, South Pole (90°S, 102°W).

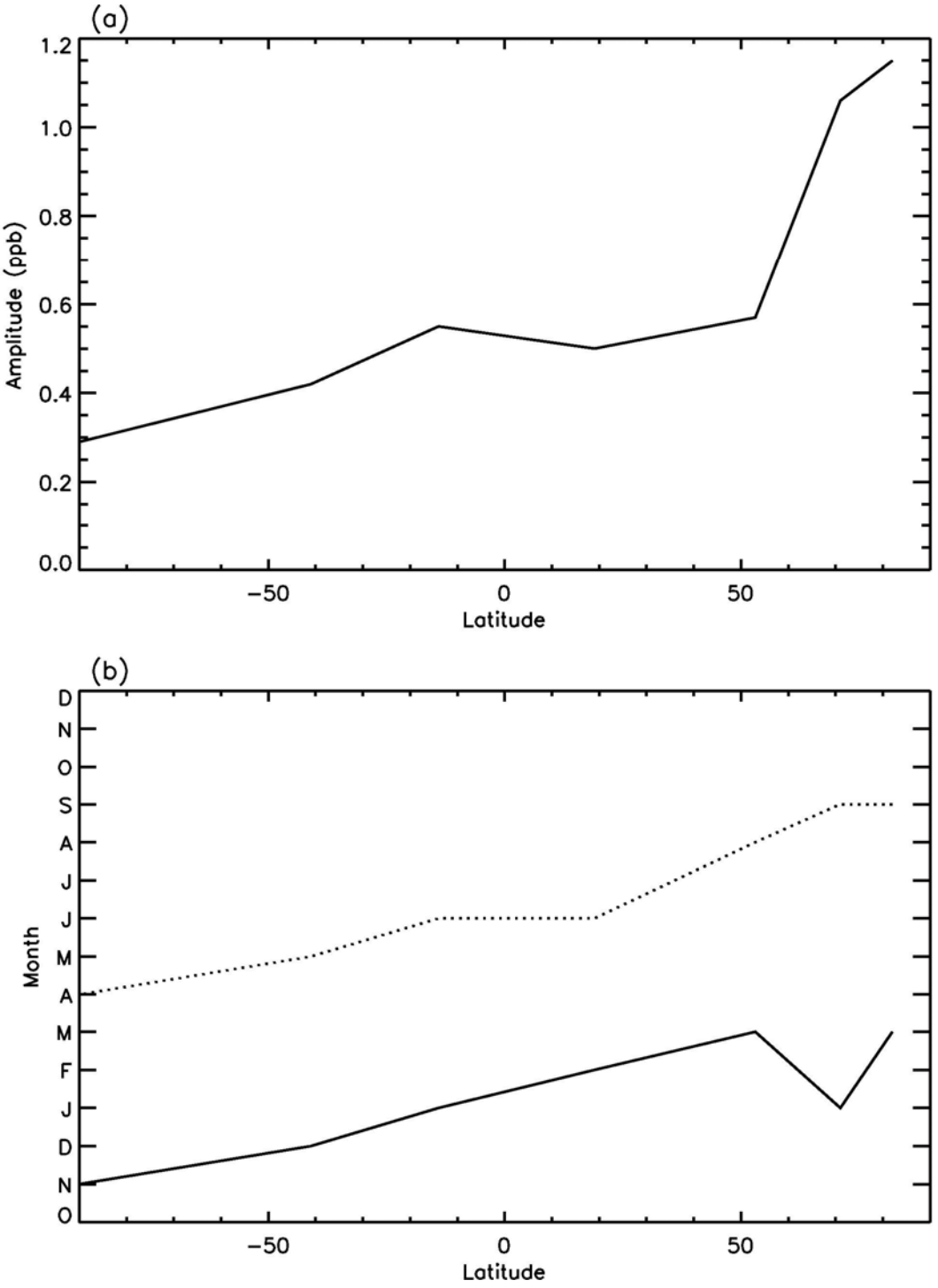

Figure 6.3: (a) N_2O seasonal cycle amplitudes for the seven stations. (b) Latitude distribution of maximum (solid line) and minimum (dotted line) month in the N_2O seasonal cycle.

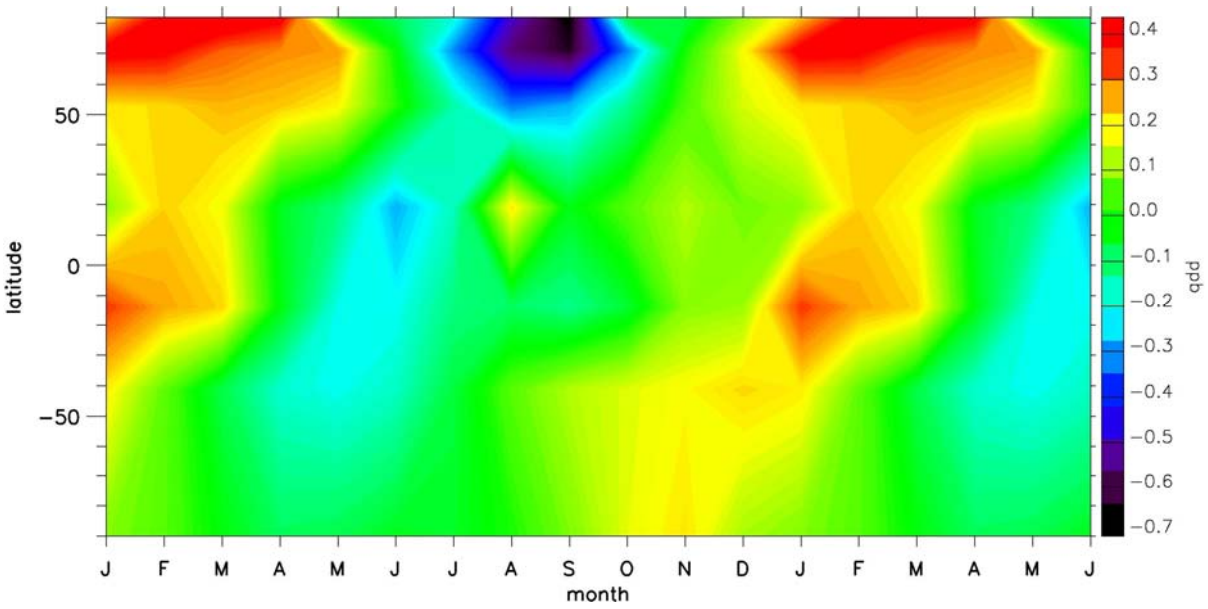

Figure 6.4: Seasonal cycle from the data of seven stations: Alert, Barrow, Cape Kumukahi, Mace Head, Cape Matatula, Cape Grim, and South Pole. The data for the first six months of the year are repeated after December.

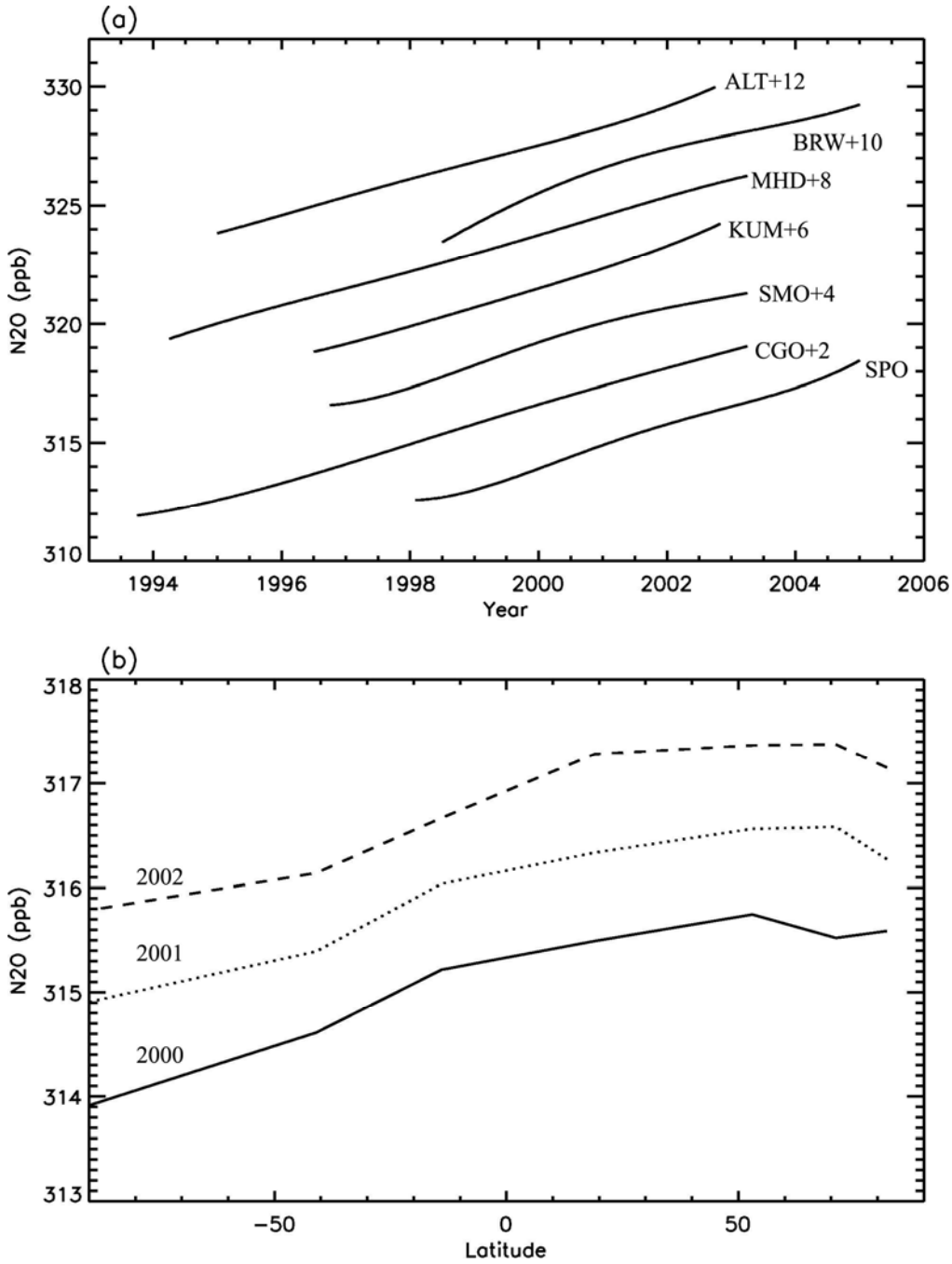

Figure 6.5: (a) Fourth order polynomial N_2O trend for the seven stations. For visualizations, the N_2O trends for Alert, Barrow, Mace Head, Cape Kumukahi, Cape Matatula, Cape Grim have been shifted upward by 12, 10, 8, 6, 4, 2 ppb respectively. (b) N_2O variation with latitude in 2000 (solid line), 2001 (dotted line), and 2002 (dashed line).

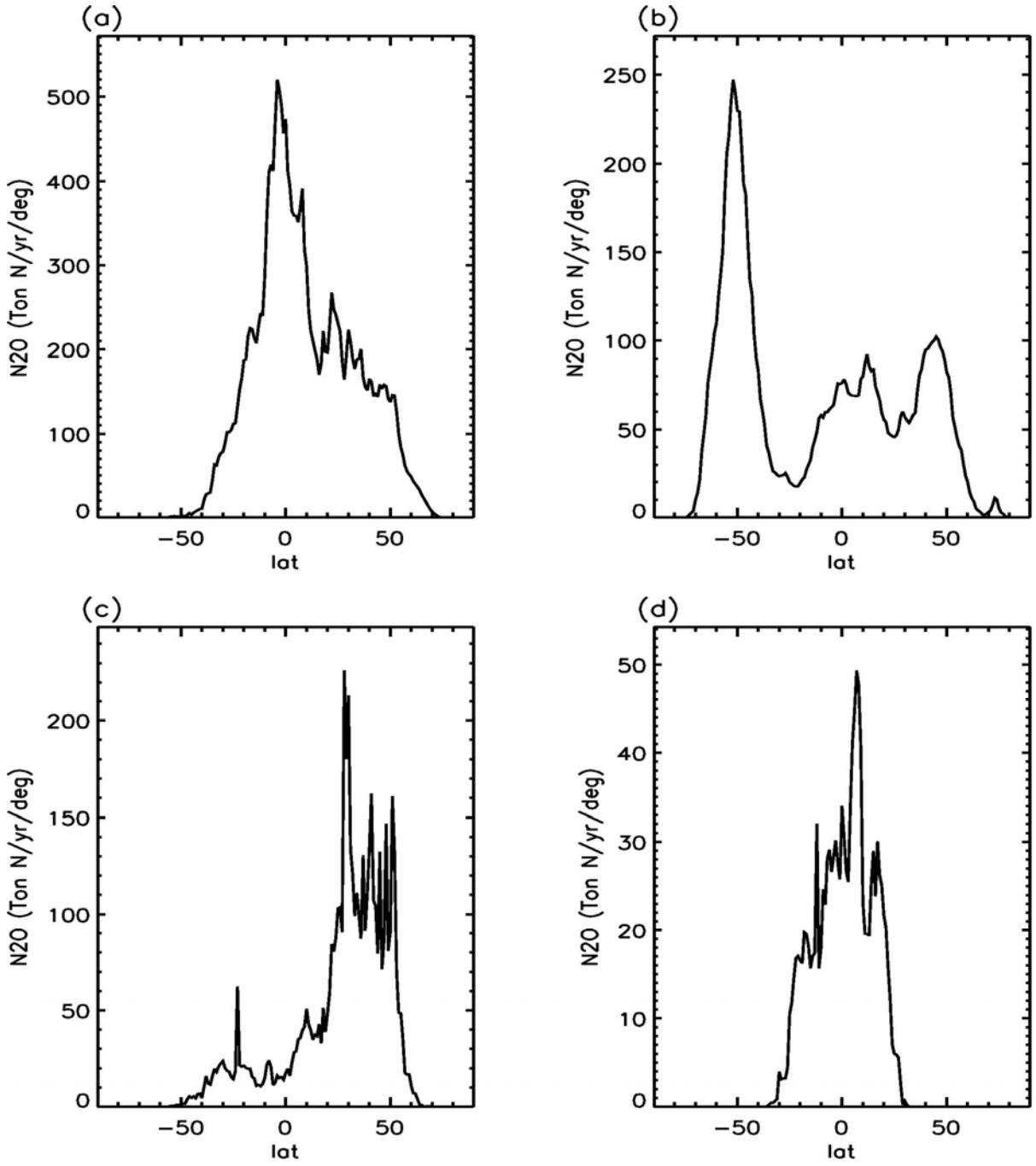

Figure 6.6: N_2O (Ton Nyr^{-1}) for the nine sources from GEIA. (a) Soil, (b) Ocean, (c) Sum of animal excreta, industry, fossil fuel burning, biofuel burning, and agriculture, (d) Sum of post-forest clearing soil and biomass burning.

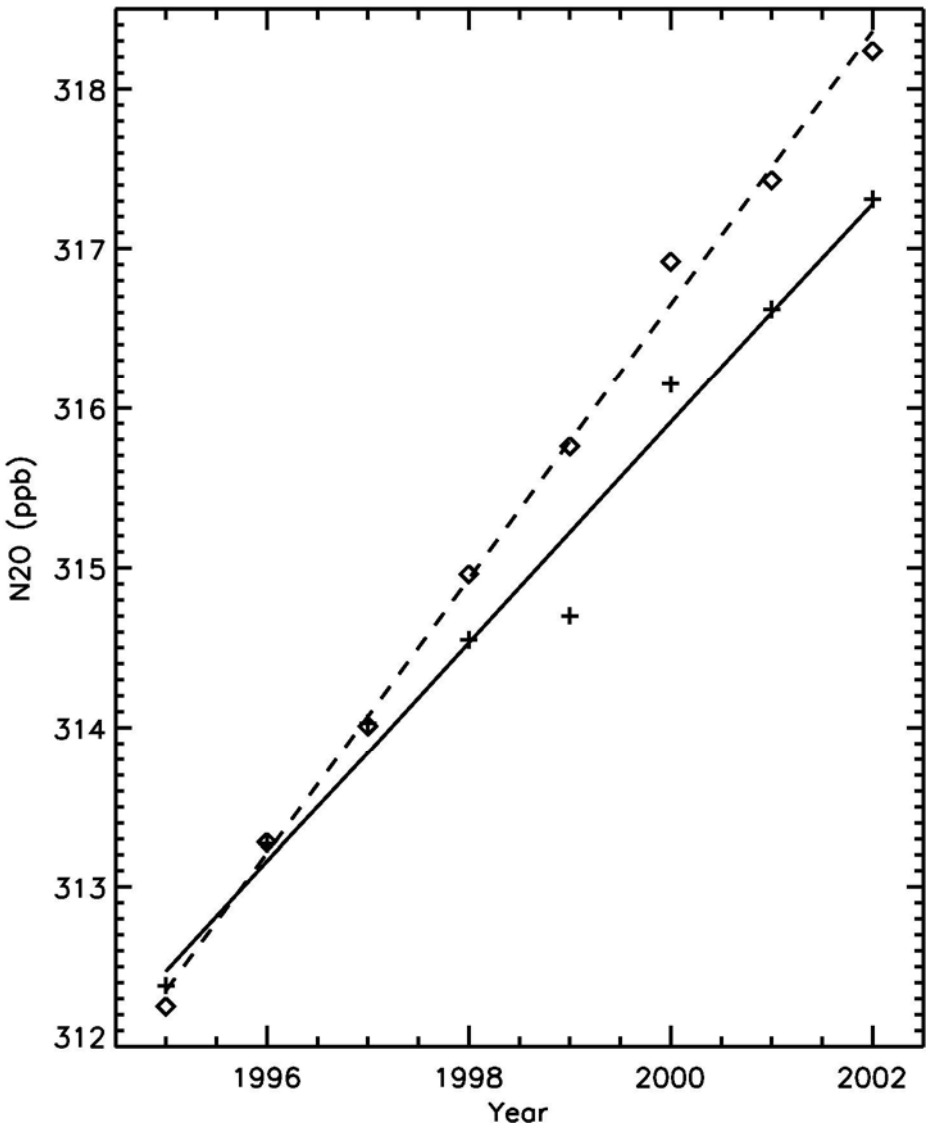

Figure 6.7: N_2O trend at Mace Head in June (solid line) and October (dashed line). Crosses and diamonds are the raw data for Mace Head in June and October, respectively.

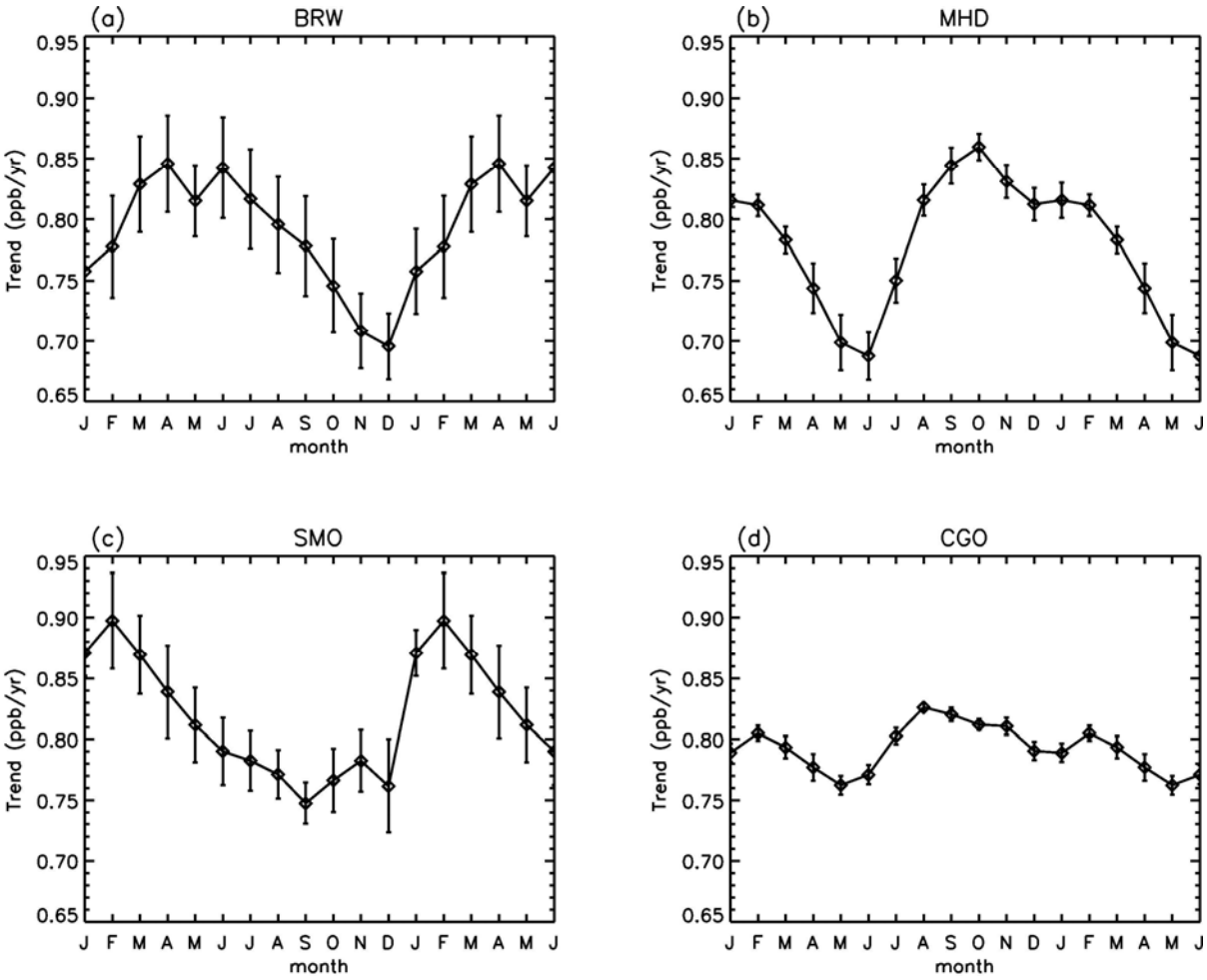

Figure 6.8: N_2O trend from the data of four stations. (a) Barrow, (b) Mace Head, (c) Cape Matatula, and (d) Cape Grim. The data for the first six months of the year are repeated after December.

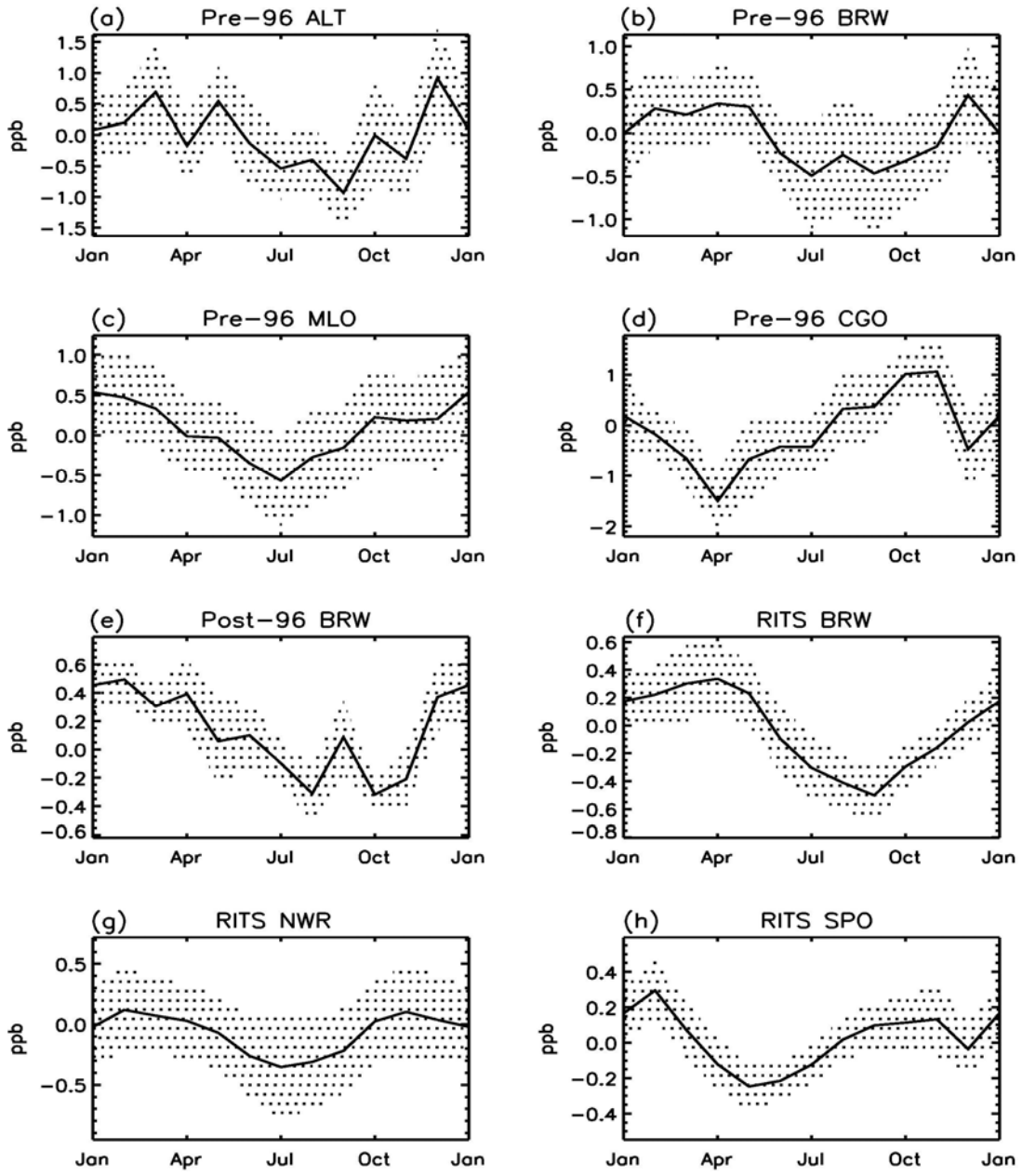

Figure 6.9: N_2O seasonal cycle (solid line) for the eight stations with large measurement errors. Shaded area represents the estimated error, $\sigma = \sqrt{\sigma_Z^2 + \sigma_S^2}$, for the seasonal cycle. (a) NOAA flask pre-1996 Alert, (b) NOAA flask pre-1996 Barrow, (c) NOAA flask pre-1996 Mauna Loa, (d) NOAA flask pre-1996 Cape Grim, (e) NOAA flask post-1996 Barrow, (f) RITS Barrow, (g) RITS Niwot Ridge (NWR), and (h) RITS South Pole.